

DEPARTMENT OF MECHANICAL
AND AERONAUTICAL ENGINEERING
UNIVERSITY OF PRETORIA



EXPERIMENTAL INVESTIGATION INTO THE
INFLUENCE OF LOW MASS AND HEAT FLUXES
AND TRANSIENT PERTURBANCES IN VAPOUR
QUALITY AND HEAT FLUX ON THE BEHAVIOUR
OF BOILING R-245FA IN HORIZONTAL PIPES

WILHELM JOHANN VAN DEN BERGH

SUPERVISED BY:

PROFESSOR J. DIRKER

PROFESSOR J.P. MEYER

PROFESSOR C.N. MARKIDES

THESIS SUBMITTED TO THE UNIVERSITY OF PRETORIA

IN PARTIAL FULFILMENT FOR THE DEGREE OF

DOCTOR OF PHILOSOPHY IN ENGINEERING

NOVEMBER 2021

“If I have seen further than other men,
it is because I have stood on the shoulders of giants”

–Isaac Newton

Vir pappa en mamma

ABSTRAK

Die gebruik van sonkrag vir die opwekking van elektrisiteit het in die afgelope paar dekades meer en meer aandag begin kry, veral om die uitermatige steun op fossiel brandstowwe en die antropogeniese effek wat dit op die klimaat het te probeer stuit. Terwyl fotovoltaïese kragopwekking 'n beduidende rol speel, is gekonsentreerde sonkrag, gekoppel met termiese stoor-metodes, meer gepas om basis opwekking te verskaf. Een van die primêre navorsings-areas wat steeds dringend aandag vereis is die effek wat die verbygaande aard van die son op die krag-omskakelings proses het.

Wanneer 'n vloeistof die kook-proses vir gebruik in termodinamiese siklusse ondergaan in die sons-vesamelings veld, stel dit direkte stoom opwekking in staat. Hierdie opwekkings-metode hou verskeie termodinamiese, asook omgewings en koste, voordele in. Die termodinamiese staat in hierdie vloei-kook scenarios is egter ook hoogs vatbaar vir kort-termyn fluktuasie in die vloei-inlaat toestande en die termiese hitte vloed grenstoestand wat veroorsaak word deur, byvoorbeeld, korstondige wolk bedekking van die versamelings veld. Min gedokumenteerde navorsing vir hierdie toestande is beskikbaar.

In 'n poging om hierdie agterstand aan te spreek, is die eksperimentele werk wat hierdie tesis bevat voltooi. Die studie het veral gefokus op hitte oordrag koëffisiënte en drukval gevalle waar min of geen data beskikbaar is nie. 'n Eksperimentele fasiliteit is ontwerp en opgerig om verskeie effekte op die hitte oordrag koëffisiënt en druk val in 'n vloei-inlaat te bestudeer. 'n Horisontale toets-seksie, wat uit 'n gelykmatig-verhitte koper pyp met 'n lengte van 800 mm en 'n binne-diameter van 8.31 mm bestaan het, is gefabriseer. R-245fa is die toets vloeistof wat gekies is omdat dit al voorgestel is vir gebruik in direkte damp opwekking organiese Rankine-siklusse. Vir praktiese redes is 'n versadigings temperatuur van 35 °C gekies en fokus is geplaas op areas wat nog nie beduidende aandag in literatuur ontvang het nie.

Eerstens is die gedrag van gestadigde hitte oordrag koëffisiënte by relatiewe lae massa- en hitte-vloede (onder 100 kg/m²s en 7.5 kW/m²) ondersoek oor die hele reeks damp kwaliteite van 0.05 tot 0.90. Dit is bevind dat 'n hoër massa vloed altyd tot 'n hoër hitte oordrag koëffisiënt gelei het vir 'n gegewe hitte vloed dwarsdeur die damp-kwaliteit reeks. By die laagste hitte-vloed wat ondersoek is, het die hitte oordrag koëffisiënt egter onreëlmatige gedrag getoon. Dit was tot 70% hoër as vir hoër hitte-vloede by damp kwaliteite van 0.15 tot 0.30.

Tweedens is die effek wat 'n skielike verandering in die damp kwaliteit by die inlaat van die toetsseksie op die hitte oordrag koëffisiënt gehad het bestudeer. Massa-vloede van 200 en 300 kg/m²s is ondersoek by damp-kwaliteite van 0.15 tot 0.40, wat gekies is om verskeie vloei-patrone te dek. Vir

‘n stap-verandering van grootte 0.13 in die damp kwaliteit is gevind dat die hitte oordrag koëffisiënt verskil het van die quasi-gestadigde voorspellings. Dit was hoër as die verwagte gedurende die afwaartse verstourings en laer gedurende die opwaartse verstourings.

Laastens is die impak wat ‘n verstouring in die hitte-vloed direk in die toetsseksie op die hitte oordrag koëffisiënt en drukval gehad het ondersoek. Hierdie toetse is gedoen teen ‘n massa-vloed van $200 \text{ kg/m}^2\text{s}$ oor ‘n damp-kwaliteit reeks van 0.10 tot 0.85. Gebaseer op feitelike direkte normale bestralings data is ‘n reduksie van 75% in die hitte vloed toegepas oor ‘n periode van 30 s met stap, driehoekige, en sinusgolf verstourings, wat in ‘n beheerde vorm toegepas is. Gedurende die skielike stap-verstouring in die hitte-vloed is gevind dat die gemiddelde hitte oordrag koëffisiënt 30% laer was as die onversteurde waarde. Vir die driehoekige en sinusgolf verstourings was die hitte oordrag koëffisiënt 8% laer as die onversteurde waarde. Die drukval was onaangetas deur enige van die verskillende verstourings.

Dit is ons erns.

ABSTRACT

The use of solar power to generate electricity has gained increasing traction over the last few decades, particularly to offset the excessive reliance on fossil fuels and the anthropogenic effect this has on the climate. While photovoltaic electricity production plays a significant role, concentrated solar power, coupled with thermal energy storage, is more suited for providing baseline grid power. One of the prime areas still needing research, however, is the transient nature of solar irradiation and its influence on the operation of the power conversion process.

When a fluid undergoes flow boiling for use in thermodynamic power cycles within the solar field, it enables the implementation of direct steam generation cycles. These offer several thermodynamic, environmental and cost advantages. However, the thermal operating state of these flow-boiling scenarios is more susceptible to short term transient changes in the fluid inlet condition and thermal heat flux boundary condition caused by, for instance, temporal cloud coverage of the collector field. Little documented research into such conditions is available.

In order to help address the current lack of data, this experimental investigation was conducted, in which, particularly, the heat transfer coefficient and pressure drop behaviour was studied for cases where little or no data is available. An experimental test installation was designed and constructed to quantify various effects on the heat transfer coefficient of the flow and pressure drop within the fluid. A horizontal test section was considered which consisted of a uniformly heated pipe with a length of 800 mm and an inner diameter of 8.31 mm. R-245fa was selected as testing fluid since it has been proposed for possible use in organic Rankine cycles which can also be operated as direct steam generation cycles. For practical reasons a saturation temperature of 35 °C was used and focus was placed on aspects that have not yet received significant attention in literature.

Firstly, the behaviour of the steady-state heat transfer coefficient for relatively low mass fluxes (less than 100 kg/m²s) and relatively low heat fluxes (less than 7.5 kW/m²) was investigated over the entire vapour quality range from 0.05 to 0.90. It was found that a higher mass flux always resulted in a higher heat transfer coefficient for a given heat flux throughout the quality range. However, at the lowest heat flux considered, the heat transfer coefficient exhibited anomalous behaviour in that it was up to 70% higher at vapour qualities of 0.15 to 0.30 than higher heat fluxes.

Secondly, the effects of an abrupt change in vapour quality at the inlet to the test section on the heat transfer coefficient was studied. Mass fluxes of 200 and 300 kg/m²s were considered at vapour qualities of 0.15 to 0.40, such that several flow pattern conditions were covered. It was found that for a step size magnitude of 0.13 in the vapour quality, the actual heat transfer coefficient differed from

the expected quasi-steady-state heat transfer coefficient during the transient. It was higher than the expected in the downward step, and lower during an upward step.

Lastly, the impact of a changing heat flux on the flow boiling heat transfer coefficient was considered. These tests were performed at a mass flux of $200 \text{ kg/m}^2\text{s}$ over a vapour quality range of 0.10 to 0.85. Based on actual DNI data, a reduction of 75% in heat flux over a period of 30 s with a step, triangular and sinusoidal waveform pulse was applied in a controlled fashion. It was found that for an abrupt step reduction in the heat flux, that the average heat transfer coefficient during the perturbation was 30% lower than the unperturbed value. For triangular and sinusoidal pulses, the heat transfer coefficient was 8% lower. During all tests, the pressure gradient through the test section was unaffected by any form of perturbation.

PUBLICATIONS

Portions of this work that have been published to date are summarised below:

ARTICLES

1. Dirker, J., **Van den Bergh, W.J.**, Moran, H.R., Markides, C.N., and Meyer, J.P., *Influence of inlet vapour quality perturbances on the transient response of flow-boiling heat transfer*, International Journal of Heat and Mass Transfer, 2021. **170**: p. 121017.
2. **Van den Bergh, W.J.**, Moran, H.R., Dirker, J., Markides, C.N., and Meyer, J.P., *Effect of low heat and mass fluxes on the boiling heat transfer coefficient of R-245fa*. International Journal of Heat and Mass Transfer, 2021. **180**: p. 121743.
3. **Van den Bergh, W.J.**, Dirker, J., Markides, C.N., and Meyer, J.P., *Influence of non-steady transient heat flux on flow boiling heat transfer and pressure drop in horizontal pipes*. International Journal of Heat and Mass Transfer, 2022. **182**: p. 121927.

CONFERENCE PAPERS

1. **Van den Bergh, W.J.**, Dirker, J., Markides, C.N., and Meyer, J.P., *Preliminary investigations into the effect of step changes in boiling heat flux on R-134a in a horizontal macro tube*, in proceedings 14th International Conference on Heat Transfer, Fluid Mechanics and Thermodynamics (HEFAT), Wicklow, Ireland, 22-24 July 2019.

ACKNOWLEDGEMENTS

Where should I start? What was originally supposed to be a relatively quick three years, in and out, turned into a five-year marathon. During those five years, I laughed a lot, cried a lot, lost people close to me, discovered reservoirs of strength and patience that I did not know I had, and was carried by giants. These deserve to be acknowledged.

- Professor J.P. Meyer, for your unwavering support and efforts to get my articles published; Professor J. Dirker, for long chats in your office and willingness to jump on some grenades for me; Professor C.N. Markides, for your easy laugh and hard questions.
- The Royal Society. Without the funding provided by the Africa Capacity Building Initiative, my dreams of becoming a doctor would have remained just that.
- Mr. C. Moon, Mr. D. Gouws, and Mr. K. Mthombeni for your willingness to work alongside me, teach me the practical skills I needed (except soldering, Koos...) and assistance in getting the experimental apparatus constructed and commissioned.
- Dr. A. Duvenage, for inspiring me not to yield against the slings and arrows of fortune.
- Ms. L. Cilliers for believing in me and advising me not to start the doctorate without securing funding. Even though we haven't seen each other in over a year, Mevrouw was always there for me.
- Prof. R. van den Bergh Schreuders and Mr. J. van den Bergh for coping with a hare-brained brother all these years. I honestly don't know how you do it.
- Ms. M. du Preez and Mr. M. du Preez, for being my second mother and father. Your support and love for my family over the last 30-plus years is priceless.

Lastly and most importantly, this doctorate is dedicated to my mother, Ms. J. van den Bergh, and my father, Mr. A.G. van den Bergh, who passed away mere weeks before I completed this thesis. I can't imagine what it must have been like for you with a thirty-one-year-old (now thirty-six!) grown man coming back to the nest, but I can say without a shadow of a doubt that I would not have been able to climb this Everest without you. The patience and love you showed me, the encouragement, the sympathetic ears when things seemed at their blackest (and trust me, there were many such occasions), all make this doctorate as much yours as it is mine.

You truly are giants.

TABLE OF CONTENTS

Abstrak.....	i
Abstract.....	iii
Publications	v
Acknowledgements	vi
Table of contents	vii
List of figures.....	x
List of tables	xiv
Nomenclature.....	xv
1. Introduction.....	1
1.1. Background.....	1
1.2. Problem statement	4
1.3. Aim and objectives	4
1.4. Delineation.....	5
1.5. Novel contributions	6
1.6. Thesis overview	7
Part I	8
2. Literature survey	9
2.1. Introduction.....	9
2.2. Concentrated solar power, direct steam generation, and organic Rankine cycles..	9
2.3. Saturated flow boiling in horizontal pipes.....	14
2.4. Steady-state predictive correlations and results.....	18
2.5. Transient-state heat and mass flux.....	25
2.6. Summary.....	28
3. Experimental apparatus	29
3.1. Introduction.....	29
3.2. Criteria for the experimental system.....	29
3.3. Facility	31
3.4. Test section	35
3.5. Apparatus specification	39
3.6. System control and data logging.....	40

3.7.	Calibration	42
3.8.	Summary	43
Part II		44
4.	Steady-state investigation methodology	45
4.1.	Introduction.....	45
4.2.	Experimental procedure	45
4.3.	Test matrix	46
4.4.	Data processing.....	49
4.5.	Uncertainty propagation analysis	52
4.6.	Validation	54
4.6.1.	Single-phase validation	54
4.6.2.	Two-phase validation	55
4.7.	Summary	57
5.	Steady-state results.....	58
5.1.	Introduction.....	58
5.2.	Low mass and heat flux steady-state results.....	58
5.2.1.	Local versus average HTCs.....	58
5.2.2.	Influence of mass flux on the average HTC	60
5.2.3.	Influence of heat flux on the average HTC	62
5.2.4.	Influence of the flow pattern on the HTC.....	64
5.2.5.	Comparison with correlations.....	67
5.3.	High mass flux steady-state results.....	70
5.3.1.	Local versus average HTCs.....	71
5.3.2.	Baseline results and repeatability	72
5.3.3.	Intermediate and interpolated results.....	73
5.4.	Summary	75
Part III.....		76
6.	Inlet vapour quality perturbation investigation methodology.....	77
6.1.	Introduction.....	77
6.2.	Experimental procedure	78
6.3.	Test matrix	79
6.4.	Data processing.....	81
6.5.	Summary	84
7.	Vapour quality perturbation results	85
7.1.	Introduction.....	85

7.2.	Example case	85
7.3.	General trends	92
7.4.	Summary	95
Part IV.....		96
8.	Heat flux perturbation investigation methodology	97
8.1.	Introduction.....	97
8.2.	Experimental procedure	98
8.3.	Test matrix	99
8.4.	Data processing.....	101
8.5.	Summary	104
9.	Heat flux perturbation results	105
9.1.	Introduction.....	105
9.2.	Example case	105
9.3.	General trends	109
9.4.	Pressure measurement results	113
9.5.	Summary	115
Part V.....		116
10.	Conclusions and recommendations.....	117
10.1.	Introduction	117
10.2.	Steady-state flow at low mass and heat flux	117
10.3.	Vapour quality perturbation	118
10.4.	Heat flux perturbation	119
10.5.	Additional recommendations.....	121
10.6.	Summary.....	123
References		124
Appendices		131

LIST OF FIGURES

Figure 1.1. Simplified schematic of a theoretical direct steam generation Rankine cycle.....	2
Figure 2.1. Global average DNI [20].....	10
Figure 2.2. Hourly average DNI in winter and summer at a station in South Africa [21]	10
Figure 2.3. Illustration of the different forms of CSP [2].....	11
Figure 2.4. Flow patterns that occur during horizontal saturated boiling from saturated liquid (blue) to saturated vapour (white)	15
Figure 2.5. Example Wojtan-Ursenbacher-Thome [42] flow pattern map for R-245fa at 35°C	17
Figure 3.1. Top-down schematic of the experimental test facility (not to scale)	32
Figure 3.2. The constructed facility ready for commissioning.....	32
Figure 3.3. Commissioned facility in the process of receiving additional insulation	33
Figure 3.4. Test section schematic (not to scale).....	35
Figure 3.5. Inlet sight glass before installation.....	36
Figure 3.6. Photograph detailing the uninsulated heated length inlet	38
Figure 3.7. Set-up with test section in view	38
Figure 3.8. Achievable inlet vapour qualities at test section inlet for R-245fa at a saturation temperature of 35 °C and subcooling of 20 °C.....	40
Figure 3.9. Facility control system	41
Figure 4.1. New steady states added in this work and its relevance to existing studies on the flow boiling of R-245fa	47
Figure 4.2. Complete test matrix for this work on a Wojtan-Ursenbacher-Thome [42] flow pattern map at a saturation temperature of 35 °C	48
Figure 4.3. Single-phase validation: Nusselt number as a function of Reynolds number for liquid R-245fa flow for fluid inlet temperature of 25 °C	55
Figure 4.4. Energy balance over the test section for a fluid inlet temperature of 25 °C	55
Figure 4.5. Two-phase flow validation, showing steady-state mean HTC for a mass flux of 200 kg/m ² s, a heat flux of 7.5 kW/m ² and a saturation temperature of 35 °C with predicted values	56
Figure 5.1. Local HTC plotted against local vapour quality for a mass flux of: (a-c) 40 kg/m ² s, (d-f), 60 kg/m ² s, and (g-i) and 80 kg/m ² s	59
Figure 5.2. Influence of mass flux on the mean HTC for heat fluxes of: (a) 2.5 kW/m ² , (b) 5.0 kW/m ² and (c) 7.5 kW/m ²	61

Figure 5.3. Influence of heat flux on the mean HTC for mass fluxes of: (a) 40 kg/m ² s, (b) 60 kg/m ² s, and (c) 80 kg/m ² s	63
Figure 5.4. Representative example where there is a large difference between entry and exit HTCs for a mass flux of 80 kg/m ² s, inlet vapour quality of 0.20, and a heat flux of 2.5 kW/m ²	64
Figure 5.5. Representative flow patterns at the inlet for a heat flux of: (a) 2.5 kW/m ² , and (b) 5.0 kW/m ² , at an inlet vapour quality of 0.20 and mass flux of 80 kg/m ² s.....	65
Figure 5.6. Flow patterns illustrating the transition from stratified wavy flows to hybrid/intermittent flows for a mass flux of 80 kg/m ² s and a heat flux of 2.5 kW/m ²	67
Figure 5.7. Comparisons with HTC predictions from well-known correlations for a mass flux of 80 kg/m ² s and a heat flux of 2.5 kW/m ²	69
Figure 5.8. Illustrative example of local HTCs at the eight thermocouple stations for an initial vapour quality of 0.15, mass flux of 200 kg/m ² s, heat flux of 7.5 kW/m ² , and saturation temperature of 35 °C	71
Figure 5.9. Steady-state HTCs gathered on different dates for mass fluxes of 200 and 300 kg/m ² s at a saturation temperature of 35 °C and a heat flux of 7.5 kW/m ²	72
Figure 5.10. Steady-state HTCs showing the flow patterns achieved	73
Figure 5.11. Measured and interpolated steady-state HTCs as a function of vapour quality for the mass flux values investigated in the transient tests at a saturation temperature of 35 °C	75
Figure 6.1. Partial shading of the Xina and Kaxu parabolic trough CSP plants, Pofadder, South Africa [106]	77
Figure 6.2. Simplified schematic of a theoretical direct steam generation Rankine cycle undergoing a DNI perturbation	78
Figure 6.3. Examples of flow pattern crossing from (a) slug and intermittent at vapour quality 0.20 to (b) intermittent and annular at vapour quality 0.30 for a mass flux of 200 kg/m ² s and a saturation temperature of 35°C.....	80
Figure 6.4. Test matrix for the transient quality perturbation tests	80
Figure 6.5. Section of test facility used for discussion.....	83
Figure 7.1. Data for a single detailed transient investigation for an initial vapour quality of 0.30, mass flux of 200 kg/m ² s, and saturation temperature of 35 °C	86
Figure 7.2. HTC behaviour for an initial vapour quality of 0.30, mass flux of 200 kg/m ² s, and saturation temperature of 35 °C, during: (a) downward, and (b) upward step changes in vapour quality	88

Figure 7.3. Percentage difference between the transient and interpolated steady-state HTC's as a function of time for an initial vapour quality of 0.30, mass flux of 200 kg/m ² s, and saturation temperature of 35 °C	89
Figure 7.4. HTC as a function of quality for an initial vapour quality of 0.30, mass flux of 200 kg/m ² s, and saturation temperature of 35 °C, during: (a) downward, (b) upward step changes in inlet vapour quality	90
Figure 7.5. HTC as a function of mass flux for an initial vapour quality of 0.30, mass flux of 200 kg/m ² s, and saturation temperature of 35 °C, during: (a) downward, and (b) upward step changes in inlet vapour quality	91
Figure 7.6. Overview of all results obtained for a mass flux of 200 kg/m ² s, exhibiting qualitative similarity	93
Figure 7.7. Maximum percentage difference between the transient and interpolated steady-state HTC's during downward and upward step changes in inlet vapour quality for an initial mass flux of: (a) 200 kg/m ² s, and (b) 300 kg/m ² s.....	94
Figure 8.1. Direct normal irradiation (DNI) measured on 26 August 2017 for: (a) all sunlit daytime hours, and (b) a 30-min view from 10:30 am to 11:00 am.	97
Figure 8.2. Applied perturbation time profiles under consideration	99
Figure 8.3. Inlet test conditions plotted on a Wojtan-Ursenbacher-Thome [42] flow pattern map, constructed specifically for a mass flux of 200 kg/m ² s, heat flux of 7.5 kW/m ² , and saturation temperature of 35 °C	100
Figure 8.4. Flow patterns observed at an inlet vapour quality of (a) 0.15, (b) 0.25, (c) 0.30, (d) 0.45, and (e) 0.85	101
Figure 9.1. (a) Step, sinusoidal and triangular heat flux perturbations, and response of (b) wall and saturation temperatures, and (c) mean HTC for a vapour quality of 0.30, mass flux of 200 kg/m ² s, and initial heat flux of 7.5 kW/m ²	106
Figure 9.2. HTC as a function of the actual heat flux for step, sinusoidal and triangular heat flux waveforms for a vapour quality of 0.30, mass flux of 200 kg/m ² s, and initial heat flux of 7.5 kW/m ²	108
Figure 9.3. The mean HTC obtained for four different vapour qualities, indicating qualitatively similar results.....	109
Figure 9.4. Maximum average difference in mean HTC for the different stages of the perturbation compared to the steady-state value for all tested qualities for a mass flux of 200 kg/m ² s, and an initial heat flux of 7.5 kW/m ²	112

Figure 9.5. (a) Step, sinusoidal and triangular heat flux perturbations, and response of (b) mass flux, and (c) pressure drop gradient for a vapour quality of 0.30, mass flux of 200 kg/m²s, and initial heat flux of 7.5 kW/m² 114

Figure 9.6. Frictional pressure drop predicted by the Müller-Steinhagen and Heck correlation compared to the experimental frictional pressure drop 115

LIST OF TABLES

Table 2.1. Overview of studies of in-tube boiling of refrigerants at low mass and heat fluxes	24
Table 3.1. Salient specifications for CSP DSG plants using horizontal pipes	30
Table 3.2. Experimental and numerical studies of direct-boiling solar ORCs in horizontal pipes	30
Table 3.3. Overall ability and range of the constructed apparatus	39
Table 4.1. Approximate increase in vapour quality in test section for different mass and heat fluxes	49
Table 4.2. Ranges and accuracies of measuring instruments	53
Table 4.3. Parameter ranges and uncertainties	53
Table 5.1. Mean absolute and relative deviations for the correlations	70
Table 7.1. Time for defined points	87
Table 9.1. Summary of HTC data for all tested inlet vapour qualities and perturbations	111

NOMENCLATURE

A	[m ²]	Area
Bi	-	Biot number
c_p	[J/kgK]	Isobaric specific heat capacity
d	[m]	Diameter
E	[J]	Energy
EB	[%]	Energy balance error
G	[kg/m ² s]	Mass flux
f	-	Friction factor
h	[J/kg]	Specific enthalpy
I	[A]	Electric current
k	[W/mK]	Thermal conductivity
L	[m]	Length
m	[kg]	Mass
\dot{m}	[kg/s]	Mass flow rate
M	[g/mol]	Molar mass
N		Number of data points
Nu	-	Nusselt number
p	[Pa]	Pressure
\dot{q}	[W/m ²]	Heat flux
\dot{Q}	[W]	Heat transfer rate
R	[K/W]	Thermal conductive resistance
Re	-	Reynolds number
s	[J/kgK]	Specific entropy
t	[s]	Time
T	[K, °C]	Temperature

U	[m/s]	Estimated fluid velocity
V	[m ³ , V]	Volume, or voltage
\dot{V}	[m ³ /s]	Volumetric flow rate
x	-	Vapour quality

Special characters

α	[W/m ² K]	Heat transfer coefficient
ε	-	Void fraction
ρ	[kg/m ³]	Density
μ	[Pa·s]	Dynamic viscosity

Subscripts

A	Point A, before preheater
B	Point B, after preheater
C	Point C, before test section
c	Characteristic or cross-sectional
cond	Condenser
Cu	Copper
D	Point D, after test section
exp	Experimental
E	Point E, before condenser
F	Point F, after condenser
frict	Friction
f	Saturated liquid
fluid	Working fluid
g	Saturated vapour
h	Heated length
i	Inner
in	Inlet

j	Time step index
m	Two-phase mixture
mom	Momentum
n	Thermocouple station number along heated length
o	Outer
out	Outlet
pre	Preheater
pred	Predicted
r	Circumferential index
red	Reduced
ref	Refrigerant
s	Surface
sat	Saturation
wall	Pipe wall
test	Test section
static	Static
total	Total
tube	Copper tube
w	Water
wall	Pipe wall

Abbreviations

CSP	Concentrated solar power
DNI	Direct normal irradiation
DSG	Direct steam generation
HTC	Heat transfer coefficient
ORC	Organic Rankine cycle
RTD	- Resistance temperature detector

1. INTRODUCTION

1.1. BACKGROUND

The scientific advances made during the 20th century led to an improvement in the quality of life for billions of people, and to a worldwide population explosion that started in the 1950s and continues unabated to this day. With increasing technological advances, and the booming world population, the need for energy, specifically electrical energy, has become one of the most pressing issues humanity faces in the 21st century. The fact that most of the electricity generation in the world relies on unsustainable fossil fuel consumption, and that the burning of these fossil fuels has been linked to human-induced climate change, highlight the urgent need for alternatives.

Sustainable energy production is a highly researched topic. Relevant technologies are powered by wind, marine, geothermal, hydraulic, and solar resources. Of these, solar energy is one of the most promising. The earth absorbs 3.85 yottajoules (1 yottajoule = 10^{24} joules) from the sun each year. This is many orders of magnitude beyond the annual energy consumption associated with human activity. The potential use of solar energy to satisfy a significant portion of the global energy requirements can thus not be ignored.

One of the methods that has received renewed attention in recent times [1] in which solar energy is utilised is via thermodynamic conversion in concentrated solar power (CSP) systems. In basic terms, this technology relies on focusing direct normal irradiation (DNI) sunlight onto a receiver, using either lenses or mirrors. DNI consists of the portion of the beam radiated sunlight which is perpendicular to the Earth's surface after it has passed through the atmosphere. These systems can be sub-divided based on the optical focusing technique used. The main methods are: point focal power towers with discrete reflectors, point focal parabolic dish reflectors, linear focal discrete Fresnel reflector sets, and linear focal parabolic trough reflectors. Of these four techniques, the parabolic trough approach is the most developed option and relies on curved mirrors to focus the solar irradiation onto a horizontally orientated collector pipe. Compared to solar power towers, it is significantly easier and more affordable to construct. Typically, the mirrors are orientated on a north-south axis, and track the sun's position through the sky from east to west via simple one-dimensional tracking systems. The concentrated heat is conducted through the collector pipe wall and is transferred to the fluid flow within via internal convection. The absorbed heat is then either transported to or directly utilized in a thermodynamic power cycle.

Generally, Rankine cycles operating with water (or organic Rankine cycles operating with an organic working fluid) are the most commonly employed thermodynamic power cycle type. The received heat is used to produce superheated vapour which is passed through a turbine to drive an

electric generator. In solar power applications, the superheated vapour can be produced either via an indirect or direct thermal coupling mechanism with the solar reflector and collector field.

Indirect coupling relies on the use of two separate flow loops: a single-phase heat transfer fluid loop between the solar collector field and the thermodynamic plant, and a different fluid loop inside the thermodynamic plant. The thermal link is often achieved with, for instance, molten salts or thermal oil, that circulates between the solar collector field and a steam generator heat exchanger (boiler) in the thermodynamic plant. Such systems are prone to exergy destruction due to the intermediate heat transfer process in the steam generator heat exchanger. Their operating temperature can also be restricted by the thermal limits of the heat transfer fluid.

Instead, on the other hand, direct coupling with the solar collector field can be achieved by producing the superheated vapour within the solar collector field directly. This is referred to as direct steam generation (DSG) and is represented in a simplified form in Figure 1.1, including a Rankine cycle schematic in terms of temperature and specific entropy. In this diagram, the boiling of the fluid and the vapour quality at point 3 is of interest for this work.

In such systems the intermediate steam generator heat exchanger is made redundant [2] because the same fluid is used throughout. This eliminates the additional thermal restrictions imposed by an intermediate fluid temperature limit, and reduces the overall entropy generation and exergy destruction.

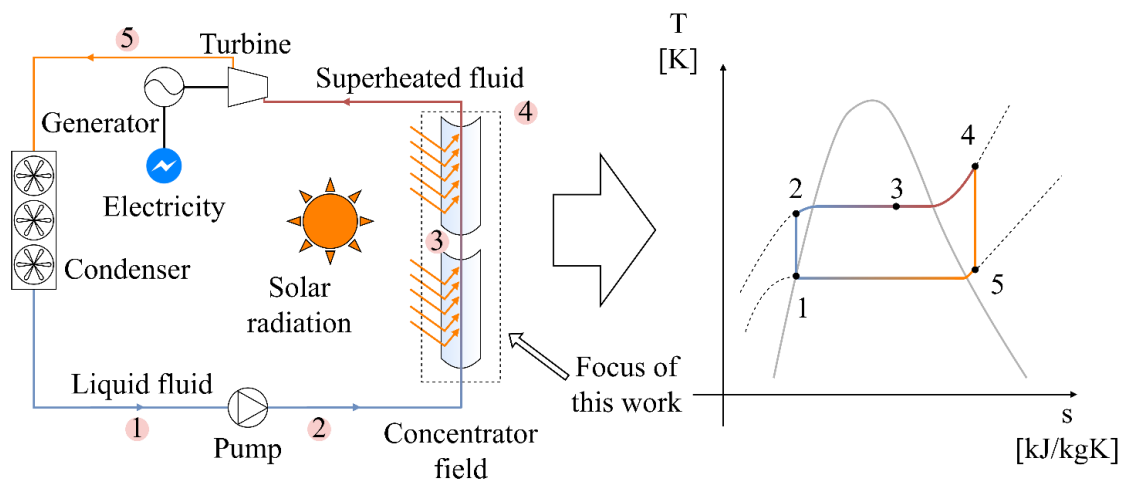


Figure 1.1. Simplified schematic of a theoretical direct steam generation Rankine cycle

When operating with water, higher steam generation temperatures can be achieved compared to systems using indirect thermal coupling with the solar field. Based on classical thermodynamic theory, any increase in the steam temperature results in improved thermodynamic power conversion efficiency. As such, DSG systems offer several advantages, including a more simplistic thermodynamic cycle requiring less components, improvement of thermal efficiency due to less

exergy destruction, possible higher operating temperatures, as well as the utilization of cheaper and more environmentally friendly fluids (particularly water).

The most common working fluid in CSP DSG plants is water/steam, but in hybrid [3] or smaller-scale and distributed systems, organic fluid can also be used [4-6]. R-245fa is particularly suitable for ORC systems [7, 8]. In this case, direct vapour generation (DVG) is used instead of DSG, but the meaning is exactly the same. Throughout this work, DSG is used.

DSG does pose some technical challenges, including a rethink of how to integrate thermal energy storage, as well as the problems associated with higher operating temperatures and pressures in the collector tubes. An important aspect associated with the latter is the internal convective heat transfer coefficient (HTC), which is vital for improved understanding of the modelling and prediction of the ability of the fluid to receive the concentrated solar energy while undergoing flow boiling. Local HTCs are required to correctly size the solar collector field in order to service the energy needs of the thermodynamic cycle. Another key aspect is the associated frictional pressure drop in the fluid which affects the pumping power requirement to push the fluid through the solar collector field.

One of the problems with CSP in general and DSG in particular, is that it relies on an inherently unstable energy supply. Whether it is the natural rising and setting of the sun, temporary cloud coverage interrupting the DNI, or the fact that at the time of writing there is no universally accepted correlation to predict the HTC with any real accuracy, it is clear that more research effort is needed to assist CSP design engineers in predicting the HTC correctly.

The instability in DNI has two significant impacts on the solar collector field operation. Firstly, the local concentrated heat flux onto the collector tube can vary significantly which might impact the HTC, and secondly the thermodynamic inflow properties of the fluid from the upstream sections could vary dramatically. Any sudden change in the heat received into the fluid upstream will result in a fluctuation in the thermodynamic state of the fluid in terms of the mass proportion that exists as a vapour (referred to as the vapour quality). Such abrupt variations in the vapour quality will travel downstream through the rest of the solar collector field that could also significantly influence the HTC.

Research into the effect that these phenomena have on the HTC is woefully lacking at present. Some studies do exist that consider the effect of changing heat flux on the HTC [9, 10], while others are focused on changing mass flux [10-12]. Very few studies have been found that use actual, non-idealised forms of the DNI often encountered in practice. Additionally, in the limited articles found covering the change in heat flux, the data processing to determine the HTC does not consider the thermal charging/discharging of the metal pipe wall, particularly during the experimental analyses.

Another area of interest in the modern context of sustainable energy is the possibility of utilising small, residential-scale CSP ORC systems for electricity generation, domestic heat pumps or refrigerators, and the plate heat exchangers used in these applications. In these systems, especially in low-concentration small-scale ORC systems, the heat flux is relatively low (less than 7.5 kW/m^2), and the mass flux is generally below $100 \text{ kg/m}^2\text{s}$. Many studies on the prediction of the HTC exist, covering a plethora of mass fluxes and heat fluxes, from micro to macro channels, with over 50 correlations being proposed [13]. The focus of these studies also lies primarily on the steady-state HTC at mass fluxes above $100 \text{ kg/m}^2\text{s}$ with a heat flux of above 7.5 kW/m^2 . As yet, little consensus has been reached regarding the effect of these two variables (the mass flux and the heat flux) on the HTC, least of all for the lower end of the envelope.

A gap addressing the effect low mass-and-heat fluxes have on the HTC thus exists, especially for R-245fa and in particular horizontal tubes which are of interest to parabolic trough reflector systems. Additionally, any information obtained in studying R-245fa would also be applicable to understanding water-based DSG systems. Therefore, based on the discussion above, there is a need for more research on DSG processes, particularly for CSP in order to better design and optimise the solar collector field while also taking into consideration the impact of abrupt changes in the temporal solar irradiance levels. This could be crucial in determining the economic viability and attractiveness of a proposed parabolic trough CSP plant over alternatives.

1.2. PROBLEM STATEMENT

Practically, the transient nature of the solar resource has an effect on the heat transfer and pressure drop in DSG systems. More research into the technical heat transfer and pressure loss performance for flow boiling is thus needed. The effect on the horizontal pipes used in DSG CSP systems with parabolic through collector fields is of particular interest. The sudden induced changes in local heat flux and inlet vapour quality by temporal change in DNI and the resulting influence on the HTC and pressure drop is not well documented or studied. There is also a need to clarify the effect a low heat and mass flux has on the steady-state HTC and pressure drop.

1.3. AIM AND OBJECTIVES

The aim of this research project was to:

- Investigate the steady-state local HTC at low (less than $100 \text{ kg/m}^2\text{s}$) mass fluxes and low (less than 7.5 kW/m^2) heat fluxes for any peculiarities.

- Evaluate the effects on the HTC of a long-term perturbation in DNI (and thus in the vapour quality) for an unperturbed test section further down the line.
- Evaluate the effects on the HTC and pressure drop for a momentary perturbation in DNI, informed by actual DNI data for a cloudy and windy day. The heat discharge of the metal pipe has to be considered as well.

In order to achieve these aims, the following had to be done:

- Design and construct an experimental facility for this investigation and future work. This necessarily required a modular test section. Critically, the facility had to be able to exert fine control over the mass flux, test section inlet vapour quality, and test section heat flux.
- Commission the designed experimental facility. This involved sourcing the parts decided upon, constructing the facility, and tweaking the construction as problems arose.
- Validate the results and repeatability of the commissioned facility by performing many steady-state single-phase and flow boiling tests at comparable mass and heat fluxes to literature and comparing the achieved results against various correlations.
- Perform the different tests, incorporating differing experimental procedures and test matrices.
- Evaluate the obtained data and explain any observed discrepancies as compared to the expected results.

1.4. DELINEATION

The scope of this study was to obtain

- HTC data for R-245fa at mass fluxes of 40, 60, and 80 kg/m²s and heat fluxes of 2.5, 5.0, and 7.5 kW/m² (Chapter 5).
- HTC data for R-245fa under a long-term step-perturbation in vapour quality at mass fluxes of 200 and 300 kg/m²s at a heat flux of 7.5 kW/m² (Chapter 7).
- HTC and pressure drop data for R-245fa under heat flux pulses at a mass flux of 200 kg/m²s and a heat flux of 7.5 kW/m² (Chapter 9).

The reasoning behind these goals is expanded upon in the appropriate chapters, as listed in Section 1.5.

1.5. NOVEL CONTRIBUTIONS

This thesis consists mostly of the original published work of three articles. A brief summary of the contributions made by each article, along with the chapter in which they appear, are listed below:

Chapter 5: *Low mass and heat flux steady states*, [14].

- Novel behavioural trends were discovered for all mass fluxes tested at the lowest heat flux of 2.5 kW/m^2 for inlet vapour qualities of 0.15 to 0.35.
- At the inlet to the test section, the HTC was up to 150% higher for a mass flux of $80 \text{ kg/m}^2\text{s}$ as compared to a mass flux of $40 \text{ kg/m}^2\text{s}$ for a heat flux of 2.5 kW/m^2 .
- When comparing the HTC for differing heat fluxes at the inlet to the test section at a mass flux of $80 \text{ kg/m}^2\text{s}$, a heat flux of 2.5 kW/m^2 yielded a HTC higher by 70% than a heat flux of 7.5 kW/m^2 .

Chapter 7: *Vapour quality perturbances*, [15].

- Novel tests were performed by implementing a step change in the vapour quality at the inlet to the test section and recording the HTC.
- The expected HTC differed by up to 30% from the actual value obtained during a vapour quality perturbation.
- A downward perturbation in vapour quality resulted in an underprediction from interpolated steady-state data.
- Conversely, an upward perturbation in vapour quality resulted in an overprediction.

Chapter 9: *Heat flux perturbances*, [16].

- Novel tests were performed by applying waveform shape perturbances to the heat flux informed by actual DNI data. These consisted of step, triangular, and sinusoidal waves.
- Relatively short temporal perturbances in the heat flux had a marked effect on the HTC
- Pressure drop was unaffected by any perturbation.

1.6. THESIS OVERVIEW

This rest of this document is divided into four distinct parts.

Part I contains the groundwork for the rest of the document, with the literature survey in Chapter 2, and the details of the experimental apparatus and its construction in Chapter 3.

Part II focuses on steady-state results which, amongst others, serve as the base of reference for comparison in the parts that follow. It contains the steady-state experimental method, a test matrix that was the focus of this work, the data processing required, an uncertainty propagation analysis, and validation of the system in Chapter 4. The achieved steady-state results for low mass and heat fluxes are discussed along with the remaining baseline comparison high mass flux cases in Chapter 5.

Part III focuses on transient-state results relating to the perturbation of the inlet vapour quality. It is divided into the experimental procedure, the focus area test matrix, and additional data processing that was required in Chapter 6. The discussion of the results of an arbitrary case and the general trends observed for all vapour quality perturbation test cases appears in Chapter 7.

Part IV focuses on transient-state results relating to the perturbation of the local heat flux. It is divided (much as Part III) into Chapter 8 which covers the rationale, experimental procedure, test matrix, and additional data processing. The results obtained are again discussed for an arbitrary example case before the general and pressure drop trends are identified in Chapter 9.

Part V ties together the conclusions reached for the steady-state, vapour quality perturbation, and heat flux perturbation results, before proposing some recommendations for future work in Chapter 10.

Several Appendices contain additional information for the interested reader. Appendix A covers the calibration of various measurement devices used in this work, Appendix B delves into the uncertainty propagation in this work, Appendix C relays additional relevant equations and correlations applied, and Appendix D contains calibration certificates for the pressure sensors utilised.

PART I

GROUNDWORK

“Quis custodiet ipsos custodes?”

–Juvenal

2. LITERATURE SURVEY

2.1. INTRODUCTION

Concentrated solar power is covered by a vast and complex area of research, encompassing many different divergent areas. This chapter aims to give some background and summarise sundry areas found in open literature pertaining to the areas of study noted in the introduction. First, an overview of concentrated solar power (CSP), with a focus on direct steam generation (DSG) and organic Rankine cycles (ORC) is presented, before the fundamentals of saturated flow boiling are briefly discussed. This is followed by a short overview of some of the many correlations proposed to predict the HTC and some steady-state HTC results. Finally, the limited transient results available in literature are considered.

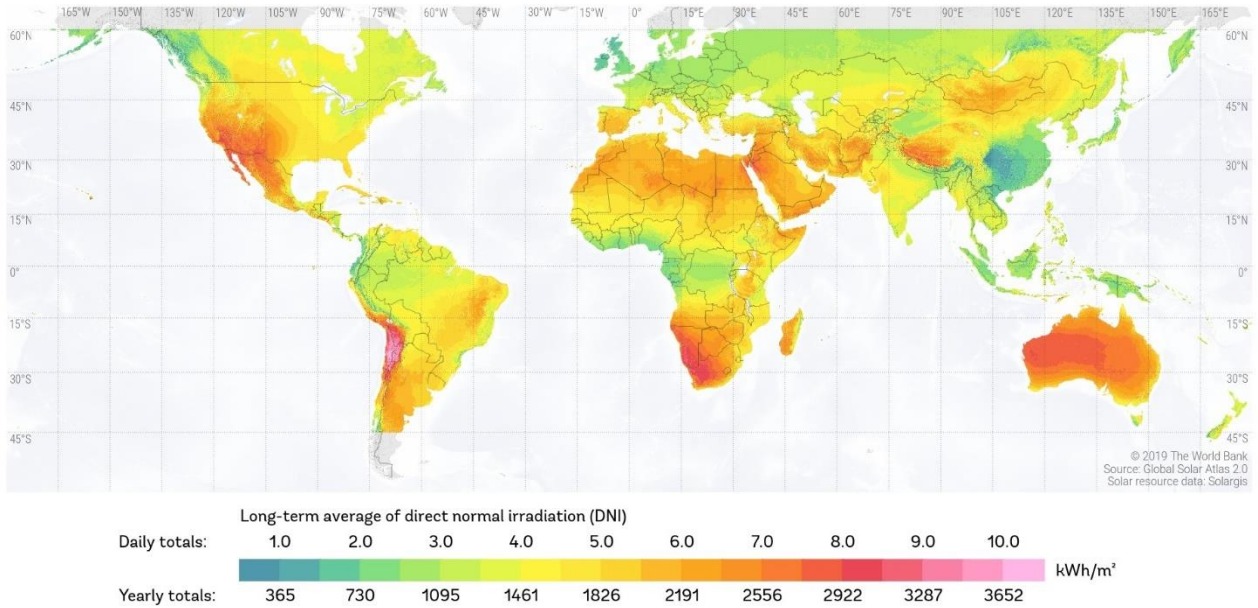
2.2. CONCENTRATED SOLAR POWER, DIRECT STEAM GENERATION, AND ORGANIC RANKINE CYCLES

Traditional fossil-fuel based power generation systems use combustion of coal, oil, or natural gas to produce a high temperature heat source to power a thermodynamic cycle. Typically, in a closed Rankine cycle, heat from the high temperature region is used to boil water. In concentrated solar power (CSP) systems, the combustion process is replaced by a heating process powered by concentrated solar thermal energy. It is particularly attractive in areas of the world with high direct normal irradiation (DNI), and reviews of this technology exist [1, 17, 18].

The daily and yearly global average DNI in kWh/m² is reported in Figure 2.1. It can be seen that the daily average DNI in large parts of Africa, southern Europe, western North America, and Australia is upwards of 6 kWh/m². This makes the exploration of CSP in these regions very attractive.

To illustrate this, the average hourly DNI in kW/m² measured by a station located in Alexander Bay, South Africa (28.5608° S, 16.7615° E, elevation 141 m), is shown in Figure 2.2. In this figure, the DNI is shown for the two days of winter and summer solstice. Even in wintertime, the average DNI is sufficient to make the employment of CSP worthwhile, including for alternative, purpose-fit applications, such as water desalination [19].

SOLAR RESOURCE MAP
DIRECT NORMAL IRRADIATION



This map is published by the World Bank Group, funded by ESMAP, and prepared by Solargis. For more information and terms of use, please visit <http://globalsolaratlas.info>.

Figure 2.1. Global average DNI [20]

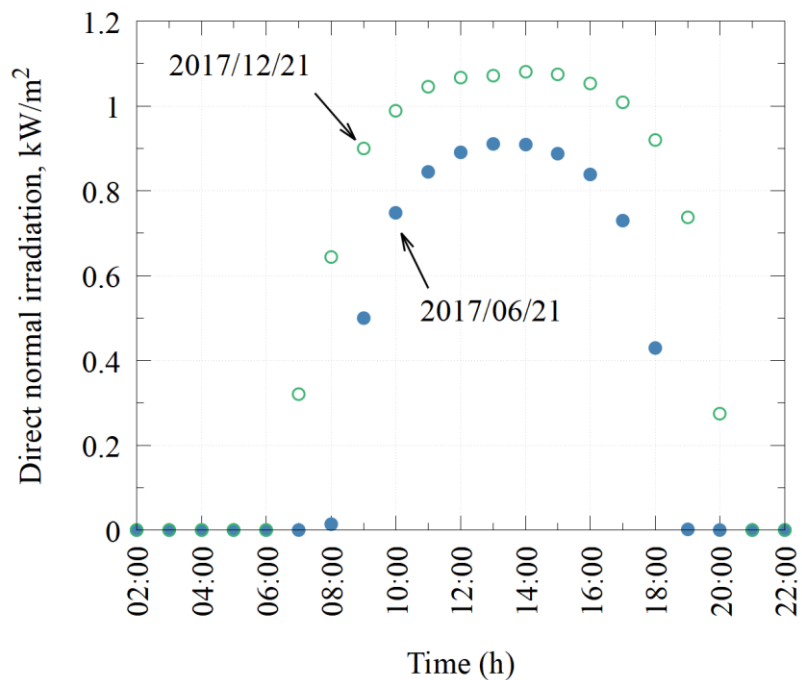


Figure 2.2. Hourly average DNI in winter and summer at a station in South Africa [21]

Regardless of the application, the heat from the sun has to be optically concentrated. As mentioned in the introduction, this can be achieved via four main approaches: Solar power towers with a central receiver, linear Fresnel concentrators, parabolic trough concentrators, and parabolic

solar dishes. These are shown schematically in Figure 2.3. Each approach has its own advantages and drawbacks.

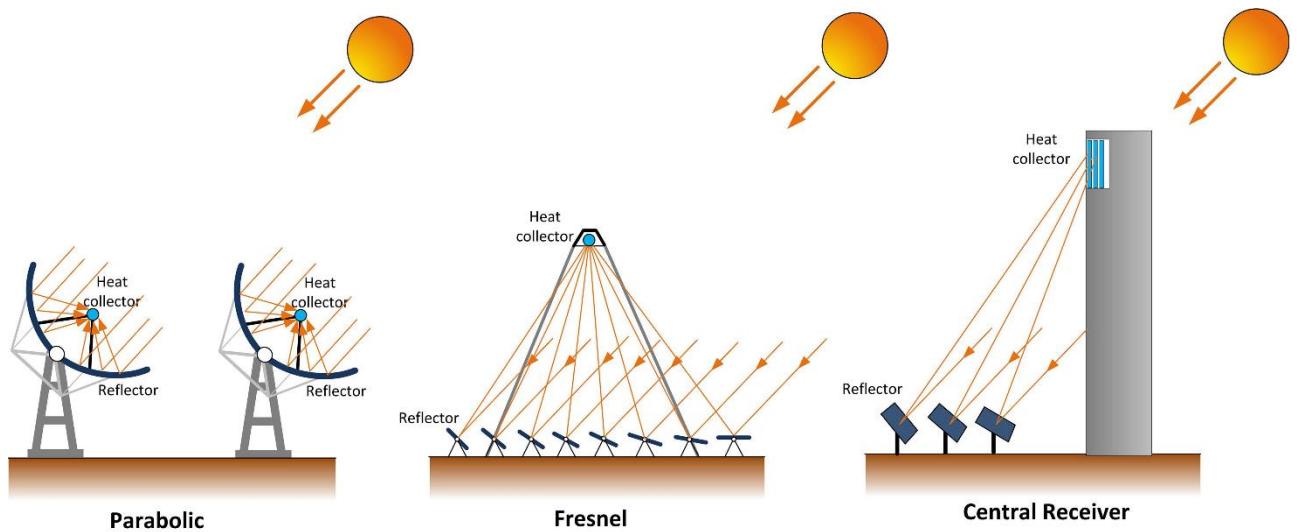


Figure 2.3. Illustration of the different forms of CSP [2]

With solar power towers, sunlight is reflected and focused via a field of individually adjustable solar tracking heliostats onto a stationary central receiver atop a tower. Each heliostat's orientation is controlled via a dual-axis system with the intention of directing the reflected solar rays onto the collector. One of the advantages of such a system is that each heliostat can be taken offline for maintenance individually. Unfortunately, the tracking system is necessarily more complex than single axis tracking systems, and environmental issues (for example, with regards to bird life) is also a concern.

On the other hand, instead of using many individually controlled reflectors, dish concentrators rely on a single parabolic dish focusing the sunlight onto its focal point, where the working fluid is located. Usually, this heated fluid is used to drive a Stirling thermodynamic cycle to generate electricity, but other cycles such as the Brayton cycle can also be used. Some of the drawbacks of this system are the structural support required by the dish and the tracking system, as well as its relatively limited concentration area and power generation size. This is an advantage, however, when considering domestic scale or modular power plants.

The linear Fresnel reflector concept utilises long, flat, mirrors that reflect light onto several receivers mounted above the mirrors. Since the receivers are stationary, this obviates the need for specialised fluid couplings. The efficiency of these systems is however worse than the other technologies noted in converting the sun's heat into electricity [1].

Lastly, with parabolic trough systems, a parabolic mirror with a line focus is used, which, when mounted correctly on a north-south axis, can be fitted with a one-dimensional tracking system to

ensure maximal focusing during the entire day. Parabolic troughs have been in commercial use since the 1870s [22], with a patent being granted to one such system in 1917 [23], but the idea of converting some of the sun's heat energy into useful work has been around since at least the 17th century, when a French engineer proposed a water pump using the sun's heat [24]. The idea languished for the first half of the 20th century, but the oil crisis of the 1970s prompted more research and projects. This interest was only exacerbated by the anthropogenic effect on the global climate, and research into making parabolic trough CSP plants economically viable continues.

In linear Fresnel and parabolic trough systems, the pipes used to contain the heat transfer fluid or the working fluid are generally oriented in a near horizontal fashion. They are also in the conventional diameter scale (larger than 3 mm [25]), meaning the construction of a test facility would be simplified. While the maximum theoretical concentration ratio (i.e., the amount by which the unconcentrated DNI of the sun is multiplied through concentration) of a parabolic trough is 107 [26], actual commercial parabolic troughs currently on the market typically achieve a concentration ratio in the range of 10-20 [22]. This concentration ratio would serve as a baseline when deciding on test conditions later in this document.

With the solar power concentrated to raise the temperature and enthalpy of a fluid, the next natural question to ask is which fluid is being heated and how power is being generated. In many CSP systems, whichever concentration method is used, a so-called heat transfer fluid is circulated through the solar collector field. The heated fluid is directed through a heat exchanger in order to transfer heat to water for steam production, which is then used in a traditional Rankine type cycle. This is attractive, since the Rankine cycle has been in use for well over a century, and all the knowledge and practical experience gained through its use is applicable.

There are problems with this two-fluid approach. For one, finding a high-performance heat transfer fluid to circulate in the solar field is a challenge, with many proprietary fluids being used in industry. These fluids are often relatively harmful, both to the environment and humans, and introduce the added problem of ensuring leaks are kept to a minimum. Second, the fact that water has to be heated to steam by this heated fluid adds to the complexity and cost of a proposed power station, necessitating some form of heat exchanger between the thermal and power loops. The exergy destruction, parasitic friction losses, and thermal inertia are all major concerns

As mentioned in Chapter 1 the alternative to this is direct steam generation (DSG), where the same fluid is used in the thermal and power loops. This simplifies the construction and apparent operation of a plant, and reviews of this methodology have been published in recent times [2, 27-29]. The fact that this fluid has no need for additional heat exchangers solves a lot of the previously mentioned problems in one swoop. This makes DSG plants very attractive from a cost/benefit

perspective, since the construction, maintenance, and operational costs are kept to a minimum. Some challenges are however associated with flow boiling process that now occurs in the solar collector tubes instead of in the steam generator.

The database for water-based parabolic trough CSP DSG systems for industrial process heating indicate that its use is steadily increasing, with over 20 plants worldwide at the time of writing [30]. Water-based parabolic trough CSP DSG for electricity production is still in its infancy when it comes to commercial adoption, however, although there are pilot plants that have been commissioned for study [31], which informed a pre-commercial plant [32]. Thailand has commissioned a parabolic trough CSP DSG plant [33], as part of its ambitious sustainable electricity production programme. The United States has experimented with a hybrid parabolic trough CSP DSG system in the Stillwater combined solar and geothermal power plant [34]. Of note is that in these plants, the piping was approximately horizontal, and the mass flux was 400 to 600 kg/m²s for the pilot plants. The mass flux generally expected in parabolic trough direct steam generation pipes is of the order of 500 kg/m²s [35].

While the most common fluid in DSG is water/steam, as has been stated, there are certain areas where using alternative, organic fluids is more attractive [4]. This is most often the case with industrial waste heat, electronic cooling, and low-concentration solar power systems, where the average temperature is much lower than those encountered in commercial power generation stations. Fortunately, access to low saturation pressure and temperature fluids is readily available, where the traditional water is replaced by a different fluid. Recent studies have investigated using organic fluids such as R-134a, R-245fa, propane, and ammonia, among a multitude of others, in an effort to find the optimal fluid for specific applications [36-38]. When an organic fluid is used instead of water, it is referred to as an organic Rankine cycle (ORC).

Hybrid power systems, such as those proposed by Pantaleo *et al.* [3], incorporating a biomass fired Brayton cycle (using a gas as the thermodynamic working fluid) in combination with a thermal energy store, a parabolic trough concentrator, and ORC system, have been shown to be economically viable. Domestic-scale power generation, such as those proposed for use in the United Kingdom by Freeman *et al.* [5, 6] show much promise, in that the average cost per unit of power produced was equivalent to a photovoltaic system of the same area. This is in addition to the advantage the system has of providing hot water as well as electricity.

2.3. SATURATED FLOW BOILING IN HORIZONTAL PIPES

Boiling is associated with the change of the thermodynamic state of a fluid as it goes from a liquid phase to a vapour phase, and occurs when the fluid is heated to above its saturation temperature at the prevailing fluid pressure. For the phase change to occur fully, a simplistic point of view is to consider saturated boiling of a saturated liquid, which has a uniform temperature equal to its saturation temperature (indicated by vapour quality, $x = 0$). As it absorbs heat, more and more liquid is converted into the vapour phase until all of the fluid mass is a saturated vapour ($x = 1$), still at a uniform temperature equal to the saturation temperature. Boiling can be classified in a broad sense as pool boiling, where the fluid is stationary, and flow boiling, where the fluid is in motion. Flow boiling can be further subdivided into external flow boiling (where the fluid flows over a warm/hot surface), and internal flow boiling, where the fluid moves inside a warm/hot duct, such as a circular pipe or a flow passage.

The latter (specifically, horizontal saturated internal flow boiling), forms the main focus of this research project. As alluded to earlier, saturated flow boiling implies that the bulk temperature of the fluid is at its saturation temperature. Crucially, at isobaric saturated fluid conditions, the bulk fluid temperature is expected to remain constant at the saturation temperature during saturated boiling. Subcooled boiling on the other hand, is where the bulk fluid temperature is below the saturation temperature, and only locally (such as at the contact surface between a warm/hot surface and the fluid) are fluid temperatures in excess of the saturation temperature, resulting in a phase change process. Subcooled boiling is beyond the scope of this work, however, and will not be discussed at length.

As is immediately apparent, the physical appearance of the fluid during saturated internal flow boiling has to change as the vapour quality increases from 0 to 1. This concept is illustrated in Figure 2.4 for horizontal flow, where gravity is perpendicular to the flow direction. Of interest is the different vapour and liquid distribution types (referred to as flow patterns).

Figure 2.4a represents a saturated liquid where $x = 0$, with the flow direction and gravity indicated applying for Figure 2.4b to Figure 2.4j as well. The liquid phase is shown as blue and the vapour phase as white in each image.

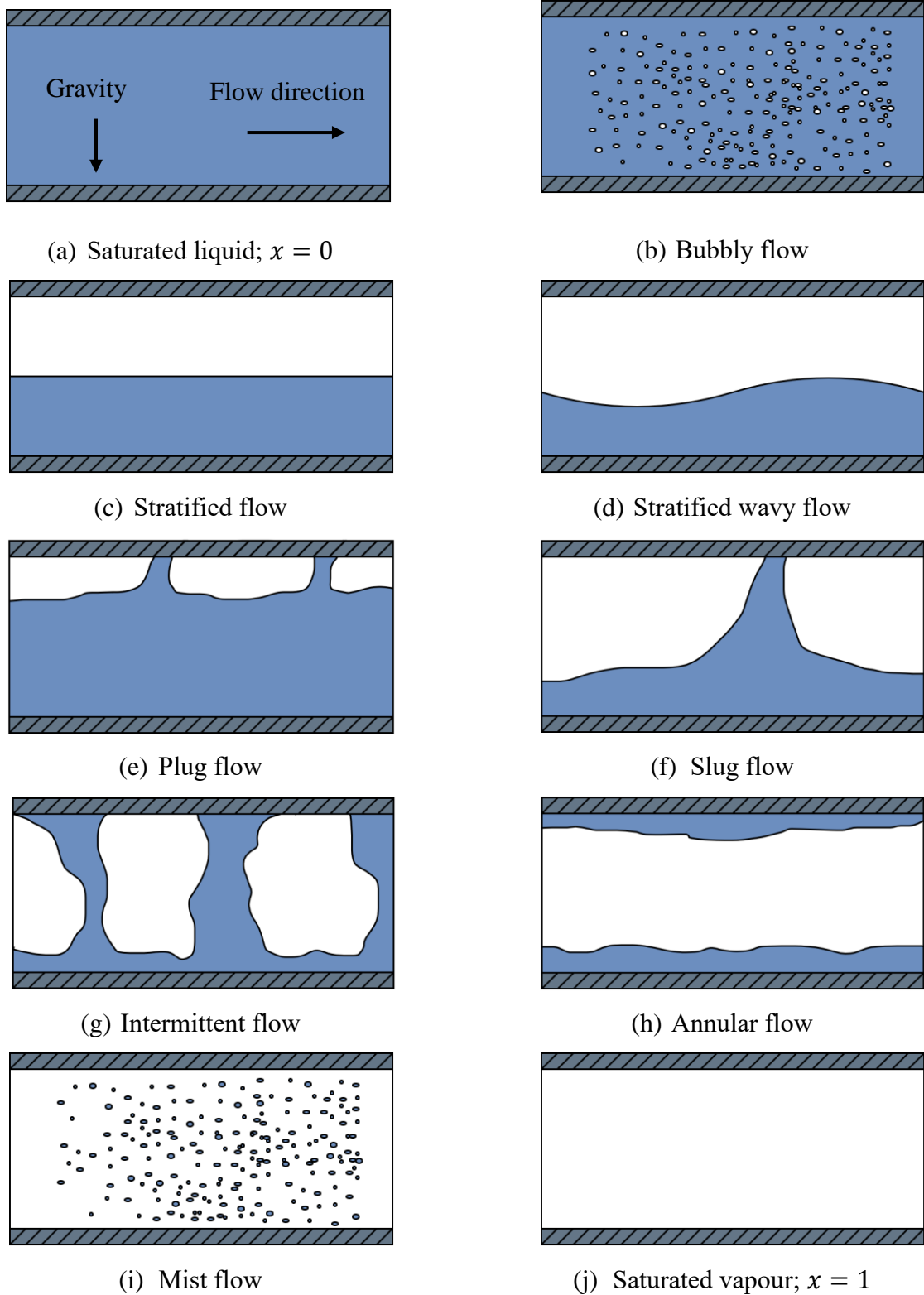


Figure 2.4. Flow patterns that occur during horizontal saturated boiling from saturated liquid (blue) to saturated vapour (white)

The bubbly flow regime is depicted in Figure 2.4b. It typically occurs when the vapour quality is low and the mass flux is high. For the stratified flow regime, shown in Figure 2.4c, the vapour and liquid regions are separated by an undisturbed interface. As the vapour quality increases, the velocity

of the vapour also rises, which cause waves to disturb this interface, resulting in the stratified wavy regime shown in Figure 2.4d. At higher mass fluxes and low vapour qualities, plug flow, represented in Figure 2.4e, can occur. In such cases, the liquid flow is separated by long bubbles of vapour. Crucially, these bubbles are much smaller than the diameter of the pipe, meaning liquid continuously covers the bottom wall. Slug flows, are indicated in Figure 2.4f. These occur at higher mass fluxes, and are similar to plug flows in many respects. The key difference between plug and slug flows is that the diameters of the vapour bubbles are much larger, approaching the diameter of the pipe. As the vapour quality increases, intermittent flow, as depicted in Figure 2.4g, occurs. With such flow, the waves of liquid wash the top of the pipe wall, such that it is continuously wetted. Annular flow, represented in Figure 2.4h, happens next, where the vapour velocity is high enough to cause a continuous liquid film around the circumference of the pipe. The liquid film is thicker at the bottom wall of the pipe than at the top. As the vapour quality increases further, the upper regions of the pipe will become dry first. Mist flow, as shown in Figure 2.4i, occurs at very high mass fluxes and vapour qualities. The liquid is stripped from the walls of the pipe and is suspended as tiny droplets, which are then transported in the vapour phase. Finally, complete dryout occurs when $x = 1$. This is represented in Figure 2.4j. From this point onwards, superheating of the vapour occurs, which is beyond the scope of this study. Vertical flow, in which gravity is parallel to the flow direction, exhibits many of the same flow patterns, save for stratified and stratified wavy flow, but these are not applicable to the horizontal pipes being considered in this work.

The ability of the fluid to have convective heat transfer with the wall is expressed by the heat transfer coefficient (HTC), and is defined as the heat flux per temperature difference between the wall and the bulk fluid. It has been found that the dry and wetted areas of the surface play a large role in the heat transfer process. Dry surfaces (such as with the upper regions in stratified flow, Figure 2.4c) exhibit a reduced heat transfer ability, whereas wetted surface (such as with the lower regions of stratified flow, or around the full circumference with annular flow) exhibit improved heat transfer ability.

As such, it has been found that the HTC depends heavily on the prevailing flow pattern during boiling. This ties directly to the two main boiling types, namely nucleate boiling and convective boiling. With nucleate boiling, which is mostly encountered when the flow is stratified (thus generally at low mass fluxes), the bubble formation rate, nucleation sites, and the applied heat flux play a dominant role. With convective boiling, on the other hand, the influence of the mass flux and vapour quality is dominant. Traditionally, it has been found that the annular flow pattern (which is associated with convective boiling) exhibits higher HTCs with an increase in the vapour quality as the liquid film gets thinner, while nucleate boiling does not depend on the vapour quality.

The prediction of the flow patterns is of great interest, and many attempts have been made in the last decades to quantify and delineate them for horizontal pipes [39-41]. One such method makes use of flow pattern maps, such as the one proposed by Wojtan, Ursenbacher and Thome [42]. An example of this map, constructed as instructed in the cited work for R-245fa at a saturation temperature of 35°C and a heat flux of 7.5 kW/m², is shown in Figure 2.5. In the map, the mass flux clearly has an important influence on the flow pattern encountered, as does the inlet vapour quality.

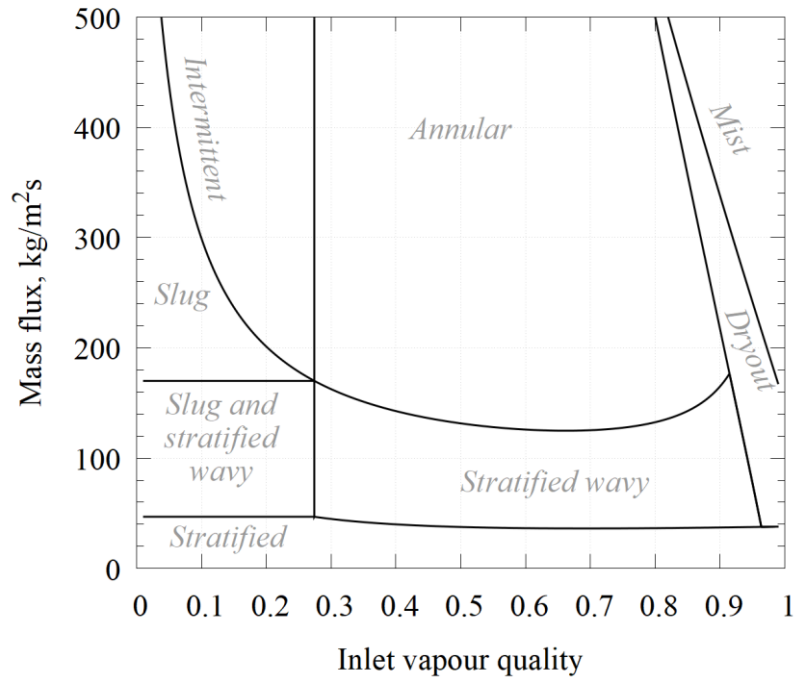


Figure 2.5. Example Wojtan-Ursenbacher-Thome [42] flow pattern map for R-245fa at 35°C

According to this flow map, pure stratified flow occurs only at mass fluxes below approximately 50 kg/m²s, persisting for the entire vapour quality range. The slug and stratified wavy flow patterns exist between 50 to 170 kg/m²s for a vapour quality of below 0.28, before transitioning to an exclusively stratified wavy pattern. Above 170 kg/m²s, the slug flow pattern and intermittent flow pattern dominate for a vapour quality of below 0.28, before the transition to the annular flow pattern for the majority of the vapour quality range. As the mass flux increases, the transition between slug and intermittent flow happens at lower vapour qualities. Importantly, while the flow pattern delineates clear boundaries between the observed flow patterns, in practice it is not that simple. The flow pattern map should be interpreted as a rough guide to the expected flow patterns, with a large amount of leeway in the experimentally obtained flow pattern.

One of the crucial aspects in designing any flow-based system is the pressure drop. The pressure drop is dictated by the fluid mass flux, its viscosity, as well as the diameter and length of pipe used, which directly translates into the size of the pump needed. Plainly speaking, more pressure drop

equates to a larger (and thus more expensive) pumping solution. Flow-boiling system designs are no different, with the added complication of the phase change contributing to the pressure change.

The pressure drop consists of three main components, namely the static, frictional, and momentum pressure differences. The static pressure difference is influenced by the gain or loss in potential energy of the fluid. For horizontal pipe installations, this is largely ignored, since the change in height over the entire system is negligible. The momentum pressure difference is an indication of the kinetic energy variation for a fluid. This is largely dependent on the vapour quality change over the length in question and the difference in density between the liquid and vapour phases. If only a certain section of the boiling length is being investigated (i.e., $0 < x < 1$), the void fraction at the inlet and outlet also plays a large part in the momentum pressure drop. The void fraction is defined as the fraction of the total volume that is occupied by the vapour phase, and can be calculated in a variety of ways. Using this method to determine the momentum pressure drop has been shown to be fairly accurate [43]. Finally, the frictional pressure drop is defined as the losses that occur due to the presence of viscosity in the fluid and interaction with the surface of the pipe. The frictional pressure drop is highly dependent on the viscosity and velocity of the fluid. As the flow pattern changes and the fluid evolves from liquid to vapour, the massively increased velocity of the vapour phase adds to the frictional pressure drop. Many correlations have been proposed in order to quantify this [44].

The (very) broad overview of flow boiling given thus far is sufficient for the purposes of this thesis, but for a more exhaustive overview of this subject, the author refers the interested reader to the convective boiling and condensation book by Collier and Thome [45]. The HTC is an important thermal quantity, and even though its definition is deceptively simple, it has been found to be highly dependent on the heat flux, mass flux, and vapour quality, as will be seen in the sections that follow.

2.4. STEADY-STATE PREDICTIVE CORRELATIONS AND RESULTS

Before the complex process of heat transfer during flow boiling can be fully appreciated, some mention of single-phase convective heat transfer is needed. Single-phase HTCs in circular pipes have been predicted to within 5% accuracy since the 1930s by making use of the Dittus-Boelter [46] formulation. Over the years, prediction accuracy improvements have been achieved [47, 48], but in essence the major dependence on the Reynolds and Prandtl number in some combination was retained.

This is not so for the two-phase flow boiling correlations. In a recent review article by Fang *et al.* [13], fifty correlations were evaluated for predictive accuracy. These run the gamut of possible proposed prediction methods, including simple enhancement factor methods, in which the

Dittus-Boelter single-phase equation is multiplied by a two-phase boiling enhancement factor, all the way up to relatively complex flow-pattern based methods, in which the flow pattern has to be predicted first based on the mass flow rate and vapour quality of interest from which an appropriate correlation can be selected and applied. None of the correlations investigated were even remotely on the level of accuracy of the single-phase correlations, apart from the correlations using knowledge of the wall temperature, which makes the prediction of the HTC moot.

A baseline understanding of the steady-state HTC and its reaction to various external factors has to be studied and understood before any change in these factors can be implemented. While the publications concerning flow boiling is multitudinous, with the number growing yearly, it is valuable to consider what researchers have found to this point. Some of the effects the mass flux, heat flux, vapour quality, enhanced heat transfer surface area (as is found in micro-fin tubes for example), and tube diameter has on the HTC for a specific fluid are noted. The effect of mass flux and heat flux on the HTC are of particular interest to this study, and an attempt was made to obtain studies covering a broad selection of these. Since this research project utilises R-245fa, the survey was limited to organic fluids.

Gómez Marzoa *et al.* [49] evaluated R-245fa in a horizontal smooth polyimide tube with an inner diameter of 2.689 mm at a mass flux ranging from 100 to 500 kg/m²s, a heat flux from 15 to 55 kW/m², and saturation temperatures of 35, 41 and 47 °C. Boiling was achieved by using hot water in an annulus around the test tube. It was found that a higher mass flux resulted in a higher HTC. At a mass flux of 100 kg/m²s, the vapour quality had a negligible effect on the HTC. The heat flux had no discernible effect, and it was hypothesised that the smoothness of the tube played a role. Increasing the saturation temperature had an almost negligible effect on the HTC at a mass flux of 200 kg/m²s and heat flux of 15 kW/m², but at higher mass and heat fluxes (400 kg/m²s and 45 kW/m²), the HTC was lowered as the temperature increased.

Tibirićá and Ribatski [50] evaluated flow boiling of R-134a and R-245fa for a horizontal stainless-steel pipe with an inner diameter of 2.3 mm and uniform joule heating. The mass fluxes considered ranged from 50 to 700 kg/m²s, while the heat fluxes varied from 5 to 55 kW/m². The saturation temperatures were 22, 31 and 41 °C. Higher mass fluxes resulted in higher HTCs. However, increasing the vapour quality below a threshold mass flux of 200 kg/m²s had a detrimental effect on the HTC. At a mass flux of 100 kg/m²s and a heat flux of 15 kW/m², an increased saturation temperature resulted in an increased HTC. It was also found that an increased heat flux resulted in an increased HTC, regardless of the mass flux or fluid type under consideration.

Contributing to the flow-boiling database in microscale channels, Kanizawa *et al.* [51] evaluated the effect of saturation temperature, mass flux, hydraulic diameter and heat flux on the HTC

of three fluids: R-134a, R-245fa and R-600a. For R-245fa, tests were conducted in tube sizes from 0.38 to 2.32 mm, at mass fluxes from 99 to 1 400 kg/m²s, heat fluxes of 10 to 163 kW/m², and saturation temperatures of 25.5 to 58.3 °C. It was found that for R-245fa, for vapour qualities below 0.40, the HTC was markedly increased with higher heat flux, regardless of the tube diameter. The influence of saturation temperature was negligible at heat fluxes of 5 kW/m², but had the effect of a higher HTC at higher saturation temperatures at increased heat fluxes. The mass flux had a minimal effect on the HTC at qualities below 0.40, but as the vapour quality increased, the increased mass flux resulted in an increased HTC.

An extensive study was carried out by Da Silva Lima *et al.* [52] on R-134a in a smooth copper tube with an inner diameter of 13.84 mm for mass fluxes of 300 and 500 kg/m²s, and heat fluxes of 7.5 and 15 kW/m². They considered saturation temperatures of 5, 15 and 20 °C and found that the HTC was higher for higher saturation temperatures at low vapour quality, but at higher vapour qualities, the opposite was true. The mass flux had a definite effect on the HTC, with the higher mass flux resulting in a higher HTC. The effect of this increase was amplified at higher vapour qualities. At low vapour qualities, higher heat fluxes resulted in higher HTCs, but this effect was decreased at higher vapour qualities.

Dorao *et al.* [53] evaluated R-134a during flow boiling in a stainless-steel pipe with an inner diameter of 5 mm at a saturation temperature of 18.6 °C for mass fluxes between 200 and 400 kg/m²s and heat fluxes between 3.9 and 47.1 kW/m². They found that the increased heat flux resulted in a higher HTC, regardless of the vapour quality. It also appeared that the highest heat flux had the effect of making the HTC independent of the mass flux and vapour quality. However, for lower heat fluxes, higher mass flux and vapour quality had the effect of increasing the HTC, with the effect of mass flux becoming more prominent at higher vapour qualities.

Celen and Dalkılıç [54] carried out a complete evaluation of the effects of mass flux, saturation temperature, heat flux and vapour quality on the HTC of R-134a in a tube with an inner diameter of 8.62 mm. They considered mass fluxes between 290 and 381 kg/m²s, heat fluxes between 10.0 and 15.0 kW/m², and saturation temperatures between 15 and 22 °C. It was found that the HTC increased with mass flux and vapour quality, due to the contribution of thinner liquid film and increased vapour velocity. This was more apparent at higher vapour qualities. Higher saturation temperatures resulted in higher HTCs irrespective of the vapour quality range. At a mass flux of 290 kg/m²s, increased heat fluxes resulted in higher HTCs, but this effect decreased for the higher mass flux of 381 kg/m²s.

Grauso *et al.* [55] compared R-134a and R-1234ze(E). The thermodynamic properties of these two fluids are similar, with R-1234ze(E) having a lower global warming potential. This study included the effect of mass flux, heat flux, vapour quality and saturation temperature on the HTC

obtained. The test section was a stainless-steel pipe with an inner diameter of 6 mm, with the test conditions covering mass fluxes between 146 and 520 kg/m²s, heat fluxes of 5.0 to 20.4 kW/m², at saturation temperatures of -2.9 to 12.1 °C. The HTC increased with vapour qualities, irrespective of the mass flux, although at higher mass fluxes, this was more pronounced. Higher mass fluxes resulted in higher HTCs. The saturation temperature and heat flux were found to have a negligible effect on the HTC.

Bamorovat Abadi *et al.* [56] investigated the effect of gravity on the heat transfer and pressure drop of R-245fa by conducting tests in horizontal and vertical stainless-steel pipes with inner diameters of 3 mm. The mass flux was ranged from 200 to 700 kg/m²s for heat fluxes from 10.0 to 40.0 kW/m², while keeping the saturation temperature at 40 °C. Their data indicated that the heat flux had a relatively minor influence on the HTC, but was more pronounced at low vapour qualities. The mass flux had a much greater influence, with the HTC being higher at increased mass fluxes. Vertical tubes also exhibited a higher HTC than horizontal tubes.

Bandarra Filho and Barbieri [57] evaluated the flow boiling performance of R-134a in horizontal microfin and smooth copper tubes. The inner diameters of the smooth tubes were 6.24 and 8.76 mm. The mass flux ranged between 100 and 500 kg/m²s at a constant heat flux of 5.0 kW/m² and a saturation temperature of 5 °C. The HTC increased with mass flux, but at values lower than 150 kg/m²s, it was unaffected by vapour quality in the smooth pipe.

Manavela Chiapero *et al.* [58] investigated the boiling HTC of R-134a at 34 °C in a smooth stainless-steel pipe with an inner diameter of 5 mm. They considered vapour qualities ranging from 0 to 1 for a mass flux between 300 and 500 kg/m²s, and heat fluxes between 10.0 and 20.0 kW/m². It was found that for lower qualities, a higher heat flux corresponded to a higher HTC, and that this effect was more pronounced at the lower mass flux. The vapour quality had a negligible effect at the lower mass flux.

Spindler and Müller-Steinhagen [59] compared flow boiling heat transfer for R-134a and R-404A at low mass fluxes in a microfin pipe as well as a smooth pipe. The smooth pipe had an inner diameter of 8.95 mm. Saturation temperatures of -20 to 0 °C were considered at mass fluxes of 25 to 150 kg/m²s and heat fluxes of 1.0 to 15.0 kW/m². For R-134a, they found that at low mass and heat fluxes, the HTC was higher than expected. It was suggested that pool-boiling correlations be investigated for adapting correlations for enhanced pipes. The flow pattern was affected by the spiral grooves in the enhanced pipe, which increased the wetted surface. A lower saturation temperature also resulted in a higher HTC.

The HTCs in flows of R-134a and R-404A were compared for saturation temperatures ranging from -15 to 0 °C in a pipe with an inner diameter of 7.49 mm by Balachander and Raja [60]. Mass

fluxes were ranged between 57 and 102 kg/m²s and the heat flux for R-134a was between 7.5 and 8.3 kW/m². An increased mass flux resulted in a higher HTC. Increasing vapour quality had a detrimental effect on the HTC, as did increasing the saturation temperature. It was concluded that this was due to the flow pattern being stratified wavy instead of annular.

Björk and Palm [61] studied the boiling heat transfer in a domestic plate-type evaporator using R-600a as refrigerant, with the presence of frequent bends and a non-circular cross-section with a hydraulic diameter of 3.21 mm. The mass flux was varied from 21 to 43 kg/m²s, and the heat flux from 1.0 to 5.0 kW/m², while the saturation temperature under consideration was -15 °C. The HTC decreased with increasing vapour quality and heat flux at the lowest mass flow rate tested. For higher mass flow rates, the HTC increased with increased vapour quality, but was largely independent of applied heat flux. The achieved HTC was higher than that predicted by correlations, and it was hypothesised that the flow pattern contributed to this discrepancy.

A study covering a fairly wide range of conditions for refrigerants R-22, R-134a and R-404A was conducted by Saiz Jabardo and Bandarra Filho [62] using a copper pipe with an inner diameter of 12.7 mm. These conditions consisted of saturation temperatures of 8 and 15 °C, mass fluxes of 50 to 500 kg/m²s, and a heat flux of between 5 and 20 kW/m². It was found that for low mass fluxes, the HTC was only weakly dependent on the vapour quality, and in fact decreased slightly for higher qualities. However, the heat flux had an effect on the HTC throughout the quality range at low mass fluxes, and at lower qualities at higher mass fluxes. At mass fluxes above 200 kg/m²s, the flow pattern transitioned from stratified to annular, and the HTC increased with increasing quality up to dryout. An increase in the saturation temperature had a positive effect on heat transfer at lower qualities.

Wattelet *et al.* [63] found that for lower mass fluxes, the HTC was also largely independent of vapour quality, but was affected to a sizable degree by the heat flux. They compared experimental HTCs for flow of R-134a, MP-39 and R-12. The mass fluxes under consideration were from 25 to 100 kg/m²s, at saturation temperatures of -15 to 5 °C and heat fluxes of 2.0 to 10.0 kW/m². Their test facility consisted of a smooth copper pipe with an inner diameter of 7.04 mm. Increasing mass and heat flux resulted in an increased HTC.

A summary of the results for the mentioned literature is given in Table 2.1. The reported influence of the saturation temperature (T_{sat}), mass flux (G), heat flux (\dot{q}) and vapour quality (x) on the HTC are indicated. Increased HTC associated with an increasing parameter is shown by “↑”, while the opposite HTC is given by “↓”.

There is consensus in the literature about the HTC being highly dependent on mass flux, but no consensus on the effect of vapour quality, saturation temperature and heat flux. Gómez Marzoa *et al.* [49] found that the effect of increasing heat flux on the HTC was mild. Björk and Palm [61] observed

that increasing heat flux had a negative effect on the HTC. The rest of the literature reviewed reported that increasing the heat flux had a significant positive effect on the HTC, either throughout the vapour quality range and mass fluxes tested, or at least for lower vapour qualities. The effect of increasing vapour quality was noted by Gómez Marzoa *et al.* [49] to be negligible at a mass flux of 100 kg/m²s, while Saiz Jabardo and Bandarra Filho [62] found that at mass fluxes of 50 and 100 kg/m²s, the increase in vapour quality actually had a negative effect on the HTC. The other studies found that for mass fluxes above 200 kg/m²s, the increase in vapour quality corresponded to an increased HTC. Of interest is that Manavela Chiapero *et al.* [58] only observed this for a mass flux of 500 kg/m²s.

These findings must be viewed in the light of the two main contributors to flow boiling, that of convective and nucleate boiling. Convective boiling dominates when the mass flux is sufficiently high, which means the flow pattern becomes annular at very low vapour qualities. As the vapour quality increases, the HTC also increases, since the annular film thickness becomes thinner. Nucleate boiling, on the other hand, depends on the bubble formation rate, nucleation sites (which depend on the pipe roughness), and the applied heat flux. This boiling mechanism dominates when the mass flux is low enough, and the flow patterns are thus stratified in some form throughout the vapour quality range. The mass flux at which nucleate boiling dominates over convective boiling is thus of particular interest for this study, since part of it is dedicated to low mass and heat fluxes.

Table 2.1. Overview of studies of in-tube boiling of refrigerants at low mass and heat fluxes

Author(s)	Fluid	Experimental apparatus	T_{sat} [°C]	G [kg/m ² s]	\dot{q} [kW/m ²]	Effect of increase on HTC
Gómez Marzoa <i>et al.</i> [49]	R-245fa	2.689 mm, horizontal smooth, non-uniform heat flux	35 to 47	100 to 500	15.0 to 55.0	T_{sat} : Negligible G : ↑ \dot{q} : Negligible x : Negligible at 100 kg/m ² s
Tibirićá and Ribatski [50]	R-134a R-245fa	2.3 mm, horizontal smooth, uniform heat flux	22 to 41	50 to 700	5 to 55	T_{sat} : ↑ for 100 kg/m ² s and 15.0 kW/m ² G : ↑ \dot{q} : ↑ x : ↑ for >200 kg/m ² s
Kanizawa <i>et al.</i> [51]	R-134a R-245fa R-600a	0.38-2.6 mm, horizontal smooth tubes, joule heated	25.5 to 58.3	99 to 1400	10 to 163	T_{sat} : ↑ for \dot{q} >5 kW/m ² G : ↑ for x >0.40 \dot{q} : ↑ for x <0.40
Da Silva Lima <i>et al.</i> [52]	R-134a	13.84 mm, horizontal smooth tube, counterflow boiled	5 to 20	300 to 500	7.5 to 17.5	T_{sat} : ↑ for lower x ; ↓ for higher x G : ↑ \dot{q} : ↑ at lower x
Dorao <i>et al.</i> [53]	R-134a	5.00 mm inner diameter, horizontal smooth tube, joule heated	18.6	200 to 400	3.9 to 47	G : ↑ \dot{q} : ↑; independent of G and x if high enough x : ↑
Celen and Dalkılıç [54]	R-134a	8.62 mm, horizontal smooth tube, electrical resistance heated	15 to 22	290 to 381	10 to 15	T_{sat} : ↑ G : ↑ \dot{q} : ↑; less of an effect at high G
Grauso <i>et al.</i> [55]	R-134a R-1234ze(E)	6 mm inner diameter, horizontal smooth tube, joule heated	-2.9 to 12.1	146 to 520.	5 to 20.4	T_{sat} : Negligible G : ↑ \dot{q} : ↑ for x <0.2
Bamorovat Abadi <i>et al.</i> [56]	R-245fa	3 mm, horizontal and vertical smooth tube, joule heated	40	200 to 700	10 to 40	G : ↑ \dot{q} : ↑ for lower G and lower x
Bandarra Filho and Barbieri [57]	R-134a	8.76 mm, horizontal smooth, herringbone and microfin tube, electrical resistance heated	5	100 to 500	5	G : ↑ \dot{q} : Single heat flux investigated x : ↑ for G >100 kg/m ² s
Manavela Chiapero <i>et al.</i> [58]	R-134a	5 mm, horizontal smooth tube, joule heated	34	300 to 500	10 to 20	G : ↑ \dot{q} : ↑ at low x x : ↑ for G =500 kg/m ² s
Spindler and Müller-Steinhagen [59]	R-134a R-404A	9.52 mm, horizontal smooth and microfin tube, electrical resistance heated	-20 to 10	25 to 150	1 to 15	T_{sat} : ↑ except for -20 °C G : ↑ \dot{q} : ↑ for low x
Balachander and Raja [60]	R-134a R-404A	7.49 mm, horizontal smooth tube, counterflow acetone heated	-15 to 0	57 to 102	2 to 18	T_{sat} : ↓ for low G G : ↓ for lower x
Björk and Palm [61]	R-600a	Cut section of a plate-type evaporator with hydraulic diameter 3.21 mm, electrical resistance heated	-15	21 to 43	1 to 5	G : ↑ \dot{q} : ↓ for G =21 kg/m ² s x : ↑ for G >21 kg/m ² s
Saiz Jabardo and Bandarra Filho [62]	R-22 R-134a R-404A	12.7 mm, horizontal smooth tube, electrical resistance heated	8 to 15	50 to 500	5 to 20	T_{sat} : ↑ for \dot{q} ≥20 kW/m ² G : ↑ \dot{q} : ↑ x : ↓ for G =50 and 100 kg/m ² s
Wattelet <i>et al.</i> [63]	R-134a R-12 MP-39	7.04 and 10.92 mm, horizontal smooth tube, electrically heated	-15 to 5	25 to 100	2 to 10	G : ↑ \dot{q} : ↑ for lower G

2.5. TRANSIENT-STATE HEAT AND MASS FLUX

In DSG systems, because flow boiling is required to occur in the solar collector tubes to produce superheated vapour (either steam or organic fluid vapour), the correct design of the solar collectors is of the utmost importance. However, as mentioned, one of the challenges faced in this application is the varying nature of the DNI due to partial and temporal cloud coverage of the collector field, or other time-varying weather conditions that can give rise to time-varying operation. Thus far, research into the effects of transient conditions on the HTC within the collector tubes has been limited.

Chen *et al.* [64] investigated the effect of an oscillating heat flux on the heat transfer of R-134a in an annular duct. The duct consisted of an outer Pyrex glass pipe with an inner diameter of 20 mm in which the refrigerant flowed. Inside this was a smooth copper pipe with an outer diameter of 10, 16, or 18 mm, corresponding to hydraulic diameters of 10, 4 and 2 mm. The inner pipe wall thicknesses were 1, 1.5, and 2.5 mm respectively. The heat flux was provided by a cartridge heater inside this copper pipe. A saturated liquid inlet state at 15 °C was used and constant mass fluxes of 300 and 500 kg/m²s were considered. The heat flux in the inner pipe was oscillated in a triangular wave between 0 and 30 kW/m² with a mean heat flux of 15 kW/m², over periods of 2 to 600 s. It was found that the influence on the time-averaged HTC was negligible, regardless of the amplitude or period of the heat flux oscillation. The wall temperature of the inner pipe followed the imposed heat flux, with a time lag due to the thermal inertia of the copper wall. When the period of oscillation was small enough (2 s), the wall temperature was unaffected.

Kingston *et al.* [65] investigated the boiling of HFE-7100 in a microchannel under a single pulse of various heat fluxes and found that during transition from single-phase liquid to boiling, the wall temperature could over- or undershoot the eventual steady-state temperature. They also studied the effect that a continuous pulse (square waveform) in heat flux had when applied at frequencies ranging from 0.1 Hz to 25 Hz, at magnitudes of 15, 75 and 150 kW/m² [66]. It was found that at low frequencies, the pulse was equivalent to multiple independent steps, while at higher frequencies, the effect approximated a constant heat flux. This was due to the microchannel wall damping out the applied heating profile.

Chen *et al.* [10] investigated the HTC of saturated liquid R-134a on the verge of commencing flow boiling under flow rate oscillations. They conducted tests in a narrow annular duct with a hydraulic diameter of 4 mm under a mean mass flux of 300 to 500 kg/m²s. Saturation temperatures were varied between 10 and 15 °C, with a heat flux of 0 to 45 kW/m². The oscillations were of a triangular form, with an amplitude varying between 0% and 30% of the mass flux under investigation. The period of the oscillation ranged between 20 and 120 s. It was found that the time-averaged HTCs were not noticeably affected by either the amplitude or the period of the mass flux oscillation.

Park *et al.* [11] conducted a study on the possible detrimental effect of repeated flow oscillations on the HTC of R-134a at a mean mass flux of 300 kg/m²s. They used a stainless-steel pipe with a 5 mm bore, at a saturation temperature of 27 °C. The heat flux was kept between 10.3 and 11.2 kW/m². The flow was oscillated sinusoidally with an amplitude of 59% to 131% of the mean mass flux, for periods between 10 and 130 s. It was found that, if the amplitude and period of oscillation remained below a certain threshold, the mean HTC remained unaffected. The wall temperature closely followed the oscillation for certain periods and amplitudes.

Similarly, Kærn *et al.* [12] investigated the HTC of R-134a in an 8 mm copper tube under pulsed flow rate conditions. The mass flux ranged from 50 to 194 kg/m²s. It was found that at higher frequencies of the pulsing mass flow, the HTC was improved.

As well as transient heat fluxes due to cloud coverage, direct steam generation solar collectors also experience non-uniformity of heat flux around their circumference due to the position of the sun. To investigate these conditions, an attempt was made by Wang *et al.* [67] to characterise the boiling of R-245fa under a non-uniform heat flux in a 10 mm stainless-steel pipe. It was found that the vapour quality at which flow pattern transition happened was lower and that the HTC was higher than that of uniform heat flux. Wani *et al.* [68] simulated a non-uniform heat flux for an NiO nanofluid heat transfer fluid in a 19 mm inner diameter, 1.3 m long pipe, and found that the temperature at the top wall differed from that at the bottom by up to 30 °C.

Zhang *et al.* [69] tested the in-tube flow-boiling characteristics of R-134a at saturation temperatures typically encountered in ORC systems, upwards of 80 °C. They found that the HTC decreased with increased vapour quality, and that it was closely related to the unwetted wall temperature. The test conditions evaluated were at a mass flux of 300 to 600 kg/m²s and a heat flux of 20 to 50 kW/m². Wang *et al.* [70] found that for R-245fa in a 7 mm outer diameter microfin pipe, the HTC increased up to a maximum with increasing vapour quality, after which it decreased with further increases in the vapour quality. Their experimental conditions covered mass fluxes of 96 to 336 kg/m²s, heat fluxes between 3 and 16 kW/m², and saturation temperatures of 25 to 45 °C.

Modelling and simulation efforts to characterise the transient behaviour of DNI include that of Desideri *et al.* [71], who simulated transient and steady-state conditions and compared with actual system results for a heat transfer fluid. Efforts at modelling transient states in heat transfer were made by Korol'kov *et al.* [72]. A numerical/analytical method was derived and applied to obtain the enthalpy under independent perturbances in mass flux and heat flux for water, and it was found that the theoretical value obtained was within 5 % of the experimentally obtained value. Ferruzza *et al.* [73] explored a different way of designing a steam generator to account for the inherent start-up and shutdown stresses in a CSP system. They investigated heat transfer fluid transferring heat to water.

Lin *et al.* [74] provided design guidelines for a direct steam generation receiver. The transient characteristics of a full-sized parabolic trough DSG system were explored by Li *et al.* [75]. They found that the superheating zone of the tube experienced the highest temperature excursion of the working fluid due to a step change in DNI of amplitudes ranging from 10 to 30%, whereas a reduced DNI expanded the size of the saturated zone. The deformation of parabolic trough collector tubes due to temperature differences was investigated by Li *et al.* [76]. For extreme changes in the DNI, or for cold starts of the CSP system, their simulation predicted a very large strain.

Regardless of the application, temporal variations in the imposed heat flux can be expected in DSG systems. Heat flux variations are directly linked to changes in the DNI which, for example, can be caused by temporary cloud coverage [77]. Ait Lahoussine Ouali *et al.* [78] found that cloud coverage had a significant impact on the simulated gross power output of a proposed CSP plant in Morocco. Feldhoff and Hirsch [79] noted that the current annual DNI yield predictions relied on steady-state heat balances and did not take into consideration short-term variations caused by cloud coverage. Eck and Hirsch [80] developed a transient simulation tool to model the impact of cloud shading and found that following a cloud disturbance on a section of the parabolic trough, a significant amount of time was needed for the system to reach steady state. The orientation of the field was also of particular importance.

The fact that the measured wall temperature fluctuates with the applied heat flux as reported in the literature relating to transient heat fluxes, opens up another possible failure mechanism particular to CSP systems. In an industrial parabolic trough system, the receiver geometry consists of a metal tube inside a glass sheath, responsible for maintaining a vacuum around the tube in order to limit heat transfer losses. This seal can be broken for many reasons, which makes the replacement of these evacuated tubes one of the chief operating costs encountered in practice [81]. Although it is not the subject of this particular study, it is interesting to note that many studies have been conducted in an attempt to quantify and solve this problem [82-87]. Any temperature response data gathered is thus also of interest to engineers developing parabolic trough systems.

The experimental studies that have been found in open literature by the author for refrigerant fluids in ORC systems thus far have focused mostly on steady-state results. The scarcity of published works dealing with transients in this field makes this study all the more relevant. The question of the effect of a perturbation in DNI (and thus local vapour quality) on the HTC during a transient in an experimental system has yet to be dealt with in the literature. This variable DNI is important for any proposed CSP systems using an organic refrigerant, since the incoming heat flux experienced by the system has a definite effect on the vapour quality and HTC in solar collector tubes.

2.6. SUMMARY

The start of this chapter introduced concentrated solar power, with the untapped worldwide solar potential and the various concentration technologies in use at present briefly explored. Direct steam generation, and the advantages it has over a two-fluid approach was discussed next, segueing into organic Rankine cycles for application in certain areas where the average boiling temperature was relatively low. Next, saturated flow boiling in horizontal pipes was discussed, with special focus on the flow patterns and the interplay between nucleate and convective boiling. The pressure drop and how it was influenced by the flow evolving from saturated liquid to saturated vapour was also mentioned. Following this, the difficulties faced in determining a universally applicable correlation to predict the HTC were highlighted, before an overview of the often-conflicting experimental results for organic fluids was given. The limited transient work found was also detailed. Certain areas underrepresented in literature were recognised, which would be addressed in this work. These were first and foremost studies on the effect a transient heat flux or vapour quality had on the HTC, and secondly the lack of data at mass fluxes below $100 \text{ kg/m}^2\text{s}$ and heat fluxes below 5.0 kW/m^2 for R-245fa.

3. EXPERIMENTAL APPARATUS

3.1. INTRODUCTION

This chapter first specifies the criteria which the proposed experimental system had to comply with in order to provide useful results for industry. It then describes the constructed facility and test section in detail, followed by the system control and data logging process, as well as the calibration of the relevant sensors.

In order to obtain heat transfer and pressure results, a basic experimental setup had to be designed and constructed. The requirement that the mass flux and heat flux had to be finely controllable and instantaneously adjustable meant that the existing two-phase boiling/condensation systems at the University of Pretoria, (which used vapour compression cycles) was not suitable, even though it has delivered reliable steady-state results in the past [88-90].

The design envelope, which consisted of the chosen organic fluid (which dictated the pressure the system was kept at), the mass flux of that fluid, and the vapour quality achievable, was purposefully kept as wide as possible in order to accommodate a wide range of conditions. The system was also designed to be modular where feasible, meaning that future tests could easily be performed by switching out the test section or other components.

3.2. CRITERIA FOR THE EXPERIMENTAL SYSTEM

Before the facility and test section are described, a short digression in terms of the criteria this system had to fulfil is given. In order to obtain a general starting point in terms of pipe diameters and mass fluxes, some of the DSG plants used for industrial heating (mentioned in Section 2.2) were investigated. Unfortunately, obtaining information on pipe diameters and mass fluxes was not possible, so instead attention was turned to the commercial and pilot plants also mentioned.

The relevant details that could be gathered from literature regarding these plants is listed in Table 3.1. This table includes the receiver pipe inner diameter, the saturation temperature, the mass fluxes, the pre-concentration DNI and the concentration ratio of the parabolic trough.

Table 3.1. Salient specifications for CSP DSG plants using horizontal pipes

Plant	Receiver inner diameter [mm]	Sat. temp. [°C]	G [kg/m ² s]	Design point DNI [kW/m ²]	Conc. ratio
Thai Solar Energy 1 [33]	60	234	1770 (overall) 148 (evaporator) 253 (super-heater)	0.80	66
Stillwater GeoSolar Hybrid Plant [34]	n/a	n/a	n/a	0.90	24
INDITEP [32]	55	286	598 (per row)	0.875	82
DISS [31]	50	311	407 (per row)	0.80	80

To the author's knowledge, no Organic Rankine cycles (ORCs) for power generation have been adopted commercially, but they have been explored in many studies gauging their potential [7]. In some of these studies, solar energy is used to experimentally boil the organic fluid directly in the solar field, while others focus purely on numerical modelling or waste heat instead of DNI. Some of the data found in literature is shown in Table 3.2.

Table 3.2. Experimental and numerical studies of direct-boiling solar ORCs in horizontal pipes

Author	Type of study	Fluid	Receiver inner diameter [mm]	Sat. temp. [°C]	G [kg/m ² s]	Design point DNI [kW/m ²]	Conc. ratio
Taccani <i>et al.</i> [91]	Experimental (solar)	R-245fa	35.5	82.1	500	0.49 to 0.59	43
Freeman <i>et al.</i> [6]	Numerical (solar)	R-245fa	20	100	318	0.5	-
Fu <i>et al.</i> [92]	Experimental (waste heat)	R-245fa	16.39	106	187 (per row)	-	-

With the data regarding actual systems in use available, one would be forgiven for thinking that it is simply a matter of matching non-dimensional numbers when designing an experimental facility. While non-dimensional numbers are key when performing experiments if the conclusions reached for

a specific test case are to be applicable to other cases, this approach is limited when applied to boiling heat transfer. The number of variables influencing this phenomenon (and thus the non-dimensional groups) become excessive.

Since satisfying all the non-dimensional criteria was not possible, a simpler approach was sought. The mass flux could be replicated to a large degree by adjusting the mass flow rate and the cross-sectional area (in other words the diameter) of the pipe. The high heat fluxes observed in the preceding tables would not be conducive to performing meaningful tests in terms of vapour quality, but since the heat flux in industry had to pass through intermediate values on its way to the design point quantities, it was considered sufficient to at least cover some of those intermediates. Additionally, the fact that the concentration ratio for small to medium parabolic trough collectors in practice is in the range of 10 to 20 [22] meant that the heat flux for these systems could be duplicated exactly. Importantly, it was realised that replicating the flow pattern was a necessary component in mimicking behaviour in industry, and so this was also part of the criteria. Crucially, Zarza *et al.* [32] states that the design point for the mass flux in the solar field of the INDITEP plant was selected specifically in an attempt to avoid *any* stratification in the solar field. Armed with these guidelines, the construction of the facility and test section could commence.

3.3. FACILITY

The apparatus consisted of a closed fluid loop, depicted schematically in Figure 3.1, which could be charged with various different fluids. As mentioned, the primary fluid of interest in this study was the refrigerant R-245fa which was used in the tests described in later chapters. A pump was used to circulate the fluid from a liquid receiver, through a mass flow meter, an electrically heated preheater, an electrically heated test section, and a water-cooled condenser back to the receiver. A bypass line was used with a needle valve to finely control the mass flow rate through the system if needed. An image of the constructed facility, just before commissioning, is shown in Figure 3.2 with some salient components noted.

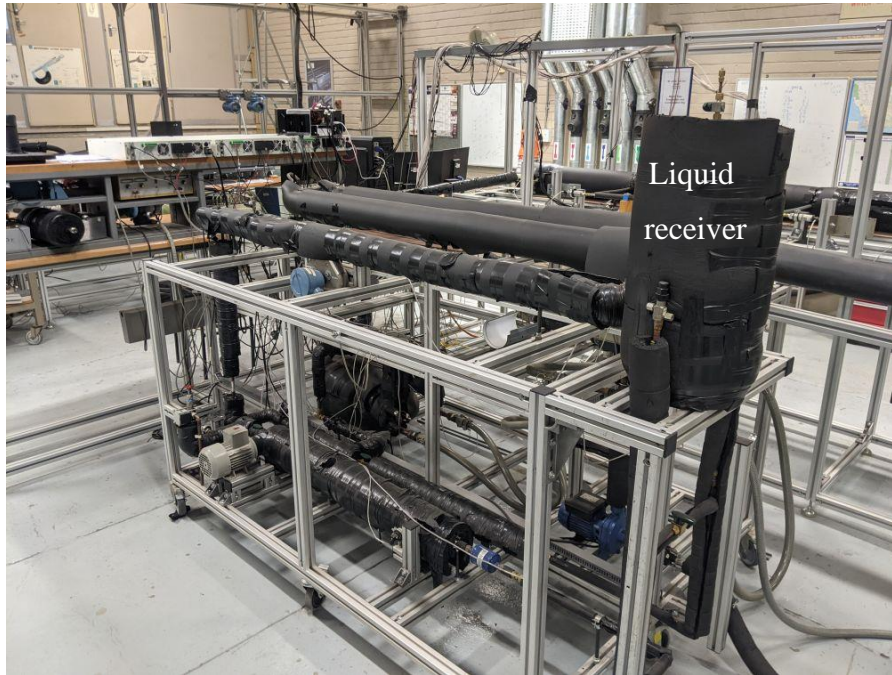


Figure 3.3. Commissioned facility in the process of receiving additional insulation

The facility, excluding the test section, was constructed from 12.7 mm outer diameter, smooth, hard-drawn copper pipe. The eventual liquid receiver had a capacity of 18 L and was placed at a height of approximately 1.5 m above the pump suction side. This provided a net positive suction head and ensured a pressure difference between the saturated fluid in the receiver and the liquid fluid at pump entry. The receiver also served as temperature buffer. A magnetically coupled speed-controlled GATHER gear pump with a maximum flow rate of 540 L/h and a minimum flow rate of 14.4 L/h was used. It was followed by a pressure relief valve with an adjustable threshold. The mass flow meter (MicroMotion CMF010 Coriolis flow meter) had an operating range of up to 0.04 kg/s with an accuracy of 0.1%. The gear pump was chosen specifically to be able to exceed the maximum flow rate of flow meter in order to enable the switching of this meter for future studies.

The preheater (between point A and B in Figure 3.1) was used to control the inlet vapour quality to the test section and consisted of two 1.9 m long, 12.7 mm outer-diameter copper pipes with tightly wound resistance wire (each with a resistance of 35 Ω). The wires were connected to two 3 kW ElektroAutomatik EA8360-30 DC power supply units with an accuracy of 0.2% of the output voltage and current.

The test section (surrounded by a dashed line in Figure 3.1), which is discussed later in more detail, had the sole purpose of collecting data from which the flow-boiling HTC could be derived. It was connected to a 1.5 kW ElektroAutomatik EA8360-15 DC power supply unit with the same accuracy as that of the preheater. The linear distance between the exit of the preheater and the inlet to the test section was 3.5 m.

The condenser consisted of a fluted tube-in-tube heat exchanger with a rated maximum capacity of 72 kW. It was serviced by either a large-capacity external chiller system, which supplied water at a steady temperature of approximately 6 °C, or a Lauda Proline RP1845C thermal bath, which supplied water at a steady temperature dependent on the test parameters. The water was driven through the condenser either by an EBARA centrifugal pump, or the thermal bath pump. The water pumping mechanism was connected to another Coriolis flow meter and a Honeywell three-way valve with which the flow rate of water from the centrifugal pump could be controlled. The water flow meter was a MicroMotion CMF025 unit with a range of 0.4 kg/s and an accuracy of 0.1% of the current flow rate. The water temperature was measured using a temperature measurement station before and after the condenser, at point E and F respectively.

The entire system was instrumented at key points with temperature and pressure measurement devices for measurement and control. The absolute pressure transducer positions are indicated Figure 3.1 with **P** symbols. Those ahead and after the gear pump were GEMS 2200 series transducers, with a stated accuracy of 0.2% of full scale (which was 2 MPa). The rest of the pressure transducers on the facility and test section were Sensotec FP2000 transducers with a stated accuracy of 0.25% of the full scale of 3.4 MPa. The pressure taps, onto which the transducers were mounted, were horizontal and drilled to a diameter of 0.8 mm. This was less than the recommended tenth of the diameter of the pipe, in order to minimise the disturbance of the flow. They were also carefully deburred to further limit this interference.

The temperature measurement stations are indicated in Figure 3.1 by the symbol **T**, and comprised four T-type thermocouples at each location. The thermocouples had a pre-calibrated accuracy of 0.1 °C (which was improved via in-house calibration, as discussed later) and were attached with thermal tape, so as to be spaced in four uniform circumferential (equidistant) locations around the pipe (above, below, left and right). The resistance temperature detectors (indicated by **RTD** in Figure 3.1) were 1/10 DIN Omega Pt100s with an accuracy of 0.03 °C.

Flow patterns could be recorded at the inlet or outlet of the test section by a specialised Photron Mini-UX high-speed camera, with a maximum resolution of 1280 by 1024 pixels, a maximum frame rate of 4000 frames per second, and an internal recording capacity of 8 gigabytes. It could be operated at various combinations of resolution and frame rate, depending on the recording time required. Back-lighting was provided by a red light-emitting diode measuring 50 mm by 50 mm.

The entire facility, including the water loop, was insulated to a minimum radius of 80 mm. This insulation had a thermal conductivity of 0.036 W/mK, according to the manufacturer [93].

3.4. TEST SECTION

The test section lay-out, shown in Figure 3.4, was constructed from a 9.53 mm outer diameter (d_o), 8.31 mm inner diameter (d_i), smooth, hard-drawn copper pipe. It consisted of a calming section of 500 mm, an inlet sight glass, a heated diabatic segment (L_h) with a total length of 800 mm, and an outlet sight glass.

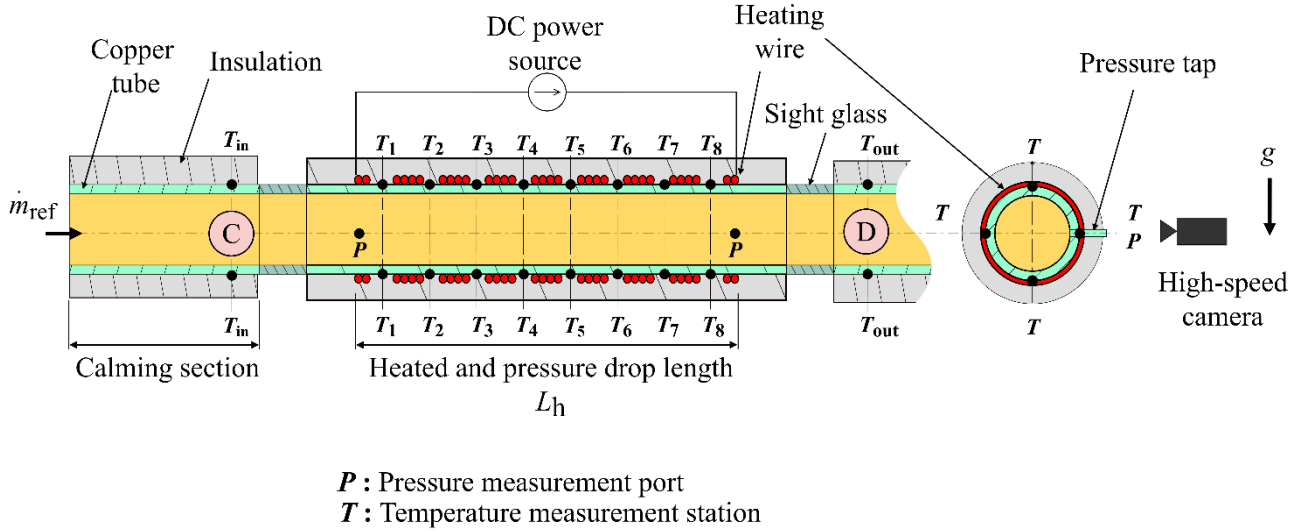


Figure 3.4. Test section schematic (not to scale)

The test section received fluid at a set mass flow rate, \dot{m}_{ref} , and inlet vapour quality, x_{in} . As mentioned, the mass flow rate was controlled by the set pump speed and the bypass line valve. The inlet vapour quality was controlled by the heat transfer rate in the preheater and the mass flow rate. Cho *et al.* [94] found that the flow disturbance caused by the geometric bends and curves of a U-tube had an effect on the HTC during two-phase flows. They reported noteworthy influences downstream up to 48 times the internal diameter of their tube. Thus, to negate any effect that the preceding bends and reduction in diameter had on the HTC or flow patterns, a calming section of 500 mm, or approximately 60 times the internal diameter of the test section, was included.

Two sight glasses, positioned just ahead of and after the heated section, were constructed from borosilicate glass pipes, with a length of 60 mm. They provided visual access to the flow pattern inside the flow path. Axial heat conduction from the heated portion was also prevented by the natural low thermal conductivity of the glass, which was estimated to be 1.14 W/mK. To ensure minimal disturbance to the flow, it was ensured that the inner diameter of the sight glasses matched the inner diameter of the copper pipe used in the test section.

The sight glass housing was fabricated from brass, with both sides of the housing being identical. One side is described here. A cavity for a seal was machined in a solid round brass rod, and an inner retaining plate was used to keep this seal secured. A safety glass was placed around both

machined components, and outer retaining plates were used to keep the entire sight glass assembly fixed. Crucially, the inner diameters of all components were equal to the copper pipe inner diameter to ensure smooth transitions throughout.

The test section thermocouple stations are indicated by the symbol **T** in Figure 3.4. These stations each consisted of four T-type thermocouples, as on the facility, spaced equally around the circumference of the pipe (above, below, left and right). The inlet and outlet saturation temperatures were measured by a thermocouple station before the inlet sight glass (T_{in}), and a thermocouple station after the outlet sight glass (T_{out}). These thermocouples were specifically placed to take advantage of the heat insulation provided by the high axial heat resistance of the sight glass. The obtained saturation temperature was cross-checked with the high-accuracy Pt100 RTDs that were installed in the flow passage directly before and after the test section. The saturation temperature was also compared to the expected saturation temperature at the operating pressure of the test section, obtained using reference libraries.

A photograph of the inlet sight glass before installation is shown in Figure 3.5, which also details the inlet thermocouple station (T_{in} in Figure 3.4). In the interests of modularity, these thermocouples were soldered to the pipe, as is described below. The location of the seal, safety glass, and retaining plates are also indicated.

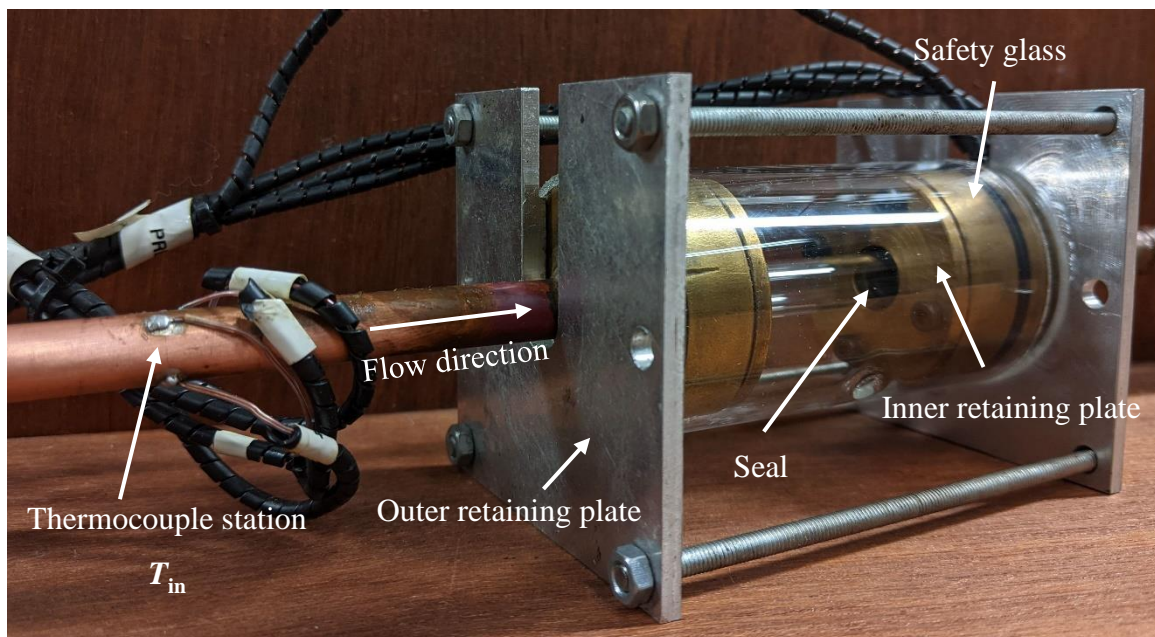


Figure 3.5. Inlet sight glass before installation

In order to obtain the wall temperature of the test section, the eight temperature measurement stations indicated in Figure 3.4 (T_1 to T_8) were used. These were situated on the heated length, and were positioned 100 mm apart. Thus, 32 thermocouples were attached to the heated section.

The repeated heating and cooling of the test section due to the applied heat flux had an adverse effect on the thermal tape adhesive, resulting in erroneous readings. Instead, the thermocouples were soldered to the test section by drilling shallow divots in the outer wall of the copper pipe, adding solder to the divots, then attaching the thermocouples.

This heating element consisted of a single constantan wire tightly wound around the heated length, providing a nominal resistance of $180\ \Omega$. Special care was taken at the locations of the soldered thermocouples to prevent direct localised heating of the thermocouple tip or leads by the neighbouring heating wires. The spacing and installation method for the thermocouples followed the empirical work by Everts [95], with the high thermal conductivity of copper compensating for the gap. The wire was connected to the previously mentioned power supply unit, which enabled a uniform heat flux that could be temporally varied by adjusting the voltage and current of the power supply.

Two pressure taps were situated 800 mm apart to match the heated length (L_h), and were machined to have the same relative size and orientation as the other pressure taps mentioned in Section 3.3. The pressure taps were connected to Sensotec FP2000 transducers (mentioned previously) and a Validyne DP15 differential pressure transducer. This differential pressure transducer had an accuracy of 0.5% of the full scale, which was determined by the diaphragm it had installed. Depending on the expected pressure difference, a 0.86 kPa, 8.6 kPa or 14 kPa membrane was installed.

A photograph indicating the inlet pressure tap, the thermocouple station T_1 , and the heating wire is shown in Figure 3.6 for clarity. This image was taken before insulation was added and the sight glass connected. Note that the sight glass connector inner diameter was equal to the inner diameter of the copper pipe to avoid sudden expansion or contraction of the fluid.

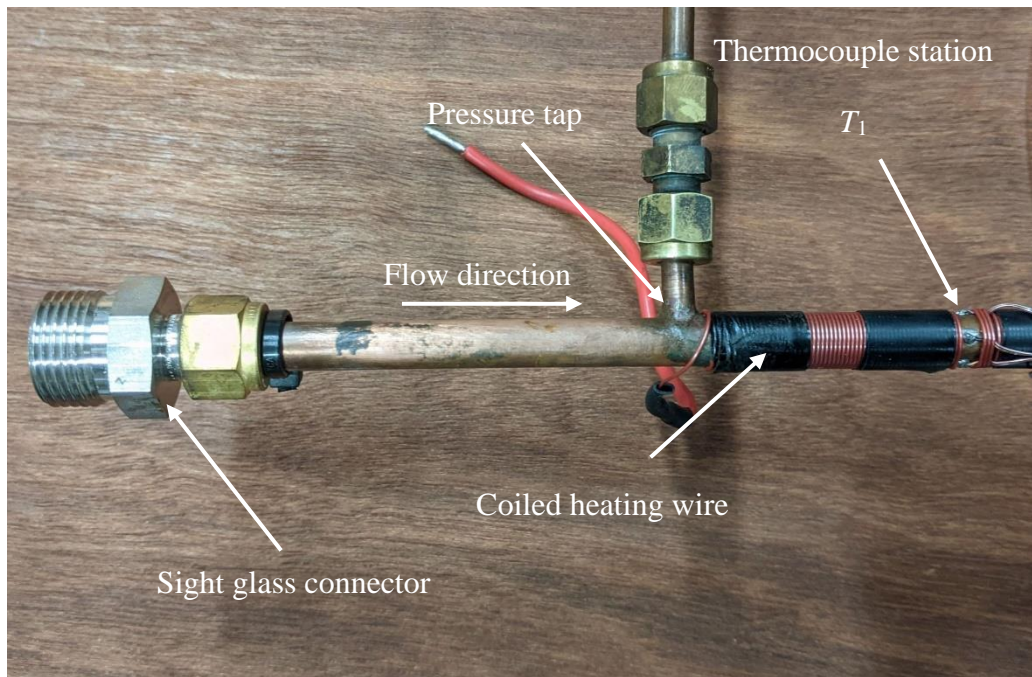


Figure 3.6. Photograph detailing the uninsulated heated length inlet

The test section was insulated to a minimum radius of 100 mm using the same type of insulation mentioned previously. Calculations were done under worst-case scenarios that showed that the heat loss from the test section and facility was less than 1%, as noted in Section 4.4.

The constructed test section, ready for commissioning, is shown in Figure 3.7, with certain components highlighted. The flow direction is from left to right. Compared to Figure 3.2, this is a view from the opposite side of the test setup.

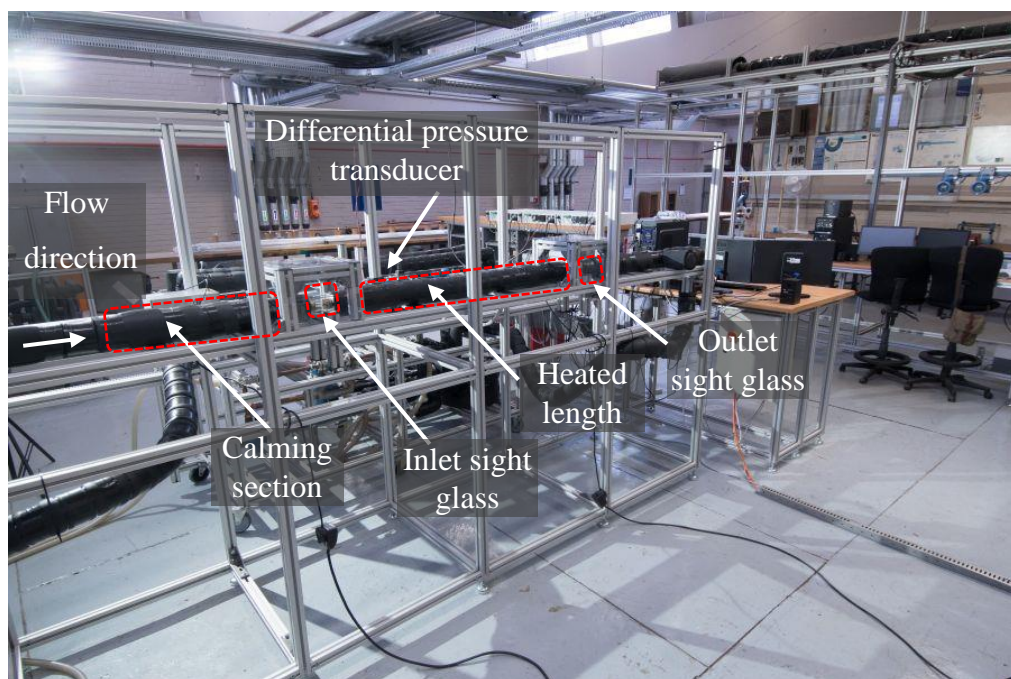


Figure 3.7. Set-up with test section in view

3.5. APPARATUS SPECIFICATION

The design specifications achieved for this experimental apparatus is listed in Table 3.3 below.

Table 3.3. Overall ability and range of the constructed apparatus

Variable	Value
Refrigerant charge	~25 kg
Operating pressure	100 kPa – 1 500 kPa
Test line mass flow rate	0.002 – 0.04 kg/s
Maximum power in the preheater	6 kW

The maximum theoretical vapour quality that could be achieved at the inlet to the test section was highly dependent on the mass flow rate and the vaporisation enthalpy at the saturation temperature of interest for the specific refrigerant being investigated. This was limited by the achievable mass flow rate of the pump and the maximum power in the preheater. The amount of subcooling present in the fluid (and thus the amount of power needed to heat the fluid to saturation conditions) was also a factor. An example of the achievable vapour qualities in terms of mass flow rate at the test section inlet (along with the mass flux for the copper pipe diameter used in this study) is shown in Figure 3.8 for the refrigerant and saturation temperature investigated in this work. In this figure, the grey shaded area indicates the achievable vapour qualities. The achievable range of vapour qualities for the mass flow rates is shown graphically for R-245fa, with a saturation temperature of 35 °C. Subcooling of 20 °C (i.e., sensible heating from 15 °C to 35 °C) is also taken into account.

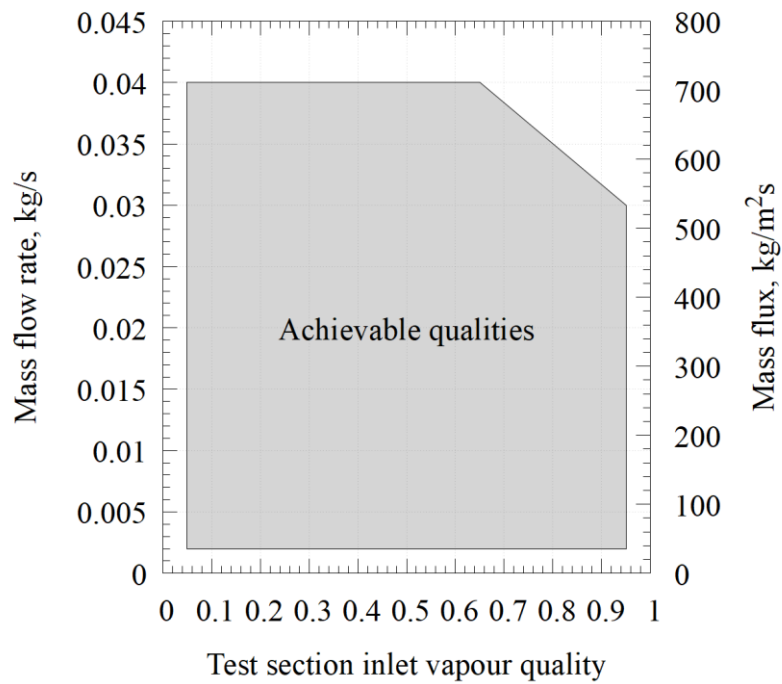


Figure 3.8. Achievable inlet vapour qualities at test section inlet for R-245fa at a saturation temperature of 35 °C and subcooling of 20 °C, along with mass flux for inner diameter of 8.31 mm

3.6. SYSTEM CONTROL AND DATA LOGGING

System control and data logging was performed by a personal desktop computer via a National Instruments data acquisition system (DAQ), using the National Instruments LabView front-end. Some of the components discussed in this section is shown in Figure 3.9.

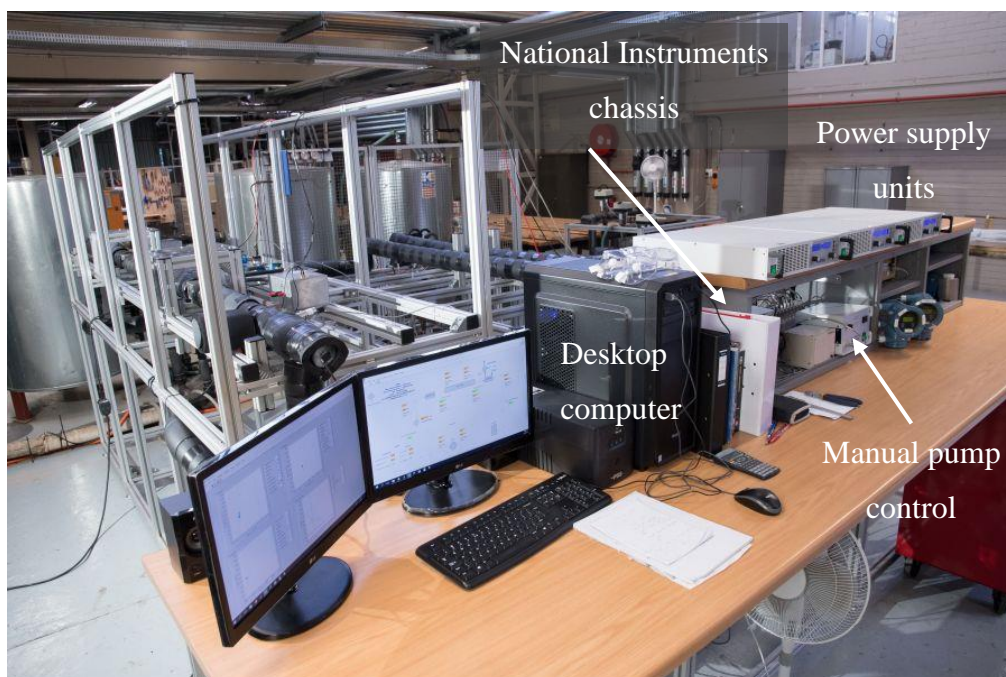


Figure 3.9. Facility control system

An SCXI-1001 chassis was used which was equipped with a number of data acquisition and control cards. The LabView sample acquisition rate was set to 300 Hz with 100 samples per channel. However, the limitations imposed by the power supplies' LabView interfaces on the desktop computer and the speed at which these interfaces could operate constrained the actual sampling rate to ~ 2 Hz.

The fluid mass flow rate was controlled by adjusting the pump speed, either physically from the GATHER control box, or electronically by sending a signal via the DAQ from LabView using a NI SCXI-1325 card. As mentioned, fine mass flow control was done manually by adjusting the bypass valve. The flow rates of both the fluid and water in the condenser loop were recorded from the flow meters using an NI SCXI-1308 card. The power supplies contained control cards, which allowed them to be connected directly to the computer via a USB connection, thus circumventing the need for a card inserted into the chassis. They could be set either to manual control or remotely controlled via a LabView interface.

The mass flow rate of the water through the condenser was controlled by the aforementioned three-way valve, which was powered by a separate AC power supply and controlled with LabView using DAQ card NI SCXI-1325. Similarly, data acquisition for the thermocouples and Pt100s was done by connecting them directly to NI SCXI-1303 and NI SCXI-1306 cards respectively, and reading the data into LabView. The absolute pressure transducers were powered by a separate DC power supply, and connected to the DAQ with an NI SCXI-1308 card. The differential pressure transducer was also connected to the DAQ using an NI SCXI-1308 card.

3.7. CALIBRATION

Before any experimental test cases were considered, the measuring components with variable accuracies, which included the temperature and pressure measurements probes, were calibrated. A complete overview of the calibrations performed is given in Appendix A, but a summary follows here.

Before the system was charged with refrigerant, the facility thermocouples and the Pt100 resistance temperature detectors (shown in Figure 3.1) were calibrated against a factory-calibrated Pt100 (with an accuracy of 0.03 °C) in a thermal bath at a series of steady-state isothermal conditions. These conditions were chosen specifically to fall outside the expected range of temperatures that would be encountered, so that the calibration could rely on interpolation. The temperatures used for calibration ranged from 15 °C to 45 °C. In order to check for possible hysteresis, the calibration readings were obtained for both an increase from 15 °C to 45 °C and a decrease from 45 °C to 15 °C in intervals of 5 °C. After calibration, the thermocouples were attached circumferentially equidistant to the relevant positions using thermal tape and thermally insulated, and the Pt100s were mounted into the system with couplings that ensured that the measuring tips were wholly in the flow.

Once the relevant calibrated Pt100s were installed at positions C and D in Figure 3.1, they were used as the reference temperature probes during the steady-state *in situ* calibration of the test section thermocouples (shown in Figure 3.4). This was accomplished by passing a single-phase refrigerant liquid through the test section at set temperatures covering a temperature range of 15 °C to 45 °C at intervals of 5 °C, again performing both an upward and downward cycle.

To be sure isothermal steady-state conditions were achieved in the test section, the Pt100s before and after the test section had to remain constant within 0.03 °C of each other for 10 minutes before the next temperature state was produced. During these calibration runs, the fluid temperature was controlled by controlling the temperature of the water with which the heat exchange in the condenser occurred. By connecting the condenser water side to the thermal bath, the outlet temperature of the working fluid in the counter-flow heat exchanger was indirectly determined by the water inlet temperature by adjusting the thermal bath temperature.

The data that was collected during the above-mentioned calibration procedures was used in Matlab to calculate linear calibration equations for each Pt100 and thermocouple. The equations were then applied to the measured values in order to display the corrected values.

Before calibration, the maximum mean standard error was 0.19 °C for the Pt100s, 0.45 °C for the facility thermocouples, and 0.66 °C for the test section thermocouples. This was reduced to

0.019 °C for the Pt100s, 0.012 °C for the facility thermocouples, and 0.045 °C for the test section thermocouples after calibration. The calibrations were checked routinely, and redone to account for drift.

All absolute pressure transducers were calibrated externally, and it was confirmed that they had an accuracy of less than 0.2%. The differential pressure transducer was calibrated using a water column to provide steady differential pressures, which were read from a Martel T140 digital manometer. The manometer had an accuracy of 0.05% of full scale. This calibration was done six monthly, according to the manufacturer's guidelines.

3.8. SUMMARY

To start with, this chapter explored some actual CSP DSG systems in industrial use at present, both for industrial heating and power generation. Because data for these types of systems was not readily available, the scope was expanded to include some of the experimental and numerical work currently being performed on ORCs. Detail on especially the pipe diameters, mass flux, heat flux, and concentration ratio were sought. This was done in an attempt to gain some guidelines for the design of the experimental apparatus that was used in this thesis. The detail of the construction of the flow-loop apparatus was split into two sections, that of the so-called facility, and that of the modular test section. The achieved apparatus specification was detailed next, along with an example of the theoretical maximum mass flow rate and vapour quality obtainable. The method of system control and data collection, along with some limitations imposed on the data logging in terms of sampling rate, was explored. Finally, the calibration of the temperature sensors (both the Pt100s and facility and test section thermocouples) was discussed next. In conclusion, a discussion of the calibration of both the absolute pressure transducers and the differential pressure transducer was given.

PART II

STEADY-STATE CONDITIONS

“Big whirls have little whirls,
that feed on their velocity;
Little whirls have lesser whirls,
and so on to viscosity.”

–L.F. Richardson

“Stratified to slug flow,
depends on mass velocity;
Intermittent to annular,
and so on to full quality.”

–W.J. van den Bergh

(with apologies to L.F. Richardson)

4. STEADY-STATE INVESTIGATION METHODOLOGY

4.1. INTRODUCTION

Before any tests gauging the effect a low mass and heat flux or a transient heat flux had on the HTC could be performed, some groundwork first had to be done. Steady state, and the experimental procedure to attain this steady state, had to be defined. Next, a test matrix had to be constructed, taking into account the gaps in literature and new work recognised in the previous chapters.

With the test matrix defined, the steady-state data processing to turn the raw results gathered into useful information had to be stipulated, and the uncertainty of these results calculated. With the uncertainty calculated, some numbers could be put to the achievement of steady state. Finally, validation of the experimental system had to be performed to ensure that the results were trustworthy. This chapter is concerned with all of the aforementioned.

4.2. EXPERIMENTAL PROCEDURE

Although the test envelope differed vastly in the ranges for both heat flux and mass flux considered for the different studies found in literature, there is one universal aspect shared amongst all the tests, that of steady state; either when the objective was to expand steady-state data, or as the base of reference for transient case perturbances. Steady-state conditions are defined as the operational state in which variables and parameters of interest are unchanged over time. It had to be achieved for all test cases in this study, even when the intention was to investigate a transient perturbation, as described in Parts III and IV. This section details the methodology applied to achieve a steady state with the constructed experimental apparatus.

The measured variables of note include the mass flux and the saturation temperature (and thus also the saturation pressure), while noteworthy calculated variables included the inlet vapour quality to the test section and the energy balance error. All of these had to be maintained within a certain band for a set amount of time before being considered steady state. The method in which the calculated values are determined, is explored in Section 4.4, while the band in which the values were to be maintained is given in Section 4.5.

The basic procedure to achieve a two-phase steady state is detailed next. First, a set point was chosen from the test matrix (detailed in Section 4.3). Each setpoint was described in terms of the saturation temperature, a test section heat flux, mass flux, and inlet vapour quality. Next, the pump was set to achieve the desired mass flux for single phase (without any heat being added or removed), and the system was monitored for any abnormal behaviour that could be caused by low fluid charge.

This step was crucial, since without fluid flow, burnout of the preheater and test section was inevitable. Once the desired mass flux was reached and maintained for a time, the heat flux in the test section was brought to the required level by adjusting the test section power supply unit upwards in increments of 50 W. After calculating the power that would be required to reach a certain quality at the required saturation temperature (detailed in Section 4.4), the preheater was also initialised in increments of 50 W. The mass flux was carefully monitored during this increase, adjusting the pump as required to maintain the desired mass flux.

With this achieved, attention was turned to the requisite saturation temperature. Since up to this point, energy had only been added to the system in the form of the test section and preheater heat flux, the temperature would naturally be rising. In order to curtail this temperature at or below the desired saturation level, the heat removal in the condenser had to be initialised. This was done by modulating the mass flow rate of cold water through the condenser. With the energy added and removed from the system in balance, fine adjustments could be made to the saturation temperature by increasing or decreasing the heat rate removed until the saturation temperature was within acceptable limits. This energy balance was critical in maintaining the saturation temperature.

With the set point values achieved in terms of mass flux, inlet vapour quality, and saturation temperature, the only thing that remained was monitoring the values in order to confirm that they stayed within the required limits for the necessary time. Once this time had elapsed, data recording could commence.

The shutdown procedure for the facility was to first reduce the heat added to the system in 50 W increments, both for the preheater and test section, until no heat was being added, then to halt the heat being removed by shutting down the water flow to the condenser. Finally, the fluid pump would be stopped, halting the flow. Special care was taken to ensure that all the heat being added to the system was halted before the mass flux was reduced.

4.3. TEST MATRIX

With the practical procedure to obtain a steady state defined, attention could be turned to which points were required. In order to obtain baseline values for validation and comparison to which a perturbation could be applied, as well as some of the new two-phase steady-state data presented in Chapter 5, a test matrix had to be constructed incorporating the mass fluxes, heat fluxes and quality ranges to be investigated at a chosen temperature.

To start with, as was seen in Table 2.1, boiling studies of mass fluxes under $100 \text{ kg/m}^2\text{s}$ and heat fluxes below 5.0 kW/m^2 have received scant attention. No consensus has been reached on the

effect of various adjustable experimental factors (i.e., the mass flux, heat flux and vapour quality) on the HTC at these conditions, and there are no guidelines for predicting the HTC by using correlations. It is therefore necessary to obtain some additional data for mass fluxes below 100 kg/m²s and heat fluxes below 7.5 kW/m².

This is especially true for R-245fa. To illustrate this point, the mass and heat fluxes that have been studied in the literature obtained for R-245fa is depicted in Figure 4.1. As can be seen, there exists a lack of work for mass fluxes below 100 kg/m²s and heat fluxes below 7.5 kW/m². This study would add to the body of literature on steady-state conditions by performing tests at mass fluxes of 40, 60, and 80 kg/m²s and heat fluxes of 2.5, 5.0, and 7.5 kW/m².

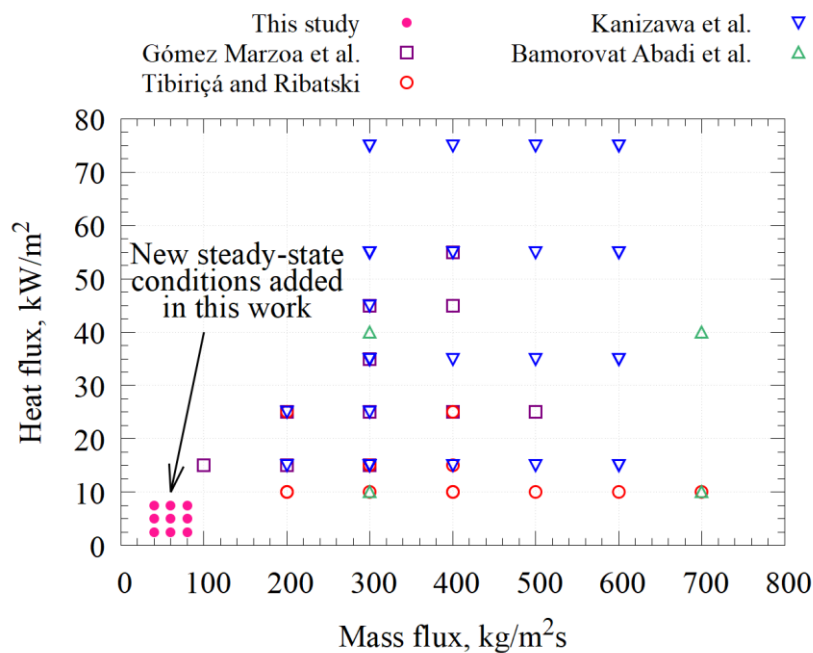


Figure 4.1. New steady states added in this work and its relevance to existing studies on the flow boiling of R-245fa

Next, after observing what has been done in literature to date, as well as what is commonly encountered in industrial and experimental applications (as seen in Section 3.2), test conditions that were to be subject to perturbances were selected. Two steady-state mass fluxes of 200 and 300 kg/m²s were chosen at a heat flux of 7.5 kW/m². The vapour qualities that would be investigated were ranged from 0.05 to 0.90, and the saturation temperature was set to be 35 °C.

The mass fluxes of 200 and 300 kg/m²s were chosen to represent typical minimum values being investigated for concentrated solar systems [35, 96], and to be in the same range as those seen in Table 3.1 and Table 3.2. These mass fluxes were also confirmed to give purely liquid turbulent flow, and to cover all the flow patterns of interest to industrial systems over the range of vapour qualities

chosen. The applied heat flux in the test section of 7.5 kW/m^2 was used to calculate the HTC. This value was chosen after considering a design point DNI of $\sim 0.5 \text{ kW/m}^2$, seen for some systems in Table 3.2, and the typical concentration ratio that is found in industrial parabolic troughs of between 10 and 20 [22]. Multiplying the DNI by this concentration ratio resulted in a heat flux of 5.0 to 10.0 kW/m^2 .

The saturation temperature of $35 \text{ }^\circ\text{C}$ was chosen after careful consideration of the advantages and disadvantages of attempting to match systems in practice (which had a much higher operating temperature, as seen in Table 3.2). It was decided to use this relatively lower temperature since the main thrust of this work was not to reproduce an actual system, but rather to investigate the possible reaction under perturbances. This was in addition to the fact that safety, insulation, and calibration at high temperatures would become problematic for the laboratory in which this apparatus was situated.

In addition, for reasons that will be explored in Chapter 7, supplementary steady-state tests at mass fluxes of 235 and $335 \text{ kg/m}^2\text{s}$ were performed specifically at vapour qualities of 0.15, 0.20, 0.25, and 0.30, at a heat flux of 7.5 kW/m^2 .

Each of the test conditions decided upon is shown is depicted by dots on a Wojtan-Ursenbacher-Thome [42] flow pattern map in Figure 4.2. It was constructed specifically for the saturation temperature, mass fluxes, and heat flux of interest by following the guidelines in Ref. [42].

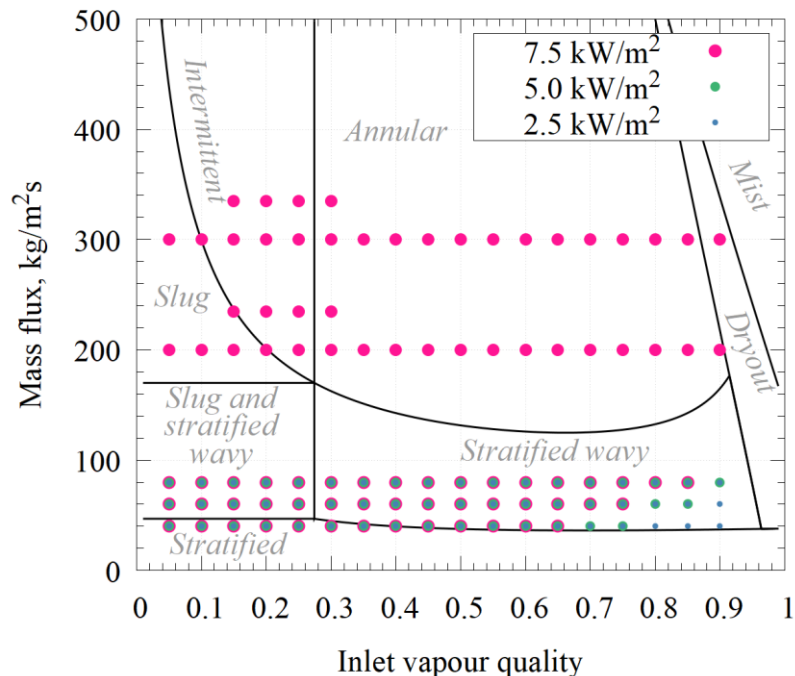


Figure 4.2. Complete test matrix for this work on a Wojtan-Ursenbacher-Thome [42] flow pattern map at a saturation temperature of $35 \text{ }^\circ\text{C}$

On this figure, the different heat fluxes at mass fluxes of 40, 60, and 80 kg/m²s are shown as different colours. It is important to note that even though the inlet vapour quality was held constant during each experiment, the applied heat flux had an influence on the outlet vapour quality in the test section. This meant that some inlet vapour qualities could not be tested, since dryout occurred. The amount by which the applied heat flux raised the vapour quality at a certain mass flux is summarised in Table 4.1.

Table 4.1. Approximate increase in vapour quality in test section for different mass and heat fluxes

	40 kg/m ² s	60 kg/m ² s	80 kg/m ² s	200 kg/m ² s	300 kg/m ² s
2.5 kW/m ²	0.13	0.09	0.07	-	-
5.0 kW/m ²	0.25	0.17	0.13	-	-
7.5 kW/m ²	0.38	0.25	0.18	0.08	0.05

The flow patterns for the mass fluxes of 200 and 300 kg/m²s, which would be the focus of any perturbation experiments in this work, avoided any stratification in the flow pattern, while the steady-state tests at 40, 60, and 80 kg/m²s covered the stratified regions.

4.4. DATA PROCESSING

Before data processing could commence, a heat loss calculation was performed to gauge the influence of the ambient laboratory conditions on the test data. A thermal resistance network was constructed in which the conductive thermal resistance of the insulation, the convective thermal resistance of the laboratory, and the radiative thermal resistance were considered. Calculations showed that the effect on the heat transfer rate in the test section was less than 1% at the worst case, and thus was disregarded in the rest of the data processing.

As mentioned in Section 4.2, one of the key metrics in achieving steady state is the diabatic energy balance error. This entails taking into consideration all of the major energy sources (in the preheater and test section) and energy sink (at the condenser):

$$\%EB = 100 \left(1 - \frac{\dot{Q}_{pre} + \dot{Q}_{test}}{\dot{Q}_{cond}} \right) \quad (4.1)$$

Here, \dot{Q}_{pre} is the heating rate in the preheater, \dot{Q}_{test} is the heating rate in the test section, and \dot{Q}_{cond} is the heating rate removed in the condenser. The pumping power to the gear pump and heat

loss or gain from the test facility tubing through the insulation were ignored. The heat loss to the environment and the pump work accounted for less than 1% of the total heat input in the worst case.

The condensation heat transfer rate was determined via the energy balance principle based on the water-side measurements:

$$\dot{Q}_{\text{cond}} = \dot{m}_w(h_{w,\text{out}} - h_{w,\text{in}}) \quad (4.2)$$

Here, \dot{m}_w is the mass flow rate of the water obtained from the water Coriolis flow meter, and $h_{w,\text{out}}$ and $h_{w,\text{in}}$ are the specific enthalpies of the water at the outlet and inlet. These were obtained from the measured water temperature at Points E and F in Figure 3.1 via the CoolProp thermodynamic library [97].

The heating rate of the preheater and test section were determined using the generalised power equation, neglecting heat loss through the preheater thermal insulation:

$$\dot{Q}_{\text{pre}} = V_{\text{pre}}I_{\text{pre}} \quad (4.3)$$

$$\dot{Q}_{\text{test}} = V_{\text{test}}I_{\text{test}}$$

Here, V_{pre} and V_{test} are the direct current (DC) voltages supplied to the preheater and test section heating elements respectively, while I_{pre} and I_{test} are the DC electric currents flowing through the preheater and test section heating elements respectively. These values were obtained from the virtual instrumentation interfaces for the power supply units in LabView.

Next, the test section inlet vapour quality of the R-245fa was determined by using the following definition:

$$x_{\text{in}} = \frac{h_{\text{in}} - h_f}{h_g - h_f} \quad (4.4)$$

Here, h_{in} is the inlet specific enthalpy, and h_f and h_g are the specific enthalpies of the saturated liquid and vapour respectively. The latter enthalpies were obtained from CoolProp [97] at the governing saturation temperature, which was calculated as the arithmetic averaged temperature in the test section based on the inlet and outlet R-245fa temperatures that were obtained from T_{in} and T_{out} in Figure 3.4 (which was taken as T_{sat} , as discussed below). h_{in} is calculated from the energy balance around the preheater located between Points A and B (see Figure 3.1), and the adiabatic fluid line between Points B and C:

$$h_{\text{in}} = h_C = h_B = \frac{\dot{Q}_{\text{pre}}}{\dot{m}_{\text{ref}}} + h_A \quad (4.5)$$

Here, \dot{m}_{ref} is the mass flow rate of the R-245fa obtained from the refrigerant line Coriolis flow meter, and h_A , h_B , and h_C are the specific enthalpies of the fluid at Points A, B, and C. h_A was obtained from the measured temperature and pressure at Point A via CoolProp [97].

The test section was divided into $N = 8$ equally sized control volumes along the test section length, each associated and centred around a thermocouple location at position $n = 1$ to N (see Figure 3.4). The local HTC for each control volume (α_n), which expresses the local ability of surface to transfer heat into the fluid by means of convection, was calculated by applying Newton's law of cooling:

$$\alpha_n = \frac{\dot{q}_{i,n}}{(T_{i,\text{wall},n} - T_{\text{fluid},n})}; n = [1,2,3,4,5,6,7,8] \quad (4.6)$$

Here \dot{q}_i is the local inner surface heat flux, $T_{i,\text{wall},n}$ is the local wetted inner wall temperature and $T_{\text{fluid},n}$ is the bulk fluid temperature. Crucially, since Equation (4.6) contains only the heat flux and temperatures, it is used to obtain the HTC for both single-phase and two-phase flows.

Because uniform heating was applied to the test section, the local heat flux could be determined from the overall test section heat transfer rate as follows:

$$\dot{q}_{i,n} = \frac{\dot{Q}_{\text{test}}}{A_{s,\text{test}}} \quad (4.7)$$

where $A_{s,\text{test}}$ is the inner wall heat transfer surface expressed in terms of the heated test section length and the inner diameter of the pipe: $A_{s,\text{test}} = \pi d_i L_h$.

To ensure that the wall thermal resistance could be neglected, the local inner wall wetted surface temperature was obtained by applying a simple one-dimensional Fourier conduction law to the measured thermocouple temperatures:

$$T_{i,\text{wall},n} = T_{o,\text{wall},n} - R_{\text{wall}} \dot{Q}_{\text{test}} \quad (4.8)$$

in which $T_{o,\text{wall},n}$ is the measured thermocouple temperature on the outer wall, and R_{wall} is the wall thermal resistance, given by:

$$R_{\text{wall}} = \frac{\ln(d_{o,\text{test}}/d_{i,\text{test}})}{2\pi k L_h} \quad (4.9)$$

where k is the thermal conductivity of the copper pipe. The maximum temperature difference between the outer and inner wall was calculated to be on the order of less than 0.01 °C, which would have a negligible effect on the HTC.

The average HTC over the entire test section was then calculated as follows:

$$\bar{\alpha} = \frac{\dot{q}_i}{(\bar{T}_{i,\text{wall}} - \bar{T}_{\text{fluid}})} \quad (4.10)$$

Here, $\bar{T}_{i,\text{wall}}$ and \bar{T}_{fluid} refer to the average wall and fluid temperatures respectively. $\bar{T}_{i,\text{wall}}$ was obtained by taking the arithmetic mean of the eight thermocouple stations along the length of the pipe, while \bar{T}_{fluid} was the mean measured fluid temperatures at the inlet and outlet of the test section.

Depending on whether single-phase, or two-phase flow boiling conditions were considered, the fluid temperature was determined differently. For single phase flow it was derived from the linear relationship between the inlet and outlet fluid temperatures at point C and D in Figure 3.1, while for two-phase cases it was simply equal to the saturation temperature: $T_{\text{fluid},n} = T_{\text{sat}}$. This saturation temperature, was obtained by taking the arithmetic mean of T_{in} and T_{out} . In order to ensure this saturation temperature was correct, these values were compared against the readings obtained from the two Pt100s before and after the test section and also cross-checked against the expected saturation temperature at the recorded absolute pressure readings from the locations indicated in Figure 3.4. It was found for adiabatic conditions that the Pt100 readings and the thermocouple readings were within 0.1 C of each other.

4.5. UNCERTAINTY PROPAGATION ANALYSIS

The uncertainty propagation analysis method by Dunn and Davis [98] was used. The methods and detailed results are given in Appendix B; however, a summary of the overall uncertainties is also given here. The stated accuracies of the various measuring instruments used are detailed in Table 4.2, as well as the calibrated value (where applicable) and the value used in the uncertainty propagation. Note that in the interests of conservatism, the lower accuracy was used in the propagation.

Table 4.2. Ranges and accuracies of measuring instruments

Instrument	Range	Stated accuracy	Post calibrated accuracy	Value used in uncertainty propagation
Pt100 RTD	-200 – 600 °C	0.06 °C	<0.04°C	0.06°C
T-type thermocouple	0 – 150 °C	0.1 °C	<0.05°C	0.1°C
Refrigerant Coriolis flow meter	0 – 0.04 kg/s	0.1%	0.1%	0.1%
Water Coriolis flow meter	0 – 0.4 kg/s	0.1%	0.1%	0.1%
Sensotec pressure transducers	0 – 2 000 kPa	4.4 kPa	~2.7 kPa	4.4 kPa
GEMS pressure transducers	0 – 2 200 kPa	5 kPa	~3 kPa	5 kPa

The average uncertainties obtained after applying the uncertainty propagation for the salient values are shown below in Table 4.3.

Table 4.3. Parameter ranges and uncertainties

Parameter	Range	Uncertainty
Singular temperature measurement point	35 – 45 °C	0.1 °C
Mass flux (G)	40-300 kg/m ² s	0.6%
Inlet vapour quality (x_{in})	0.05 – 0.90	0.0053
Heat flux (\dot{q})	1.9 – 7.5 kW/m ²	0.4%
Local HTC (α_n , Equation (4.6))	0.5 – 7.0 kW/m ² K	5.7%
Average HTC ($\bar{\alpha}$, Equation (4.10))	0.5 – 7.0 kW/m ² K	2%

With the uncertainties known, the band in which the values identified as crucial for steady state could be defined on surer footing. The mass flux had to be within 5% of the chosen mass flux, the

test section inlet vapour quality within 0.01 of the chosen vapour quality, the saturation temperature within 0.5 °C of the chosen saturation temperature, and the energy balance unchanged for at least 20 minutes before the readings could be considered steady state.

4.6. VALIDATION

4.6.1. Single-phase validation

Before moving on to any two-phase boiling tests, single-phase liquid validation had to be conducted to ensure the correct operation of the facility. This was done by determining the experimental Nusselt number (which involved the HTC), and plotting it as a function of the Reynolds number (which involved the mass flux), while keeping the test section inlet temperature constant. This result was compared with some correlations found in the literature. In order to ensure that fluid stayed liquid throughout this validation, special care was taken to ensure that the wall temperature in the test section never exceeded the saturation temperature of the fluid, which would result in sub-cooled boiling.

The obtained results for a fluid temperature at the test section inlet of 25 °C are shown in Figure 4.3. This figure presents a comparison of the achieved Nusselt number values over a range of Reynolds numbers with the Gnielinski [47] and Meyer *et al.* [48] correlations. The experimentally determined Nusselt number was well within 10% of the values predicted by both correlations.

Importantly, for these results to be meaningful, the energy lost to the environment had to be as close as possible to zero. The energy balance was thus also recorded, and is shown in Figure 4.4. This energy balance was considered satisfactory.

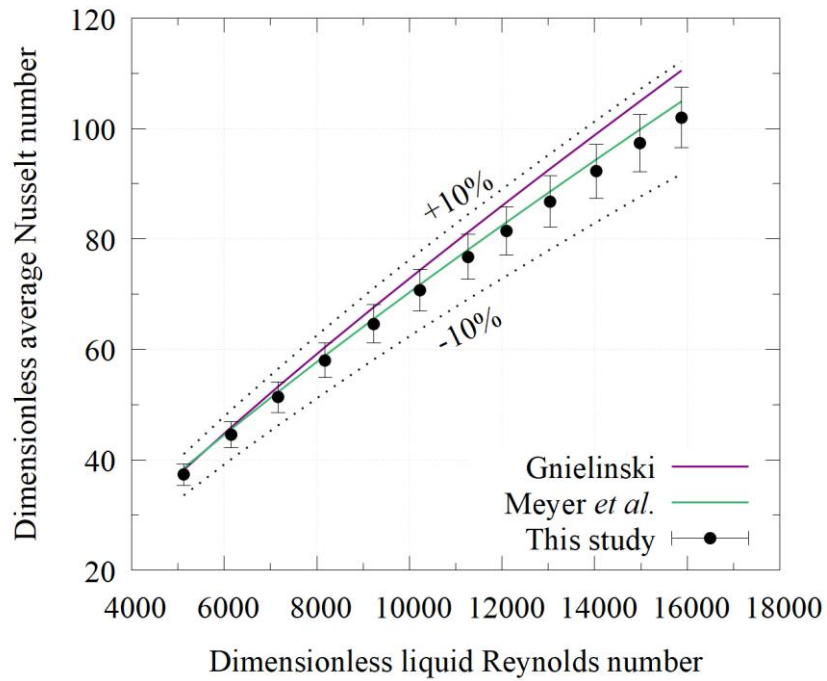


Figure 4.3. Single-phase validation: Nusselt number as a function of Reynolds number for liquid R-245fa flow for fluid inlet temperature of 25 °C

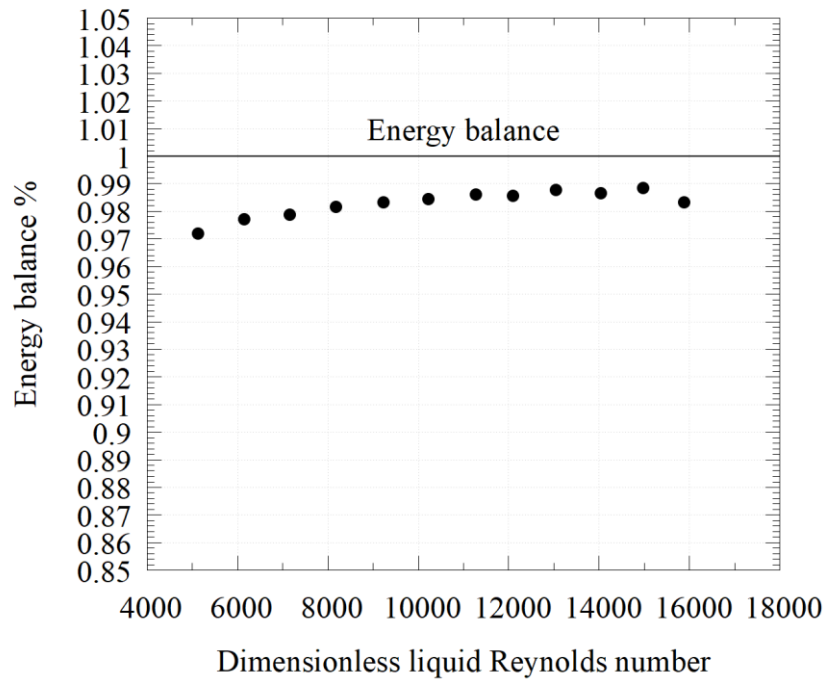


Figure 4.4. Energy balance over the test section for a fluid inlet temperature of 25 °C

4.6.2. Two-phase validation

With the system providing valid single-phase results, two-phase boiling results had to be validated. A steady-state test, with a mass flux of 200 kg/m²s and heat flux of 7.5 kW/m², at a saturation

temperature of 35 °C, was done over the full range of vapour qualities. The resulting HTC is shown in Figure 4.5.

Since no results found in the literature replicate the current study exactly for comparison, existing correlations to predict the HTC were used instead. These are the Gungor-Winterton [99] and Fang *et al.* [100] enhancement factor models, as well as the Wojtan-Ursenbacher-Thome [101] flow pattern based model. The equations for these correlations are provided in Appendix C. The predicted correlation values are also shown in Figure 4.5.

The experimental HTC was within $\pm 10\%$ of that predicted by the Wojtan-Ursenbacher-Thome [101] correlation, except at the extreme values of vapour quality. It also fell well within this range for predictions by the Fang *et al.* [100] correlation, and within $\pm 30\%$ for predictions by the Gungor-Winterton [99] correlation.

This was comparable with most other published works for the mass flux, heat flux and pipe diameter considered. Therefore, it could be deduced that the facility and test section produced satisfactory boiling results in accordance with reported work in the literature.

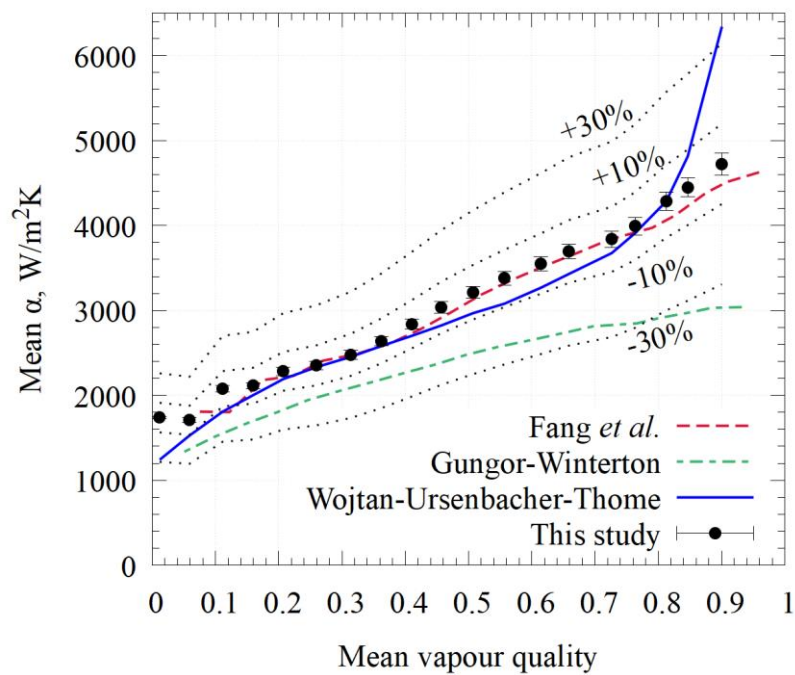


Figure 4.5. Two-phase flow validation, showing steady-state mean HTC for a mass flux of 200 kg/m²s, a heat flux of 7.5 kW/m² and a saturation temperature of 35 °C with predicted values

4.7. SUMMARY

The criteria for steady state were important in this study, since it laid the foundation for everything that would follow. These criteria were elucidated in this chapter, with the experimental procedure that was followed to achieve a steady state, the test matrix that would be used, the steady state data processing that would be applied, and the uncertainty propagation analysis all being explored. Importantly, the test matrix was informed by factors encountered in industry, or where there is no data available. The single- and two-phase validation of the experimental system were also given.

5. STEADY-STATE RESULTS

5.1. INTRODUCTION

Obtaining the HTC for the steady state at mass and heat fluxes that are generally available in literature would show nothing extraordinary, and, while useful, would not contribute much to the knowledge base for in-channel saturated flow boiling. In order for the transient tests to have a solid footing, however, the baseline steady-state results had to be reported. A gap in the literature was recognised in Section 2.4 with regards to low mass and heat fluxes. This gap is the main focus of the remainder of this chapter, with the results being discussed. After this, the steady-state results on which the transient tests would build is given as well. The conclusion to the new data is in Chapter 10.

5.2. LOW MASS AND HEAT FLUX STEADY-STATE RESULTS

5.2.1. Local versus average HTCs

The local HTCs obtained with Equation (4.6)) using data from the eight measuring stations along the test section length are shown in Figure 5.1. Instead of the axial location along the length of the test section, the local vapour quality as determined from Equation (4.4) is used on the horizontal axis. Each combination of heat flux and mass flux in the test matrix is contained in individual plots (Figure 5.1a to Figure 5.1i).

For clarity, the associated set of eight local HTCs along the length of the test section obtained for a single test case at an inlet vapour quality condition (as in the test matrix, Figure 4.2), are grouped by faint lines. These lines are most visible in Figure 5.1a, d, and g. The blue to red shaded line represents a general increase in the inlet vapour quality in each data set (blue indicating the lower vapour qualities and red indicating the higher vapour qualities).

Figure 5.1a contains a dashed line box around a single test case for an inlet vapour quality of 0.05, indicating the inlet thermocouple by the number one, and the outlet thermocouple by the number eight. Also included for illustrative purposes in this enlargement are the uncertainty bars. It is clear that the variations along the axis of the pipe far exceed the uncertainty value. Also plotted in Figure 5.1, and given in black, is the mean HTC for each test case, as determined with Equation (4.10).

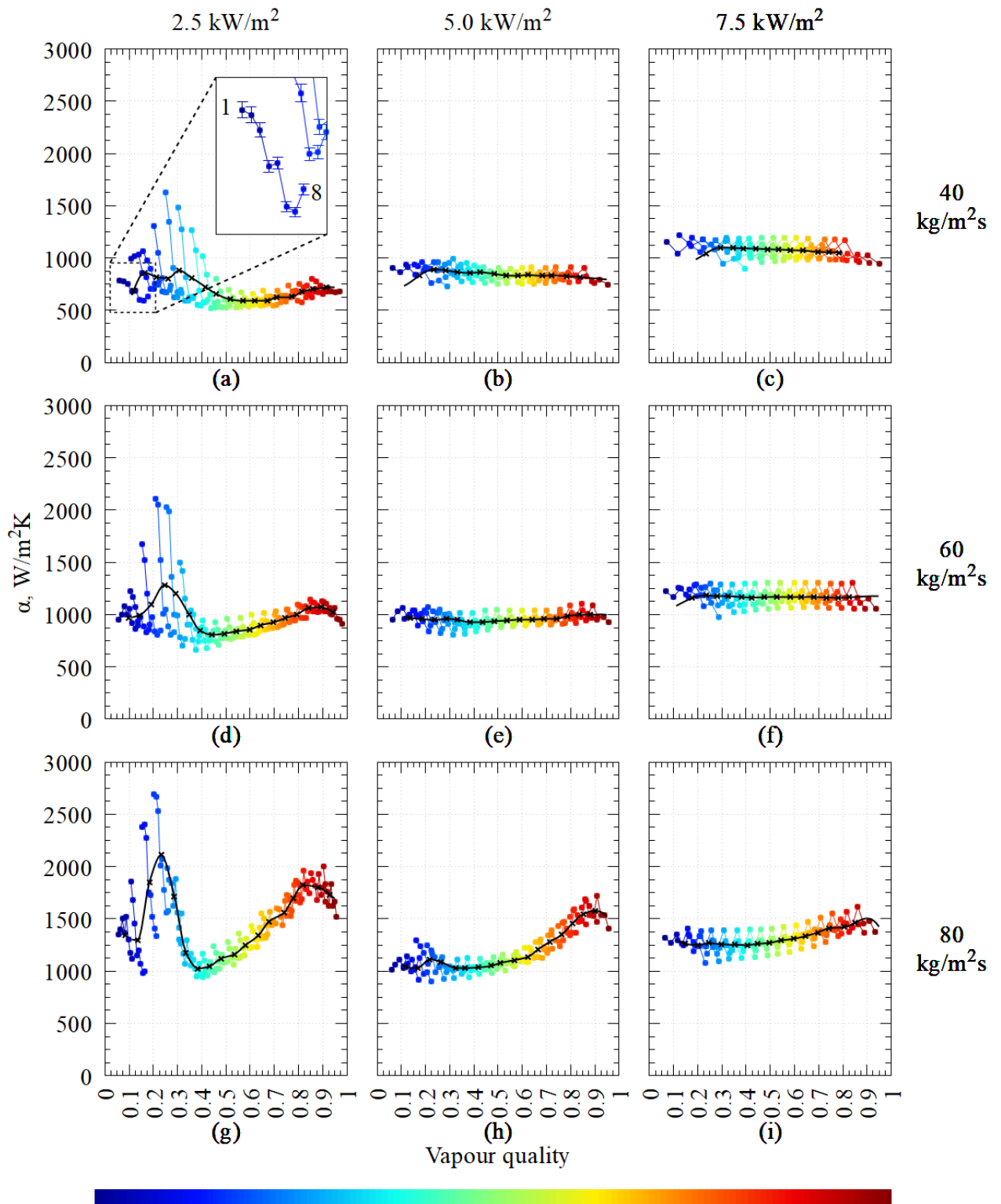


Figure 5.1. Local HTC plotted against local vapour quality for a mass flux of: (a-c) 40 kg/m²s, (d-f), 60 kg/m²s, and (g-i) and 80 kg/m²s

It can be seen that for the heat fluxes of 5.0 and 7.5 kW/m², for all the mass fluxes considered, all eight local HTCs were much the same, such that the average HTC is a reasonable representation of the HTC along the length of the test section. However, as can be seen in Figure 5.1a, d, and g, for

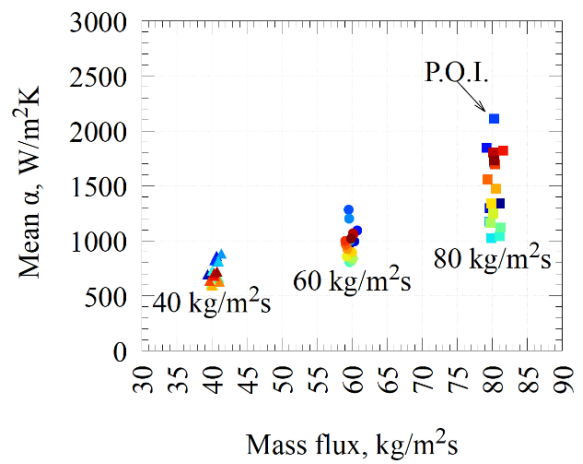
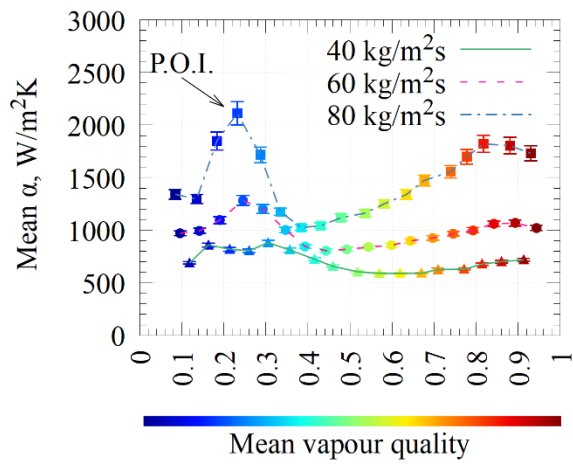
cases with a heat flux of 2.5 kW/m^2 , there was a significant spread in the local HTC, which is not well represented by the length-wise average HTC.

For these cases, the HTC in the first half of the pipe was significantly higher. Because these high HTCs were observed for all three mass fluxes, with separate mass fluxes being tested on different days, this was deemed noteworthy, and will be discussed in the following sections. The high local HTC at the inlet to the test section necessarily results in an elevated average HTC at some vapour qualities. This phenomenon has not been reported widely.

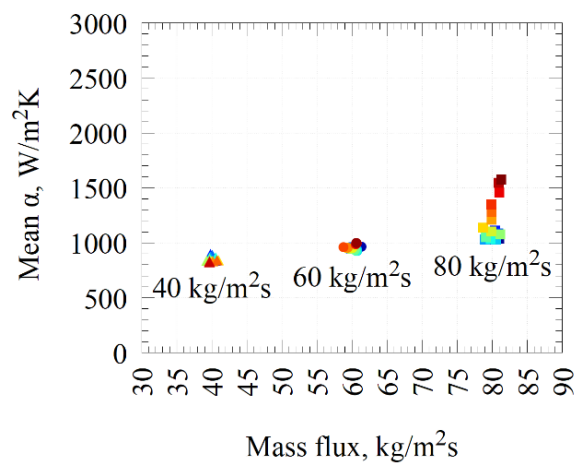
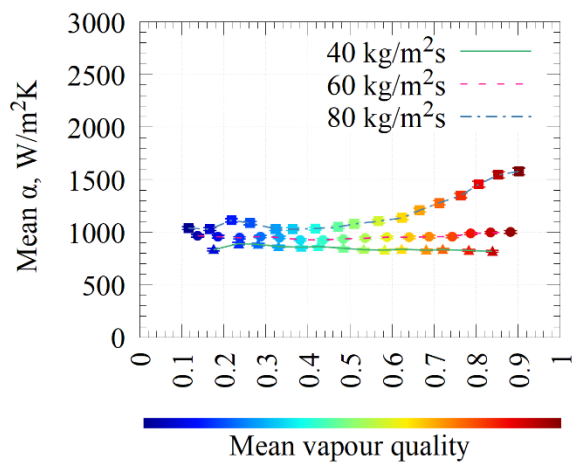
5.2.2. Influence of mass flux on the average HTC

The influence of mass flux on the average HTC, as obtained with Equation (4.10), is illustrated in Figure 5.2. Here the mean HTC profiles for different mass fluxes are plotted against the mean test section vapour quality and the mass flux at heat fluxes of 2.5 kW/m^2 (Figure 5.2a), 5.0 kW/m^2 (Figure 5.2b) and 7.5 kW/m^2 (Figure 5.2c). The vapour quality is again indicated as a palette colour, in which blue is a quality of 0 and red a quality of 1.0. To show that these charts depict the same data, but from a different perspective, a point of interest (P.O.I.) is highlighted in Figure 5.2a. This point was selected to help discuss the spike in HTC at a mean vapour quality of approximately 0.25.

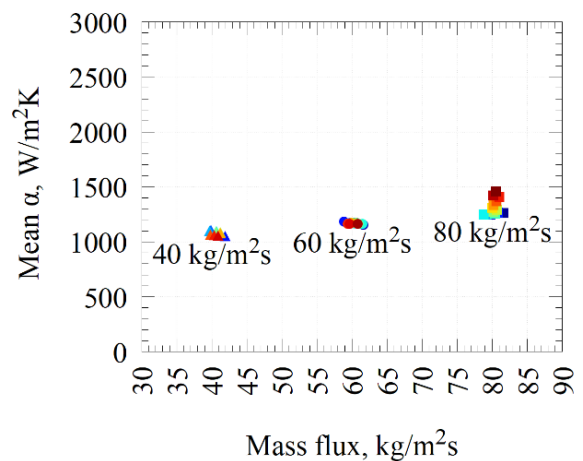
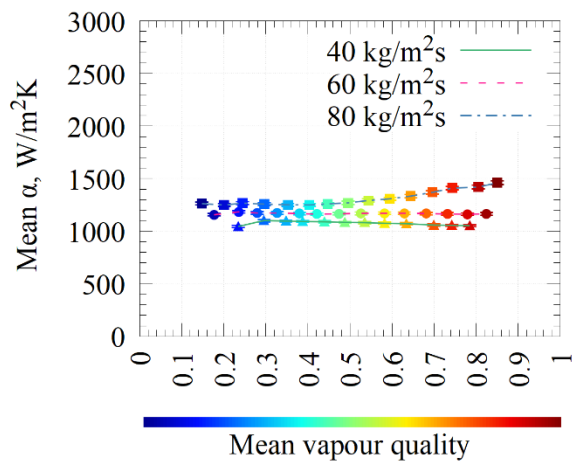
For the 2.5 kW/m^2 cases in Figure 5.2a, it is clear that the mass flux has a marked influence on the magnitude of the average HTC. The $80 \text{ kg/m}^2\text{s}$ line is always above the $60 \text{ kg/m}^2\text{s}$ line, which is, in turn, always above the $40 \text{ kg/m}^2\text{s}$ line. As mentioned, a local maximum at a vapour quality of approximately 0.25 (the designated P.O.I.) occurs. Here, there is an almost 150% increase in the HTC between mass fluxes 40 and $80 \text{ kg/m}^2\text{s}$. Increasing the vapour quality beyond this resulted in a steep decrease until a vapour quality threshold value of 0.40. Beyond this threshold, a mass flux of $80 \text{ kg/m}^2\text{s}$ exhibited a steady increase in the average HTC as the vapour quality increased, indicating that convective boiling was dominant. This type of influence was significantly subdued at mass fluxes of 40 and $60 \text{ kg/m}^2\text{s}$, showing that convective boiling played a lesser role at these mass fluxes and this heat flux. A second local maximum difference in HTC between mass fluxes of 40 and $80 \text{ kg/m}^2\text{s}$ was observed in Figure 5.2a at a vapour quality of approximately 0.80. Here, the higher mass flux shows a 125% increase in HTC.



(a) 2.5 kW/m²



(b) 5.0 kW/m²



(c) 7.5 kW/m²

Figure 5.2. Influence of mass flux on the mean HTC for heat fluxes of: (a) 2.5 kW/m², (b) 5.0 kW/m² and (c) 7.5 kW/m²

When considering a higher heat flux of 5.0 kW/m^2 , as shown in Figure 5.2b, it was found that the higher mass flux still influenced the average HTC, but to a lesser extent. The initial local maximum at a vapour quality of 0.25 was absent, while the influence of the increasing HTC beyond a threshold in vapour quality of 0.40 (and thus convective boiling) was still present for a mass flux of $80 \text{ kg/m}^2\text{s}$. Its impact was lower than for a heat flux of 2.5 kW/m^2 . The maximum difference between the HTC at 40 and $80 \text{ kg/m}^2\text{s}$ occurred at an approximate vapour quality 0.85. For mass fluxes of 40 and $60 \text{ kg/m}^2\text{s}$, increasing the vapour quality actually slightly reduced the HTC. The observed flow patterns for these mass fluxes were predominantly slug and stratified wavy. The flow patterns and the reduction in HTC will be discussed more fully in Section 5.2.4.

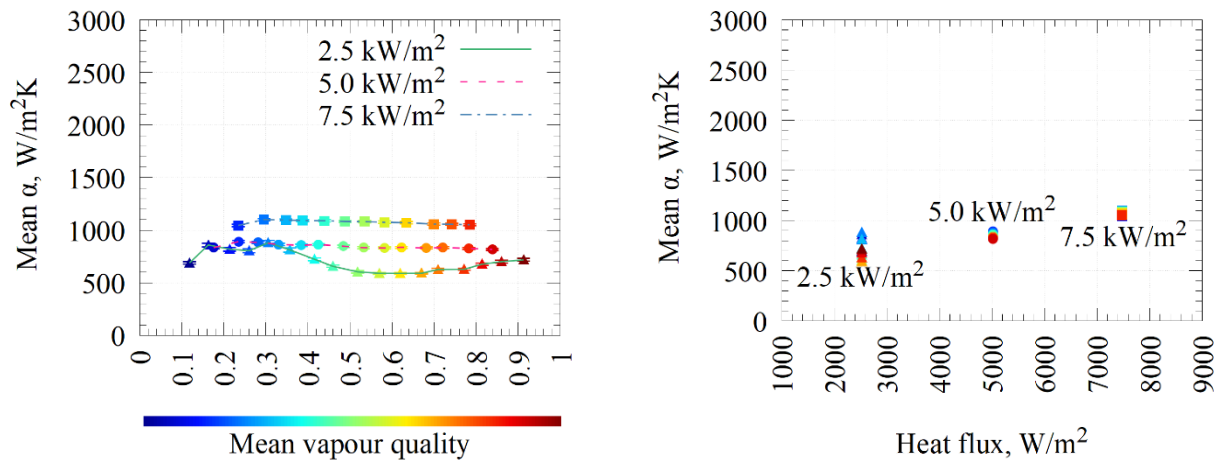
At these mass fluxes, nucleate boiling was dominant, since the increase in quality had only a minor effect on the HTC (as discussed in Section 2.3).

Finally, for the tests with 7.5 kW/m^2 , shown in Figure 5.2c, the behaviour mirrored that of the two other heat fluxes in that the higher mass flux always had a higher HTC. The initial peak for the heat flux of 2.5 kW/m^2 was absent, and the increase in HTC due to convective boiling beyond a vapour quality of 0.40 for a mass flux of $80 \text{ kg/m}^2\text{s}$ was further subdued. Nucleate boiling was still dominant at this heat flux for mass fluxes of 40 and $60 \text{ kg/m}^2\text{s}$ throughout the vapour quality range.

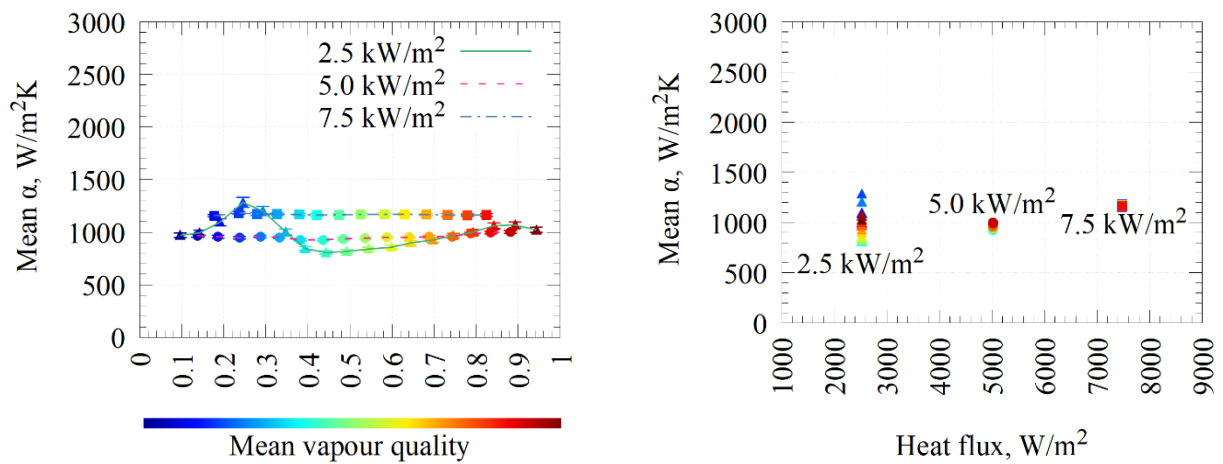
5.2.3. Influence of heat flux on the average HTC

The mean HTC profiles for different heat fluxes are plotted against the mean test section vapour quality at mass fluxes of $40 \text{ kg/m}^2\text{s}$ (Figure 5.3a), $60 \text{ kg/m}^2\text{s}$ (Figure 5.3b) and $80 \text{ kg/m}^2\text{s}$ (Figure 5.3c) to illustrate the influence of the heat flux on the HTC. Again, the vapour quality is indicated as a palette of colours on both charts. The same point of interest (P.O.I.) that was shown in Figure 5.2a, at the highest HTC, is indicated in Figure 5.3c.

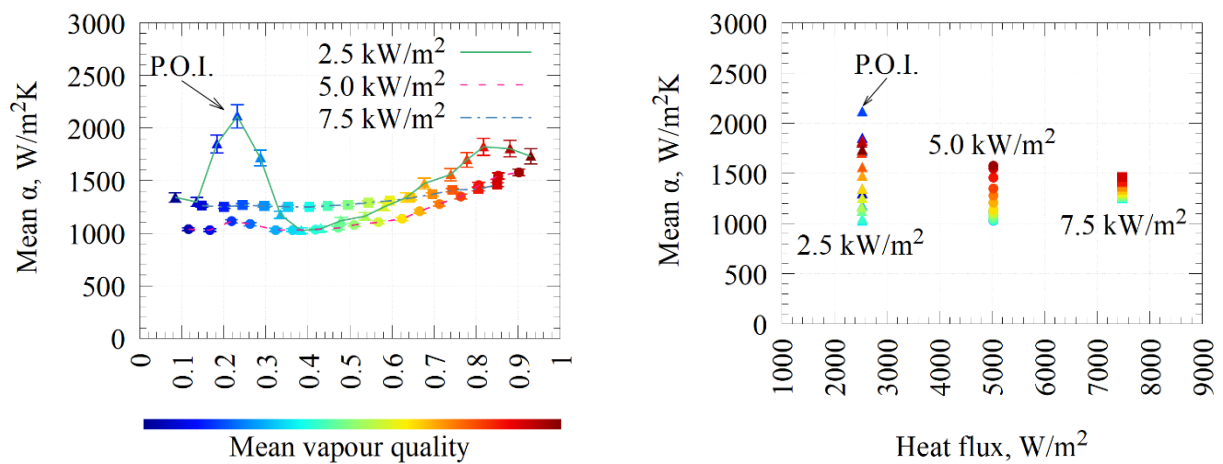
Consider Figure 5.3a for a mass flux of $40 \text{ kg/m}^2\text{s}$. For all data points, except for the results at the vapour qualities less than 0.40 at a heat flux of 2.5 kW/m^2 , it is clear that an increased heat flux resulted in an increased HTC. This did not happen only at low vapour qualities, as reported by [51, 52, 55, 56, 58, 59], but throughout the quality range. Figure 5.3b indicates that for a mass flux of $60 \text{ kg/m}^2\text{s}$ (when disregarding the heat flux of 2.5 kW/m^2), the HTC was higher with the higher heat flux throughout the quality range. In Figure 5.3c, for a mass flux of $80 \text{ kg/m}^2\text{s}$, it can be observed, at vapour qualities in the region of 0.7 to 0.9, a peak in the HTC was present. At a vapour quality exceeding approximately 0.40, the HTC increased with vapour quality, as reported by [50, 53, 54, 62], but for a heat flux of 2.5 and 5.0 kW/m^2 this influence was more pronounced at a mass flux of $80 \text{ kg/m}^2\text{s}$.



(a) 40 kg/m²s



(b) 60 kg/m²s



(c) 80 kg/m²s

Figure 5.3. Influence of heat flux on the mean HTC for mass fluxes of: (a) 40 kg/m²s, (b) 60 kg/m²s, and (c) 80 kg/m²s

5.2.4. Influence of the flow pattern on the HTC

As discussed in the previous sections, the HTC exhibited some peculiarities. One of these was that at the lowest heat flux, low vapour qualities exhibited a far larger HTC than expected at pipe entry. The HTC was up to 70% higher at test section entry than at the test section exit for an inlet vapour quality of 0.20 and mass flux of $80 \text{ kg/m}^2\text{s}$, as indicated in Figure 5.4. This figure shows the local HTCs zoomed for a single inlet vapour quality test at the different thermocouple stations. Additionally, increased vapour quality resulted in a higher HTC for a heat flux of 2.5 , 5.0 and 7.5 kW/m^2 beyond a vapour quality of 0.40 for this mass flux. The lower heat fluxes showed a larger effect, as can be seen in Figure 5.3c.

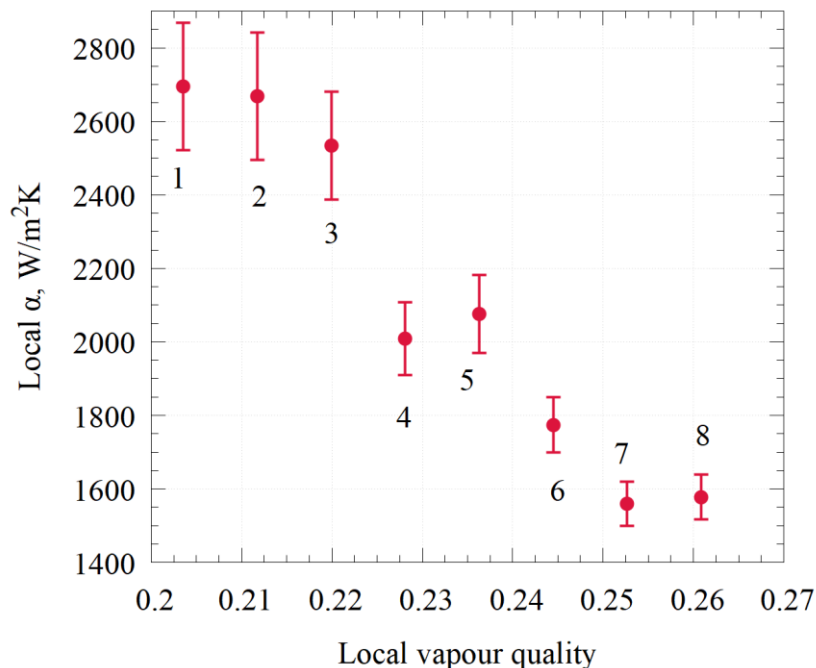


Figure 5.4. Representative example where there is a large difference between entry and exit HTCs for a mass flux of $80 \text{ kg/m}^2\text{s}$, inlet vapour quality of 0.20 , and a heat flux of 2.5 kW/m^2

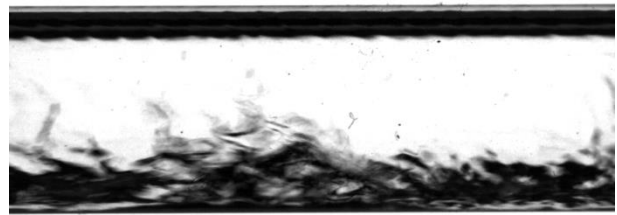
The spike in HTC at the inlet at a heat flux of 2.5 kW/m^2 will be discussed first. Initially, it was thought that steady state had not been achieved for the specific qualities that showed a higher HTC (between 0.15 and 0.35), but that idea was discarded, since after cursory investigation, the temperatures at all thermocouple stations were stable for the required time before the data was recorded. The possibility of user error in setting up the experiment was also discarded, because the data was gathered over different days for the different conditions.

The possibility that the flow patterns differed between heat fluxes at the inlet due to intra-fluid axial heat conduction was investigated next. High-speed recordings at a frame rate of 1000 frames per second and a resolution of 1280 by 720 pixels for inlet vapour qualities of 0.15 to 0.35 were

The flow patterns and heat flux also hold the explanation for why the HTC's increased for a vapour quality beyond 0.40 and a mass flux of 80 kg/m²s, while reducing for mass fluxes of 40 and 60 kg/m²s. To illustrate this, the flow patterns obtained at a vapour quality of 0.40 for the three different mass fluxes are shown in Figure 5.6a, c, and e for a heat flux of 2.5 kW/m². As can be seen, the flow patterns for all three mass fluxes at this vapour quality were stratified wavy. This agrees with the flow pattern map in Figure 4.2. The flow pattern observed for a mass flux of 40 kg/m²s is on the boundary of fully stratified flow, and the flow patterns for 60 and 80 kg/m²s are fully stratified wavy. The HTC for all three mass fluxes at this vapour quality were within 300 W/m²K of each other, as seen in Figure 5.2a. Contrasted to this is the HTC at a vapour quality of 0.70, where the difference between the highest value at 80 kg/m²s and the lowest value at 40 kg/m²s is 900 W/m²K.



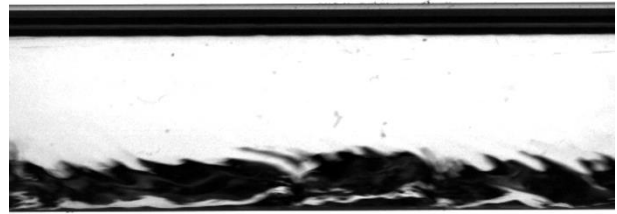
(a) $G = 80 \text{ kg/m}^2\text{s}; x_{\text{in}} = 0.40$



(b) $G = 80 \text{ kg/m}^2\text{s}; x_{\text{in}} = 0.70$



(c) $G = 60 \text{ kg/m}^2\text{s}; x_{\text{in}} = 0.40$



(d) $G = 60 \text{ kg/m}^2\text{s}; x_{\text{in}} = 0.70$



(e) $G = 40 \text{ kg/m}^2\text{s}; x_{\text{in}} = 0.45$



(f) $G = 40 \text{ kg/m}^2\text{s}; x_{\text{in}} = 0.70$

Figure 5.6. Flow patterns illustrating the transition from stratified wavy flows to hybrid/intermittent flows for a mass flux of $80 \text{ kg/m}^2\text{s}$ and a heat flux of 2.5 kW/m^2

The reason for this difference can be observed in the flow patterns captured at a vapour quality of 0.70 for the three mass fluxes, shown in Figure 5.6b, d, and f. Here, the flow patterns for mass fluxes of 40 and $60 \text{ kg/m}^2\text{s}$ were again stratified wavy (as predicted by Figure 4.2), while the flow pattern for a mass flux of $80 \text{ kg/m}^2\text{s}$ exhibited a stratified wavy to annular flow pattern transition. This is different from what Figure 4.2 predicts, showing that the flow pattern map might need some adjustment, with perhaps an additional flow pattern type or region added to distinguish this transitional pattern. Regardless, this flow pattern will result in a higher HTC than the stratified wavy forms observed for lower mass fluxes, due to the complete wetting of the wall.

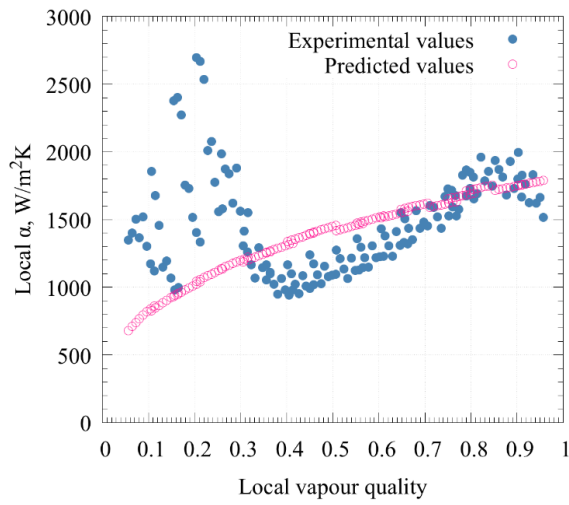
For the transition between stratified wavy and annular flow patterns, as the vapour quality increases, the liquid film wetting the top of the pipe becomes thinner, facilitating the higher HTC for a mass flux of $80 \text{ kg/m}^2\text{s}$. The decrease in heat transfer as the vapour quality increases for the stratified wavy flow pattern is due to a higher fraction of the pipe wall being dry, with the mass flux being insufficient to wet the pipe wall even partially. The reason for the lower heat fluxes amplifying this effect is thought to be the partial dryout of the pipe wall caused by the higher heat fluxes, negating the improvement that is obtained with a thinner liquid film.

5.2.5. Comparison with correlations

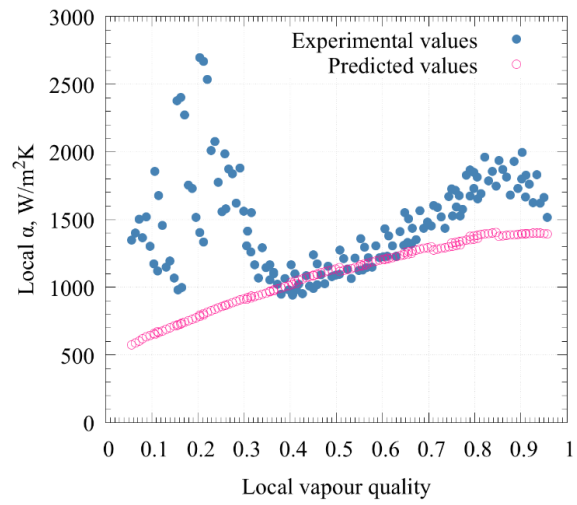
Several correlations were used in an attempt to examine if any could capture the behaviour shown in Figure 5.2a, Figure 5.3c and Figure 5.4. Specifically, the behaviour that needed to be replicated was the spike in HTC for lower vapour qualities in the first stages of the test section and the drastic reduction towards the exit of the pipe. Consider Figure 5.7, in which the values of predicted HTC (pink empty circles) are compared with the actual HTC (blue filled circles) for a mass flux of $80 \text{ kg/m}^2\text{s}$ and heat flux of 2.5 kW/m^2 . The equations for the correlations used are given for reference in Appendix C.

These correlations, apart from the Fang *et al.* [100] correlation, all incorporate the nucleate boiling contribution in some way. In the Liu-Winterton [102] and Gungor-Winterton [99] correlations, a boiling suppression factor is introduced, which is multiplied by the nucleate boiling contribution in the eventual summation to obtain the two-phase HTC. In the Bertsch *et al.* [103] correlation, the vapour quality for which the HTC is being predicted is combined with the nucleate boiling HTC before summation with the convective liquid and vapour HTCs. The Kandlikar [104] correlation calculates the boiling HTC with a set of constants for the nucleate and convective boiling region

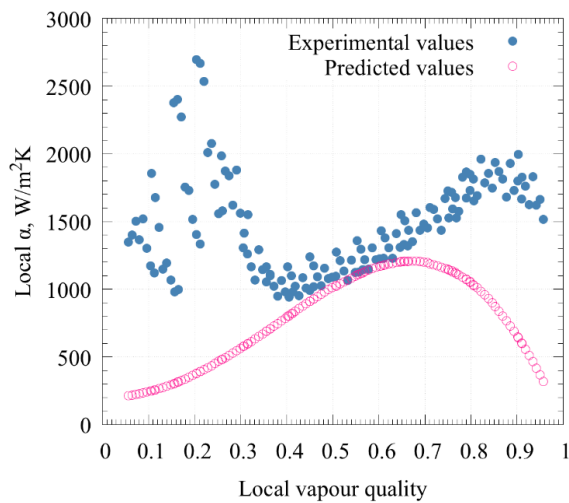
separately, and chooses the maximum HTC thus calculated. The Wojtan-Ursenbacher-Thome [101] correlation implements the nucleate boiling contribution in their calculation of the wetted perimeter HTC.



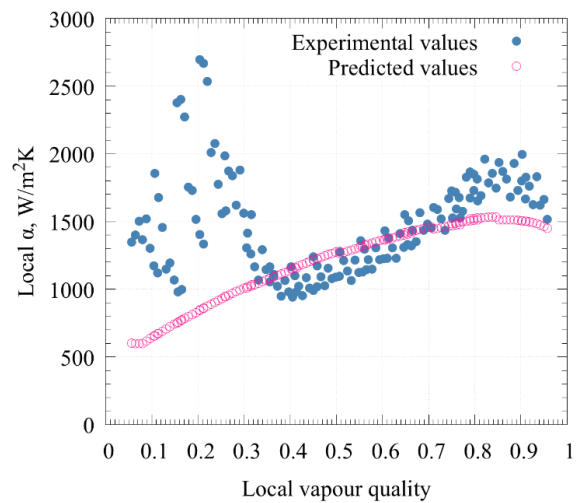
(a) Liu-Winterton [102]



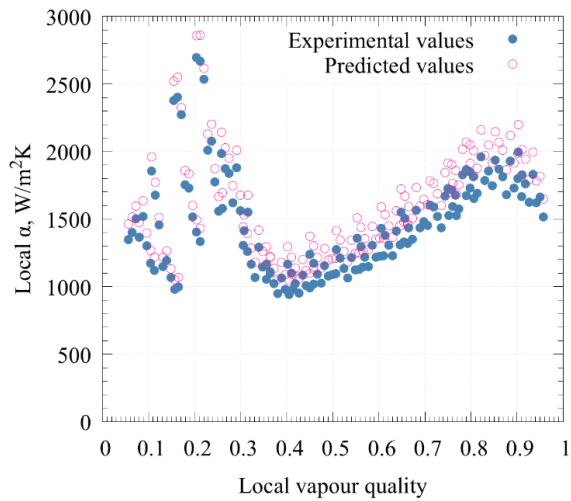
(b) Gungor-Winterton [99]



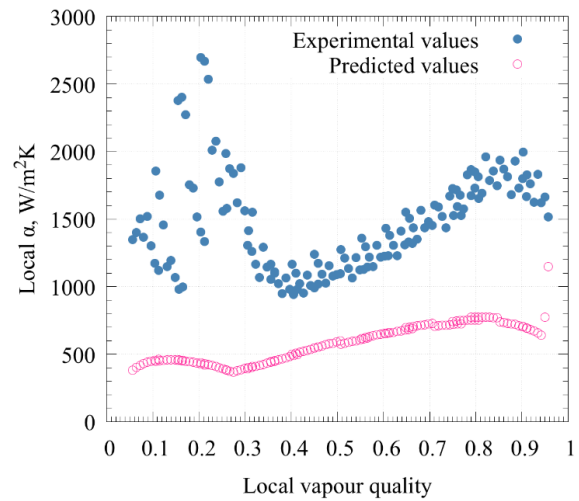
(c) Bertsch *et al.* [103]



(d) Kandlikar [104]



(e) Fang *et al.* [100]



(f) Wojtan-Ursenbacher-Thome [101]

Figure 5.7. Comparisons with HTC predictions from well-known correlations for a mass flux of $80 \text{ kg/m}^2\text{s}$ and a heat flux of 2.5 kW/m^2

As can be seen in Figure 5.7a to Figure 5.7d, the correlations do not predict the spike at all, and only at higher qualities, where the flow pattern is assumed to be largely the same throughout the pipe length, do the correlations of Liu-Winterton [102], Gungor-Winterton [99], and Kandlikar [104] start to predict within acceptable levels. The Fang *et al.* [100] correlation, shown in Figure 5.7e, utilises the viscosity of the fluid at the wall in its formulation. Since the wall temperature was known from measurements in this study, it is deceptively accurate, since this viscosity could be calculated exactly. In practice, however, an estimate of the viscosity would have to be done. On the other hand, the flow pattern-based correlation of Wojtan-Ursenbacher-Thome [101] captures the general trend of the HTC fairly well, although the accuracy is unsatisfactory.

Taking a step back to consider the correlations in Figure 5.7a to Figure 5.7d, and the data used to predict the HTC, it becomes clear that none of the correlation formulations have any way of accounting for changes between pipe inlet and outlet. In hindsight, it seems obvious that some way of including the changes occurring in the pipe needs to be applied. The Fang *et al.* [100] correlation takes this into consideration by using the actual wall temperature in the correlation. The flow pattern-based correlation of Wojtan-Ursenbacher-Thome [101] takes changes in the pipe into consideration by predicting the flow pattern and adjusting the heat transfer correlation accordingly. Though the flow map is incorrect in exactly determining which flow pattern is present, and its accuracy is not sufficient for this case, it is felt that this approach is the only way to for calculate the HTC where the flow pattern changes inside the pipe.

For reference, the mean absolute deviation (MAD) and mean relative deviation (MRD) for each correlation is given in Table 5.1.

Table 5.1. Mean absolute and relative deviations for the correlations

Correlation	Mean absolute deviation (%) $\%MAD = \frac{100}{N} \sum_{i=1}^N \left \frac{\alpha_{i,pred} - \alpha_{i,exp}}{\alpha_{i,exp}} \right $	Mean relative deviation (%) $\%MRD = \frac{100}{N} \sum_{i=1}^N \frac{\alpha_{i,pred} - \alpha_{i,exp}}{\alpha_{i,exp}}$
Liu-Winterton [102]	21.1	-1.65
Gungor-Winterton [99]	23.9	-22.5
Bertsch <i>et al.</i> [103]	42.6	-42.6
Kandlikar [104]	21.6	-14.4
Fang <i>et al.</i> [100]	9.59	9.59
Wojtan- Ursenbacher- Thome [101]	58.9	-59.9

Future studies will need to gather more data before attempting to adjust the correlation and the flow pattern map. Incorporating the known conditions and fluid properties into the flow pattern maps, and adjusting the hard cut-off lines for qualities and mass fluxes between flow patterns, seem to be the focus of future studies. Regardless, this study showed that flow pattern-based correlations are perhaps the only applicable means of predicting the HTC in modern industrial applications where the mass and heat flux are relatively low.

5.3. HIGH MASS FLUX STEADY-STATE RESULTS

With the new data for low mass and heat fluxes successfully gathered, a repeatable set of values to serve as baseline for the tests involving perturbances at higher mass fluxes, had to be gathered. Additionally, while performing these perturbation tests, it became clear that supplementary tests were needed.

5.3.1. Local versus average HTC

As was seen in Figure 5.1, for some mass fluxes and heat fluxes, the HTC along the length of the test section differed wildly. Thus, before the rest of the high mass flux results are presented, it was important to check whether any significant variations in the local HTC was observed. As with the low mass flux cases, Equation (4.6) was used to determine the HTC profile along the length of the test section. An example of the HTCs thus obtained is presented in Figure 5.9 for a case with a mass flux of $200 \text{ kg/m}^2\text{s}$, a heat flux of 7.5 kW/m^2 , and an inlet vapour quality of 0.15. Instead of the axial location along the length of the test section, the local vapour quality, as determined from Equation (4.4), is used as the horizontal axis, as before in Figure 5.1.

It can be seen that the HTCs differed by a maximum of approximately 10% for a mass flux of $200 \text{ kg/m}^2\text{s}$ at an inlet vapour quality of 0.15. This behaviour was observed up to dryout. For a mass flux of $300 \text{ kg/m}^2\text{s}$, this difference was approximately 10% up to a vapour quality of 0.50, from which it degraded to approximately 20% at dryout. This was nowhere near the deviation observed in Figure 5.1.

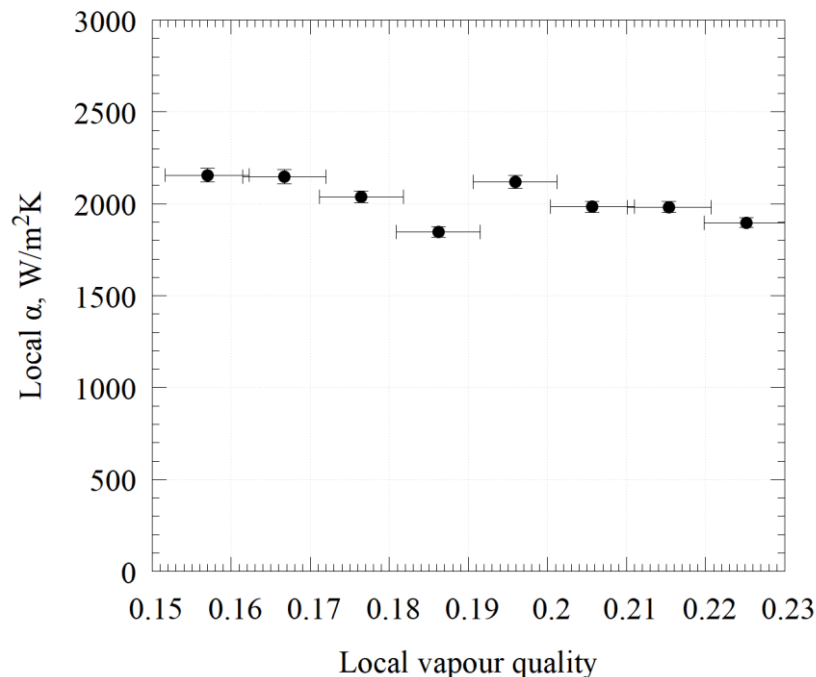


Figure 5.8. Illustrative example of local HTCs at the eight thermocouple stations for an initial vapour quality of 0.15, mass flux of $200 \text{ kg/m}^2\text{s}$, heat flux of 7.5 kW/m^2 , and saturation temperature of $35 \text{ }^\circ\text{C}$

The mean of the local HTCs obtained from the eight thermocouple stations along the length of the pipe was thus used as representative of the overall HTC in the rest of this work. This was done since the deviation was considered acceptable, and to limit the amount of visual noise in the figures.

5.3.2. Baseline results and repeatability

In order to prove repeatability of the baseline results gathered, staggered tests were performed on different dates at exactly the same conditions. Mean HTC_s as determined with Equation (4.10) at a saturation temperature of 35 °C, and heat flux of 7.5 kW/m² at 200 and 300 kg/m²s that were gathered on separate occasions, are shown in Figure 5.9. Uncertainty bars for the vapour quality and HTC are included. Note that due to the relatively small vapour quality uncertainties, the associated error bars are short and might not be clearly visible. They are thus only shown on selected figures in the rest of this work.

It can be seen that HTC results obtained on the different dates were in close agreement. Because this difference was less than 5% (apart from one outlier at a vapour quality of 0.90), and fell within experimental uncertainty, it indicates that the system results were repeatable.

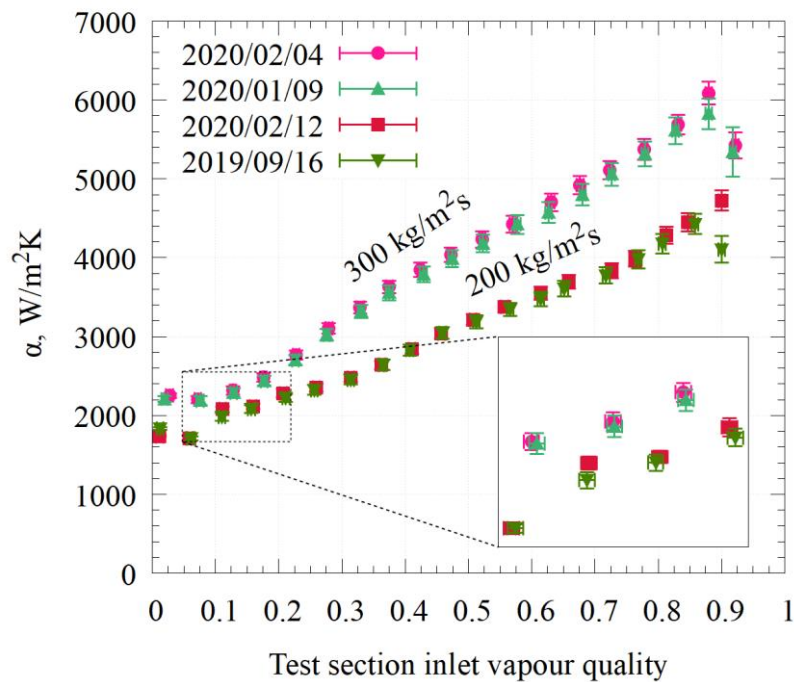


Figure 5.9. Steady-state HTC_s gathered on different dates for mass fluxes of 200 and 300 kg/m²s at a saturation temperature of 35 °C and a heat flux of 7.5 kW/m²

To be able to fully discuss the results in Figure 5.9, an additional figure showing the flow patterns achieved is shown in Figure 5.10. The flow patterns were compared to those predicted by the flow pattern map by checking the high-speed video footage captured, and, as indicated on the figure, ranged across slug, intermittent, and annular flow patterns, before reaching dryout. As has been observed by other authors (for example Da Silva Lima *et al.* [52]), the HTC reaches a local minimum

for the slug flow pattern, before increasing steadily as the flow pattern evolves into intermittent and annular patterns.

It is assumed that at low vapour qualities (and thus the slug flow pattern), the convective boiling contribution is limited, since the vapour velocity contribution is small. Nucleate boiling dominates at these flow patterns and vapour qualities. The reason for the increased HTC for intermittent and annular flow is that the entire pipe wall is covered with a liquid film. As the vapour quality increases, this liquid film becomes thinner and the convective contribution increases, facilitating an increased HTC. At dryout, where the liquid no longer covers the entire pipe wall and a portion of the pipe wall is permanently dry, the HTC drops off abruptly.

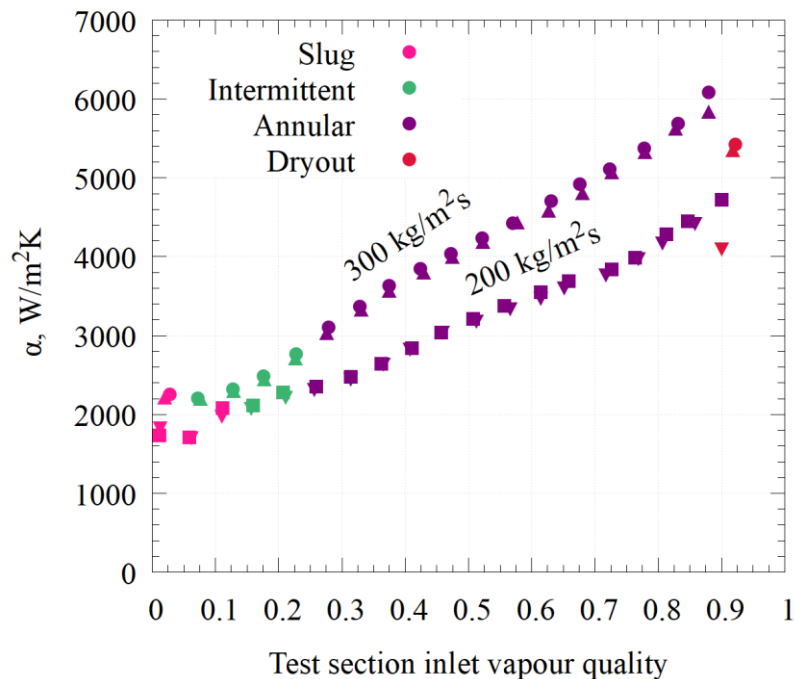


Figure 5.10. Steady-state HTCs showing the flow patterns achieved

5.3.3. Intermediate and interpolated results

The base-line measurements at 200 and 300 kg/m²s in the previous section formed the foundation of the transient analysis in this study. However, as will be shown later, significant variations in the mass flux were present during transient-state conditions. For comparative purposes, it was required to accurately determine the steady-state HTCs at several additional mass fluxes. Because doing multiple sets of steady-state experiments, each at a slightly different mass flux, would have been impractical, another method to calculate steady-state HTCs at intermediate mass fluxes was needed. As will be shown later, mass fluxes of 235 and 335 kg/m²s were particularly relevant during some of the transient-state cases, and required special attention.

A linear interpolation scheme was adopted to predict the HTC's at these intermediate mass fluxes. This was based on observations from several other studies that focused on the effect of mass flux on the HTC during steady state. From literature it was found that for a mass flux of between 200 and 300 kg/m²s and a vapour quality of between 0.15 and 0.80 during steady state, the HTC behaved in a pseudo-linear fashion over the range of qualities under consideration for a specific mass flux for organic refrigerants [55, 57, 105]. The vapour qualities where the HTC does not follow a pseudo-linear trend, were reported to be below 0.10 and above 0.90 [52], which falls on the extreme edges of the test matrix in the current investigation.

When compared with different mass fluxes for a specific vapour quality, pseudo-linear behaviour was also observed by the author of this work. For the narrow range of mass fluxes that was required in this study, a linear interpolation was thus considered sufficient, as will be discussed shortly. The applicable steady-state results for 200 and 300 kg/m²s are repeated in Figure 5.11 in terms of vapour quality. Suitable curve fits were applied to the data to enable data extraction at any vapour quality value. The obtained linearly interpolated curve for a mass flux of 235 kg/m²s, as well as the linearly extrapolated curve for 335 kg/m²s, are also shown. In order to check the correctness of these interpolated and extrapolated HTC's, a few additional steady-state experiments were performed at 235 and 335 kg/m²s. The results obtained at these mass fluxes are shown as empty circles in Figure 5.11.

It was found that the difference between the interpolated/extrapolated HTC's were within 3% of the experimentally obtained values. This indicates the validity of using a linear interpolation/extrapolation scheme to determine additional steady state HTC's at intermediate mass flux conditions.

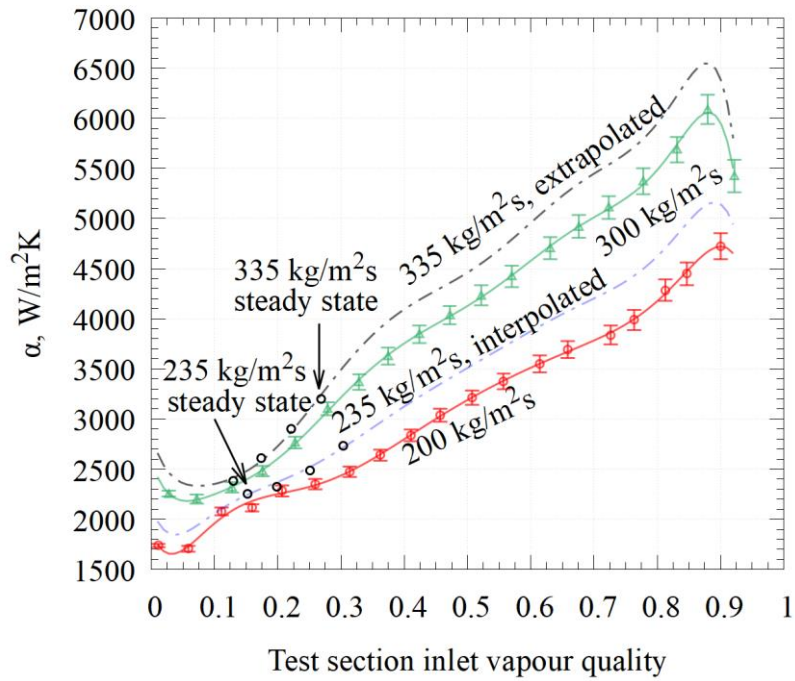


Figure 5.11. Measured and interpolated steady-state HTCs as a function of vapour quality for the mass flux values investigated in the transient tests at a saturation temperature of 35 °C

5.4. SUMMARY

In this chapter the steady state HTC results were presented for the low and high mass flux bands under consideration in this investigation. At low mass fluxes it was found that the HTC was unexpectedly high at low heat fluxes at the entry to the test section, and that none of the correlations applied captured this behaviour. The higher mass flux cases (200 and 300 kg/m²s), which act as the baseline conditions for the rest of this investigation, was also presented. It was shown that a simple linear interpolation scheme can be used to derive steady state HTCs for other mass flux values.

PART III

TRANSIENT INLET VAPOUR QUALITY PERTURBANCE

“In God we trust; all others bring data.”

–W.E. Deming

6. INLET VAPOUR QUALITY PERTURBANCE INVESTIGATION

METHODOLOGY

6.1. INTRODUCTION

One of the tests of interest was the reaction of the HTC under a drastic change in vapour quality. This is relevant for industrial CSP systems both for cloud coverage of a section of the solar receiver, and for sunrise and sunset. As shown in Chapter 5, the HTC can be independent of the vapour quality at lower mass fluxes. At higher mass fluxes, such as those encountered in a commercial setting, however, it can be highly sensitive to the vapour quality. How the HTC reacts when a system transitions between discrete steady states or differing flow patterns caused by a vapour quality perturbation in these higher mass flux cases is still an open question.

In industrial parabolic trough CSP systems, the length of piping in the solar field is on the scale of kilometres. It is possible that a change in the DNI will affect only certain sections of this receiver, either at sunrise and sunset, or because of cloud cover. This is shown in the photograph in Figure 6.1, in which the receiver field is partially shaded due to a passing cloud.



Figure 6.1. Partial shading of the Xina and Kaxu parabolic trough CSP plants, Pofadder, South Africa [106]

Recalling Figure 1.1, a section of the concentrator field undergoing a perturbation in DNI will cause the thermodynamic operating point to change, as depicted in Figure 6.2. The vapour quality will reduce from point 3 to point 3', and this reduction in vapour quality will have an effect in sections of the concentrator field further downstream that are not experiencing the same perturbation.

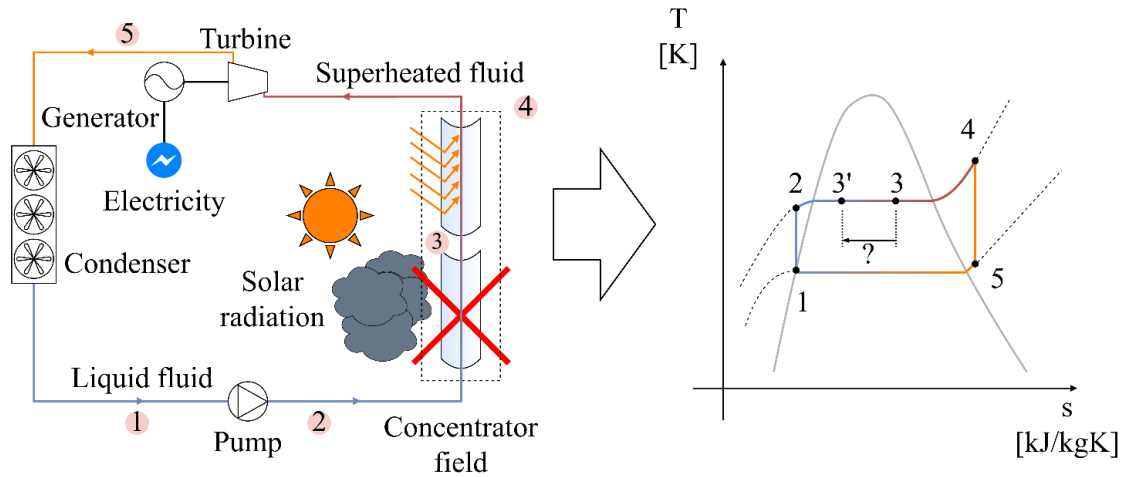


Figure 6.2. Simplified schematic of a theoretical direct steam generation Rankine cycle undergoing a DNI perturbation

This observation germinated into the basic idea behind this set of experiments. What would the effect on the HTC be in the undisturbed section of the concentrator field in such cases? A steady state at some mass and heat flux was observed, following which a perturbation in the upstream DNI (and thus test section inlet vapour quality) was caused. Data was gathered on the behaviour of the HTC in response to this perturbation. Importantly, the test section was left undisturbed, simulating the unshaded part in Figure 6.2.

This chapter lays the groundwork in the experimental procedure that would be followed to achieve this. It also refines the test matrix that would be the focus of this specific study, and provides the additional data processing that was required.

6.2. EXPERIMENTAL PROCEDURE

In order to design an experiment with which to investigate the impact of a sudden perturbation in the inlet vapour quality, certain assumptions had to be made. The first was the magnitude of the DNI disturbance, and the effect it would have on the vapour quality. The magnitude of this disturbance could be inferred from the weather station on the University of Pretoria's main campus in South Africa [107].

On an arbitrary day, the DNI varies by a minimum of approximately 200 W/m^2 , depending on the weather situation. When considering the simulated CSP system that was represented by the current work's experimental apparatus, the inlet vapour quality could be calculated based on this varying DNI by combining Equations (4.4) and (4.5):

$$x_{\text{in}} = \frac{\left(h_A + \frac{\dot{Q}_{\text{pre}}}{\dot{m}} \right) - h_f}{h_g - h_f} \quad (6.1)$$

Thus, to vary the inlet vapour quality, the heat added in the preheater had to be adjusted in some way, with a magnitude comparable to that observed. It was found that adjusting \dot{Q}_{pre} by between 200 and 300 W resulted in a change in vapour quality of roughly 0.10, depending on the mass flow rate being considered. The absolute value of the inlet vapour quality perturbation (Δx_{in}) that would be investigated for this set of experiments was thus chosen to be 0.10.

For the operating mass flow rate, the required change in the preheater power rate ($\Delta \dot{Q}_{\text{pre}}$) can be expressed as follows:

$$\Delta \dot{Q}_{\text{pre}} = \dot{m} \Delta x_{\text{in}} (h_g - h_f) \quad (6.2)$$

With the magnitude of the perturbation fixed, the period over which a perturbation would be applied (and thus its profile) had to be selected. Considering the size of the solar field, and the relatively small diameter of the pipes, it was decided on a step profile to minimise complications.

Finally, the procedure was to reach a steady state at a given inlet quality, as described in Section 4.2, and maintaining it for 60 s, at which point the heat rate was reduced by $\Delta \dot{Q}_{\text{pre}}$ in a stepwise fashion. This was accomplished by activating a LabView script once steady state had been achieved. This script waited for exactly the prescribed time, then decreased the power supplied by the preheater power supply units (thus affecting \dot{Q}_{pre}) by a set amount by interfacing with the manufacturer's virtual instrumentation. The system would then be allowed to seek a new steady state for 300 s, before the heat rate was increased back to its original value. The original steady state would then be reached, with data being recorded throughout the transient. The reduction and increase in $\Delta \dot{Q}_{\text{pre}}$ at the same mass flux provided valuable insights into the behaviour of the HTC.

6.3. TEST MATRIX

As part of the transient nature of the DNI (either reducing or increasing), it was realised that the change in vapour quality, Δx_{in} , would necessarily involve crossing between flow patterns. Looking at Figure 4.2, especially the vapour qualities between 0.15 and 0.40 at a mass flux of 200 kg/m²s, it is evident that the flow pattern changes from slug to intermittent to annular in a very confined vapour quality range.

To drive this point home, flow patterns captured for adiabatic test conditions at the test section inlet for a mass flux of $200 \text{ kg/m}^2\text{s}$ are shown for a vapour quality of 0.20 and 0.30 in Figure 6.3.

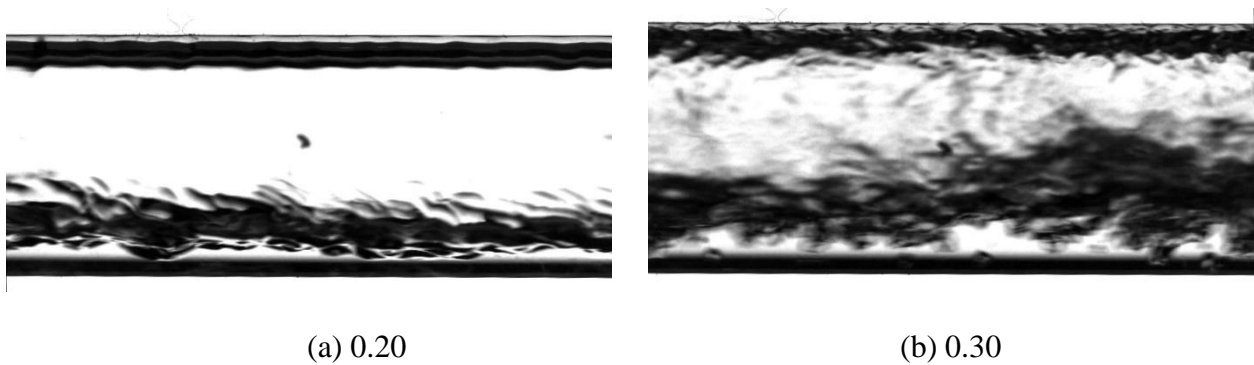


Figure 6.3. Examples of flow pattern crossing from (a) slug and intermittent at vapour quality 0.20 to (b) intermittent and annular at vapour quality 0.30 for a mass flux of $200 \text{ kg/m}^2\text{s}$ and a saturation temperature of 35°C

Fortuitously, the DNI and vapour quality change discussed in Section 6.2 aligned with the quality change that resulted in differing flow patterns. The decision was thus made to limit the perturbances for this test to range from 0.15 to 0.40 to investigate possible flow pattern change effects. This test matrix is depicted in Figure 6.4, in which the proposed application of Δx_{in} is illustrated.

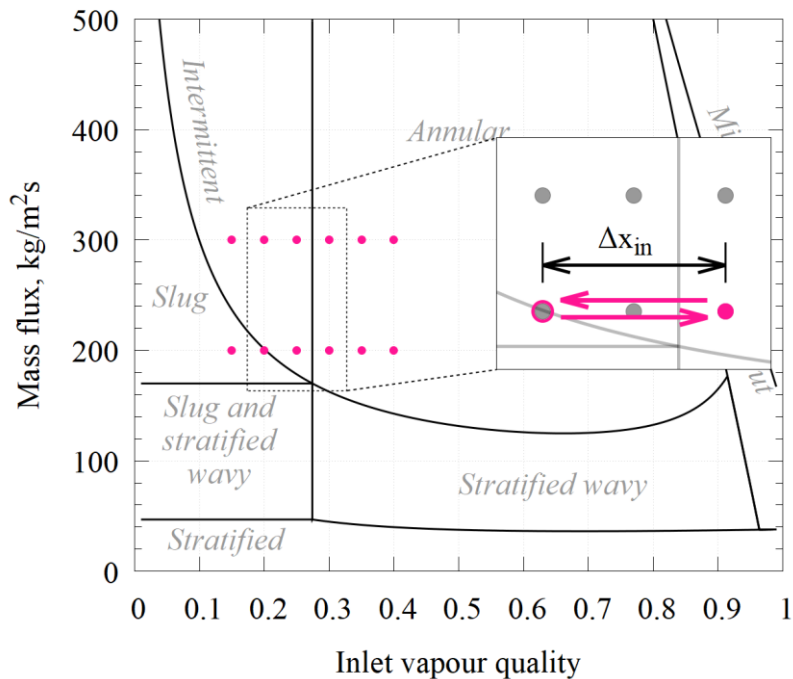


Figure 6.4. Test matrix for the transient quality perturbation tests

6.4. DATA PROCESSING

The equation for the HTC during a transient process is similar to Equation (4.10), with the addition of the temporal aspect, as follows:

$$\bar{\alpha}(t) = \frac{\dot{q}_i(t)}{(\bar{T}_{i,\text{wall}}(t) - \bar{T}_{\text{sat}}(t))} \quad (6.3)$$

In this, the instantaneous mean HTC values, $\bar{\alpha}(t)$, are calculated by taking the instantaneous heat flux using the readings from the power supply, and the instantaneous temperature readings.

It is clear from Equation (6.1) that the inlet quality to the test section depended on the heat rate supplied, \dot{Q}_{pre} , and the mass flow rate. However, using only this data reduction for the period during and shortly after the introduction of the vapour quality perturbation was insufficient. During a step change in \dot{Q}_{pre} (physically changing the required heat rate the power supply delivered by a set amount $\Delta\dot{Q}_{\text{pre}}$), the calculated quality using this data reduction exhibited a physically unrealistic step.

What happened practically was that, while the change in \dot{Q}_{pre} from the power supply was instantaneous, the actual heat rate supplied to the fluid through the pipe wall was not, due to the energy discharge from the copper pipe wall in the preheater. In addition, the physical distance between the preheater and test section (Points B and C in Figure 3.1) would result in a time delay until the inlet vapour quality perturbation reached the inlet to the test section.

The thermal storage of the copper pipe of the preheater also had a contributing effect and would act as a dampening mechanism of any sudden change in the thermal heating state at the preheater. This meant that the inlet quality of the test section would reduce or increase over a finite time based on this. Thus, while \dot{Q}_{pre} was taken as the read value of the power supplies for the steady-state results in Chapter 5, the actual \dot{Q}_{pre} delivered to the fluid during a step transient had to be approximated. In order to obtain an estimate of the actual heat rate, and thus of the inlet vapour quality during this step change, the wall temperature of the copper pipe in the preheater was required, which could be predicted using a lumped system analysis in lieu of the lacking temperature instrumentation on the preheater.

Mixed boundary conditions of heat supply and convection heat transfer were present, and the temperature prediction method used to obtain the instantaneous preheater wall temperature over time is detailed in Özişik [108]. It includes the specific heat capacity of the copper pipe wall, and the linear differential equation obtained is reproduced in Appendix C. The solution to calculate the temperature is given here:

$$T(t) = (T_0 - T_{\text{sat}})e^{-mt} + (1 - e^{-mt}) \frac{\dot{Q}_{\text{pre}}(t)}{\alpha_{\text{pre}} A_{\text{s,pre}}} + T_{\text{sat}} \quad (6.4)$$

In this, T_0 is the wall temperature of the preheater just before the perturbation, $A_{\text{s,pre}} = \pi d_{\text{i,pre}} L_{\text{pre}}$ is the heat transfer surface area of the preheater pipe, $m = \frac{\alpha_{\text{pre}}}{\rho_{\text{Cu}} c_{\text{p,Cu}} L_{\text{c,pre}}}$, while α_{pre} is the HTC of the refrigerant in the preheater.

In order for this to be valid, a low Biot number in the preheater is required, defined as:

$$Bi_{\text{pre}} = \frac{\alpha_{\text{pre}} L_{\text{c}}}{k_{\text{Cu}}} \quad (6.5)$$

where L_{c} is the characteristic length of the preheater pipe. The characteristic length is defined as:

$$L_{\text{c}} = \frac{V_{\text{pre}}}{A_{\text{s,pre}}} \quad (6.6)$$

where $V_{\text{pre}} = \frac{\pi}{4} (d_{\text{o,pre}}^2 - d_{\text{i,pre}}^2) L_{\text{pre}}$ is the volume of the copper preheater pipe.

In order to simplify calculations, it was assumed that the HTC in the preheater was approximately equivalent to the steady-state HTC for the test section documented just before the perturbation, and that the preheater was also at saturated conditions. Furthermore, T_0 was calculated using \dot{Q}_{pre} and \bar{T}_{sat} just before the perturbation.

With these approximations, the Biot number was calculated, and was found to be two orders of magnitude lower than 0.1, which typically indicates a less than 5% error in temperature prediction when using the lumped capacitance model. It was also assumed that due to the Biot number being so low that the inner and outer wall temperatures were equivalent at a specific time t (i.e., $\bar{T}_{\text{i,wall,pre}}(t) \approx \bar{T}_{\text{o,wall,pre}}(t)$).

Since the wall temperature could be predicted fairly accurately over time, $\dot{Q}_{\text{actual,pre}}$ could be calculated using Newton's law of cooling:

$$\dot{Q}_{\text{actual,pre}}(t) = \frac{\alpha_{\text{pre}} A_{\text{s,pre}}}{(\bar{T}_{\text{wall,pre}}(t) - \bar{T}_{\text{sat}}(t))} \quad (6.7)$$

Finally, the inlet vapour quality to the test section could be determined using Equation (6.1). In order to continue the discussion, part of Figure 3.1 is reproduced below in Figure 6.5.

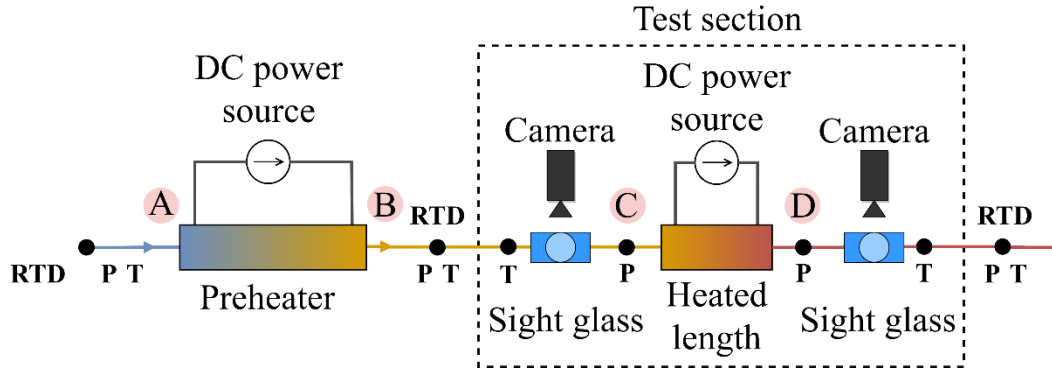


Figure 6.5. Section of test facility used for discussion.

The approximate vapour quality at point B now being known, attention was turned to the time delay for the flow to reach point C. With the system being well insulated, and no work being done or heat being added between points B and C, the vapour quality was assumed to be equal, as has been stated for the enthalpy.

The spatial separation between Points B and C was taken into consideration by monitoring the measurements at the inlet to the test section at Point C for abrupt variations. In addition, the time delay of the perturbation was estimated based on the velocity of the fluid two-phase mixture (U_m) by using:

$$U_m = \frac{\dot{V}_{\text{total}}}{A_{c,\text{pre}}} \quad (6.8)$$

where \dot{V}_{total} is the total volumetric flow rate of the liquid and gas phases, and $A_{c,\text{pre}}$ is the cross-sectional area for the length between the preheater and the test section. The total volumetric flow rate was the sum of the liquid and gas volumetric flow rates, which are given by:

$$\dot{V}_f = \frac{\dot{m}(1 - x_{\text{in}})}{\rho_f(1 - \varepsilon)} \quad (6.9)$$

$$\dot{V}_g = \frac{\dot{m}x_{\text{in}}}{\rho_g\varepsilon} \quad (6.10)$$

where \dot{V}_f and \dot{V}_g refer to the volumetric flow rate of the liquid and gas, ρ_f and ρ_g are the densities of the two saturated phases, and ε is the void fraction determined using the Steiner [109] modification to the Rouhani-Axelsson drift flux model [110], as discussed in more detail in Section 8.4.

The obtained mixture velocity was then used with the measured distance between the preheater outlet and the test section inlet sight glass to adjust the predicted quality for time. The time taken was generally below 1 s, which was confirmed via the observed disturbance at the inlet to the test section.

6.5. SUMMARY

The effect on HTC of a sudden change in vapour quality in sections downstream of a DNI perturbation is of interest. In order to gauge this, the experimental procedure that was followed was described. The test matrix covering the selection of the baseline values to which this procedure was applied was also given, followed by additional data processing required.

7. VAPOUR QUALITY PERTURBANCE RESULTS

7.1. INTRODUCTION

With the experimental procedure described and an appropriate test matrix selected, testing could commence. This chapter is concerned with presenting an in-depth discussion of a single test case, before showing that all the tests that were performed behaved similarly in a qualitative sense. After this, an overview of the differences between the expected and achieved HTC is given. The conclusions reached in this study are given in Chapter 10.

7.2. EXAMPLE CASE

An overview of the recorded data showed that they exhibited qualitatively similar results during the transient, no matter at which quality or mass flux the test was conducted. Since the behaviour of the HTC and mass flux was very similar for each initial quality and mass flux, an example of the obtained results for an initial inlet vapour quality of 0.30 and a mass flux of 200 kg/m²s is shown in Figure 7.1.

The vapour quality perturbation starts at $t = 0$. It can be seen that as a response to a downward step of the preheater heat flux (shown in grey) at approximately 0 s, the inlet vapour quality (shown in purple, and determined as described earlier) reduced by 0.13 from 0.30 to 0.17, the mass flux (shown in blue) increased from 200 kg/m²s to approximately 235 kg/m²s, the saturation temperature (shown in green) decreased slightly, and the average wall temperature decreased. The converse occurred at the upward step of the preheater heat flux at approximately 300 s.

Also included in Figure 7.1 are the derived HTC (shown in pink) using Equation (6.3), and the expected interpolated quasi-steady-state HTC (teal), as discussed in Section 5.3.3.

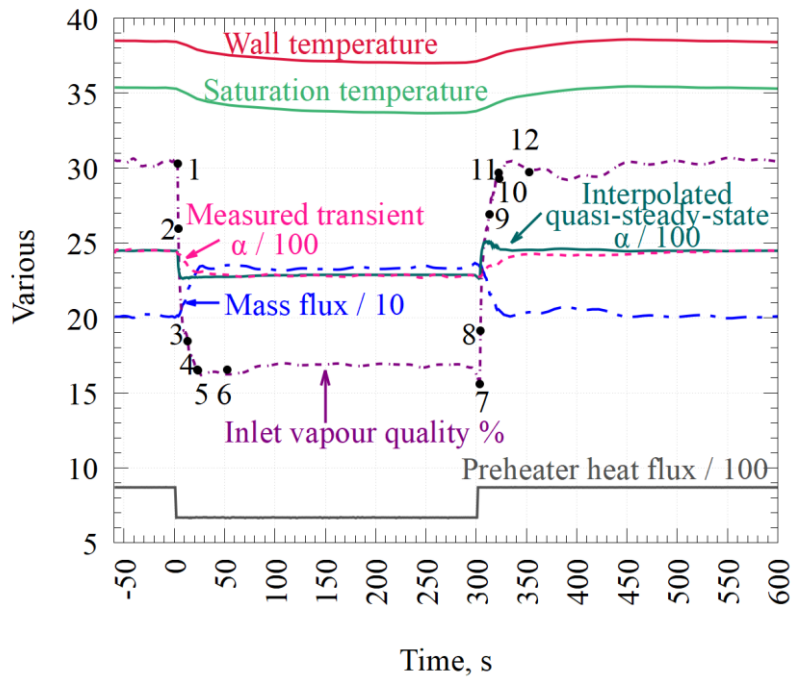


Figure 7.1. Data for a single detailed transient investigation for an initial vapour quality of 0.30, mass flux of $200 \text{ kg/m}^2\text{s}$, and saturation temperature of $35 \text{ }^\circ\text{C}$

For ease of further discussion, Points 1 to 6, indicating the downward step in vapour quality, and Points 7 to 12, indicating the upward step, are introduced in Figure 7.1. The time for each point is indicated in Table 7.1 for clarity.

Figure 7.2 offers a closer view of the HTC at time period between Points 1 and 6, during the downward step (a), and between Points 7 to 12, during the upward step (b).

Table 7.1. Time for defined points

Point	Time instant in Figure 7.1 (s)	Time lapse between points (s)	Vapour quality
1	3.2	-	0.30
2	3.9	0.7	0.26
3	13.2	9.3	0.18
4	23.1	9.9	0.17
5	23.8	0.7	0.17
6	52.8	29.0	0.17
	Total time	49.5	
7	304.4	-	0.18
8	305.3	0.9	0.19
9	313.7	8.4	0.26
10	322.8	9.1	0.29
11	322.4	0.6	0.29
12	353.3	29.9	0.30
	Total time	49.5	

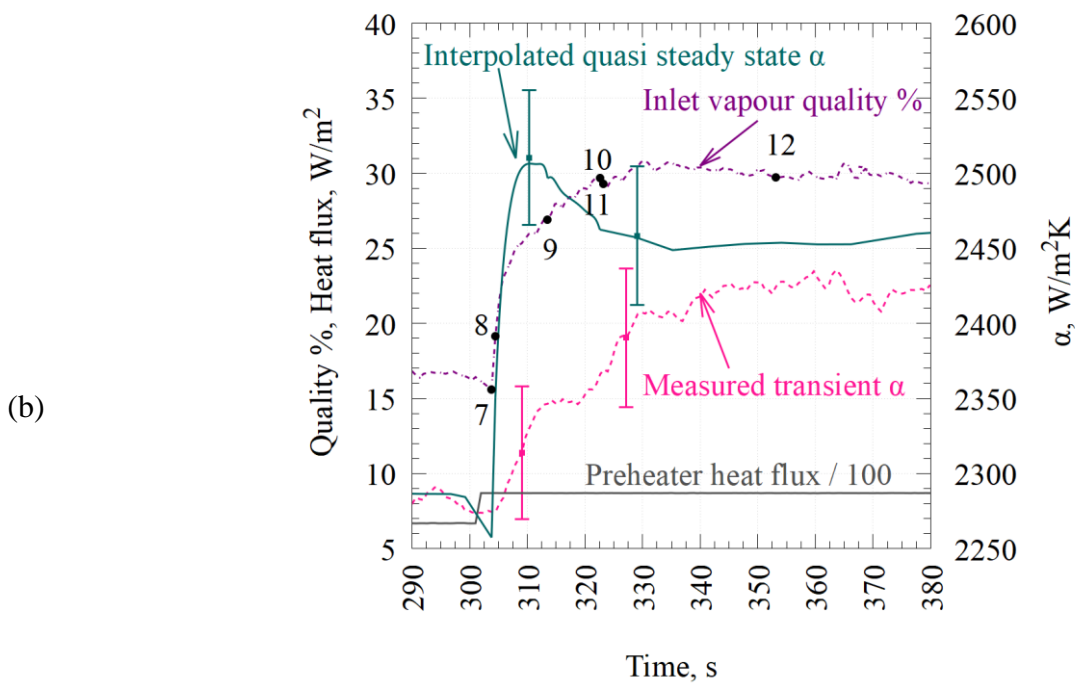
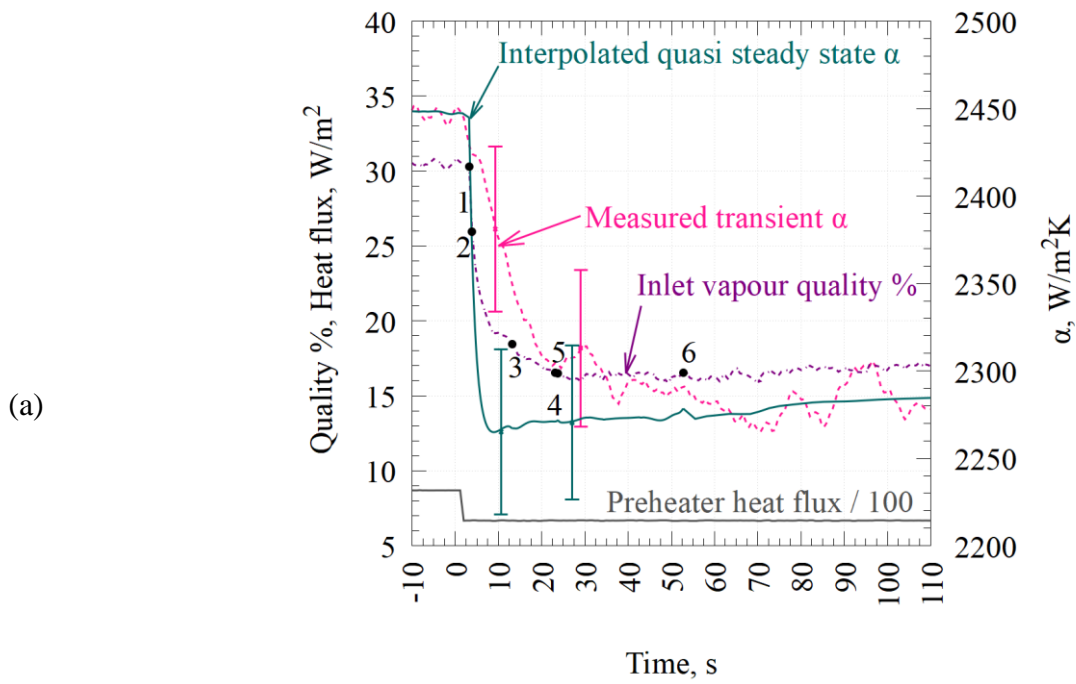


Figure 7.2. HTC behaviour for an initial vapour quality of 0.30, mass flux of $200 \text{ kg/m}^2\text{s}$, and saturation temperature of $35 \text{ }^\circ\text{C}$, during: (a) downward, and (b) upward step changes in vapour quality

Of interest is the fact that the actual HTC's are higher than the predicted quasi-steady-state HTC's between Points 1 and 6, and lower in between Points 7 and 12. These differences fall outside the uncertainty, which are plotted for selected points. These relative differences, expressed as percentages, are shown in Figure 7.3.

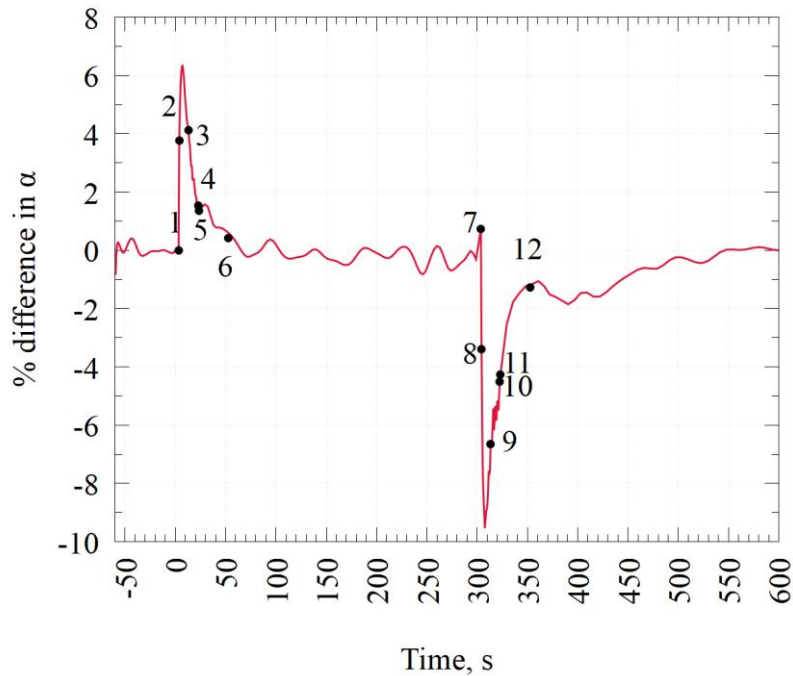


Figure 7.3. Percentage difference between the transient and interpolated steady-state HTC's as a function of time for an initial vapour quality of 0.30, mass flux of 200 kg/m²s, and saturation temperature of 35 °C

As can be seen in this case, the HTC is higher by up to 6.3% than the quasi-steady-state value during the downward perturbation, and up to 9.9% lower during the upward step.

Figure 7.4 illustrates the effect of the perturbation on the HTC in another fashion. It shows the HTC as a function of quality, along with two steady-state lines for mass fluxes of 200 and 235 kg/m²s, with the downward step being shown in (a) and the upward step in (b). The red and blue lines represent the experimentally obtained and interpolated steady-state values at mass fluxes of 200 and 235 kg/m²s, respectively, whilst the teal line represents the expected transient behaviour based on the system conditions. The purple line shows the experimentally observed transient behaviour

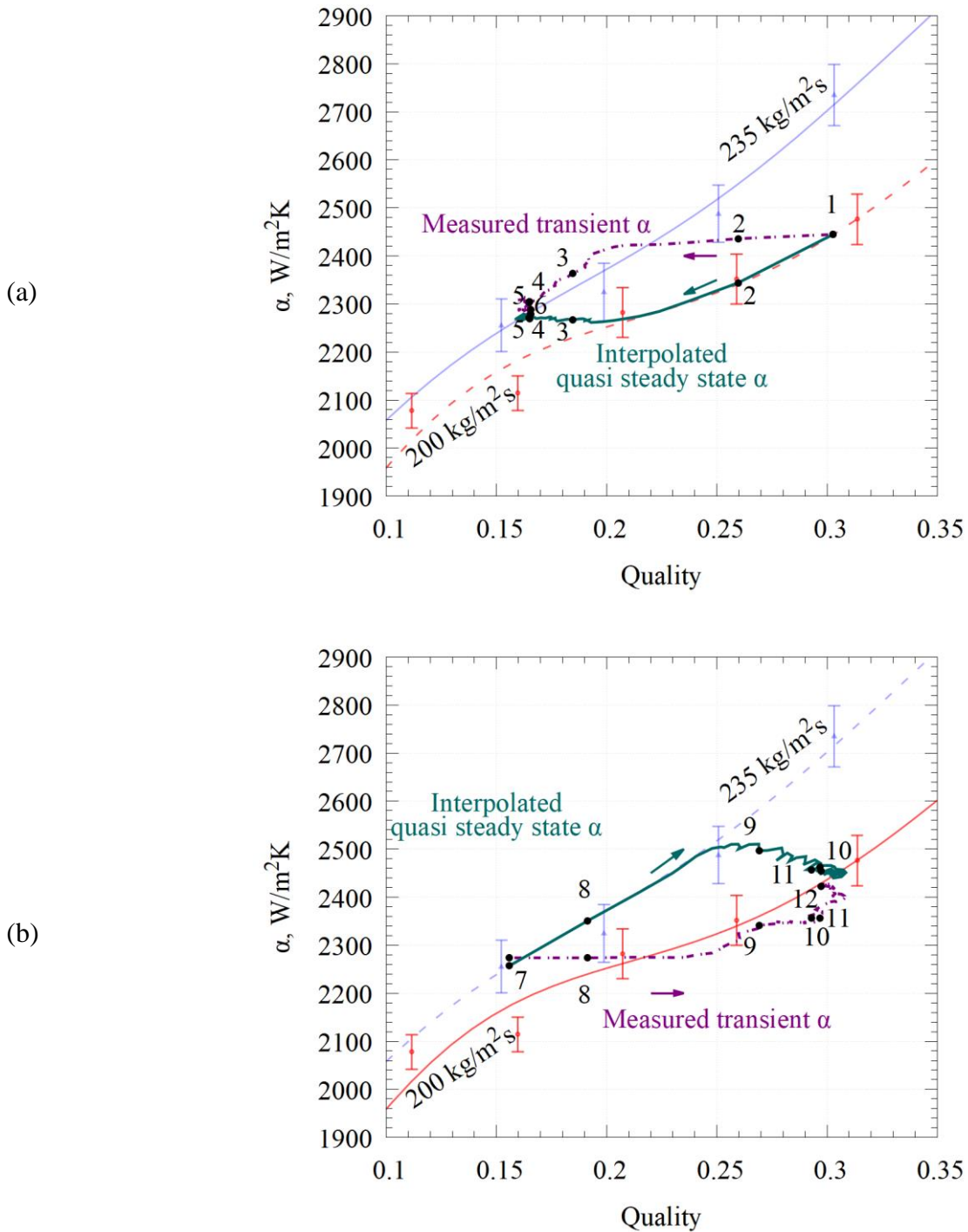


Figure 7.4. HTC as a function of quality for an initial vapour quality of 0.30, mass flux of $200 \text{ kg/m}^2\text{s}$, and saturation temperature of $35 \text{ }^\circ\text{C}$, during: (a) downward, (b) upward step changes in inlet vapour quality

From Figure 7.4 it appears that the interpolated HTC follows the steady-state lines almost exactly during both the downward and upward steps. However, an alternative representation in Figure 7.5a for the downward step and Figure 7.5b for the upward step illustrates more clearly the large difference in the actual versus the expected quasi-steady-state value. The red and blue points

indicate the steady-state experimental values for mass fluxes of 200 and 235 kg/m²s, respectively, whilst the purple and teal lines represent the experimentally observed and predicted HTC respectively.

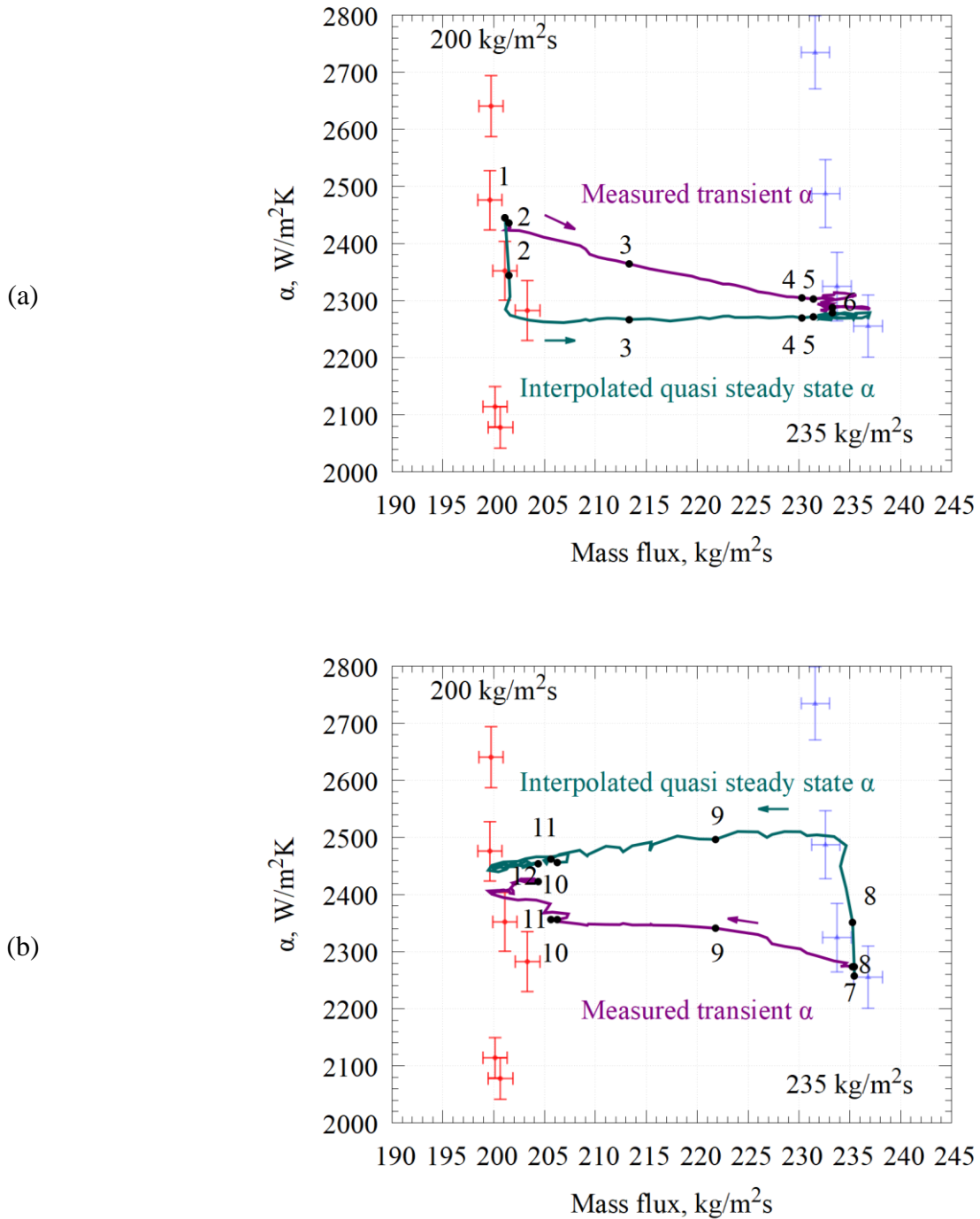
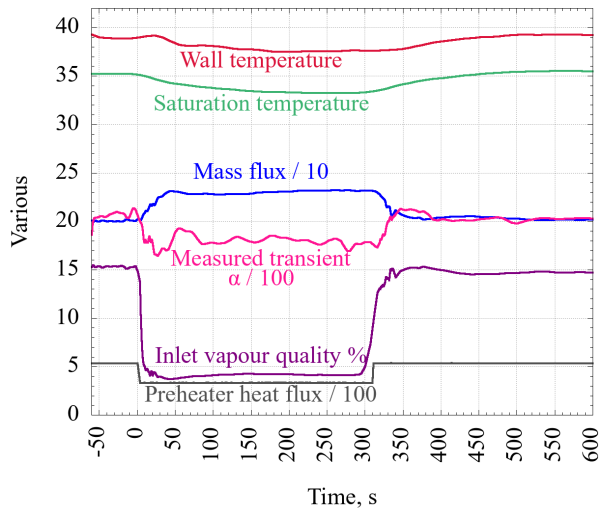


Figure 7.5. HTC as a function of mass flux for an initial vapour quality of 0.30, mass flux of 200 kg/m²s, and saturation temperature of 35 °C, during: (a) downward, and (b) upward step changes in inlet vapour quality

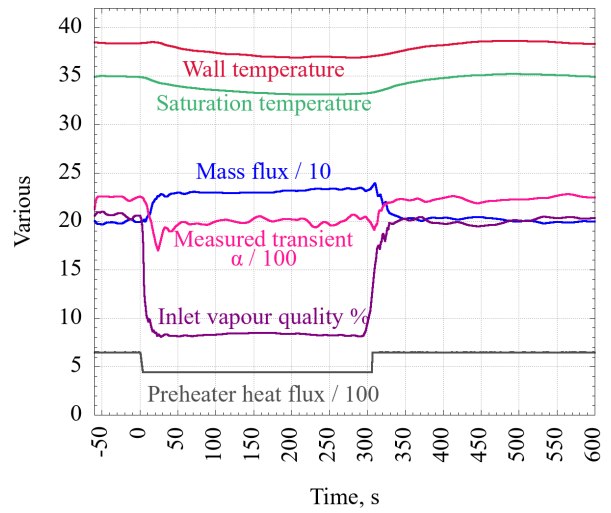
7.3. GENERAL TRENDS

Qualitatively similar behaviour was observed for all vapour qualities and mass fluxes investigated. The results for the all the vapour qualities tested for a mass flux of $200 \text{ kg/m}^2\text{s}$ are shown in Figure 7.6 to illustrate this.

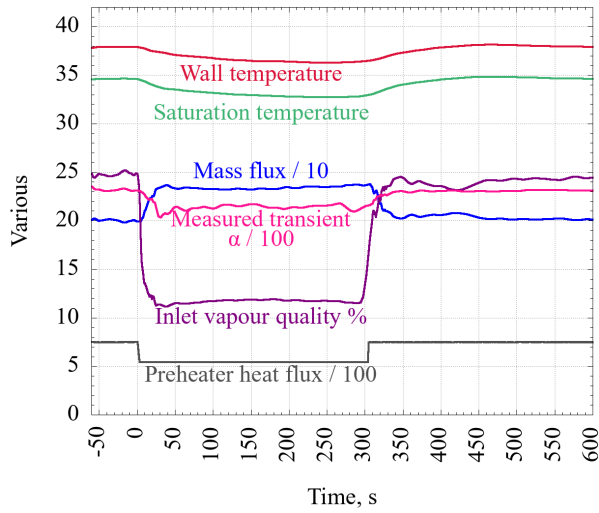
The difference between the expected quasi-steady-state values and obtained HTCs observed for all test points used in this analysis are summarised in Figure 7.7. It is apparent that the increased HTC observed during the downward step was at all times lower than the decreased HTC in the upward step for lower qualities. As the qualities increased, the difference decreased. The flow pattern present could be a major influence on this observation. When compared with the test matrix flow patterns, it is apparent that the intermittent and slug flow patterns exhibited a larger difference between the downward and upward steps than the annular flow pattern for a mass flux of $200 \text{ kg/m}^2\text{s}$. Whereas it was less pronounced for a mass flux of $300 \text{ kg/m}^2\text{s}$, the difference between the downward and upward steps at lower vapour qualities was still larger. Further study is required to determine the cause of this effect. For a mass flux of $200 \text{ kg/m}^2\text{s}$, the maximum increase for the downward step was 11.7% for a vapour quality of 0.40, while the maximum decrease during the upward step was 26.0% for a vapour quality of 0.15. For a mass flux of $300 \text{ kg/m}^2\text{s}$, the maximum increase for the downward step was 16.7% for a vapour quality of 0.30, while the maximum decrease during the upward step was 17.8% for a vapour quality of 0.15.



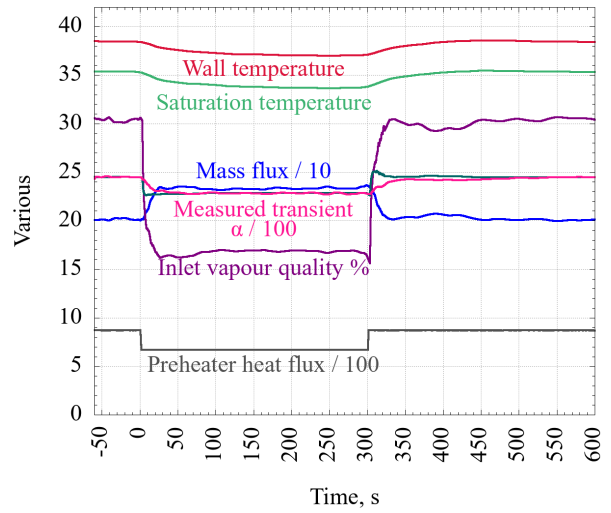
(a) $x_{in} = 0.15$



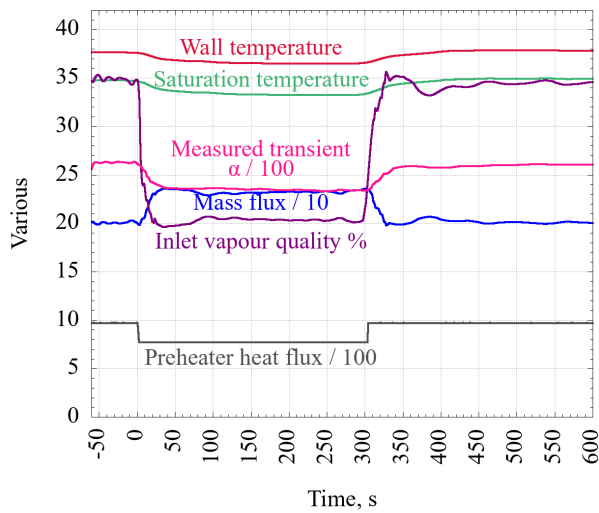
(b) $x_{in} = 0.20$



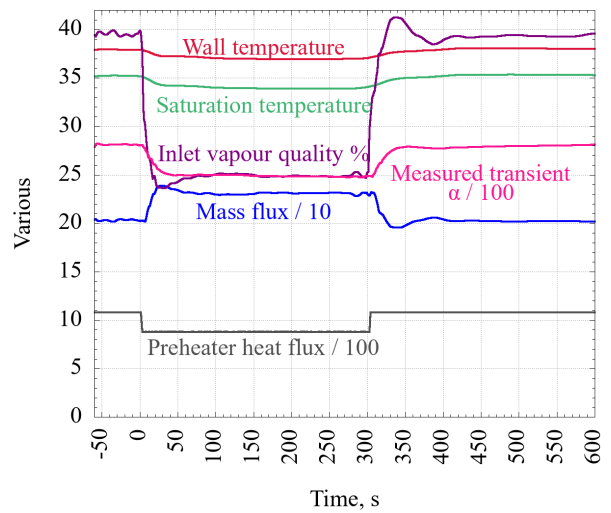
(c) $x_{in} = 0.25$



(d) $x_{in} = 0.30$

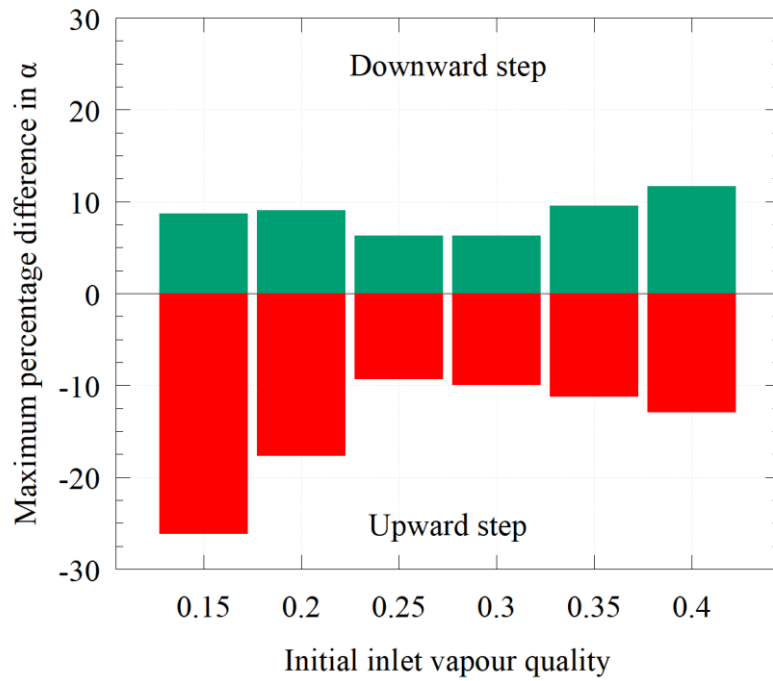


(e) $x_{in} = 0.35$

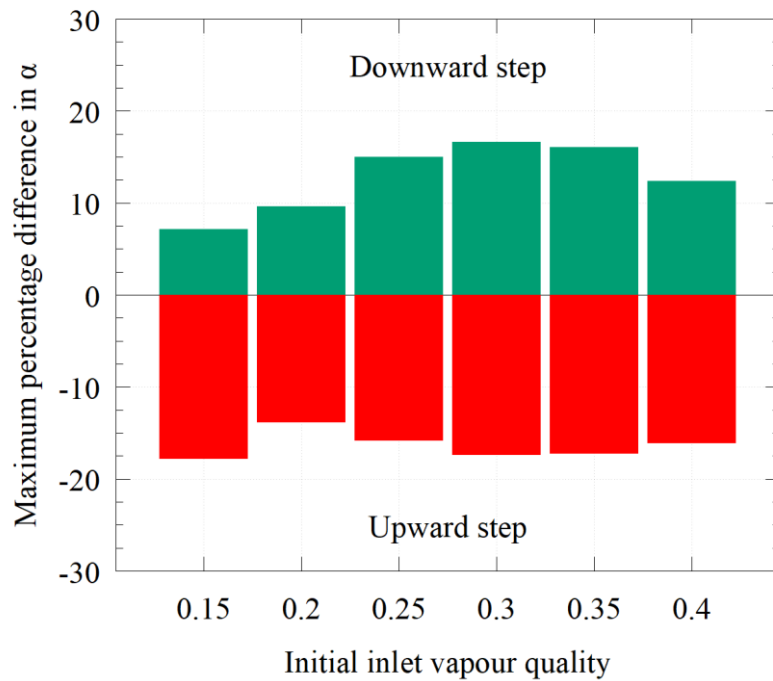


(f) $x_{in} = 0.40$

Figure 7.6. Overview of all results obtained for a mass flux of $200 \text{ kg/m}^2\text{s}$, exhibiting qualitative similarity



(a) 200 kg/m²s



(b) 300 kg/m²s

Figure 7.7. Maximum percentage difference between the transient and interpolated steady-state HTC during downward and upward step changes in inlet vapour quality for an initial mass flux of: (a) 200 kg/m²s, and (b) 300 kg/m²s

This study has implications for the design of evaporators that are subject to strong temporal variations in inlet and/or boundary conditions including, in particular, industrial CSP systems based

on DSG technology, since even a slight perturbation in DNI, and thus vapour quality, can be expected, depending on the design of the system, to have an effect on the system as a whole. While the initial HTC during a downward step in vapour quality would be higher than the quasi-steady-state values, during the inevitable upward step the HTC would be much lower than the predicted value resulting in reduced performance of the CSP facility. The design of any parabolic trough CSP DSG system will have to take these factors into account. As seen in this study, a minor perturbation in the vapour quality has a pronounced effect on the HTC.

7.4. SUMMARY

Long term cloud cover, or the rising or setting of the sun, has a definite effect on the vapour quality in the solar collector field. This change in vapour quality necessarily affects the flow pattern present, and the behaviour of the HTC. In this chapter, a detailed discussion was shown for one such case, the qualitative similarity of all cases considered was shown, as was the deviation from predicted steady-state HTCs.

PART IV

TRANSIENT HEAT FLUX PERTURBANCE

“To measure is to know.”

–Lord Kelvin

8. HEAT FLUX PERTURBANCE INVESTIGATION

METHODOLOGY

8.1. INTRODUCTION

One of the burning questions in the design of concentrated solar power systems is how the facility reacts with the slightest perturbation in the DNI, and thus the heat flux. This is a persistent problem encountered in many practical situations, since there are few places in the world that allow consistent sunshine on cloudless days. Inevitably, at some point, clouds will cover the sun, and that will affect the plant. The HTC and pressure drop could be unduly affected by such a relatively minor disturbance.

Often, on a cloudy day, one can see a patchwork of shadows moving across the ground. The effect this has on the DNI is illustrated in Figure 8.1. In this figure, the DNI data shown (measured by a Kipp and Zonen CHP1 pyrliometer, with a maximum uncertainty of 2% of the current reading, and logged at intervals of 60 s) was obtained from a weather station located at the University of Pretoria in South Africa (25.7545° S, 28.2314° E, elevation 1 339 m). A typical cloudy and windy day on 26 August 2017 was selected at random. The recorded DNI data from 06:00 in the morning to 18:00 in the evening is presented in Figure 8.1a. A detailed 30-min window during mid-morning between 10:30 am and 11:00 am, is shown in Figure 8.1b, along with the measurement accuracy of each data point. Even though the rate of the decrease in DNI depended on aspects such as cloud density and wind speeds, some insights were obtained from the weather station data.

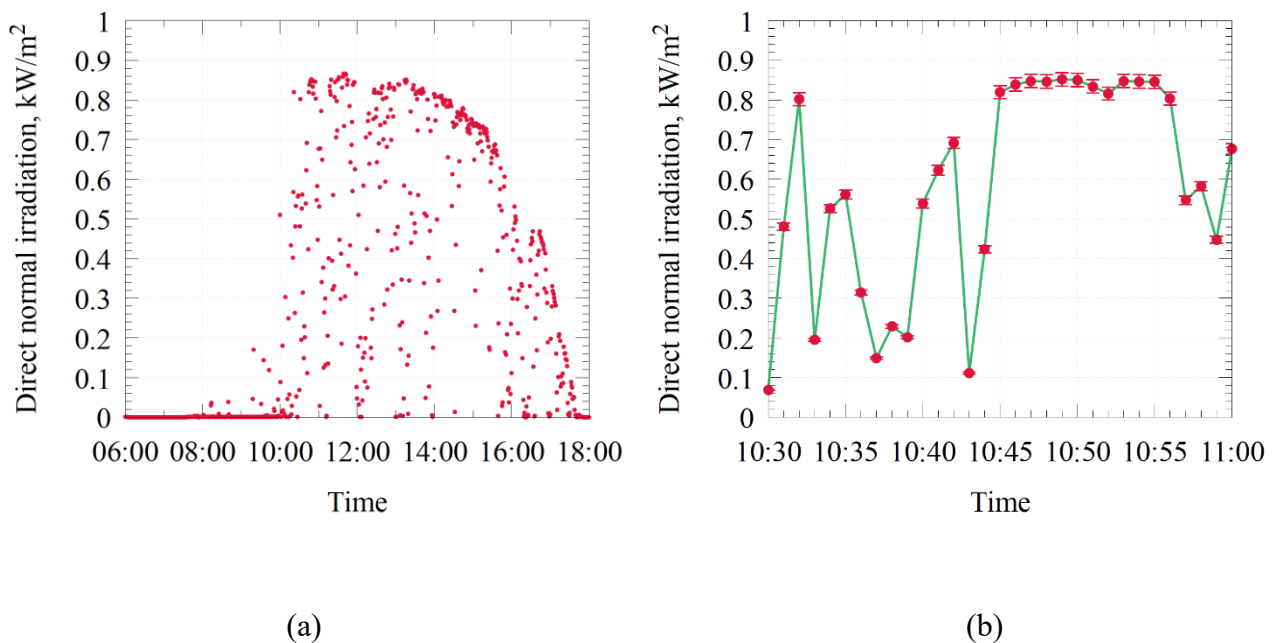


Figure 8.1. Direct normal irradiation (DNI) measured on 26 August 2017 for: (a) all sunlit daytime hours, and (b) a 30-min view from 10:30 am to 11:00 am.

Figure 8.1b indicates that the DNI varied significantly from a high of approximately 0.8 kW/m^2 at 10:32 to a low of 0.2 kW/m^2 at 10:33, which represented a DNI reduction of 75%. The recorded wind speed was approximately 20 km/h. Coupled with the cloud-cover, this scatter is understandable. Unfortunately, the temporal resolution of the recording instrumentation was not high enough to capture the actual DNI on a sub-minute scale, but based on the minute scale data, it is clear that within a one-minute time interval, large perturbances in the DNI were present.

This chapter focuses on quantifying the tests that would be performed and the procedure used to enable testing of this phenomenon. Next, it covers the test matrix that was used and the additional data processing required.

8.2. EXPERIMENTAL PROCEDURE

In order to represent a hypothetical set of sub-minute scale behaviours, three DNI perturbation time profile types were proposed for this research. These are indicated in Figure 8.2 and include a step pulse (indicated in blue), a triangular ramp-down and ramp-up pulse (indicated in pink) and a sinusoidal reduction and recovery pulse (indicated in teal).

In all of these profiles, a temporal reduction of 75% of the concentrated DNI was considered, and was based on the measured DNI reductions mentioned previously. A time length of 30 s was selected because it reflected the timescale of the drastic changes presented in Figure 8.1b. The three shapes of the perturbances were chosen to vary between extremely rapid cloud coverage (the step perturbation) and a more moderate, constant rate of cloud coverage (the triangular perturbation). The sinusoid was chosen to represent winds driving clouds that can affect the incident sunlight. These shapes also corresponded to the observed shapes in Figure 8.1b. The indicated numbers (1 to 4) in Figure 8.2 signify the time instance points at the start, middle and end of the perturbation pulses, as well as a restored steady state after the perturbation. These instances are referred to in Chapter 9.

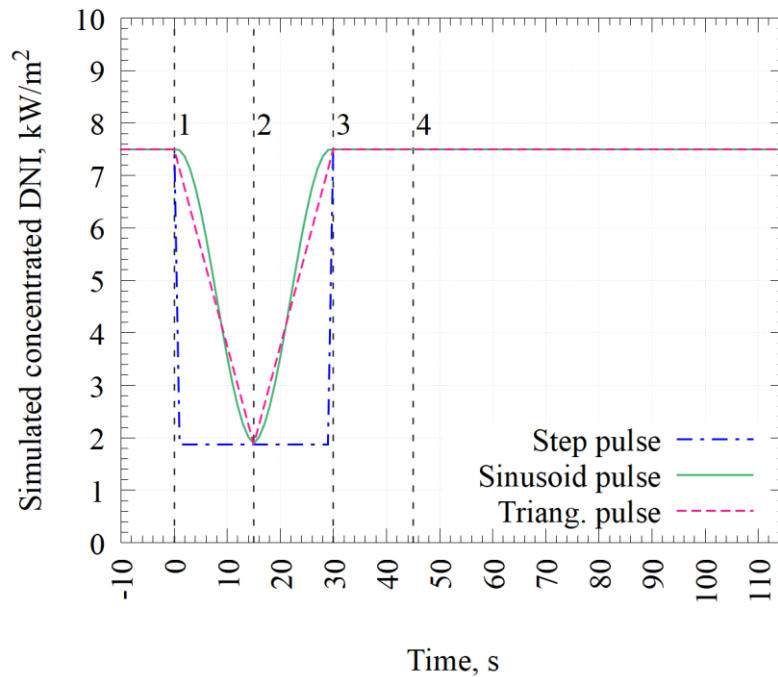


Figure 8.2. Applied perturbation time profiles under consideration

With the magnitude, profiles, and period of the perturbances that would be applied fixed, the experimental procedure is detailed next. First, steady state would be achieved, as described in Section 4.2. Once this was done, a LabView script was activated, in which the steady state would be maintained for a further 10 s before initiating a perturbation profile. The chosen profile was one of the three profiles in Figure 8.2, with a period of 30 s. The power required of the test section power supply unit (which was calculated by LabView) was communicated to the virtual instrumentation with a frequency of 2 Hz, which was limited by the system architecture. Data samples were also captured at approximately 2 Hz to match this.

8.3. TEST MATRIX

In pursuit of uniformity with the rest of this work, a mass flux of $200 \text{ kg/m}^2\text{s}$, heat flux of 7.5 kW/m^2 , and a saturation temperature of $35 \text{ }^\circ\text{C}$ was chosen as baseline for this study. The inlet thermodynamic state to the test section was primarily selected to cover some commonly expected flow patterns. Figure 8.3 shows the selected set points on a Wojtan-Ursenbacher-Thome [42] flow pattern map constructed based on the selected mass flux, heat flux and saturation temperature. Tests were conducted at 16 different inlet vapour quality conditions (x_{in}) ranging from 0.1 to 0.85 at intervals of 0.05. The figure indicates that the majority of test conditions were anticipated to fall within the annular flow pattern region, with the rest being slug or intermittent flow. The prevalence of these flow patterns was visually confirmed via the high-speed camera, as shown later in Figure 8.4.

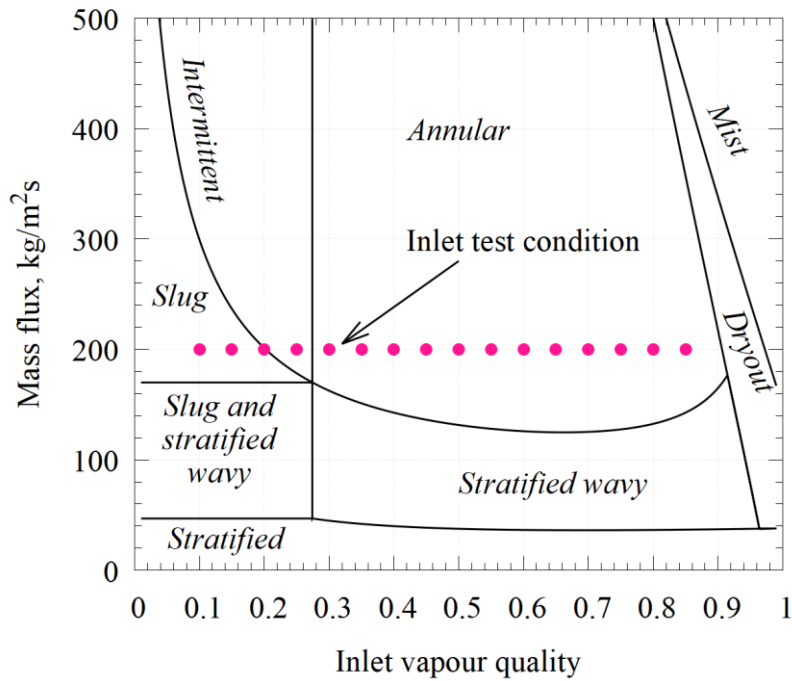


Figure 8.3. Inlet test conditions plotted on a Wojtan-Ursenbacher-Thome [42] flow pattern map, constructed specifically for a mass flux of 200 kg/m²s, heat flux of 7.5 kW/m², and saturation temperature of 35 °C

It is important to note that even though the inlet vapour quality was held constant during each experiment, the variation of the applied heat flux had an influence on the average vapour quality in the test section. At steady-state conditions, the vapour quality increased by approximately 0.08 from the inlet to the outlet of the heated length, as noted in Table 4.1. All inlet conditions were investigated for each of the previously-mentioned perturbation cases (Figure 8.2), while the behaviour under steady-state conditions was used as the reference datum condition.

In order to confirm the presence of the flow patterns indicated in Figure 8.3, a high-speed camera at the inlet sight glass (Figure 3.1) was utilised. Recordings of all the vapour qualities in the test matrix were captured at 2 000 frames per second at a resolution of 1 280 by 720 pixels at the inlet sight glass. Screenshots of the recordings for specific vapour qualities of interest are shown in Figure 6. The vapour qualities of 0.15 (Figure 8.4a), 0.25 (Figure 8.4b), and 0.30 (Figure 8.4c) were chosen since they straddle the transition lines in Figure 8.3 at a mass flux of 200 kg/m²s, while the vapour qualities of 0.45 and 0.85 (Figure 8.4d and Figure 8.4e) were used to confirm annular behaviour.

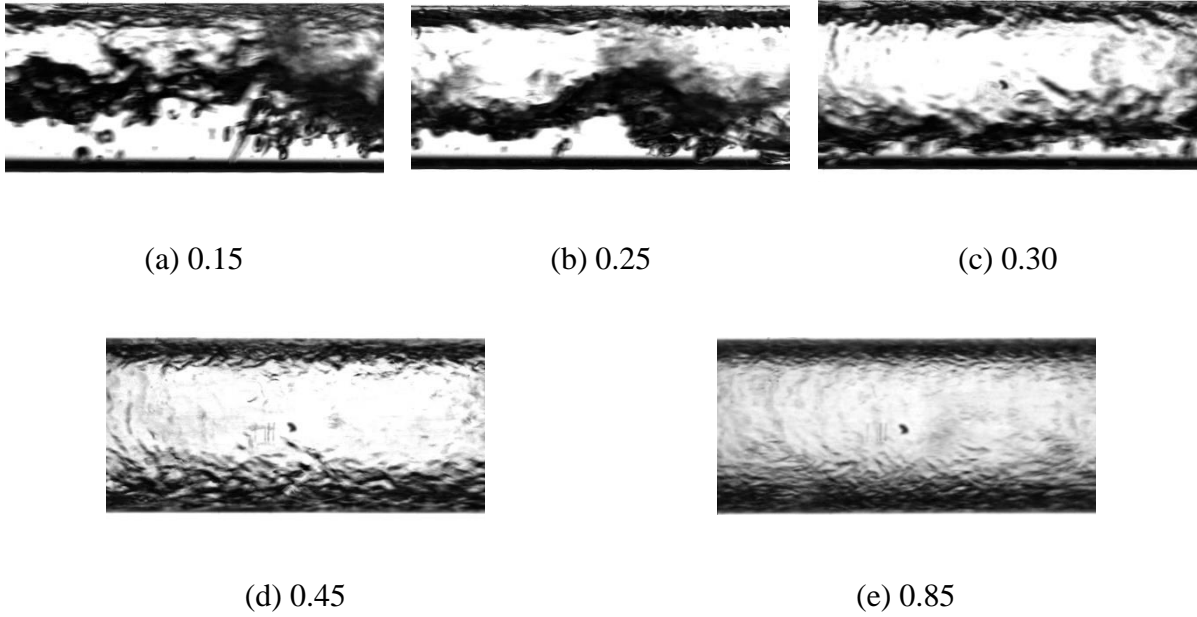


Figure 8.4. Flow patterns observed at an inlet vapour quality of (a) 0.15, (b) 0.25, (c) 0.30, (d) 0.45, and (e) 0.85

According to Figure 8.3, a vapour quality of 0.15 should show a slug flow pattern. The observed flow pattern alternated between intermittent and slug flow however, which should only happen at a vapour quality of 0.20. This indicates that the flow pattern map transition between slug and intermittent flow possibly needs adjustment. A vapour quality of 0.25 showed the intermittent flow pattern, agreeing with the flow pattern map. The annular flow pattern was visible for vapour qualities 0.30 and up, confirming the accuracy of the flow pattern map. The flow patterns for the majority of vapour qualities tested (0.30 to 0.85) were thus of the form most often encountered in industrial systems (that of annular) and the flow pattern map was deemed sufficiently accurate.

8.4. DATA PROCESSING

When a transient heat flux is applied, it would be correct to state the HTC as a function of time, as in Equation (6.3):

$$\bar{\alpha}(t) = \frac{\dot{q}_i(t)}{(\bar{T}_{i,\text{wall}}(t) - \bar{T}_{\text{fluid}}(t))} \quad (8.1)$$

This would enable the determination of the HTC at a certain time t . The problem encountered in Section 6.4, that of the instantaneous (and unrealistic) abrupt change in vapour quality when a step was introduced would now manifest itself in the test section HTC. If the heat flux was changed drastically over a short time, the HTC, by Equation (8.1), would mirror this behaviour. An important realisation has to be made that the heat flux in the wound wire around the pipe in Figure 3.6 first has

to pass through the copper pipe wall before it can reach the fluid, meaning that the copper pipe wall temperature (which does not instantaneously change) has to be taken into consideration as well.

The inner-surface heat flux was calculated from an unsteady energy equation, as follows:

$$\dot{q}_i(t) = \frac{\dot{Q}_i}{A_s} \quad (8.2)$$

Here, $A_s = \pi d_i L_h$ is the inner-wall surface area based on the inner pipe diameter and the heated length, and \dot{Q}_i is the inner wall heat transfer rate from the copper to the fluid. This heat transfer rate was determined by applying an energy balance for the copper wall and the heating element material:

$$\frac{dE}{dt} \approx \frac{dE_{Cu}}{dt} = \dot{Q}_{test} - \dot{Q}_i - \dot{Q}_o \quad (8.3)$$

Here, $\frac{dE}{dt}$ is the rate of change of the internal energy which was approximated to be dominated by the copper pipe wall internal energy (E_{Cu}). \dot{Q}_{test} is the electric heating power which was being applied at a specific instance by LabView, and \dot{Q}_o is the outer heat transfer rate from the heating wire through the insulation, which was assumed to be negligible ($\dot{Q}_o \approx 0$). Under steady state conditions $\frac{dE}{dt} = 0$, which reduces the above equation to $\dot{Q}_i = \dot{Q}_{test}$.

The change in internal energy in the copper wall was expressed as follows:

$$\dot{Q}_{Cu}(t) = m_{Cu} c_p \frac{dT_{Cu}(t)}{dt} \quad (8.4)$$

where m_{Cu} is the mass of the pipe, determined by multiplying the density of copper with the volume of copper in the test section, c_p is the specific heat capacity of the pipe wall material, and T_{Cu} represents the average wall temperature which was obtained by considering $T_{Cu} = T_{o,wall}$.

This implicit assumption that the wall temperature of the copper pipe was approximately uniform in the radial direction at a certain time-step was made after calculating the Biot number for the test section (as in Section 6.4 for the preheater) defined as:

$$Bi_{test} = \frac{\alpha_{test} L_{c,test}}{k_{Cu}} \quad (8.5)$$

It is important to note that this Biot number applies to the test section itself, and not the preheater as previously. The characteristic length for the test section is defined as:

$$L_{c,test} = \frac{V_{test}}{A_{s,test}} \quad (8.6)$$

Here, $V_{\text{test}} = V_{\text{Cu}} = \frac{\pi}{4}(d_{\text{o,test}}^2 - d_{\text{i,test}}^2)L_{\text{test}}$ is the volume of the copper preheater pipe and $A_{\text{s,test}} = \pi d_{\text{i,test}}L_{\text{test}}$ is the heat transfer surface area of the test section.

It was observed that the Biot number in these tests was an order of magnitude smaller than 0.1 in the worst case considered, indicating that there would be an undetectable instantaneous difference between the outer-wall (measured), inner-wall, and average wall temperatures, i.e., $T_{\text{Cu}}(t) = T_{\text{i,wall}}(t) = T_{\text{o,wall}}(t)$. Furthermore, in Equation (8.4), the temperature gradient was obtained from the sampled outer-wall temperature data taken with a sampling interval of $\Delta t \approx 0.5$ s. This differs from the way the temperature had to be predicted in Section 6.4 in order to account for the energy storage of the copper.

This assumption that there would be a negligible difference between the inner and outer wall temperature was borne out by the inner wall temperature calculated previously (as in Equation (4.8)), which accounted for the thermal resistance of the copper pipe.

The effect a short duration perturbation would have on the pressure drop was also of concern. The total pressure difference (Δp_{total}) was obtained from the differential pressure transducer. This difference could be separated into the contributions of the static pressure difference (Δp_{static}), the momentum pressure difference (Δp_{mom}), and the frictional pressure drop (Δp_{frict}) as:

$$\Delta p_{\text{total}} = \Delta p_{\text{static}} + \Delta p_{\text{mom}} + \Delta p_{\text{frict}} \quad (8.7)$$

Because the test section was horizontal, the static pressure difference (elevation head) was disregarded. The frictional pressure drop is predicted by many correlations, so Δp_{frict} had to be isolated in Equation (8.7). Since the heated length, L_{h} , was also the length between the pressure ports on the test section, the frictional pressure drop gradient was calculated as follows:

$$\frac{\Delta p_{\text{frict}}}{L_{\text{h}}} = \frac{\Delta p_{\text{total}} - \Delta p_{\text{mom}}}{L_{\text{h}}} \quad (8.8)$$

The momentum pressure drop was calculated using the following equation [43]:

$$\Delta p_{\text{mom}} = G^2 \left\{ \left[\frac{(1 - x_{\text{out}})^2}{\rho_{\text{f}}(1 - \varepsilon_{\text{out}})} + \frac{x_{\text{out}}^2}{\rho_{\text{g}}\varepsilon_{\text{out}}} \right] - \left[\frac{(1 - x_{\text{in}})^2}{\rho_{\text{f}}(1 - \varepsilon_{\text{in}})} + \frac{x_{\text{in}}^2}{\rho_{\text{g}}\varepsilon_{\text{in}}} \right] \right\} \quad (8.9)$$

in which G is the mass flux of the refrigerant through the test section, ρ_{f} and ρ_{g} are the densities of the saturated liquid and vapour respectively, and ε_{out} and ε_{in} refer to the void fraction at the outlet and inlet to the test section. The void fraction was calculated using the Steiner [109] adaptation for horizontal tubes of the Rouhani-Axelsson [111] drift flux model:

$$\varepsilon = \frac{x}{\rho_g} \left\{ [1 + 0.12(1 - x)] \left(\frac{x}{\rho_g} + \frac{1 - x}{\rho_f} \right) + \frac{1.18}{G} \left[\frac{g\sigma(\rho_f - \rho_g)}{\rho_f^2} \right]^{0.25} (1 - x) \right\}^{-1} \quad (8.10)$$

in which σ refers to the surface tension of the fluid and x refers to the relevant local vapour quality (inlet or outlet). The frictional pressure drop could thus be calculated from the measured value.

8.5. SUMMARY

Justification for the experimental conditions and the experimental procedure was given in this chapter. A test matrix, informed by actual DNI data, was presented, before the additional data processing above and beyond the steady-state procedures described in Section 4.2 was detailed. This data processing included the necessary methods in order to gauge the effect a transient heat flux would have on the HTC as well as pressure drop.

9. HEAT FLUX PERTURBANCE RESULTS

9.1. INTRODUCTION

The groundwork having been laid for tests concerning the effect a transient heat flux would have on the HTC, attention could now be turned to addressing this issue. As before, this chapter is concerned with providing a detailed discussion of an arbitrary case in terms of HTC, before showing qualitative similarity between all cases tested. Finally, the pressure measurement results are considered for the arbitrary and general cases. The conclusions reached in this study are given in Chapter 10.

9.2. EXAMPLE CASE

As in Section 7.2, examination of the data gathered indicated that the results were qualitatively similar. The same form of presentation is thus followed, with an arbitrary general case being considered in detail, before attention is turned to the general case.

Consider Figure 9.1 for an inlet vapour quality of 0.30. The response for all three perturbation types (step, sinusoidal and triangular) is included and indicated by the blue, teal and pink lines, respectively. The instantaneous inner-wall heat flux (Equation (8.2)) is plotted in Figure 9.1a, while the response of the measured wall and saturation temperatures is given in Figure 9.1b. The spatially-averaged HTCs are shown in Figure 9.1c. The mean HTC shown is the instantaneous value obtained using Equation (8.1). The timescale covered is 90 s, starting 10 s before the introduction of the perturbation, including the 30 s span of the perturbation, and running until 50 s after the perturbation was completed. The cause for the jagged appearance of the heat flux is the sampling rate at which the power supply interfaces responded to commands from the controlling software, as discussed in Section 8.2.

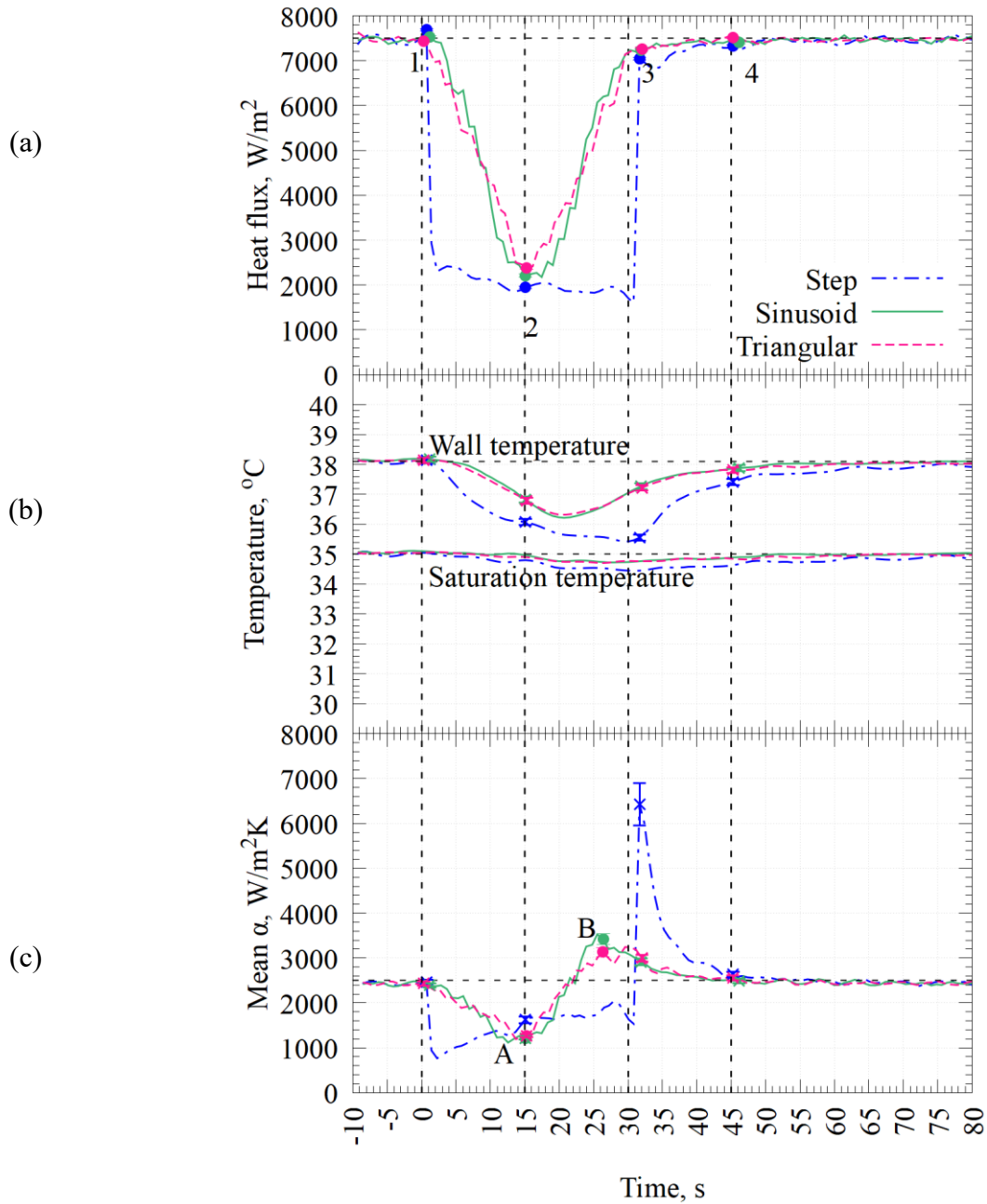


Figure 9.1. (a) Step, sinusoidal and triangular heat flux perturbations, and response of (b) wall and saturation temperatures, and (c) mean HTC for a vapour quality of 0.30, mass flux of 200 kg/m²s, and initial heat flux of 7.5 kW/m²

For ease of discussion, the four instance points indicated in Figure 8.2 are also highlighted in Figure 9.1. As mentioned, these points represent the moments immediately before the perturbation at time 0 s (1), midway through the perturbation at time 15 s (2), the end of the perturbation at time 30 s (3), and long after the perturbation pulse to represent a return to steady state at time 45 s (4). The uncertainties for the temperatures and HTC are also shown at these points for illustrative purposes.

During the step perturbation (the blue line in Figure 9.1), the discharge from the copper pipe is most visible, as can be judged by the steady downward gradient in the instantaneous inner-surface heat flux between Points 1 and 3. During this time, the copper discharged approximately 70% of its available thermal energy to the fluid. The rate at which this discharge occurred decreased as the wall temperature approached the R-245fa saturation temperature. The initiation of the single-step perturbation at Point 1 (at time reference 0 s) almost immediately had an effect on the HTC. The coefficient dropped from the initial steady-state value of approximately 2 400 W/m²K to a value of approximately 800 W/m²K (33% of its initial value), and recovered to a pseudo-steady-state value of approximately 1 900 W/m²K (80% of its initial value) in the first 25 s of the perturbation, before the upward step occurred. Almost immediately after the upward step occurred, the HTC spiked to a value of approximately 6 400 W/m²K (166% higher than the initial value) before settling back to its pre-perturbation value of 2 400 W/m²K at Point 4. It is important to note that the HTC did not mirror the applied heat flux during the time span of the heat flux perturbation. This is clear from the mentioned relative percentage increases or decreases in the HTC, which do not align with the relative reduction and increase in the inner-wall heat flux. Of interest to note is that due to the thermal wall storage effect, the heat flux did not immediately return to its unperturbed level of 7.5 kW/m² at Point 3, but rather took approximately ten seconds to do so.

Next, the sinusoidal and triangular perturbations (teal and pink lines in Figure 9.1) are considered. Based on the actual inner-wall heat flux profiles, these two perturbations are almost indistinguishable, meaning the resulting temperature measurements and calculated HTC will largely be the same. Therefore, the general trends of both perturbation types are discussed together. Also included in Figure 9.1c are Points A and B, which denote the time during these perturbations when the HTC exhibited a local minimum and maximum respectively. For the example case presented in Figure 9.1 with an inlet vapour quality of 0.30, the minimum and maximum HTC occurred at approximately 14 s and 26 s after the initiation of the perturbation. While Point A almost coincided with Point 2 (when the applied heat flux was at its lowest), Point B occurred before the maximum heat flux was at its highest (i.e., before Point 3).

Once again, the HTC did not mirror the applied heat flux. The HTC reached a local minimum of approximately 1 200 W/m²K (50% of the initial value) at Point A, even though the inner-wall heat flux was at its minimum at that point (75% lower than the unperturbed value). However, at Point B, the HTC reached a maximum of 3 400 W/m²K (42% higher than its initial value), while the inner-wall heat flux was still recovering and was at 80% of its initial value. Once the perturbation was complete, the HTC again returned to the unperturbed level at Point 4.

Figure 9.2 offers a different perspective on the obtained results and can be used to better visualise the influence of the heat flux on the HTC. The instantaneous HTC is plotted against the instantaneous inner-wall heat flux for each of the perturbation profiles. For reference, the same time instance points (1 to 4), as well as Points A and B in Figure 9.1c, are included. For reference, the uncertainty is also shown for these points, being most visible at Point 3 of the step perturbation.

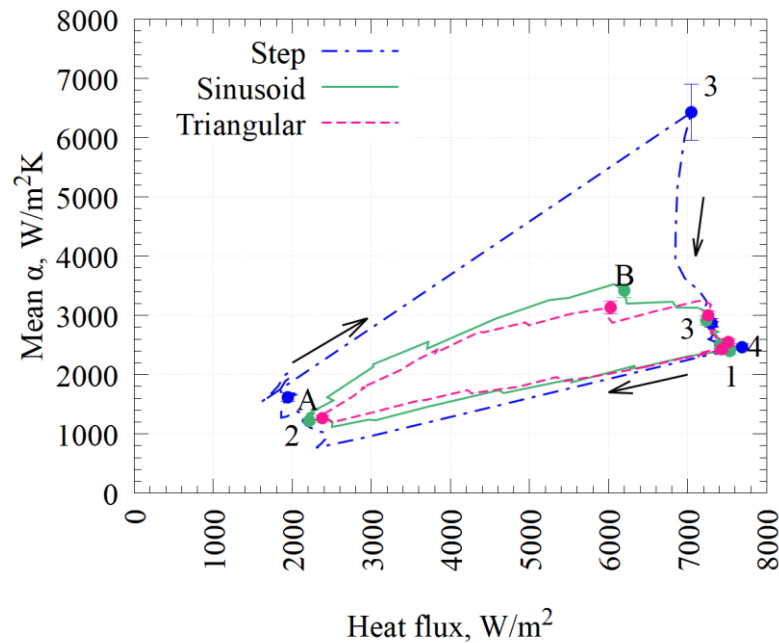


Figure 9.2. HTC as a function of the actual heat flux for step, sinusoidal and triangular heat flux waveforms for a vapour quality of 0.30, mass flux of 200 kg/m²s, and initial heat flux of 7.5 kW/m²

It is evident that for all the perturbation profile cases, significant hysteresis-type effects were present. The average HTC during the first 15 s of the perturbation (Points 1 to 2) was always significantly lower than during the last 15 s (Points 2 to 3) and during the steady-state recovery period (Point 3 to 4), even though the mass flux remained constant. The variation in the HTC was the greatest during the step perturbation profile (blue line). The average HTC from Points 1 to 2 was 1 180 W/m²K, while for Points 2 to 3 and 3 to 4, the coefficients were 1 750 and 3 440 W/m²K respectively. For the sinusoidal and triangular perturbation responses, again appearing relatively similar to each other in Figure 9.2 (as was the case in Figure 9.1), the average HTC during Periods 1 to 2, 2 to 3, and 3 to 4 were approximately 1 720, 2 700 and 2 640 W/m²K.

9.3. GENERAL TRENDS

Besides for the inlet vapour quality case of 0.30 considered up to this point, similar trends were observed at the other vapour qualities. This is highlighted by the HTC results included in Figure 9.3 for vapour qualities of 0.15, 0.30, 0.45, and 0.60.

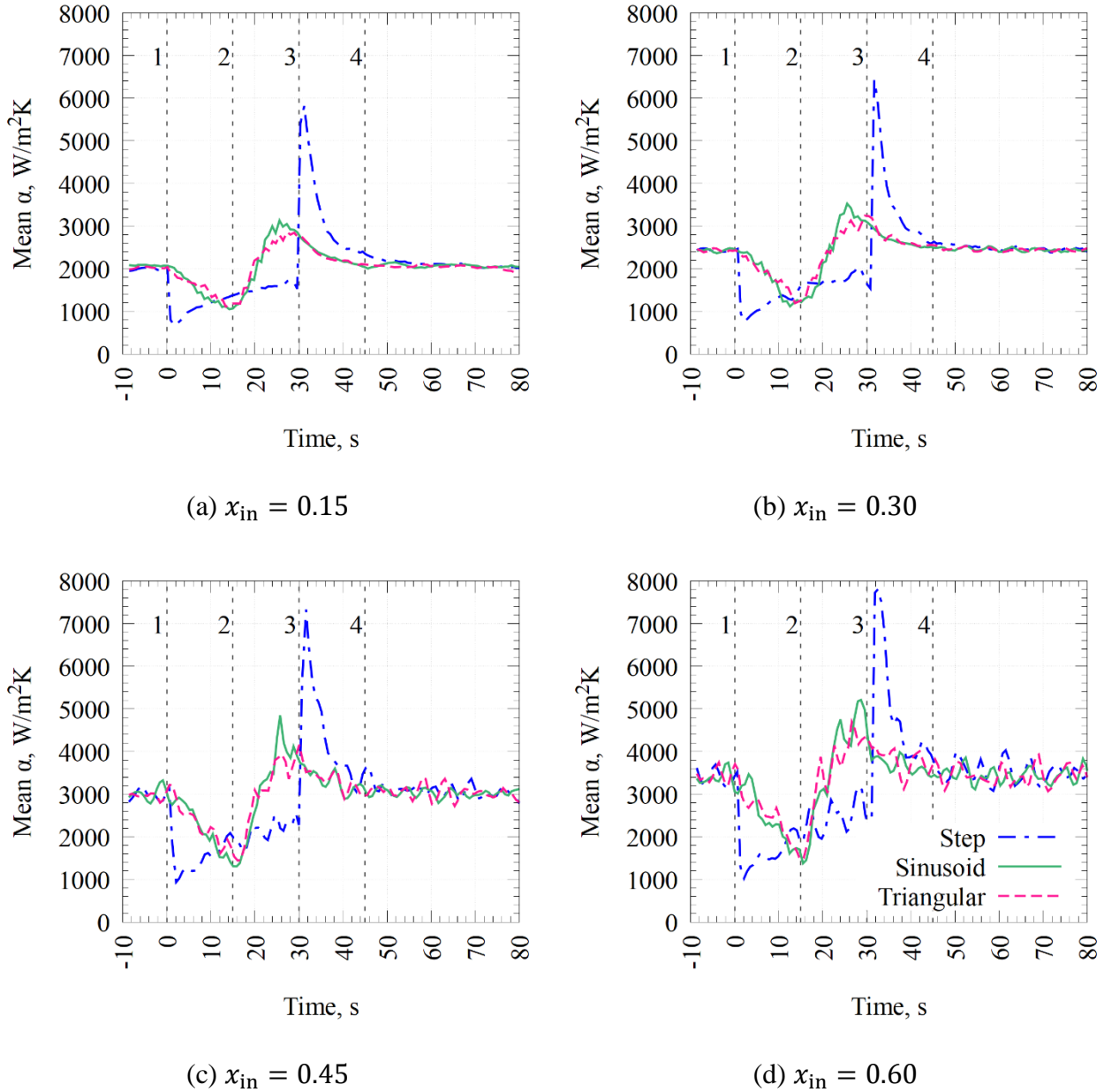


Figure 9.3. The mean HTC obtained for four different vapour qualities, indicating qualitatively similar results

Although it was not possible to see the behaviour of the actual fluid in the test section itself, certain hypotheses can be made to attempt to explain the decrease in HTC. It is accepted that flow boiling consists of two major contributors: that of convective boiling (affected by the mass flux) and that of nucleate boiling (affected by the heat flux and nucleation sites). Because the mass flow rate remained relatively constant (as is shown later) and the heat flux was changed, it is plausible that the

impact of nucleate boiling was the lead cause of the reduction of the HTC. It is possible that the bubble formation (especially for the step perturbation) was curtailed by the decrease, and amplified by the increase. The resolution and frame rate of the outlet sight glass videos was unfortunately too low to capture this behaviour, if it occurred. The outlet sight glass may also have been too far from the heated length, causing any bubbles formed to collapse before being visible.

As mentioned previously, the variation in the heat flux influenced the average vapour quality in the test section during an experiment. Because the HTC was affected by the vapour quality (as is evident in Figure 4.5) it should be pointed out that the variations in the average HTCs (visible in Figure 9.1c and Figure 9.2) cannot be attributed to the change in the average vapour quality in the test section. At the operating mass flux of 200 kg/m²s, the reference-applied heat flux of 7.5 kW/m² (at approximately Points 1 and 4) resulted in a maximum steady-state vapour quality increase ($\Delta x_{\max} = \frac{\dot{Q}_{\text{test,max}}}{h_g - h_f}$) over the test section of 0.08 (or 8%). As the applied heat flux changed, the vapour quality difference over the test section also changed, and at the lowest applied heat flux (such as at approximately Point 2), the equivalent minimum steady-state vapour quality increase (Δx_{\min}) over the test section could be expected to be only 0.02 (or 2%). Thus, even though the inlet vapour quality remained constant during an experiment, the average vapour quality in the test section, $x_{\text{ave}} = \frac{1}{2}(x_{\text{in}} + x_{\text{out}})$, was influenced by the applied heat flux. During any experiment (irrespective of the inlet vapour quality), the variation of the average vapour quality was at most 0.03 (or 3%), determined as follows: $\Delta x_{\text{ave}} = \frac{1}{2}(\Delta x_{\max} - \Delta x_{\min})$.

When considering the impact of x_{ave} on the average HTC in Figure 4.5, it is noted that a change of 0.03 in x_{ave} will result in a change of only ~90 W/m²K in the HTC. This is based on a first-order linear approximation of data in Figure 4.5, which has an average gradient ($\frac{\Delta \alpha}{\Delta x_{\text{ave}}}$) of about 3 100 W/m²K from $x = 0$ to $x = 1$. Therefore, the large variations in the HTC (for example the 1 600 W/m²K drop during the step perturbation) during the time span of a perturbation cannot be explained in terms of the vapour quality.

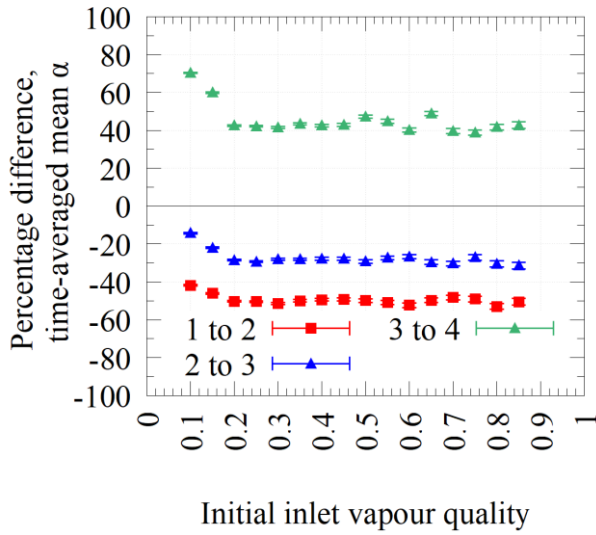
To illustrate this, relevant average HTCs for the Periods 1 to 2, 2 to 3, and 3 to 4, as well as the baseline steady-state condition for all flow test cases are tabulated in Table 9.1 and plotted in Figure 9.4. This is meant to illustrate the percentage difference between a steady, unperturbed HTC and a perturbed average. This average obviously depends on the time between each point, which is 15 s in this case. While this is an extremely coarse way of depicting the effect a perturbation in DNI can have on the HTC, it drives the point home.

Table 9.1. Summary of HTC data for all tested inlet vapour qualities and perturbations

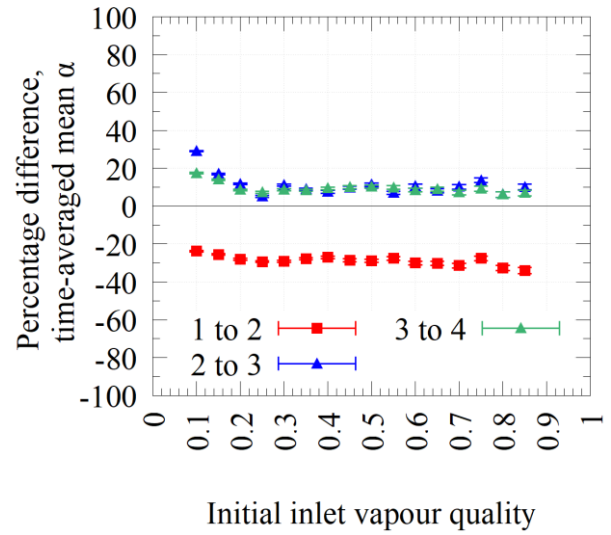
x_{in}	Steady-state HTC (W/m ² K)	Average HTC (W/m ² K)								
		Point 1 to 2			Point 2 to 3			Point 3 to 4		
		Step	Sin.	Triang.	Step	Sin.	Triang.	Step	Sin.	Triang.
0.10	1 890	1 100	1 440	1 480	1 620	2 440	2 320	3 220	2 220	2 160
0.15	2 000	1 080	1 490	1 540	1 560	2 340	2 270	3 200	2 280	2 230
0.20	2 210	1 100	1 590	1 640	1 580	2 470	2 400	3 150	2 400	2 380
0.25	2 320	1 150	1 640	1 690	1 640	2 440	2 450	3 300	2 490	2 520
0.30	2 430	1 180	1 720	1 770	1 750	2 700	2 640	3 440	2 640	2 650
0.35	2 600	1 300	1 880	1 900	1 870	2 830	2 810	3 730	2 820	2 840
0.40	2 770	1 401	2 020	2 070	2 000	2 980	3 060	3 950	3 030	3 060
0.45	2 980	1 510	2 130	2 270	2 150	3 270	3 230	4 260	3 280	3 270
0.50	3 110	1 560	2 210	2 300	2 200	3 460	3 210	4 580	3 430	3 410
0.55	3 260	1 600	2 360	2 370	2 370	3 490	3 570	4 720	3 580	3 570
0.60	3 400	1 620	2 380	2 350	2 490	3 760	3 680	4 770	3 690	3 770
0.65	3 520	1 770	2 460	2 560	2 480	3 810	3 760	5 240	3 830	3 940
0.70	3 730	1 930	2 560	2 620	2 600	4 110	3 930	5 210	4 000	4 040
0.75	3 810	1 940	2 760	2 820	2 780	4 330	4 340	5 290	4 160	4 150
0.80	4 100	1 930	2 760	2 800	2 850	4 350	4 420	5 810	4 350	4 390
0.85	4 330	2 140	2 860	3 150	2 970	4 770	4 690	6 180	4 630	4 710

In the figure, the difference between the time-averaged HTC for each perturbation and the steady state average HTC is shown as a percentage. They are shown for the time periods discussed before (1 is pre-perturbation, 2 is midway through the perturbation, 3 is at the end of the perturbation, and 4 is 15 s after the perturbation). The step perturbation is shown in Figure 9.4a, the sinusoidal perturbation in Figure 9.4b, and the ramp triangular perturbation in Figure 9.4c.

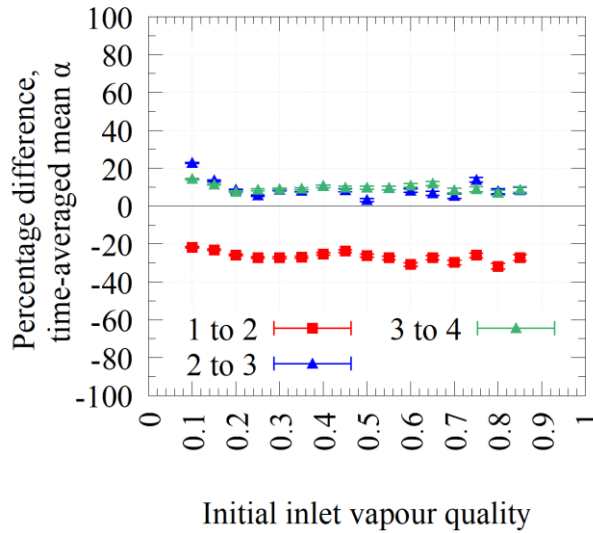
Figure 9.4 indicates that, apart from at the low vapour qualities of 0.10 and 0.15 (where the flow pattern was not yet fully annular), similar behaviour can be observed for all vapour qualities. The average HTC is always less than the steady-state value. This is true even though, during the time period from point 3 to point 4, the measured HTC is higher than the steady-state HTC.



(a) Step perturbation



(b) Sinusoid perturbation



(c) Triangular perturbation

Figure 9.4. Maximum average difference in mean HTC for the different stages of the perturbation compared to the steady-state value for all tested qualities for a mass flux of $200 \text{ kg/m}^2\text{s}$, and an initial heat flux of 7.5 kW/m^2

However, the magnitude of this reduction in HTC cannot be compared with the 75% reduction in simulated DNI. The HTC was on average 30% lower from points 1 to 3 for the step perturbation in Figure 9.4a than for steady state. For the sinusoidal and triangular perturbations, the HTCs from point 1 to 3 in Figure 9.4b and Figure 9.4c, were also on average 8% lower than for steady state, in spite of the HTC being momentarily higher than the steady-state HTC between Points 2 and 3 (as indicated in Figure 9.1c).

Comparing the triangular perturbation in this study with similar work by Chen *et al.* [64], many similarities are noted, most notably that their HTC also reached a local minimum at approximately the same time as the applied heat flux, but reached a local maximum appreciably higher than for the steady state before the heat flux had returned to its unperturbed level. They also found that vapour quality had a negligible qualitative effect. However, they found that the time-averaged HTC was not appreciably affected by any amplitude or period of perturbation, while in this study that difference was on average 8%.

The step perturbation can be compared with the work by Wang *et al.* [9]. Although they tested the commencement of flow boiling from a vapour quality of 0, many similarities can still be seen. The increase in heat flux (as opposed to the strict decrease in this study) showed the opposite behaviour of what was observed in Figure 9.1c. The sharp decrease and gradual recovery of HTC in Figure 9.1c is mirrored by an increase and recovery in their work.

9.4. PRESSURE MEASUREMENT RESULTS

Finally, the pressure drop was considered for each perturbation, and no significant differences between the perturbation types were found to exist. This is illustrated in Figure 9.5 for a representative example at a vapour quality of 0.30. Uncertainties are again included at the points of interest. As can be seen, the influence of any pulse perturbation is undetectable. In hindsight, this is understandable, since the change in mass flux and vapour quality was not large enough to significantly impact either the friction or momentum pressure drop. The reason for the mass flux changing almost imperceptibly after a perturbation is due to the closed nature of the system and the fact that the volume and density of the fluid changes with the small vapour quality change.

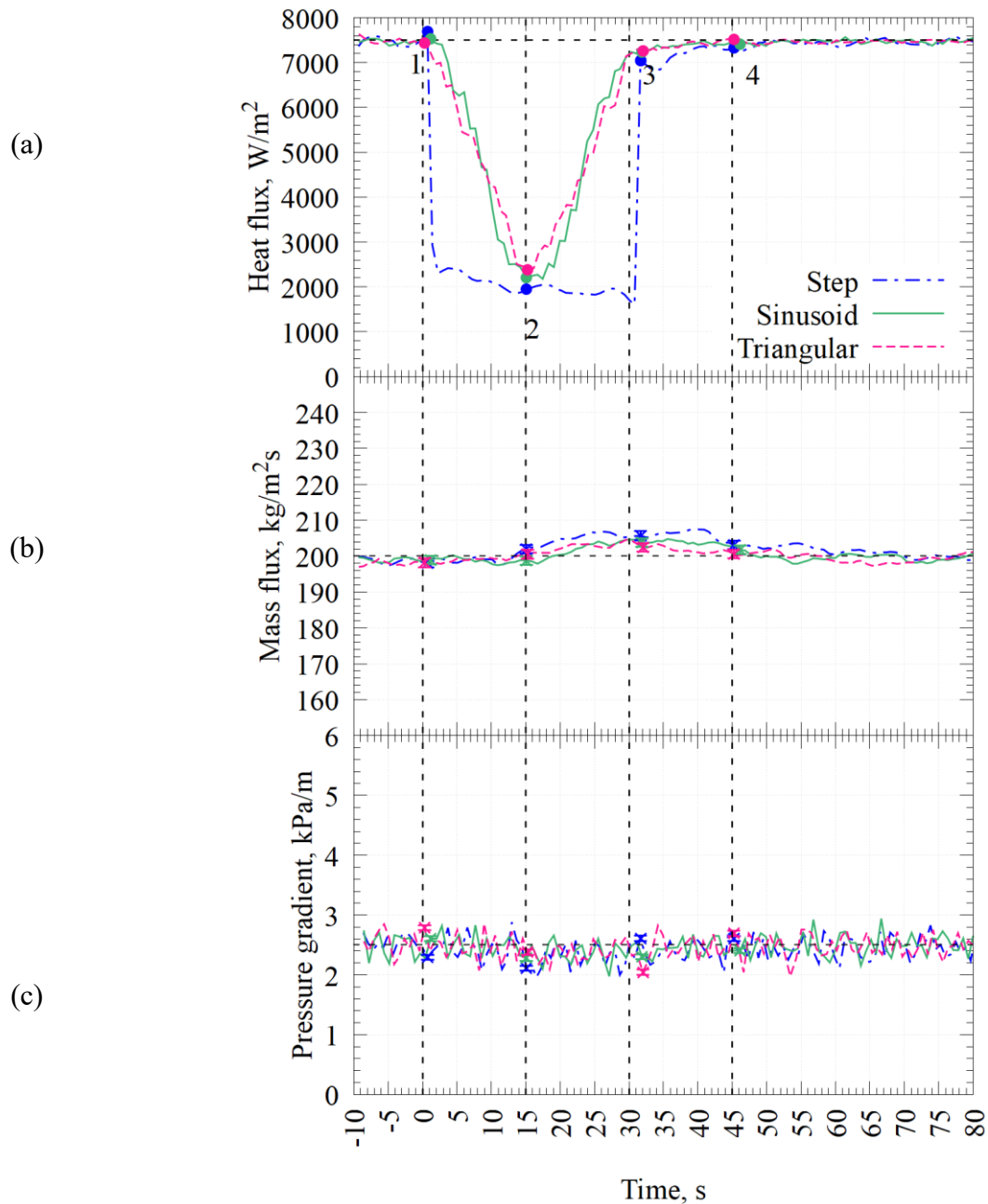


Figure 9.5. (a) Step, sinusoidal and triangular heat flux perturbations, and response of (b) mass flux, and (c) pressure drop gradient for a vapour quality of 0.30, mass flux of $200 \text{ kg/m}^2\text{s}$, and initial heat flux of 7.5 kW/m^2

The frictional pressure drop gradient, as calculated in Equation (8.8), was compared to that predicted by the Müller-Steinhagen and Heck correlation [112] (given in Appendix C) for all vapour qualities considered. This correlation was selected due to its simplicity and robustness. The results are shown in Figure 9.6.

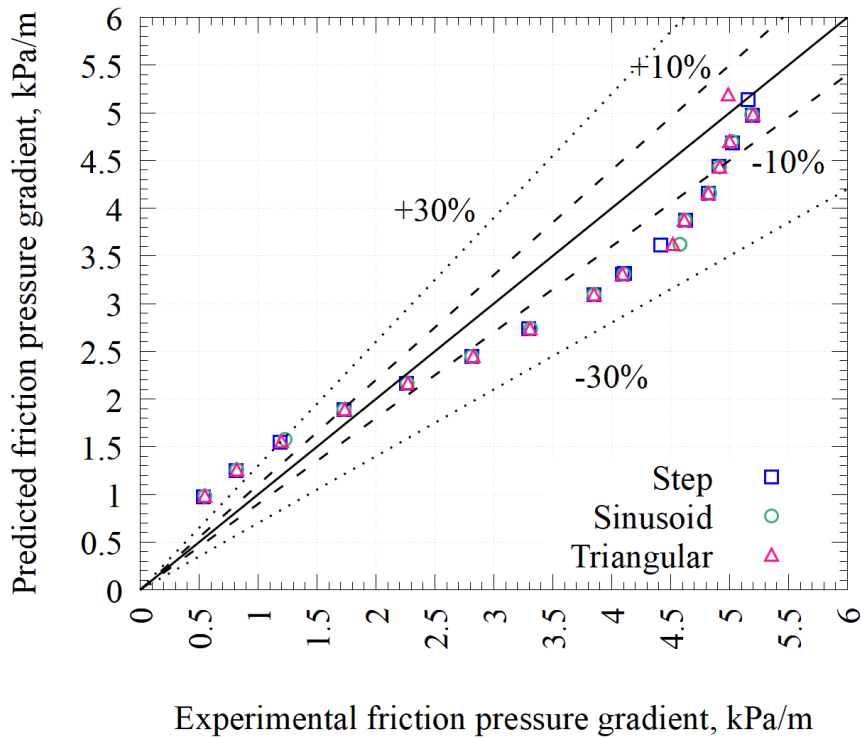


Figure 9.6. Frictional pressure drop predicted by the Müller-Steinhagen and Heck correlation compared to the experimental frictional pressure drop

The predicted frictional pressure drop for all three perturbations are almost identical, indicating that this prediction was unaffected by the perturbation type. The predictions fall within the expected accuracy for the correlation as has been observed by other authors.

9.5. SUMMARY

The impact of a varying DNI, no matter how brief or how small, has an effect on the overall HTC, and may influence the initial phases of economic justification for a CSP project. This chapter showed this effect, containing a detailed discussion of one such case, before providing qualitatively similar results for all tests performed. The effect on pressure drop, shown next was negligible, and was independent of perturbation type.

In practical CSP applications, engineers responsible for the design of the solar collector need to take the prevailing weather conditions into account. If large clouds and windy conditions occur regularly, affecting the DNI (as shown in the step perturbation), the expected HTC can be lower by up to 30%. If the cloud cover is relatively sparse and intermittent, the reduction in HTC will be less, but as shown by the triangular and sinusoidal perturbations, can still be significant.

PART V

CLOSING

“It was a dark road. I have come as I could.”

–*The Silmarillion*, J.R.R. Tolkien

“Ek het die goeie stryd gestry;

ek het die wedloop voleindig;

ek het die geloof behou.”

–2 Timóteüs 4:7

10. CONCLUSIONS AND RECOMMENDATIONS

10.1. INTRODUCTION

The studies performed as part of this thesis led to some important conclusions, encountered difficulties, and posed some interesting questions that, while beyond the scope of this work, show the potential to be investigated in future. This final chapter contains the concluding remarks out of the three preceding parts with recommendations for future work included for each case. It also contains general recommendations to improve the quality of the work done to this point, and highlights further possible future avenues of exploration.

10.2. STEADY-STATE FLOW AT LOW MASS AND HEAT FLUX

Low mass and heat flux applications are becoming more prevalent, as are components and systems that rely on the boiling of refrigerants and specifically of R-245fa, making studies of the in-tube boiling behaviour of such refrigerants and at these conditions increasingly of interest. In particular, there is a growing need to find applicable correlations to predict the HTC in relevant flows. The following observations can be made for the in-tube flow boiling R-245fa at low heat and mass fluxes, which was investigated experimentally in a dedicated facility in this work:

- The mass flux had an influence on the HTC, with an increasing mass flux resulting in a higher HTC, as found by most authors listed in Table 2.1.
- The results corresponding to flows with imposed mass flux values of 40 and 60 kg/m²s and heat flux values of 5.0 and 7.5 kW/m² showed the HTC was weakly dependent on the vapour quality. This agrees with findings from related research [62, 63].
- However, for flows with a higher mass flux of 80 kg/m²s and for vapour qualities above 0.40, the HTC showed a definite increase with increasing vapour quality for all investigated heat fluxes. This was explained in terms of the flow pattern transitioning from a stratified wavy to an annular hybrid/intermittent flow. It was also hypothesised that this was amplified at lower heat fluxes due to the properties of the fluid and the absence of dryout in the pipe.
- For flows with the lowest imposed heat flux of 2.5 kW/m², peculiar behaviour was observed in the local HTCs for vapour qualities between 0.15 and 0.35 at the inlet to the pipe. When compared to extant values found in literature, those obtained for the two higher heat fluxes considered, and those predicted by common correlations, the HTCs were abnormally high. This correlated with direct visual observations which confirmed the intermittent wetting of

the pipe wall by the combined slug and stratified wavy flow patterns. The conditions resulted in the pipe wall staying wet for a larger portion of the test length.

- Well-known correlations were applied in an attempt to capture the peaks in HTC at a mass flux of $80 \text{ kg/m}^2\text{s}$ and a heat flux of 2.5 kW/m^2 .
- The flow pattern-based method was the only correlation that could capture these peaks, although the accuracy was considered unsatisfactory for most design requirements.
- The flow pattern map was not sufficiently accurate to detect the flow pattern shift in the pipe.
- Additional work needs to be done in order to improve the predictive power of such correlations which relies critically upon correctly capturing the flow patterns to account for these peaks.

It is recommended that more studies be conducted at low heat fluxes in order to verify the results of this study and to capture both the inlet and outlet flow pattern for comparison. The amount of contribution of pool-boiling correlations to the overall HTC could also be investigated in the flow-boiling correlations.

10.3. VAPOUR QUALITY PERTURBANCE

As concentrated solar power (CSP) technology becomes increasingly commercially and economically viable, the use of direct steam generation (DSG) with water or organic fluids is emerging as an attractive option that can give rise to higher-efficiency systems. Research is needed to gain a better understanding of the possible effects of intermittent solar radiation, or other conditions, on the operation and performance of the solar field, and by extension on the wider system. Similar challenges exist in other industrial applications involving flow boiling with intermittent inlet or boundary conditions.

This study was conducted on a small scale (laboratory) tube-boiling test facility in order to gain an understanding of the behaviour of the HTC when subjected to transient conditions. The inlet vapour quality to the test section was perturbed by introducing a step change in the preheater heat flux while keeping the rest of the conditions unchanged. Transient tests at conditions spanning two mass fluxes and six initial inlet vapour qualities exhibited similar behaviour, and a detailed transient analysis was conducted for a representative case at a mass flux of $200 \text{ kg/m}^2\text{s}$ and an inlet vapour quality of 0.30.

The HTC did not follow the expected quasi-steady-state predictions during either downward or upward step changes imposed on the inlet vapour quality to the test section in the present work. The

value of the HTC was always higher during the downward step and lower during the upward step than quasi-steady-state expectations, with deviations as high as 20-30% observed in the worst cases which was an order of magnitude greater than the experimental uncertainty involved in this work in the determination of the HTC (2%). The deviation was generally larger during the upward step and at lower vapour qualities, which corresponded to intermittent and slug flow patterns for both investigated mass fluxes. At higher vapour qualities corresponding to annular flow patterns, the deviation was similar in value during both the upward and downward steps.

To extend the work in this study, a number of further investigations could be made. Extension of the test matrix to cover higher vapour qualities would give insight into the annular flow pattern, which could be achieved by utilising higher initial inlet vapour qualities or by implementing step changes of different values to that used in this study. Also, of interest would be an in-depth study of pressure drop over the test section and its corresponding transient behaviour. Better utilisation of the high-speed cameras could capture the effects of crossing flow pattern transition boundaries in more detail, whilst the application of advanced optical measurement techniques such as laser induced fluorescence (LIF) and particle image velocimetry (PIV) would provide insights into the hydrodynamic and thermal interactions in these boiling flows. Such techniques have been used successfully for similar flows at adiabatic conditions [113, 114].

The influence void fraction has on the HTC is also of interest, and needs to be addressed in follow up studies, possibly replacing the vapour quality as primary variable. Local HTCs and void fractions also need to be studied. An optical method [115] or a capacitance-based method [116] will need to be explored to determine the void fraction in order to decouple it from vapour quality-based void fraction equations.

The results obtained in this study are of use in the design and operation of commercial CSP DSG systems for effective and optimised performance across all expected conditions.

10.4. HEAT FLUX PERTURBANCE

The response of two-phase flow boiling to intermittent variations in imposed wall heat flux was presented. It was motivated by a number of practical applications and solar DSG applications in particular where any irradiance variation will result in direct heat flux variations on the internal boiling flows.

In particular, the aim was to simulate the effect of partial sub-minute cloud coverage variations on the DNI, with the values and shapes of the perturbations being informed by actual data.

Experiments were conducted in a laboratory set-up specially built for this purpose. Data gathered from this study will inform future experimental and computational work in this space.

Tests were done over inlet vapour qualities ranging from 0.10 to 0.85, at a mass flux of $200 \text{ kg/m}^2\text{s}$, a base heat flux of 7.5 kW/m^2 , and a saturation temperature of $35 \text{ }^\circ\text{C}$. Simulated DNI profiles were imposed using a single-pulse perturbation of step, sinusoidal and triangular ramp waveforms. The most important conclusions are as follows:

- All vapour qualities considered showed qualitatively similar results.
- During a step perturbation, the applied heat flux was supplemented visibly by the thermal inertia of the copper pipe.
- Importantly, the HTC did not mirror the applied heat flux, as exhibited by the differing percentages of reduction or increase.
- The sinusoidal and triangular waveforms exhibited almost indistinguishable results.
- During the sinusoidal and triangular perturbations, while the applied heat flux was increasing, the HTC reached a local maximum higher than the unperturbed value before the perturbation was complete.
- The total average HTC was significantly lower during all perturbations than the unperturbed value.
- The change in vapour quality over the test section during the perturbation tests did not account for the change in HTC.
- The pressure drop was unaffected by any perturbation.
- The Müller-Steinhagen and Heck correlation provided acceptable pressure drop predictions.

In closing, it should be noted while the gathered HTC data following the conventional definition based on Newton's law of cooling (Equation (8.1)) is useful for practical applications, some questions do arise concerning the usefulness of using this particular definition in unsteady heat transfer problems. For example: Are the extreme values of the HTC when a step change to the heat flux is imposed truly representative of the flow's ability to remove heat from the solid, or just a mathematical artefact due to the formulation of the HTC definition?

In steady-state problems, the conventional HTC definition is a powerful tool in designing thermal systems, but interpreting heat transfer results through the lens of this definition in an unsteady problem has known limitations however. Furthermore, in unsteady problems the simultaneous heat conduction through the solid pipe wall and the convective heat transfer to/from the fluid phase can

lead to so-called ‘conjugate’ heat transfer phenomena in which the solid itself is actively controlling the thermal performance of the system. Alternative definitions of the HTC were presented and discussed, and the possibility of heat transfer augmentation in a fluid exposed to unsteady conjugate heat transfer was investigated by Mathie and Markides [117], and applied by Mathie *et al.* [118] who confirmed (and quantified) this phenomenon experimentally in falling film flows. The complexity concerning the definition, calculation and interpretation (or usefulness) of the HTC that was raised in this work, has also been considered in other studies in the literature. For example, an alternative to using the HTC to predict the wall temperature was also explored by Degiovanni and Remy [119], while the thermal losses associated with conjugate heat transfer in thermal machines were considered by Mathie *et al.* [120]. This research is ongoing, and until a consensus emerges concerning an improved methodology for characterising and quantifying heat transfer in unsteady flows, the HTC as defined by Newton’s law of cooling remains the more common approach used in the literature and in engineering practice. In order to quantify the effect of changing heat flux further, more tests are recommended at different mass fluxes, heat fluxes, and time periods for the perturbations. The results of this study will be useful in the design and sizing of solar collector fields, but are also transferrable to similar applications where flow boiling occurs in the presence of heat flux transients.

10.5. ADDITIONAL RECOMMENDATIONS

Since many of the contributions by this work are novel, it is inevitable that during the course of the tests performed, certain prime areas of research that were not considered in this work would appear. Some of the recognized topics are listed here.

- Perform tests with stainless-steel pipes.

Steel piping is the norm in industrial CSP systems. As was observed in Chapters 7 and 9, the heat capacity of the copper played a significant part. The wall thickness in industry is typically on an order of magnitude higher than the wall thickness in this study. This means that the mass of piping (and thus the heat absorbed) is much higher. Additionally, the difference in temperature measurements on the inner and outer wall of this pipe could prove enlightening.

- Perform tests perturbing the mass flux.

As was seen, it was very difficult to keep all variables constant while only modifying the heat flux. Testing the effect of mass flux on the HTC would enable accounting for the change in this flux more accurately.

- Modify the test section to be more representative of actual CSP parabolic troughs.

As has been noted by Wang *et al.* [67], the number of studies that focus on the actual non-uniform heat flux encountered in industrial CSP systems is limited. As part of the effort to model real life systems, an effort should be made to enable this type of testing.

After the experimental apparatus was commissioned, it was found to provide satisfactory test results. However, certain areas that would refine these results, and general quality of life improvements were recognised. These are listed here.

- Optimise the LabView codebase to overcome the limitations on sampling rate imposed by the power supply interfaces.

One of the major hurdles encountered during the transient tests is that the sampling rate was tied to the power supply interfaces. Incorporating an asynchronous threading system should alleviate this problem.

- Replace the DAQ with a modern 64-bit interface.

Due to funding constraints, the DAQ utilised dated from circa 2004. This model is limited to 32-bit communication, hamstringing efforts to standardise to 64-bit (i.e., the computer hardware was 64-bit, but the software and operating system were limited to 32-bit, introducing support problems).

- Add a subcooler after the pump.

The need for this was recognised during the *in situ* calibration of the test section thermocouples. While the water temperature flowing through the existing condenser could be used to modulate the fluid temperature, it took an exorbitant amount of time to reach a set temperature, owing to the size of the receiver. Adding a subcooler after the pump will enable the temperature and pressure to be more finely and instantaneously controllable.

- Install a water mixing bench to finely control the saturation temperature.

While the three-way valve on the condenser can be used to adjust the water flow rate in the condenser, the temperature of that water is set by the external supply. That is partially why a thermal bath was used to conduct the low mass and heat flux tests. The thermal bath's capacity was much too low to enable higher flux tests. A mixing bench ahead of the condenser (and the aforementioned subcooler) would go a long way to alleviating this problem.

- Instrument the facility more thoroughly.

As seen in Chapter 6, the wall temperature of the preheater was required. It would be a simple tweak to add thermocouples to enable this temperature to be determined exactly, as opposed to relying on the lumped system analysis.

- Replace tube-in-tube condenser with a brazed plate heat exchanger.

While the condenser performed well, its shape made mounting and insulating it problematic. A rectangular brazed plate heat exchanger would simplify things greatly.

- Add a level indicator on the receiver.

While the system was made as leak proof as possible, it is unavoidable that a certain amount of fluid will escape, either by accident, or through long periods of quiescence. A level indicator on the receiver would allow visual confirmation of the amount of fluid still in the system.

10.6. SUMMARY

This final chapter was concerned with tying all the results together into a coherent conclusion for all the seemingly disparate work conducted. First, the steady-state HTC at low mass and heat fluxes was explored, with anomalies being noted at the lowest heat flux of 2.5 kW/m^2 . The reaction of the HTC to a fixed vapour quality perturbation was noted next. The HTC was always higher than the predicted value during a reduction in vapour quality, and always lower during an increase in vapour quality. A direct perturbation on the heat flux was investigated, and it was found that the HTC was affected disproportionately compared to the magnitude of the perturbation. The pressure drop, on the other hand, remained unaffected. The applicability of the traditional HTC in transient studies was also questioned. Some additional recommendations for possible future work were made, and general improvements to the experimental apparatus that would greatly aid this work were also stated.

While this work in its entirety is but a drop in the ocean in freeing future generations from fossil fuels, it is hoped that it contributes in some small way. Perhaps this study will enable more concentrated solar power plants to be built in future, and from such small pebbles an avalanche can occur. It is the fervent hope of the author to leave this world better than it was found, which is perhaps the noblest legacy anyone could wish for.

REFERENCES

1. Zhang, H.L., Baeyens, J., Degève, J., and Cacères, G., *Concentrated solar power plants: Review and design methodology*. Renewable and Sustainable Energy Reviews, 2013. **22**: p. 466-481.
2. Dirker, J., Juggurnath, D., Kaya, A., Osowade, E., Simpson, M., Lecompte, S., Noori Rahim Abadi, S.M.A., Voulgaropoulos, V., Adelaja, A., Dauhoo, M., Khoodaruth, A., Obayopo, S., Olakoyejo, O., Khalil, M., De Paepe, M., Meyer, J., and Markides, C., *Thermal energy processes in direct steam generation solar systems: Boiling, condensation and energy storage – A review*. Frontiers in Energy Research, 2018.
3. Pantaleo, A.M., Camporeale, S.M., Sorrentino, A., Miliozzi, A., Shah, N., and Markides, C.N., *Hybrid solar-biomass combined Brayton/organic Rankine-cycle plants integrated with thermal storage: Techno-economic feasibility in selected Mediterranean areas*. Renewable Energy, 2020. **147**: p. 2913-2931.
4. Markides, C.N., *Low-concentration solar-power systems based on organic Rankine cycles for distributed-scale applications: Overview and further developments*. Frontiers in Energy Research, 2015. **3**(47).
5. Freeman, J., Hellgardt, K., and Markides, C.N., *Working fluid selection and electrical performance optimisation of a domestic solar-ORC combined heat and power system for year-round operation in the UK*. Applied Energy, 2017. **186**: p. 291-303.
6. Freeman, J., Hellgardt, K., and Markides, C.N., *An assessment of solar-powered organic Rankine cycle systems for combined heating and power in UK domestic applications*. Applied Energy, 2015. **138**: p. 605-620.
7. Park, B.-S., Usman, M., Imran, M., and Pesyridis, A., *Review of organic Rankine cycle experimental data trends*. Energy Conversion and Management, 2018. **173**: p. 679-691.
8. Ramos, A., Chatzopoulou, M.A., Freeman, J., and Markides, C.N., *Optimisation of a high-efficiency solar-driven organic Rankine cycle for applications in the built environment*. Applied Energy, 2018. **228**: p. 755-765.
9. Wang, S.L., Chen, C.A., Lin, Y.L., and Lin, T.F., *Transient oscillatory saturated flow boiling heat transfer and associated bubble characteristics of FC-72 over a small heated plate due to heat flux oscillation*. International Journal of Heat and Mass Transfer, 2012. **55**(4): p. 864-873.
10. Chen, C., Chang, W., and Lin, T., *Time periodic flow boiling heat transfer of R-134a and associated bubble characteristics in a narrow annular duct due to flow rate oscillation*. International Journal of Heat and Mass Transfer, 2010. **53**(19): p. 3593-3606.
11. Park, I.W., Ryu, J., Fernandez, M., and Dorao, C.A., *Can flow oscillations during flow boiling deteriorate the heat transfer coefficient?* Applied Physics Letters, 2018. **113**(15): p. 154102.
12. Kærn, M.R., Markussen, W.B., Meyer, K.E., Elmegaard, B., and Palm, B., *Experimental comparison and visualization of in-tube continuous and pulsating flow boiling*. International Journal of Heat and Mass Transfer, 2018. **125**: p. 229-242.
13. Fang, X., Zhuang, F., Chen, C., Wu, Q., Chen, Y., Chen, Y., and He, Y., *Saturated flow boiling heat transfer: review and assessment of prediction methods*. Heat and Mass Transfer, 2019. **55**(1): p. 197-222.
14. Van den Bergh, W.J., Moran, H.R., Dirker, J., Markides, C.N., and Meyer, J.P., *Effect of low heat and mass fluxes on the boiling heat transfer coefficient of R-245fa*. International Journal of Heat and Mass Transfer, 2021. **180**: p. 121743.
15. Dirker, J., Van den Bergh, W.J., Moran, H.R., Markides, C.N., and Meyer, J.P., *Influence of inlet vapour quality perturbations on the transient response of flow-boiling heat transfer*. International Journal of Heat and Mass Transfer, 2021. **170**: p. 121017.

16. Van den Bergh, W.J., Dirker, J., Markides, C.N., and Meyer, J.P., *Influence of non-steady transient heat flux on flow boiling heat transfer and pressure drop in horizontal pipes*. International Journal of Heat and Mass Transfer, 2022. **182**: p. 121927.
17. Müller-Steinhagen, H. and Trieb, F., *Concentrating solar power, - A review of the technology*. Ingénia, 2004. **18**: p. 43-50.
18. Islam, M.T., Huda, N., Abdullah, A.B., and Saidur, R., *A comprehensive review of state-of-the-art concentrating solar power (CSP) technologies: Current status and research trends*. Renewable and Sustainable Energy Reviews, 2018. **91**: p. 987-1018.
19. Bundschuh, J., Kaczmarczyk, M., Ghaffour, N., and Tomaszewska, B., *State-of-the-art of renewable energy sources used in water desalination: Present and future prospects*. Desalination, 2021. **508**: p. 115035.
20. SolarGIS. *Solar resource maps of World*. 2021 [cited 2021 2021/07/03]; Global average DNI]. Available from: <https://solargis.com/maps-and-gis-data/download/world>.
21. Southern African Universities Radiometric Network. *Station GIZ Richtersveld*. [cited 2021 2021/10/25]; Available from: <https://sauran.ac.za/>.
22. Fernández-García, A., Zarza, E., Valenzuela, L., and Pérez, M., *Parabolic-trough solar collectors and their applications*. Renewable and Sustainable Energy Reviews, 2010. **14**(7): p. 1695-1721.
23. F. Shuman, C.V.B., *Sun boiler*, U.S.p. office, Editor. 1917: United States.
24. Pytilinski, J.T., *Solar energy installations for pumping irrigation water*. Solar Energy, 1978. **21**(4): p. 255-262.
25. Kandlikar, S.G. and Grande, W.J., *Evolution of microchannel flow passages: thermohydraulic performance and fabrication technology*. Heat Transfer Engineering, 2003. **24**(1): p. 3-17.
26. Fuqiang, W., Ziming, C., Jianyu, T., Yuan, Y., Yong, S., and Linhua, L., *Progress in concentrated solar power technology with parabolic trough collector system: A comprehensive review*. Renewable and Sustainable Energy Reviews, 2017. **79**: p. 1314-1328.
27. Hirsch, T., Feldhoff, J.F., Hennecke, K., and Pitz-Paal, R., *Advancements in the Field of Direct Steam Generation in Linear Solar Concentrators—A Review*. Heat Transfer Engineering, 2014. **35**(3): p. 258-271.
28. Giglio, A., Lanzini, A., Leone, P., Rodríguez García, M.M., and Zarza Moya, E., *Direct steam generation in parabolic-trough collectors: A review about the technology and a thermo-economic analysis of a hybrid system*. Renewable and Sustainable Energy Reviews, 2017. **74**: p. 453-473.
29. Sandá, A., Moya, S.L., and Valenzuela, L., *Modelling and simulation tools for direct steam generation in parabolic-trough solar collectors: A review*. Renewable and Sustainable Energy Reviews, 2019. **113**: p. 109226.
30. SHIPPlants, A.I. *Solar Thermal Plants Database*. 2018 [cited 2021 2021/08/31]; Available from: http://ship-plants.info/solar-thermal-plants?collector_type=5.
31. Zarza, E., Valenzuela, L., León, J., Hennecke, K., Eck, M., Weyers, H.D., and Eickhoff, M., *Direct steam generation in parabolic troughs: Final results and conclusions of the DISS project*. Energy, 2004. **29**(5): p. 635-644.
32. Zarza, E., Rojas, M.E., González, L., Caballero, J.M., and Rueda, F., *INDITEP: The first pre-commercial DSG solar power plant*. Solar Energy, 2006. **80**(10): p. 1270-1276.
33. Khenissi, A., Krüger, D., Hirsch, T., and Hennecke, K., *Return of experience on transient behavior at the DSG solar thermal Power plant in Kanchanaburi, Thailand*. Energy Procedia, 2015.
34. Zhu, G. and Turchi, C., *Solar Field Optical Characterization at Stillwater Geothermal/Solar Hybrid Plant*. Journal of Solar Energy Engineering, 2017. **139**(3).
35. Odeh, S.D., Behnia, M., and Morrison, G.L., *Hydrodynamic Analysis of Direct Steam Generation Solar Collectors*. Journal of Solar Energy Engineering, 1999. **122**(1): p. 14-22.
36. Feng, Y., Hung, T., Zhang, Y., Li, B., Yang, J., and Shi, Y., *Performance comparison of low-grade ORCs (organic Rankine cycles) using R-245fa, pentane and their mixtures based on the*

- thermoeconomic multi-objective optimization and decision makings*. Energy, 2015. **93**: p. 2018-2029.
37. Ye, Z., Yang, J., Shi, J., and Chen, J., *Thermo-economic and environmental analysis of various low-GWP refrigerants in Organic Rankine cycle system*. Energy, 2020. **199**: p. 117344.
 38. Rayegan, R. and Tao, Y.X., *A procedure to select working fluids for solar organic Rankine cycles (ORCs)*. Renewable Energy, 2011. **36**(2): p. 659-670.
 39. Kattan, N., Thome, J., and Favrat, D., *Flow boiling in horizontal tubes: Part I—Development of a diabatic two-phase flow pattern map*. Journal of Heat Transfer, 1998. **120**(1): p. 140-147.
 40. Baker, O. *Design of Pipelines for the Simultaneous Flow of Oil and Gas*. in *Fall Meeting of the Petroleum Branch of AIME*. 1953.
 41. Taitel, Y. and Dukler, A.E., *A model for predicting flow regime transitions in horizontal and near horizontal gas-liquid flow*. AIChE journal, 1976. **22**(1): p. 47-55.
 42. Wojtan, L., Ursenbacher, T., and Thome, J.R., *Investigation of flow boiling in horizontal tubes: Part I—A new diabatic two-phase flow pattern map*. International Journal of Heat and Mass Transfer, 2005. **48**(14): p. 2955-2969.
 43. Moreno Quibén, J. and Thome, J.R., *Flow pattern based two-phase frictional pressure drop model for horizontal tubes. Part I: Diabatic and adiabatic experimental study*. International Journal of Heat and Fluid Flow, 2007. **28**(5): p. 1049-1059.
 44. Thome, J.R., *Wolverine engineering databook III*. 2006, (web book updated yearly).
 45. Collier, J.G. and Thome, J.R., *Convective boiling and condensation*. 1994: Clarendon Press.
 46. Cengel, Y.A., *Heat and mass transfer : a practical approach : SI units*. 2006, Singapore: McGraw-Hill.
 47. Gnielinski, V., *New equations for heat and mass transfer in turbulent pipe and channel flow*. Int. Chem. Eng., 1976. **16**(2): p. 359-368.
 48. Meyer, J.P., Everts, M., Coetzee, N., Grote, K., and Steyn, M., *Heat transfer coefficients of laminar, transitional, quasi-turbulent and turbulent flow in circular tubes*. International Communications in Heat and Mass Transfer, 2019. **105**: p. 84-106.
 49. Gómez Marzoa, M., Ribatski, G., and Thome, J.R., *Experimental flow boiling heat transfer in a small polyimide channel*. Applied Thermal Engineering, 2016. **103**: p. 1324-1338.
 50. Tibiriçá, C.B. and Ribatski, G., *Flow Boiling Heat Transfer of R-134a and R-245fa in a 2.3 mm Tube*. International Journal of Heat and Mass Transfer, 2010. **53**(11): p. 2459-2468.
 51. Kanizawa, F.T., Tibiriçá, C.B., and Ribatski, G., *Heat transfer during convective boiling inside microchannels*. International Journal of Heat and Mass Transfer, 2016. **93**: p. 566-583.
 52. Da Silva Lima, R.J., Quibén, J.M., and Thome, J.R., *Flow boiling in horizontal smooth tubes: New heat transfer results for R-134a at three saturation temperatures*. Applied Thermal Engineering, 2009. **29**(7): p. 1289-1298.
 53. Dorao, C.A., Fernandez, O.B., and Fernandino, M., *Experimental Study of Horizontal Flow Boiling Heat Transfer of R-134a at a Saturation Temperature of 18.6 °C*. Journal of Heat Transfer, 2017. **139**(11).
 54. Celen, A. and Dalkılıç, A.S., *A complete evaluation method for the experimental data of flow boiling in smooth tubes*. International Communications in Heat and Mass Transfer, 2017. **89**: p. 108-121.
 55. Grauso, S., Mastrullo, R., Mauro, A., Thome, J., and Vanoli, G., *Flow pattern map, heat transfer and pressure drops during evaporation of R-1234ze (E) and R-134a in a horizontal, circular smooth tube: Experiments and assessment of predictive methods*. international journal of refrigeration, 2013. **36**(2): p. 478-491.
 56. Bamorovat Abadi, G., Moon, C., and Kim, K.C., *Effect of gravity vector on flow boiling heat transfer, flow pattern map, and pressure drop of R-245fa refrigerant in mini tubes*. International Journal of Multiphase Flow, 2016. **83**: p. 202-216.

57. Bandarra Filho, E.P. and Barbieri, P.E.L., *Flow boiling performance in horizontal microfinned copper tubes with the same geometric characteristics*. Experimental Thermal and Fluid Science, 2011. **35**(5): p. 832-840.
58. Manavela Chiapero, E., Fernandino, M., and Dorao, C.A., *Experimental results on boiling heat transfer coefficient, frictional pressure drop and flow patterns for R-134a at a saturation temperature of 34 °C*. International Journal of Refrigeration, 2014. **40**: p. 317-327.
59. Spindler, K. and Müller-Steinhagen, H., *Flow boiling heat transfer of R-134a and R-404A in a microfin tube at low mass fluxes and low heat fluxes*. Heat and Mass Transfer, 2009. **45**(7): p. 967-977.
60. Balachander, P. and Raja, B., *Investigation on the boiling heat transfer characteristics of R-404A and R-134a under stratified flow condition*. Heat and Mass Transfer, 2015. **51**(6): p. 825-835.
61. Björk, E. and Palm, B., *Flow boiling heat transfer at low flux conditions in a domestic refrigerator evaporator*. International Journal of Refrigeration, 2008. **31**(6): p. 1021-1032.
62. Saiz Jabardo, J.M. and Bandarra Filho, E.P., *Convective boiling of halocarbon refrigerants flowing in a horizontal copper tube – an experimental study*. Experimental Thermal and Fluid Science, 2000. **23**(3): p. 93-104.
63. Wattelet, J.P., Chato, J.C., Souza, A.L., and Christoffersen, B.R., *Evaporative characteristics of R-134a, MP-39, and R-12 at low mass fluxes*. ASHRAE Transactions, 1994. **100**: p. 603-615.
64. Chen, C.A., Lin, T.F., and Yan, W.-M., *Experimental study on time periodic evaporation heat transfer of R-134a in annular ducts due to wall heat flux oscillation*. International Journal of Heat and Mass Transfer, 2017. **106**: p. 1232-1241.
65. Kingston, T.A., Weibel, J.A., and Garimella, S.V., *Time-resolved characterization of microchannel flow boiling during transient heating: Part 1 – Dynamic response to a single heat flux pulse*. International Journal of Heat and Mass Transfer, 2020. **154**: p. 119643.
66. Kingston, T.A., Weibel, J.A., and Garimella, S.V., *Time-resolved characterization of microchannel flow boiling during transient heating: Part 2 – Dynamic response to time-periodic heat flux pulses*. International Journal of Heat and Mass Transfer, 2020. **154**: p. 119686.
67. Wang, D., Zhao, L., Nie, X., Lu, Y., and Deng, S., *Experimental study on flow boiling characteristics of R-245fa in circular tube under non-uniform heat flux*. International Journal of Heat and Mass Transfer, 2019. **143**: p. 118570.
68. Wani, N.A. and Nandan, G. *Modelling of Solar parabolic trough collector considering Unsymmetrical Heat Flux*. in *2019 3rd International Conference on Recent Developments in Control, Automation & Power Engineering (RDCAPE)*. 2019.
69. Zhang, Y., Tian, R., Dai, X., Wang, D., Ma, Y., Li, H., and Shi, L., *Experimental study of R-134a flow boiling in a horizontal tube for evaporator design under typical organic Rankine cycle pressures*. International Journal of Heat and Fluid Flow, 2018. **71**: p. 210-219.
70. Wang, Z.-q., He, N., Xia, X.-x., and Liu, L.-w., *Experimental investigation on boiling heat transfer and pressure drop of R-245fa in a horizontal micro-fin tube*. Journal of Central South University, 2019. **26**(11): p. 3200-3212.
71. Desideri, A., Dickes, R., Bonilla, J., Valenzuela, L., Quoilin, S., and Lemort, V., *Steady-state and dynamic validation of a parabolic trough collector model using the ThermoCycle Modelica library*. Solar Energy, 2018. **174**: p. 866-877.
72. Korol'kov, B.P. and Tairov, E.A., *A numerical-analytical method for solving the non-linear problem of the dynamics of heat transfer in channels*. International Journal of Heat and Mass Transfer, 1991. **34**(2): p. 331-340.
73. Ferruzza, D., Kærn, M.R., and Haglind, F., *A method to account for transient performance requirements in the design of steam generators for concentrated solar power applications*. Applied Energy, 2020. **269**: p. 114931.

74. Lin, M., Reinhold, J., Monnerie, N., and Haussener, S., *Modeling and design guidelines for direct steam generation solar receivers*. Applied Energy, 2018. **216**: p. 761-776.
75. Li, L., Sun, J., Li, Y., He, Y.-L., and Xu, H., *Transient characteristics of a parabolic trough direct-steam-generation process*. Renewable Energy, 2019. **135**: p. 800-810.
76. Li, L., Yu, H., Li, Y., and He, Y.-L., *Characteristics of the transient thermal load and deformation of the evacuated receiver in solar parabolic trough collector*. Science China Technological Sciences, 2020.
77. Chu, Y., Pedro, H.T.C., Li, M., and Coimbra, C.F.M., *Real-time forecasting of solar irradiance ramps with smart image processing*. Solar Energy, 2015. **114**: p. 91-104.
78. Ait Lahoussine Ouali, H., Guechchati, R., Moussaoui, M.A., and Mezrhab, A., *Performance of parabolic through solar power plant under weather conditions of the Oujda city in Morocco*. Applied Solar Energy, 2017. **53**(1): p. 45-52.
79. Feldhoff, J.F. and Hirsch, T., *An approach to DNI transients characterization for system evaluation*. AIP Conference Proceedings, 2017. **1850**(1): p. 160007.
80. Eck, M. and Hirsch, T., *Dynamics and control of parabolic trough collector loops with direct steam generation*. Solar Energy, 2007. **81**(2): p. 268-279.
81. Mahoney, R. *Trough technology heat collector element (HCE) solar selective absorbers*. in *Trough Workshop ASES 2000m*. 2000.
82. Lei, D., Wang, Z., and Li, J., *The analysis of residual stress in glass-to-metal seals for solar receiver tube*. Materials & Design, 2010. **31**(4): p. 1813-1820.
83. Shekoofa, O., Wang, J., Qi, J., Zhang, J., and Yin, Z., *Analysis of residual stress for mismatch metal-glass seals in solar evacuated tubes*. Solar Energy Materials and Solar Cells, 2014. **128**: p. 421-426.
84. Abedini-Sanigy, M.H., Ahmadi, F., Goshtasbirad, E., and Yaghoubi, M., *Thermal stress analysis of absorber tube for a parabolic collector under quasi-steady state condition*. Energy Procedia, 2015. **69**: p. 3-13.
85. Fuqiang, W., Jianyu, T., Lanxin, M., and Chengchao, W., *Effects of glass cover on heat flux distribution for tube receiver with parabolic trough collector system*. Energy Conversion and Management, 2015. **90**: p. 47-52.
86. Flores, V. and Almanza, R., *Behavior of the compound wall copper–steel receiver with stratified two-phase flow regimen in transient states when solar irradiance is arriving on one side of receiver*. Solar Energy, 2004. **76**(1): p. 195-198.
87. Wang, F., Shuai, Y., Yuan, Y., Yang, G., and Tan, H., *Thermal stress analysis of eccentric tube receiver using concentrated solar radiation*. Solar Energy, 2010. **84**(10): p. 1809-1815.
88. Meyer, J.P. and Ewim, D.R.E., *Heat transfer coefficients during the condensation of low mass fluxes in smooth horizontal tubes*. International Journal of Multiphase Flow, 2018. **99**: p. 485-499.
89. Ewim, D.R.E., Meyer, J.P., and Noori Rahim Abadi, S.M.A., *Condensation heat transfer coefficients in an inclined smooth tube at low mass fluxes*. International Journal of Heat and Mass Transfer, 2018. **123**: p. 455-467.
90. Ewim, D.R.E. and Meyer, J.P., *Pressure drop during condensation at low mass fluxes in smooth horizontal and inclined tubes*. International Journal of Heat and Mass Transfer, 2019. **133**: p. 686-701.
91. Taccani, R., Obi, J.B., De Lucia, M., Micheli, D., and Toniato, G., *Development and Experimental Characterization of a Small Scale Solar Powered Organic Rankine Cycle (ORC)*. Energy Procedia, 2016. **101**: p. 504-511.
92. Fu, B.-R., Lee, Y.-R., and Hsieh, J.-C., *Design, construction, and preliminary results of a 250-kW organic Rankine cycle system*. Applied Thermal Engineering, 2015. **80**: p. 339-346.
93. Armacell. *HVAC-R & Process Specification Guide*. 2021; Available from: <https://local.armacell.com/fileadmin/cms/uk/service/en/ArmaflexUKSpecGuideDigital.pdf>.

94. Cho, K. and Tae, S.-J., *Condensation heat transfer for R-22 and R-407C refrigerant–oil mixtures in a microfin tube with a U-bend*. International Journal of Heat and Mass Transfer, 2001. **44**(11): p. 2043-2051.
95. Everts, M., *Single-phase mixed convection of developing and fully developed flow in smooth horizontal tubes in the laminar, transitional, quasi-turbulent and turbulent flow regimes*. 2017, University of Pretoria.
96. Lobón, D.H., Valenzuela, L., and Baglietto, E., *Modeling the dynamics of the multiphase fluid in the parabolic-trough solar steam generating systems*. Energy Conversion and Management, 2014. **78**: p. 393-404.
97. Bell, I.H., Wronski, J., Quoilin, S., and Lemort, V., *Pure and pseudo-pure fluid thermophysical property evaluation and the open-source thermophysical property library CoolProp*. Industrial & Engineering Chemistry Research, 2014. **53**(6): p. 2498-2508.
98. Dunn, P.F., *Measurement and data analysis for engineering and science*. 2nd ed. ed. 2010, Boca Raton, FL: CRC Press/Taylor & Francis.
99. Gungor, K.E. and Winterton, R.H.S., *A general correlation for flow boiling in tubes and annuli*. International Journal of Heat and Mass Transfer, 1986. **29**(3): p. 351-358.
100. Fang, X., Wu, Q., and Yuan, Y., *A general correlation for saturated flow boiling heat transfer in channels of various sizes and flow directions*. International Journal of Heat and Mass Transfer, 2017. **107**: p. 972-981.
101. Wojtan, L., Ursenbacher, T., and Thome, J.R., *Investigation of flow boiling in horizontal tubes: Part II—Development of a new heat transfer model for stratified-wavy, dryout and mist flow regimes*. International Journal of Heat and Mass Transfer, 2005. **48**(14): p. 2970-2985.
102. Liu, Z. and Winterton, R.H.S., *A general correlation for saturated and subcooled flow boiling in tubes and annuli, based on a nucleate pool boiling equation*. International Journal of Heat and Mass Transfer, 1991. **34**(11): p. 2759-2766.
103. Bertsch, S.S., Groll, E.A., and Garimella, S.V., *Refrigerant flow boiling heat transfer in parallel microchannels as a function of local vapor quality*. International Journal of Heat and Mass Transfer, 2008. **51**(19): p. 4775-4787.
104. Kandlikar, S.G., *A general correlation for saturated two-phase flow boiling heat transfer inside horizontal and vertical tubes*. Journal of Heat Transfer, 1990. **112**(1): p. 219-228.
105. Balcilar, M., Aroonrat, K., Dalkilic, A.S., and Wongwises, S., *A numerical correlation development study for the determination of Nusselt numbers during boiling and condensation of R-134a inside smooth and corrugated tubes*. International Communications in Heat and Mass Transfer, 2013. **48**: p. 141-148.
106. EEPublishers. *Power from the sun: An overview of CSP in South Africa*. 2018 [cited 2021 2021/08/10]; Available from: <https://www.ee.co.za/article/power-from-the-sun-an-overview-of-csp-in-south-africa.html>.
107. Southern African Universities Radiometric Network. *Station GIZ University of Pretoria*. [cited 2020 2020/07/31]; Available from: <https://sauran.ac.za/>.
108. Özişik , M.N., *Heat transfer: a basic approach*. Vol. 1. 1985: McGraw-Hill New York.
109. Steiner, D., *Heat Transfer to Boiling Saturated Liquids (VDI-Wärmeatlas)*. VDI Heat Atlas. VDI-Gesellschaft Verfahrenstechnik und Chemieingenieurwesen (GCV), Düsseldorf, Germany (JW Fullarton, translator), 1993.
110. Rouhani, S.Z. and Axelsson, E., *Calculation of void volume fraction in the subcooled and quality boiling regions*. 1968, AB Atomenergi.
111. Rouhani, S.Z. and Axelsson, E., *Calculation of void volume fraction in the subcooled and quality boiling regions*. International Journal of Heat and Mass Transfer, 1970. **13**(2): p. 383-393.
112. Müller-Steinhagen, H. and Heck, K., *A simple friction pressure drop correlation for two-phase flow in pipes*. Chemical Engineering and Processing: Process Intensification, 1986. **20**(6): p. 297-308.

113. Charogiannis, A., An, J.S., and Markides, C.N., *A simultaneous planar laser-induced fluorescence, particle image velocimetry and particle tracking velocimetry technique for the investigation of thin liquid-film flows*. Experimental Thermal and Fluid Science, 2015. **68**: p. 516-536.
114. Zadrazil, I. and Markides, C.N., *An experimental characterization of liquid films in downwards co-current gas-liquid annular flow by particle image and tracking velocimetry*. International Journal of Multiphase Flow, 2014. **67**: p. 42-53.
115. Ursenbacher, T., Wojtan, L., and Thome, J.R., *Interfacial measurements in stratified types of flow. Part I: New optical measurement technique and dry angle measurements*. International Journal of Multiphase Flow, 2004. **30**(2): p. 107-124.
116. De Paepe, M., Canière, H., T'Joen, C., Steeman, H.-J., Willockx, A., Christians, M., van Rooyen, E., Liebenberg, L., and Meyer, J., *Refrigerant Flow Regime Detection with a Capacitance Void Fraction Sensor*, in *9th AIAA/ASME Joint Thermophysics and Heat Transfer Conference*. 2006, American Institute of Aeronautics and Astronautics.
117. Mathie, R. and Markides, C.N., *Heat transfer augmentation in unsteady conjugate thermal systems – Part I: Semi-analytical 1-D framework*. International Journal of Heat and Mass Transfer, 2013. **56**(1): p. 802-818.
118. Mathie, R., Nakamura, H., and Markides, C.N., *Heat transfer augmentation in unsteady conjugate thermal systems – Part II: Applications*. International Journal of Heat and Mass Transfer, 2013. **56**(1): p. 819-833.
119. Degiovanni, A. and Remy, B., *An alternative to heat transfer coefficient: A relevant model of heat transfer between a developed fluid flow and a non-isothermal wall in the transient regime*. International Journal of Thermal Sciences, 2016. **102**: p. 62-77.
120. Mathie, R., Markides, C.N., and White, A.J., *A framework for the analysis of thermal losses in reciprocating compressors and expanders*. Heat Transfer Engineering, 2014. **35**(16-17): p. 1435-1449.
121. Huber, M.L., Laesecke, A., and Perkins, R.A., *Model for the viscosity and thermal conductivity of refrigerants, including a new correlation for the viscosity of R-134a*. Industrial & Engineering Chemistry Research, 2003. **42**(13): p. 3163-3178.
122. Akasaka, R., Zhou, Y., and Lemmon, E.W., *A Fundamental Equation of State for 1,1,1,3,3-Pentafluoropropane (R-245fa)*. Journal of Physical and Chemical Reference Data, 2015. **44**(1): p. 013104.
123. Bell, I.H. and Laesecke, A. *Viscosity of refrigerants and other working fluids from residual entropy scaling*. in *16th International Refrigeration and Air Conditioning Conference at Purdue*. 2016.
124. Cooper, M.G., *Saturation nucleate pool boiling - a simple correlation*, in *First U.K. National Conference on Heat Transfer*, H.C. Simpson, et al., Editors. 1984, Pergamon. p. 785-793.
125. Dittus, F.W. and Boelter, L.M.K., *Heat transfer in automobile radiators of the tubular type*. 1930, Berkeley, Calif: University of California Press.

APPENDICES

“If in other sciences we should arrive
at certainty without doubt and truth without error,
it behooves us to place the foundations of knowledge
in mathematics.”

–R. Bacon

APPENDIX TABLE OF CONTENTS

Appendix list of figures	133
Appendix list of tables	134
A. Calibration	135
A.1. Introduction	135
A.2. Pt100 and facility thermocouple calibration	135
A.3. Test section in situ thermocouple calibration.....	138
A.4. Absolute pressure transducer calibration	140
B. Uncertainty propagation.....	141
B.1. Introduction	141
B.2. Uncertainty summary	141
B.3. Uncertainty propagation methods.....	143
B.4. Instrumentation values.....	144
B.5. Calculated values.....	145
C. Relevant equations	153
C.1. Introduction	153
C.2. HTC correlations	153
C.3. Lumped system temperature prediction model	158
C.4. Pressure drop correlation	159
D. Calibration certificates.....	161
D.1. Introduction	161
D.2. Certificates	162

APPENDIX LIST OF FIGURES

Figure A.1. Example of the calibration curves obtained for (a) a Pt100 and (b) a facility thermocouple	136
Figure A.2. Temperature difference between target temperature for uncalibrated and calibrated values of (a) a Pt100 and (b) a facility thermocouple.....	137
Figure A. 3. Example calibration curve for a test section thermocouple	139
Figure A.4. Temperature difference between target temperature for uncalibrated and calibrated values of a test section thermocouple	139
Figure D. 1. Calibration certificate for pressure transducer ahead of pump	162
Figure D. 2. Calibration certificate for pressure transducer after pump.....	163
Figure D. 3. Calibration certificate for pressure transducer ahead of preheater.....	164
Figure D. 4. Calibration certificate for pressure transducer after condenser.....	165
Figure D. 5. Calibration certificate for pressure transducer ahead of calming section	166
Figure D. 6. Calibration certificate for pressure transducer ahead of heated length	167
Figure D. 7. Calibration certificate for pressure transducer after heated section	168
Figure D. 8. Calibration certificate for pressure transducer after test section.....	169

APPENDIX LIST OF TABLES

Table B. 1. Ranges and accuracies of measuring instruments.....	142
Table B. 2. R-245fa fundamental value accuracies	142
Table B. 3. Parameter ranges and uncertainties.....	143
Table C. 1. Froude number correction factors.....	156
Table C. 2. Constants for use in the Kandlikar correlation	157

A. CALIBRATION

A.1. INTRODUCTION

Calibration of the temperature and pressure sensors is discussed in more detail in this appendix. First, the calibration of the Pt100 RTDs used on the experimental apparatus is discussed, along with the calibration of the facility thermocouples (which would be attached with thermal tape). Next, the *in situ* calibration of the thermocouples on the test section is considered, before the equations that were obtained for the absolute pressure sensor calibration is provided.

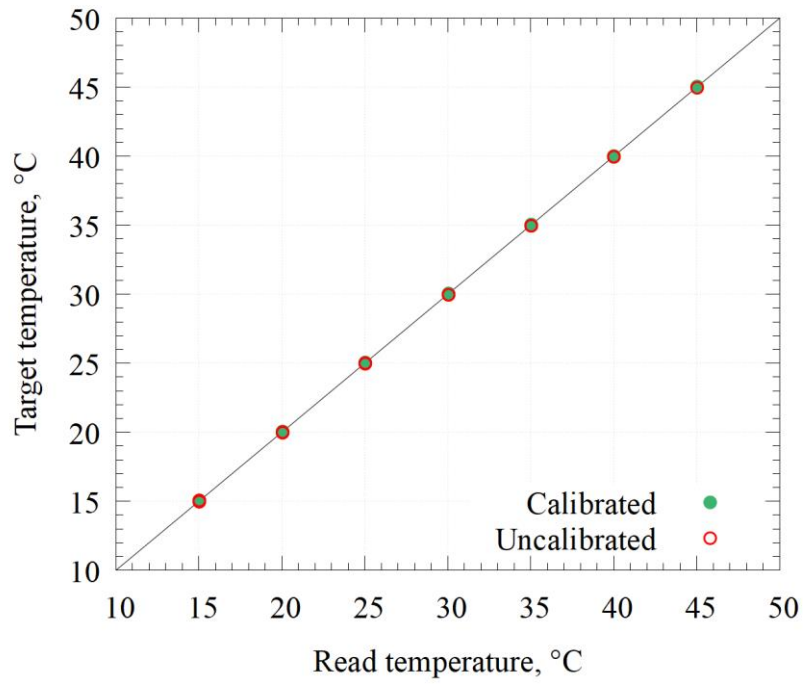
A.2. PT100 AND FACILITY THERMOCOUPLE CALIBRATION

In order to calibrate the Pt100 RTDs used in the experimental setup, as well as the thermocouples attached to the facility, depicted in Figure 3.1, they had to be exposed to a series of set temperatures. The measured temperature could then be compared to the expected temperature and calibration curves could be constructed.

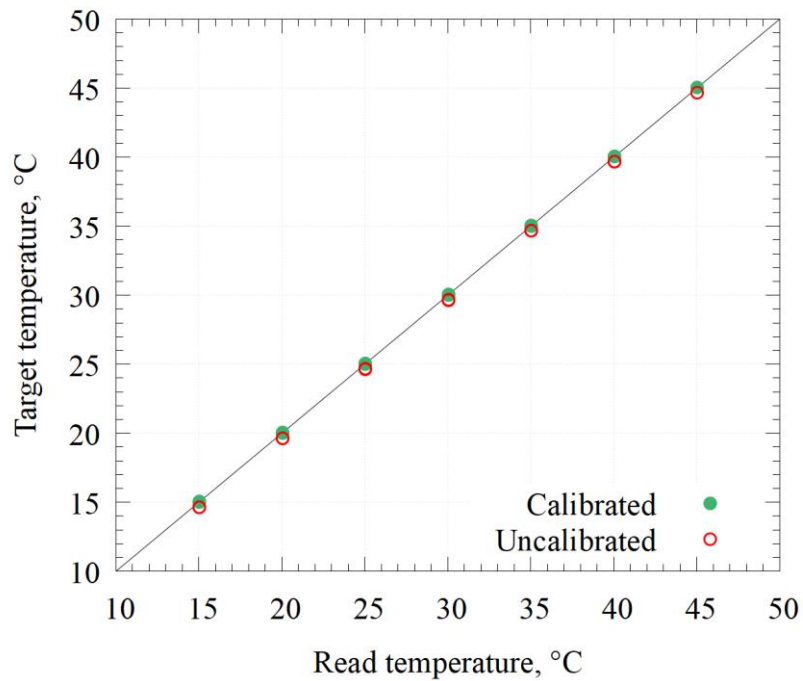
In order to provide the set temperatures, a Lauda Proline RP1845C thermostat controlled thermal bath was used. A factory calibrated Lauda DigiCal DCS2 temperature probe with an accuracy of 0.03 °C was used to obtain the expected set point temperatures. The series of set temperatures were chosen to stretch from 15 °C to 45 °C, in 5 °C intervals.

The procedure was to insert the calibrated temperature probe, the Pt100s, and thermocouples in the water bath, and set the thermostat to the lowest desired calibration temperature. It was then allowed to reach a stability before readings were recorded. The number of readings recorded were 200, of which the mean would be used in calculating the calibration curve. The process was then repeated, increasing the water bath temperature in increments of 5 °C, until the highest temperature was reached. At this point the process was reversed, decreasing the temperature in 5 °C increments until the lowest temperature was reached, following the same data recording procedure. This upward and downward calibration was performed in order to isolate possible hysteresis effects in the equipment used.

The calibration curves were obtained by performing a linear curve fit over the collected means. A representative example of the calibration curves obtained for a Pt100 is shown in Figure A.1a, and for a facility thermocouple in Figure A.1b:



(a) Pt100

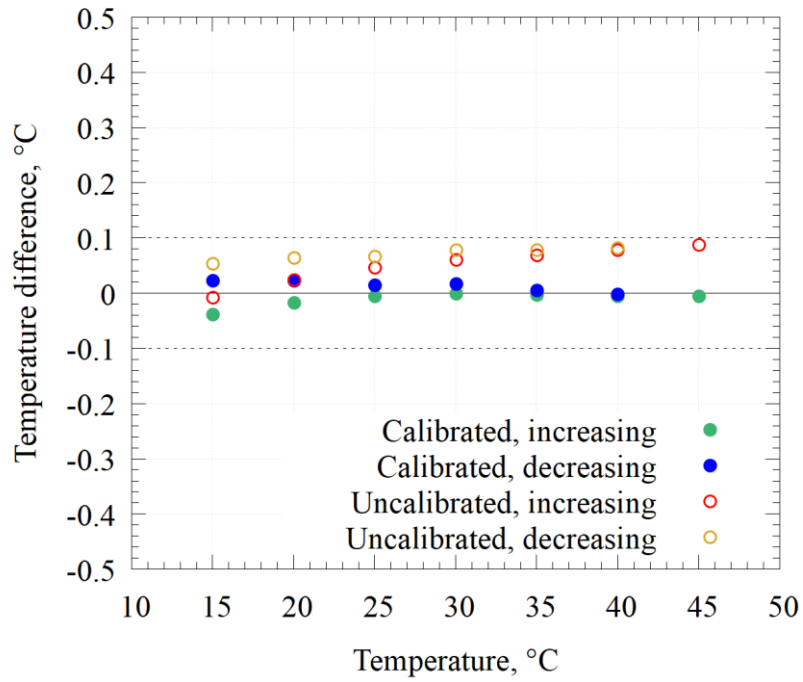


(b) Facility thermocouple

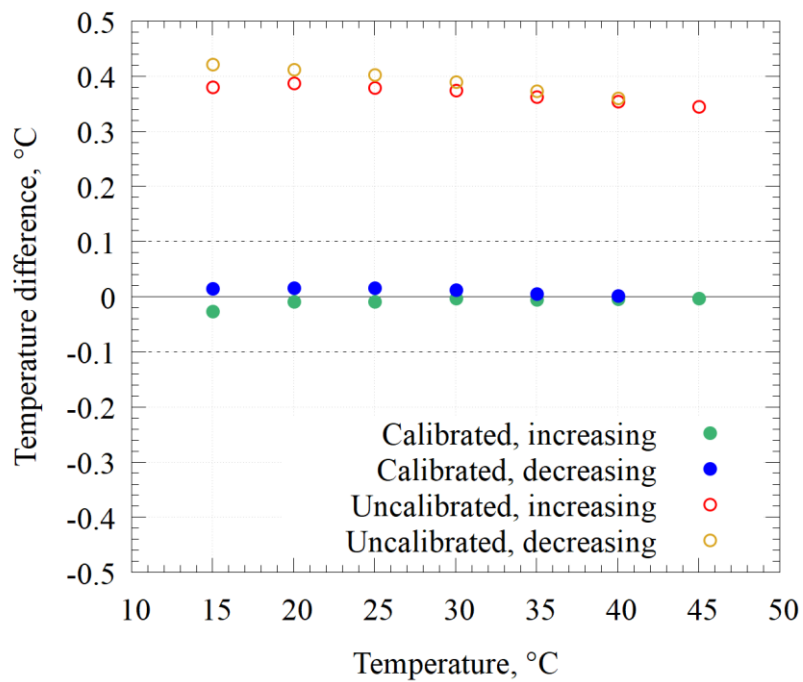
Figure A.1. Example of the calibration curves obtained for (a) a Pt100 and (b) a facility thermocouple

The readings on the upward and downward calibration are not clear in this figure. Thus, in order to visualise the effect of calibration more clearly, the difference in temperature is plotted as a function of the target temperature. A representative example is given in Figure A.2a for a Pt100, and

Figure A.2b for a facility thermocouple. Both the upward and downward sweeps of the calibration are included.



(a) Pt100



(b) Facility thermocouple

Figure A.2. Temperature difference between target temperature for uncalibrated and calibrated values of (a) a Pt100 and (b) a facility thermocouple

The hysteresis in both the Pt100 and thermocouple is evident at temperatures between 15 and 30 °C, but was on the order of 0.02 °C, and thus was disregarded. It is evident that the calibration much improved the reading of the temperatures, and it was found that the uncertainty for all Pt100s and thermocouples was below 0.05 °C after calibration.

A.3. TEST SECTION IN SITU THERMOCOUPLE CALIBRATION

Since the properties of a thermocouple would be affected by the method of attachment (soldering) to the test section, as shown in Figure 3.4, calibrating them before attachment, as was described for the facility thermocouples and Pt100s previously, was not optimal. Instead, they were attached to the test section, and calibrated in place after the system was charged with refrigerant. This was done by using measurements obtained from the already calibrated Pt100s immediately before and after the test section while circulating liquid fluid through an adiabatic test section.

The mass flux of the fluid was maintained upwards of 700 kg/m²s, and it was heated by a combination of the preheater and condenser (coupled to the thermal bath) over a range of temperatures from 15 to 45 °C in 5 °C increments, both upwards and downwards, as described previously. The temperatures of the Pt100s were maintained within 0.03 °C of each other for at least 10 minutes for each set temperature before data recording could take place. Logically, if the temperatures between both Pt100s pre- and post- test conformed to set temperature, the temperature between them on the test section was also at the set temperature. At each temperature set point, 200 data points were recorded, of which the mean was used in the calibration process. As before, an example of the calibration curve obtained is shown in Figure A. 3.

Again, the measurements were already so close it becomes hard to discern the fact that calibration improves the readings at all. The difference between the uncalibrated and the calibrated temperatures and the set point temperature given by the Pt100s is shown in Figure A.4. Both the upwards and downwards calibration sweeps are included, and the hysteresis was again negligible.

The calibration much improves all the thermocouples' accuracy, resulting in an uncertainty of less than 0.05°C.

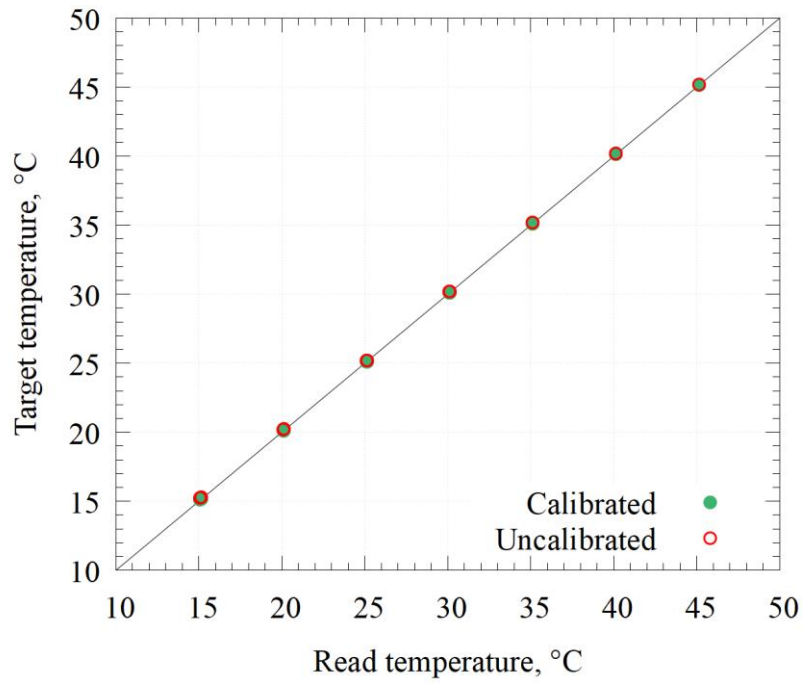


Figure A. 3. Example calibration curve for a test section thermocouple

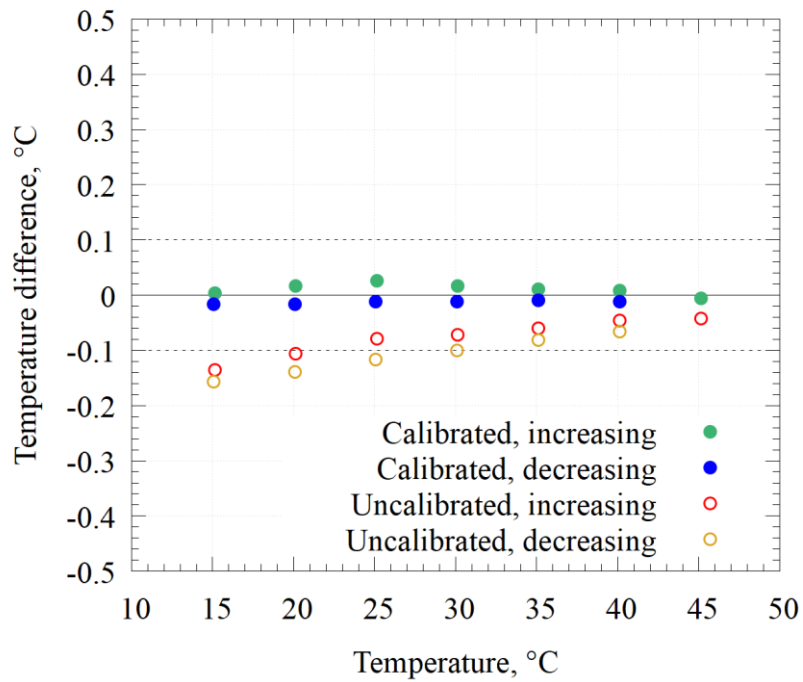


Figure A.4. Temperature difference between target temperature for uncalibrated and calibrated values of a test section thermocouple

A.4. ABSOLUTE PRESSURE TRANSDUCER CALIBRATION

The absolute pressure transducers were sent to WIKA, an external calibration company. A scanned version of the first page of the physical calibration certificate documents is included in Appendix D. The equations provided on the last page of these (rather lengthy) documents are shown below for the GEMS 2200 sensors before and after the pump in Equation (A.1), and for the Sensotec FP2000 sensors in Equation (A.2). These equations convert the mA reading from the transducers to an absolute pressure in kPa.

$$P = 100(1.25I - 5) + 83 \quad (\text{A.1})$$

$$P = 6.89(31.25I - 125) + 83 \quad (\text{A.2})$$

B. UNCERTAINTY PROPAGATION

B.1. INTRODUCTION

When driving on the road, one will often see signs indicating the distance to the next town in kilometres, or warning to look out for a certain distance ahead in metres. When gauging this distance using an odometer, it will invariably show that the stated roadside distance and the measured distance differ by some number. This is true for many different reasons. For example, what was used in the road measurement when the sign was made? How accurate is the odometer that was utilised? More importantly, is this difference large enough to make one doubt the stated distance? This, in a nutshell, is what is meant by uncertainty in scientific experiments. This appendix contains the manufacturers' stated accuracy, the accuracy of the various fluid values (such as enthalpy), and the calculated uncertainties. Then, it defines the means by which the uncertainty and its propagation is defined, before showing more details on the instrumentation accuracies. Finally, it relays the obtained equations which were used to calculate the values given initially.

B.2. UNCERTAINTY SUMMARY

B.2.1. Instrument accuracies

Before delving into the way in which the uncertainties were calculated, first some instrument accuracies are noted in Table B. 1. The instruments are as noted in Section 3.3 and 3.4. The worst-case accuracies were used in the uncertainty propagation in the interests of conservatism.

Table B. 1. Ranges and accuracies of measuring instruments

Instrument	Range	Stated accuracy	Post calibrated accuracy	Value used in uncertainty propagation
Pt100 RTD	-200 – 600 °C	0.06 °C	<0.04°C	0.06°C
T-type thermocouple	0 – 150 °C	0.1 °C	<0.05°C	0.1°C
Refrigerant Coriolis flow meter	0 – 0.04 kg/s	0.1%	0.1%	0.1%
Water Coriolis flow meter	0 – 0.4 kg/s	0.1%	0.1%	0.1%
Sensotec pressure transducers	0 – 2 000 kPa	4.4 kPa	~2.7 kPa	4.4 kPa
GEMS pressure transducers	0 – 2 200 kPa	5 kPa	~3 kPa	5 kPa

B.2.2. Fundamental value accuracies

Uncertainty plays a role in any scientific quantity, and the thermophysical properties used for the fluid in this study are no different. The way these are calculated, by applying certain governing equations, also has uncertainty. Listed in Table B. 2 are the uncertainties for the thermal conductivity, the density, specific heat capacity, viscosity, density, and enthalpy used in the equations in the preceding chapters. The fluid values were obtained using CoolProp [97], with the source of the uncertainty referenced for each value.

Table B. 2. R-245fa fundamental value accuracies

Property	Uncertainty
Thermal conductivity (k)	5% [121]
Isobaric specific heat capacity (c_p)	1% [122]
Dynamic viscosity (μ)	7.4% [123]
Liquid density (ρ_f)	0.1% [122]
Vapour density (ρ_g)	0.3% [122]
Enthalpy (h)	0.5% [122]

B.2.3. Calculated uncertainties

The uncertainties that were calculated with the method described in the next section are shown in Table B. 3.

Table B. 3. Parameter ranges and uncertainties

Parameter	Range	Uncertainty
Singular temperature measurement point	35 – 45 °C	0.1 °C
Mass flux (G)	40-300 kg/m ² s	0.6%
Inlet vapour quality (x_{in})	0.05 – 0.90	0.0053
Heat flux (\dot{q})	1.9 – 7.5 kW/m ²	0.4%
Local HTC (α_n , Equation (4.6))	0.5 – 7.0 kW/m ² K	5.7%
Average HTC ($\bar{\alpha}$, Equation (4.10))	0.5 – 7.0 kW/m ² K	2%

B.3. UNCERTAINTY PROPAGATION METHODS

According to Dunn and Davis [98], the uncertainty in any measurement consists of both the bias and precision. Bias is related to the limits of the measuring instrument. One cannot measure down to a micron level with a basic ruler marked in centimetres, for example. Precision, on the other hand, relates to the repeatability of a measurement. In other words, it is a given that a measure will be wrong, but is it consistently wrong? This bias and precision are combined in the Euclidean norm for a single measurement below:

$$\delta x_i = (b_i^2 + p_i^2)^{\frac{1}{2}} \quad (\text{B.1})$$

in which δx_i is the uncertainty for a single measurement in a variable x_i , b_i is the bias for that measurement, and p_i the precision. Where more than one variable influences a measurement R , the following can be stated:

$$R = f(x_1, x_2, x_3, \dots, x_n) \quad (\text{B.2})$$

The contribution of each uncertainty δx_i to the overall uncertainty δR can be determined by taking the partial derivatives of the function with respect to each x_i and multiplying it by δx_i :

$$\delta R_{x_i} = \frac{\partial R}{\partial x_i} \delta x_i \quad (\text{B.3})$$

The total uncertainty for a measurement R is then the Euclidean norm of all the individual partial derivatives and uncertainties:

$$\delta R = \left[\sum_{i=1}^n \left(\frac{\partial R}{\partial x_i} \delta x_i \right)^2 \right]^{\frac{1}{2}} \quad (\text{B.4})$$

The total uncertainty for the many instruments and values used in this thesis, was taken as the value given by the manufacturer of the sensor or the software used to calculate the thermodynamic properties. The accuracy of the temperature measurements, however, were the most critical element in the whole study, and thus extra care was taken by determining the uncertainty manually, and comparing the obtained value to the manufacturers' stated specifications. This was done in Appendix A, in the same way as stated in [95].

B.4. INSTRUMENTATION VALUES

As stated, any sensor used to measure a quantity has a built-in uncertainty. Before the methods detailed in the preceding section could be applied to determine the uncertainty of the variables under investigation, this uncertainty had to be quantified.

B.4.1. Pt100 resistance temperature detectors

After calibrating the high-accuracy Pt100 RTDs as described in the calibration appendix, it was found that the uncertainty was less than the manufacturer's stated uncertainty of 0.06 °C. Conservatively, the stated uncertainty of 0.06 °C was used.

B.4.2. Thermocouples

Following the calibration, the thermocouples were found to have a post-calibration uncertainty of less than the manufacturer's stated accuracy for the T-type thermocouples of 0.1 °C. In the interests of conservatism, this value of 0.1 °C was used instead of the calculated value.

B.4.3. Flow meters

The Coriolis flow meters used during this study had an uncertainty of 0.1% of the current flow rate. This accuracy was applicable to both the water and the refrigerant loops, with the range of the water loop flow meter being 0.4 kg/s and that of the refrigerant loop 0.04 kg/s.

B.4.4. Pressure transducers

The absolute pressure transducers utilised were calibrated and certified by an external company to have an uncertainty of less than 0.2 % of the full scale. In the interest of conservatism, the manufacturers' stated uncertainties of 0.2% of full scale for the GEMS 2200 and 0.25% of full scale for the Sensotec FP2000 transducers fitted to the system were used.

B.4.5. Power supplies

The DC power supplies used during this study were rated at 3 kW each for the preheater and 1.5 kW for the test section. The maximum voltage and current of the preheater power supplies was 360 V and 30 A, while the test section power supply had maximums of 360 V and 15 A. The uncertainty of both these values was 0.2 % of the present reading.

B.4.6. Length and diameter

The length of the appropriate sections was measured using a steel ruler with an accuracy of 1 mm. Thus, the uncertainty of the length measurements was 0.5 mm. The diameters were all determined using a Vernier calliper with an accuracy of 0.02 mm, and an uncertainty of 0.01 mm.

B.5. CALCULATED VALUES

With all the uncertainties known for the quantities that would be used in calculations, attention could be turned to deriving the equations used to calculate the final uncertainties.

B.5.1. Average temperatures

Temperatures per measurement station n was averaged in order to reduce the uncertainty beyond the bias stated by the manufacturer. The average temperatures that were used in this work were determined as follows:

$$T_n = \frac{T_{n,1} + T_{n,2} + T_{n,3} + T_{n,4}}{4} \quad (\text{B.5})$$

The partial derivatives of this each take the form:

$$\frac{\partial T_n}{\partial T_{n,r}} = \frac{1}{4}; r = [1,2,3,4] \quad (\text{B.6})$$

The uncertainty for a thermocouple station average temperature reading is thus:

$$T_n = \left[4 \left(\frac{\delta T}{4} \right)^2 \right]^{\frac{1}{2}} \quad (\text{B.7})$$

B.5.2. Cross-sectional area

The cross-sectional area of the test section pipe was calculated using:

$$A_c = \frac{\pi}{4} d_i^2 \quad (\text{B.8})$$

The applicable partial derivative is:

$$\frac{\partial A_c}{\partial d_i} = \frac{\pi}{2} d_i \quad (\text{B.9})$$

The uncertainty of the cross-sectional area is then:

$$\delta A_c = \left[\left(\frac{\partial A_c}{\partial d_i} \delta d_i \right)^2 \right]^{\frac{1}{2}} \quad (\text{B.10})$$

B.5.3. Heat transfer area

The area used for heat transfer was calculated as:

$$A_s = \pi d_i L_h \quad (\text{B.11})$$

Partial derivatives that determined the uncertainty were:

$$\frac{\partial A_c}{\partial d_i} = \pi L_h \quad (\text{B.12})$$

$$\frac{\partial A_c}{\partial L_h} = \pi d_i \quad (\text{B.13})$$

The uncertainty for the heat transfer area is:

$$\delta A_s = \left[\left(\frac{\partial A_c}{\partial L_h} \delta L_h \right)^2 + \left(\frac{\partial A_c}{\partial d_i} \delta d_i \right)^2 \right]^{\frac{1}{2}} \quad (\text{B.14})$$

B.5.4. Mass flux

The mass flux is simply the mass flow rate divided by the cross-sectional area of the pipe:

$$G = \frac{\dot{m}}{A_c} \quad (\text{B.15})$$

Partial derivatives determining the uncertainty for this were:

$$\frac{\partial G}{\partial A_c} = -\frac{\dot{m}}{A_c^2} \quad (\text{B.16})$$

$$\frac{\partial G}{\partial \dot{m}} = \frac{1}{A_c} \quad (\text{B.17})$$

Thus, the uncertainty for the mass flux is:

$$\delta G = \left[\left(\frac{\partial G}{\partial \dot{m}} \delta \dot{m} \right)^2 + \left(\frac{\partial G}{\partial A_c} \delta A_c \right)^2 \right]^{\frac{1}{2}} \quad (\text{B.18})$$

B.5.5. Boiling heat rate

The heat rate applied to both the test section and the preheater were assumed to be the full power provided by the voltage and current according to the generalised power equation:

$$\dot{Q} = VI \quad (\text{B.19})$$

The partial derivatives to calculate the uncertainty are:

$$\frac{\partial \dot{Q}}{\partial V} = I \quad (\text{B.20})$$

$$\frac{\partial \dot{Q}}{\partial I} = V \quad (\text{B.21})$$

The uncertainty of the heat rate is then:

$$\delta \dot{Q} = \left[\left(\frac{\partial \dot{Q}}{\partial I} \delta I \right)^2 + \left(\frac{\partial \dot{Q}}{\partial V} \delta V \right)^2 \right]^{\frac{1}{2}} \quad (\text{B.22})$$

B.5.6. Boiling heat flux

The boiling heat flux for the test section was simply the heat rate divided by the heat transfer area:

$$\dot{q} = \frac{\dot{Q}_{\text{test}}}{A_s} \quad (\text{B.23})$$

The partial derivatives to calculate the uncertainty are:

$$\frac{\partial \dot{q}}{\partial \dot{Q}_{\text{test}}} = \frac{1}{A_s} \quad (\text{B.24})$$

$$\frac{\partial \dot{q}}{\partial A_s} = \frac{-\dot{Q}_{\text{test}}}{A_s^2} \quad (\text{B.25})$$

The uncertainty of the heat flux is:

$$\delta \dot{q} = \left[\left(\frac{\partial \dot{q}}{\partial \dot{Q}_{\text{test}}} \delta \dot{Q}_{\text{test}} \right)^2 + \left(\frac{\partial \dot{q}}{\partial A_s} \delta A_s \right)^2 \right]^{\frac{1}{2}} \quad (\text{B.26})$$

B.5.7. Condenser heat rate

The heat rate removed by the condenser was determined by a simple energy balance over the condenser inlet and outlet on the water side:

$$\dot{Q}_{\text{cond}} = \dot{m}_w c_{p,w} (T_{w,\text{out}} - T_{w,\text{in}}) \quad (\text{B.27})$$

Taking the appropriate partial derivatives results in:

$$\frac{\partial \dot{Q}_{\text{cond}}}{\partial \dot{m}_w} = C_{p,w}(T_{w,\text{out}} - T_{w,\text{in}}) \quad (\text{B.28})$$

$$\frac{\partial \dot{Q}_{\text{cond}}}{\partial C_{p,w}} = \dot{m}_w(T_{w,\text{out}} - T_{w,\text{in}}) \quad (\text{B.29})$$

$$\frac{\partial \dot{Q}_{\text{cond}}}{\partial T_{w,\text{out}}} = \dot{m}_w C_{p,w} \quad (\text{B.30})$$

$$\frac{\partial \dot{Q}_{\text{cond}}}{\partial T_{w,\text{in}}} = -\dot{m}_w C_{p,w} \quad (\text{B.31})$$

The uncertainty is thus:

$$\delta \dot{Q}_{\text{cond}} = \left[\left(\frac{\partial \dot{Q}_{\text{cond}}}{\partial T_{w,\text{in}}} \delta T_{w,\text{in}} \right)^2 + \left(\frac{\partial \dot{Q}_{\text{cond}}}{\partial T_{w,\text{out}}} \delta T_{w,\text{out}} \right)^2 + \left(\frac{\partial \dot{Q}_{\text{cond}}}{\partial C_{p,w}} \delta C_{p,w} \right)^2 + \left(\frac{\partial \dot{Q}_{\text{cond}}}{\partial \dot{m}_w} \delta \dot{m}_w \right)^2 \right]^{\frac{1}{2}} \quad (\text{B.32})$$

B.5.8. Test section wall thermal resistance

The wall thermal resistance was calculated using:

$$R_{\text{wall}} = \frac{\ln(d_{o,\text{test}}/d_{i,\text{test}})}{2\pi k L_h} \quad (\text{B.33})$$

The partial derivatives are:

$$\frac{\partial R_{\text{wall}}}{\partial k} = \frac{-\ln \frac{d_{o,\text{test}}}{d_{i,\text{test}}}}{2\pi k^2 L_h} \quad (\text{B.34})$$

$$\frac{\partial R_{\text{wall}}}{\partial L_{\text{test}}} = \frac{\ln \frac{d_{o,\text{test}}}{d_{i,\text{test}}}}{2\pi k L_h^2} \quad (\text{B.35})$$

$$\frac{\partial R_{\text{wall}}}{\partial d_i} = \frac{-1}{2\pi k L_h d_{i,\text{test}}} \quad (\text{B.36})$$

$$\frac{\partial R_{\text{wall}}}{\partial d_o} = \frac{-1}{2\pi k L_h d_{o,\text{test}}} \quad (\text{B.37})$$

The uncertainty for the thermal resistance of the pipe wall is:

$$\delta R_{\text{wall}} = \left[\left(\frac{\partial R_{\text{wall}}}{\partial d_o} \delta d_{o,\text{test}} \right)^2 + \left(\frac{\partial R_{\text{wall}}}{\partial d_i} \delta d_{i,\text{test}} \right)^2 + \left(\frac{\partial R_{\text{wall}}}{\partial L_h} \delta L_h \right)^2 + \left(\frac{\partial R_{\text{wall}}}{\partial k} \delta k \right)^2 \right]^{\frac{1}{2}} \quad (\text{B.38})$$

B.5.9. Test section inlet enthalpy

The test section inlet enthalpy, used to calculate the vapour quality, was determined using:

$$h_{\text{in}} = \frac{\dot{Q}_{\text{pre}}}{\dot{m}_{\text{ref}}} + h_{\text{liquid}} \quad (\text{B.39})$$

The relevant partial derivatives are:

$$\frac{\partial h_{\text{in}}}{\partial \dot{Q}_{\text{pre}}} = \frac{1}{\dot{m}_{\text{ref}}} \quad (\text{B.40})$$

$$\frac{\partial h_{\text{in}}}{\partial \dot{m}_{\text{ref}}} = \frac{-\dot{Q}_{\text{pre}}}{\dot{m}_{\text{ref}}^2} \quad (\text{B.41})$$

$$\frac{\partial h_{\text{in}}}{\partial h_{\text{liquid}}} = 1 \quad (\text{B.42})$$

The uncertainty for the test section inlet enthalpy is:

$$\delta h_{\text{in}} = \left[\left(\frac{\partial h_{\text{in}}}{\partial h_{\text{liquid}}} \delta h_{\text{liquid}} \right)^2 + \left(\frac{\partial h_{\text{in}}}{\partial \dot{m}_{\text{ref}}} \delta \dot{m}_{\text{ref}} \right)^2 + \left(\frac{\partial h_{\text{in}}}{\partial \dot{Q}_{\text{pre}}} \delta \dot{Q}_{\text{pre}} \right)^2 \right]^{\frac{1}{2}} \quad (\text{B.43})$$

B.5.10. Test section inlet vapour quality

The test section inlet quality was calculated using:

$$x_{\text{in}} = \frac{h_{\text{in}} - h_{\text{f}}}{h_{\text{g}} - h_{\text{f}}} \quad (\text{B.44})$$

The relevant partial derivatives are:

$$\frac{\partial x_{\text{in}}}{\partial h_{\text{in}}} = \frac{1}{h_{\text{g}} - h_{\text{f}}} \quad (\text{B.45})$$

$$\frac{\partial x_{\text{in}}}{\partial h_{\text{f}}} = \frac{-1}{h_{\text{g}} - h_{\text{f}}} \quad (\text{B.46})$$

$$\frac{\partial x_{\text{in}}}{\partial h_{\text{g}}} = \frac{-(h_{\text{in}} - h_{\text{f}})}{(h_{\text{g}} - h_{\text{f}})^2} \quad (\text{B.47})$$

The uncertainty for the test section inlet vapour quality is:

$$\delta x_{\text{in}} = \left[\left(\frac{\partial x_{\text{in}}}{\partial h_{\text{g}}} \delta h_{\text{g}} \right)^2 + \left(\frac{\partial x_{\text{in}}}{\partial h_{\text{f}}} \delta h_{\text{f}} \right)^2 + \left(\frac{\partial x_{\text{in}}}{\partial h_{\text{in}}} \delta h_{\text{in}} \right)^2 \right]^{\frac{1}{2}} \quad (\text{B.48})$$

B.5.11. Test section outlet enthalpy

This enthalpy was calculated in a similar fashion to the test section inlet enthalpy using:

$$h_{\text{out}} = \frac{\dot{Q}_{\text{test}}}{\dot{m}_{\text{ref}}} + h_{\text{in}} \quad (\text{B.49})$$

The relevant partial derivatives are:

$$\frac{\partial h_{\text{out}}}{\partial \dot{Q}_{\text{test}}} = \frac{1}{\dot{m}_{\text{ref}}} \quad (\text{B.50})$$

$$\frac{\partial h_{\text{out}}}{\partial \dot{m}_{\text{ref}}} = \frac{-\dot{Q}_{\text{test}}}{\dot{m}_{\text{ref}}^2} \quad (\text{B.51})$$

$$\frac{\partial h_{\text{out}}}{\partial h_{\text{in}}} = 1 \quad (\text{B.52})$$

The uncertainty for the test section outlet enthalpy is:

$$\delta h_{\text{out}} = \left[\left(\frac{\partial h_{\text{out}}}{\partial h_{\text{in}}} \delta h_{\text{in}} \right)^2 + \left(\frac{\partial h_{\text{out}}}{\partial \dot{m}_{\text{ref}}} \delta \dot{m}_{\text{ref}} \right)^2 + \left(\frac{\partial h_{\text{out}}}{\partial \dot{Q}_{\text{test}}} \delta \dot{Q}_{\text{test}} \right)^2 \right]^{\frac{1}{2}} \quad (\text{B.53})$$

B.5.12. Test section outlet vapour quality

The test section outlet quality was calculated using:

$$x_{\text{out}} = \frac{h_{\text{out}} - h_{\text{f}}}{h_{\text{g}} - h_{\text{f}}} \quad (\text{B.54})$$

The relevant partial derivatives are:

$$\frac{\partial x_{\text{out}}}{\partial h_{\text{out}}} = \frac{1}{h_{\text{g}} - h_{\text{f}}} \quad (\text{B.55})$$

$$\frac{\partial x_{\text{out}}}{\partial h_{\text{f}}} = \frac{-1}{h_{\text{g}} - h_{\text{f}}} \quad (\text{B.56})$$

$$\frac{\partial x_{\text{out}}}{\partial h_{\text{g}}} = \frac{-(h_{\text{out}} - h_{\text{f}})}{(h_{\text{g}} - h_{\text{f}})^2} \quad (\text{B.57})$$

The uncertainty for the test section outlet vapour quality is:

$$\delta x_{\text{out}} = \left[\left(\frac{\partial x_{\text{out}}}{\partial h_g} \delta h_g \right)^2 + \left(\frac{\partial x_{\text{out}}}{\partial h_f} \delta h_f \right)^2 + \left(\frac{\partial x_{\text{out}}}{\partial h_{\text{out}}} \delta h_{\text{out}} \right)^2 \right]^{\frac{1}{2}} \quad (\text{B.58})$$

B.5.13. Mean test section vapour quality

Where it was used, the mean vapour quality between test section inlet and outlet was determined as:

$$x_{\text{mean}} = \frac{x_{\text{in}} + x_{\text{out}}}{2} \quad (\text{B.59})$$

The relevant partial derivatives are:

$$\frac{\partial x_{\text{mean}}}{\partial x_{\text{in}}} = \frac{\partial x_{\text{mean}}}{\partial x_{\text{out}}} = \frac{1}{2} \quad (\text{B.60})$$

The uncertainty for the mean test section vapour quality is:

$$\delta x_{\text{mean}} = \left[\left(\frac{\partial x_{\text{mean}}}{\partial x_{\text{out}}} \delta x_{\text{out}} \right)^2 + \left(\frac{\partial x_{\text{mean}}}{\partial x_{\text{in}}} \delta x_{\text{in}} \right)^2 \right]^{\frac{1}{2}} \quad (\text{B.61})$$

B.5.14. Heat transfer coefficient (HTC)

The HTC is given by Newton's law of cooling:

$$\alpha = \frac{\dot{Q}_{\text{test}}}{A_s(T_{\text{wall},i} - T_{\text{sat}})} \quad (\text{B.62})$$

The partial derivatives required to calculate the uncertainty are with respect to area, the temperature readings, and heating power:

$$\frac{\partial \alpha}{\partial T_{\text{sat}}} = \frac{\dot{Q}_{\text{test}}}{A_s(T_{\text{wall},i} - T_{\text{sat}})^2} \quad (\text{B.63})$$

$$\frac{\partial \alpha}{\partial T_{\text{wall},i}} = \frac{-\dot{Q}_{\text{test}}}{A_s(T_{\text{wall},i} - T_{\text{sat}})^2} \quad (\text{B.64})$$

$$\frac{\partial \alpha}{\partial A_s} = \frac{-\dot{Q}_{\text{test}}}{A_s^2(T_{\text{wall},i} - T_{\text{sat}})} \quad (\text{B.65})$$

$$\frac{\partial \alpha}{\partial \dot{Q}_{\text{test}}} = \frac{1}{A_s(T_{\text{wall},i} - T_{\text{sat}})} \quad (\text{B.66})$$

The uncertainty of the HTC is thus calculated as:

$$\delta\alpha = \left[\left(\frac{\partial\alpha}{\partial\dot{Q}_{\text{test}}} \delta\dot{Q}_{\text{test}} \right)^2 + \left(\frac{\partial\alpha}{\partial A_s} \delta A_s \right)^2 + \left(\frac{\partial\alpha}{\partial T_{\text{wall},i}} \delta T_{\text{wall},i} \right)^2 + \left(\frac{\partial\alpha}{\partial T_{\text{sat}}} \delta T_{\text{sat}} \right)^2 \right]^{\frac{1}{2}} \quad (\text{B.67})$$

C. RELEVANT EQUATIONS

C.1. INTRODUCTION

The work done by other authors that was used to include boiling HTC correlations, lumped analysis temperature prediction models, and pressure drop correlations, is detailed in this section. First, the HTC correlations are given by detailing the shared dimensionless numbers and shared correlations between them, and finally the HTC correlations themselves. Next, the lumped system temperature prediction model used is given, before the pressure drop prediction method utilised is presented. The interested reader is directed to the original publications cited.

C.2. HTC CORRELATIONS

The HTC correlations that were used to validate the boiling results the facility produced in Section 4.6.2, and in an attempt to capture the behaviour of the HTC in Section 5.2.5, are well established and have been used in industry and academia. Some of them share many fundamental dimensionless values and correlations, differing in the way they apply them. The first section of this includes these dimensionless numbers, after which the correlations they share, and finally the correlations themselves are provided.

C.2.1. Shared dimensionless numbers

Reynolds number

The Reynolds number forms the basis of much of fluid dynamics, and is simply the ratio of inertial to viscous forces. Many of the correlations applied in this work use only the liquid Reynolds number, Re_f . The traditional form of the Reynolds number (which includes density, characteristic lengths, and velocity) is rewritten here in a simpler format:

$$Re_f = \frac{(1-x)Gd_i}{\mu_f} \quad (\text{C. 1})$$

Bond number

The Bond number is the ratio of gravitational forces to surface tension, and is used to determine the interplay between these two factors.

$$Bd = \frac{g(\rho_f - \rho_g)d_i^2}{\sigma} \quad (\text{C. 2})$$

Boiling number

The Boiling number represents the ratio of the actual heat flux, q , and the maximum achievable heat flux should all the fluid be evaporated. This is used to characterise the effect of heat flux on nucleate boiling.

$$Bo = \frac{\dot{q}}{Gh_{fg}} \quad (C. 3)$$

Convection number

The convection number is simply the ratio of the vapour to the liquid density, and is a means of measuring the dominance of convective boiling.

$$Co = \left(\frac{1-x}{x}\right)^{0.8} \left(\frac{\rho_g}{\rho_f}\right)^{0.5} \quad (C. 4)$$

Confinement number

The confinement number is a way of relating the pipe diameter to the surface tension (similar to the Bond number) and is especially important in pipes with diameters smaller than 3 mm.

$$Cn = \left(\frac{\sigma}{g(\rho_f - \rho_g)d_i}\right)^{0.5} \quad (C. 5)$$

Froude number

The Froude number is the ratio of inertial forces to gravity, and is especially important in low mass flux flows. The liquid Froude number is given by:

$$Fr_f = \frac{G^2}{gd_i\rho_f^2} \quad (C. 6)$$

Martinelli parameter

Used in separated flow models (in which each phase is considered on its own) for both HTC and pressure drop predictions, the Martinelli parameter is defined as:

$$X_{tt} = \left(\frac{1-x}{x}\right)^{0.9} \left(\frac{\rho_g}{\rho_f}\right)^{0.5} \left(\frac{\mu_f}{\mu_g}\right)^{0.1} \quad (C. 7)$$

C.2.2. Shared correlations

Most of the correlations elucidated in this appendix utilise a shared correlation to quantify liquid flow HTCs and nucleate boiling HTCs. These are given next.

Cooper correlation for nucleate boiling [124]

The Cooper correlation for nucleate boiling produces a HTC for the nucleate contribution to the overall HTC.

$$\alpha_{nb} = 55p_r^{0.12}(-0.4343 \ln p_r)^{-0.55}M^{-0.5}q^{0.67} \quad (C. 8)$$

Dittus-Boelter liquid correlation [125]

The Dittus-Boelter correlation for pure liquid flows is often used as a basis for two-phase flows.

$$\alpha_f = 0.023Re_f^{0.8}Pr^{0.4} \left(\frac{k_f}{d_i} \right) \quad (C. 9)$$

C.2.3. HTC correlations

With the foundation being laid, attention can now be turned to the two-phase HTC correlations.

Gungor-Winterton correlation [99]

The Gungor-Winterton correlation falls under the so-called superposition type models, in which the contribution of the forced convective and nucleate boiling mechanisms is purely additive:

$$\alpha_{tp} = E\alpha_{conv} + S\alpha_{nb} \quad (C. 10)$$

The convective contribution is simply the Dittus-Boelter pure liquid flow correlation, such that $\alpha_{conv} = \alpha_f$. E and S are convective boiling enhancement and nucleate boiling suppression factors, calculated as follows:

$$E = 1 + 24000Bo^{1.16} + 1.37 \left(\frac{1}{X_{tt}} \right)^{0.86} \quad (C. 11)$$

$$S = [1 + 0.00000115E^2Re_f^{1.17}]^{-1} \quad (C. 12)$$

Liu-Winterton correlation [102]

The Liu-Winterton correlation is an asymptotic model which takes the contributions of the nucleate and convective boiling portions into account with the following form:

$$\alpha = [(e_E E \alpha_{conv})^2 + (e_S S \alpha_{nb})^2]^{0.5} \quad (C. 13)$$

Again, $\alpha_{conv} = \alpha_f$, and E and S are enhancement and suppression factors, given by:

$$E = \left[1 + xPr_f \left(\frac{\rho_f}{\rho_g} - 1 \right) \right]^{-0.35} \quad (C. 14)$$

$$S = [1 + 0.055E^{0.1}Re_L^{0.16}]^{-1} \quad (C. 15)$$

The factors e_E and e_S are only applied in horizontal pipes if the Froude number is less than 0.05, as indicated in Table C. 1.

Table C. 1. Froude number correction factors

Correction factor	$Fr_f \leq 0.05$	$Fr_f > 0.05$
e_E	$Fr_f^{(0.1-2Fr_f)}$	1
e_S	$Fr_f^{0.5}$	1

Bertsch correlation [103]

Originally developed for mini- and microchannel flow boiling (i.e., $d_i < 3 \text{ mm}$), it was found by Fang *et al.* [13] that this correlation performed remarkably well for macro pipes as well.

$$\alpha = \alpha_{nb}(1 - x) + \alpha_{conv}(1 + 80(x^2 + x^6)e^{-0.6cn}) \quad (\text{C. 16})$$

Interestingly, α_{conv} , is not taken to be the Dittus-Boelter liquid HTC correlation, but rather a combination of the liquid and vapour HTC resulting from the Hausen correlation for laminar flow:

$$\alpha_f = \left(3.66 + \frac{0.0668 \frac{d_i}{L} Re_f Pr}{1 + 0.04 \left[\frac{d_i}{L} Re_f Pr \right]^{0.66}} \right) \frac{k_f}{d_i} \quad (\text{C. 17})$$

$$\alpha_g = \left(3.66 + \frac{0.0668 \frac{d_i}{L} Re_g Pr}{1 + 0.04 \left[\frac{d_i}{L} Re_g Pr \right]^{0.66}} \right) \frac{k_g}{d_i} \quad (\text{C. 18})$$

$$\alpha_{conv} = \alpha_f(1 - x) + \alpha_g x \quad (\text{C. 19})$$

Importantly, Re_f and Re_g are calculated as if the entire flow was either liquid or vapour (i.e., disregarding the vapour quality in Equation (C. 1)).

Fang correlation [100]

A correlation developed for cases where the wall temperature and heat flux are known, this correlation is given as:

$$\alpha = \frac{k_f}{d_i} F_f M^{-0.18} Bo^{0.98} Fr^{0.48} Bd^{0.72} \left(\frac{\rho_f}{\rho_g} \right)^{0.29} \left[\ln \frac{\mu_f}{\mu_{f,wall}} \right]^{-1} Y \quad (\text{C. 20})$$

In this, F_f is a fluid dependent parameter, taken as 1 850 for R-245fa, and Y is a factor determined by the reduced pressure, as shown below:

$$Y = 1 \text{ for } p_r \leq 0.43 \quad (\text{C. 21})$$

$$Y = 1.38 - p_r^{1.15} \text{ for } p_r > 0.43$$

Kandlikar correlation [104]

The Kandlikar correlation is of the class of correlations that calculate the nucleate and convective boiling HTC separately, picking the largest resulting value. The equation is shown below:

$$\alpha = \alpha_f [C_1 Co^{C_2} (25 Fr_f)^{C_5} + C_3 Bo^{C_4} F_f] \quad (C. 22)$$

The various constants (C_1 to C_5), were determined and are shown for both the convective and nucleate boiling region in Table C. 2. Note that C_4 is constant for both convective and nucleate boiling, and that C_5 depends on the liquid Froude number.

Table C. 2. Constants for use in the Kandlikar correlation

Constant		Convective boiling region	Nucleate boiling region
C_1		1.136	0.6683
C_2		-0.9	-0.2
C_3		667.2	1058
C_4		0.7	
C_5	$Fr_f \leq 0.04$	0.3	
	$Fr_f > 0.04$	0	

Wojtan-Ursenbacher-Thome correlation [101]

The Wojtan-Ursenbacher-Thome HTC correlation differs from the other correlations covered thus far in that it is a flow-pattern based method. This means that it is an involved process to obtain the predicted flow pattern, and from there the HTC. The equation for HTC is given first:

$$\alpha = \frac{d_i \theta_{\text{dry}} \alpha_{\text{vapor}} + d_i (2\pi - \theta_{\text{dry}}) \alpha_{\text{wet}}}{2\pi d_i} \quad (C. 23)$$

In this, the wetted perimeter of the pipe provides a nucleate boiling and convective boiling contribution:

$$\alpha_{\text{wet}} = ((S\alpha_{\text{nb}})^3 + \alpha_{\text{conv}}^3)^{0.33} \quad (C. 24)$$

Here, the nucleate boiling suppression factor is a fixed value, $S = 0.8$. The nucleate boiling contribution, α_{nb} , is given by the Cooper correlation given previously, while the convective contribution is given by:

$$\alpha_{conv} = 0.0133 \left[\frac{4G(1-x)\delta}{(1-\varepsilon)\mu_f} \right]^{0.69} \left[\frac{c_{p,f}\mu_f}{k_f} \right]^{0.4} \frac{k_f}{\delta} \quad (C. 25)$$

A film flow rather than a tubular flow is considered when calculating the convective contribution, and the void fraction, ε , as well as the film thickness, δ , are required. The void fraction is calculated using the horizontal Steiner [109] modification to the Rouhani-Axelsson [111] drift flux model:

$$\varepsilon = \frac{x}{\rho_g} \left\{ [1 + 0.12(1-x)] \left(\frac{x}{\rho_g} + \frac{1-x}{\rho_f} \right) + \frac{1.18}{G} \left[\frac{g\sigma(\rho_f - \rho_g)}{\rho_f^2} \right]^{0.25} (1-x) \right\}^{-1} \quad (C. 26)$$

The film thickness is calculated using the area occupied by the liquid phase, A_L :

$$\delta = \frac{d_i}{2} - \left[\left(\frac{d_i}{2} \right)^2 - \frac{2A_L}{2\pi - \theta_{dry}} \right]^{0.5} \quad (C. 27)$$

This area, A_L , is calculated using the void fraction and the total cross-sectional area, A_c :

$$A_L = A_c(1 - \varepsilon) \quad (C. 28)$$

Finally, a tubular flow on the dry perimeter of the pipe is considered in order to calculate the HTC contribution of α_{vapor} :

$$\alpha_{vapor} = 0.023 \left[\frac{Gxd_i}{\varepsilon\mu_g} \right]^{0.8} \left[\frac{c_{p,g}\mu_g}{k_f} \right]^{0.4} \frac{k_g}{d_i} \quad (C. 29)$$

Calculating the dry angle on the perimeter of the pipe, θ_{dry} , and determining what the flow pattern is, is beyond the scope of this appendix. Interested readers are referred to the cited source. Should the flow pattern be annular or intermittent, the perimeter of the pipe is always completely wet, and thus $\theta_{dry} = 0$.

C.3. LUMPED SYSTEM TEMPERATURE PREDICTION MODEL

As discussed in Section 6.4, the temperature of the copper pipe was needed for the preheater during the transient to capture the energy discharge of the copper when a step heat flux was applied. Since

it was not instrumented, no instantaneous temperature readings could be taken with which to characterise this. A different way was thus sought to predict the wall temperature.

Since the Biot number was so low, a lumped system analysis was performed, as was found in Özişik [108]. Because the boundary conditions were mixed (i.e., one surface of the pipe was exposed to convection, the other to a heat flux), the resulting linear homogeneous differential equation is:

$$\frac{d(T(t) - T_{\infty})}{dt} + \frac{\alpha_{\text{pre}}}{\rho_{\text{Cu}} c_{\text{p,Cu}} L_{\text{c,pre}}} (T(t) - T_{\infty}) = \frac{q_{\text{pre}}}{\rho_{\text{Cu}} c_{\text{p,Cu}} L_{\text{c,pre}}} \quad (\text{C. 30})$$

The solution to this differential equation is:

$$T(t) = (T_0 - T_{\text{sat}})e^{-mt} + (1 - e^{-mt}) \frac{\dot{Q}_{\text{pre}}(t)}{\alpha_{\text{pre}} A_{\text{s,pre}}} + T_{\text{sat}} \quad (\text{C. 31})$$

$$\text{where } m = \frac{\alpha_{\text{pre}}}{\rho_{\text{Cu}} c_{\text{p,Cu}} L_{\text{c,pre}}}.$$

C.4. PRESSURE DROP CORRELATION

The number of correlations to predict frictional pressure drops for two-phase boiling almost rivals the number used to predict the HTC. In the interests of keeping this study focused, a simple pressure drop correlation that was sufficiently accurate was sought. The Müller-Steinhagen and Heck [112] correlation was found to be one of the simplest most robust predictive methods. It is given in abbreviated form here:

$$\left(\frac{dp}{dz}\right)_{\text{frict}} = H(1 - x)^{0.33} + Bx^3 \quad (\text{C. 32})$$

The factor G is given as

$$H = A + 2(B - A)x \quad (\text{C. 33})$$

A and B are the frictional pressure gradients considering all the flow as liquid or all the flow as vapour, respectively:

$$A = \left(\frac{dp}{dz}\right)_{\text{frict,f}} = f_f \frac{2G^2}{d_i \rho_f} \quad (\text{C. 34})$$

$$B = \left(\frac{dp}{dz}\right)_{\text{frict,g}} = f_g \frac{2G^2}{d_i \rho_g} \quad (\text{C. 35})$$

The friction factors, f_f and f_g , are determined from:

$$f_f = \frac{0.079}{Re_f^{0.25}} \quad (\text{C. 36})$$

$$f_g = \frac{0.079}{Re_g^{0.25}} \quad (\text{C. 37})$$

The Reynolds number is calculated using Equation (C. 1), but crucially, the quality is neglected.

D. CALIBRATION CERTIFICATES

D.1. INTRODUCTION

The absolute pressure sensors used in this work had been in service since 2010, and thus required recalibration and possible replacement if the calibration results were unsatisfactory. Fortunately, this was not the case. The calibration certificates are provided in this appendix, with the calibration equations being provided in Appendix A.4.

D.2. CERTIFICATES

**WIKA Instruments (Pty) Ltd.
South Africa**

**SANAS Accredited Laboratory
Number 246
for
Pressure Metrology**



Certificate Number 01-00001749

CALIBRATION CERTIFICATE

<p>Calibration of a Manufacturer Type Serial number Customer Order No. Number of pages of the calibration certificate Date of calibration Recalibration Date As Per Customer</p>	<p>Pressure transmitter GEMS Sensors & Controls 2200BGB2501A3UB P075690 University of Pretoria Engineering 3 - Lynnwood Road Hatfield Campus Hatfield 0083 560172 5 22/02/2018 February 2019</p>	<p>This calibration certificate documents the traceability to national standards and international standards, which realise the units of measurement according to the International System of Units (SI).</p> <p>The South African National Accreditation System (SANAS) is a member of the International Laboratory Accreditation Cooperation (ILAC) Mutual Recognition Arrangement (MRA). This arrangement allows for the mutual recognition of technical test and calibration data by member accreditation bodies worldwide. For more information on the arrangement please consult www.ilac.org</p> <p>The measurement results recorded in this certificate were correct at the time of calibration and the results are only valid for the instrument calibrated. The subsequent accuracy of the instrument will depend on factors such as care, handling, frequency of use, operating temperature and use under conditions other than specified by the manufacturer and or conditions of calibration. It is recommended that recalibration be undertaken, by the user, at an interval that will ensure that the instrument remains within the desired limits.</p> <p>Legal liability shall be limited to the cost of recalibration and or certification, but the applicant indemnifies WIKA INSTRUMENTS against any consequential or other loss.</p>
--	--	---

This calibration certificate may not be reproduced other than in full except with the permission of the issuing laboratory. Calibration certificates without Technical Signatory's signature and seal are not valid.

<p>Date of issue 22/02/2018</p>	<p>Calibrated by Peresh Wellcome Metrologist and Lab Manager</p>	<p>Technical Signatory Peresh Wellcome</p>	<p>Seal </p>
--	---	---	------------------

Wika Instruments (Pty) Ltd
Chilvers Street, Denver, 2094
Johannesburg, South Africa
PO Box 75225, Gardenview, 2047

Tel: (011) 621 0000
Fax: (011) 621 0059
email: sales.za@wika.com

Figure D. 1. Calibration certificate for pressure transducer ahead of pump

**WIKA Instruments (Pty) Ltd.
South Africa**

**SANAS Accredited Laboratory
Number 246
for
Pressure Metrology**



Certificate Number 01-00001750

CALIBRATION CERTIFICATE

<p>Calibration of a Manufacturer Type Serial number Customer Order No. Number of pages of the calibration certificate Date of calibration Recalibration Date As Per Customer</p>	<p>Pressure transmitter GEMS Sensors & Controls 2200BGB2501A3UB P075694 University of Pretoria Engineering 3 - Lynnwood Road Hatfield Campus Hatfield 0083 560172 5 22/02/2018 February 2019</p>	<p>This calibration certificate documents the traceability to national standards and international standards, which realise the units of measurement according to the International System of Units (SI).</p> <p>The South African National Accreditation System (SANAS) is a member of the International Laboratory Accreditation Cooperation (ILAC) Mutual Recognition Arrangement (MRA). This arrangement allows for the mutual recognition of technical test and calibration data by member accreditation bodies worldwide. For more information on the arrangement please consult www.ilac.org</p> <p>The measurement results recorded in this certificate were correct at the time of calibration and the results are only valid for the instrument calibrated. The subsequent accuracy of the instrument will depend on factors such as care, handling, frequency of use, operating temperature and use under conditions other than specified by the manufacturer and or conditions of calibration. It is recommended that recalibration be undertaken, by the user, at an interval that will ensure that the instrument remains within the desired limits.</p> <p>Legal liability shall be limited to the cost of recalibration and or certification, but the applicant indemnifies WIKA INSTRUMENTS against any consequential or other loss.</p>
--	--	---

This calibration certificate may not be reproduced other than in full except with the permission of the issuing laboratory. Calibration certificates without Technical Signatory's signature and seal are not valid.

<p>Date of issue 22/02/2018</p>	<p>Calibrated by Peresh Wellcome Metrologist and Lab Manager</p>	<p>Technical Signatory Peresh Wellcome</p>	<p>Seal </p>
--	---	---	------------------

WIKAI Instruments (Pty) Ltd.
Chivers Street, Denver, 2094
Johannesburg, South Africa
PO Box 75225, Gardenview, 2047

Tel.: (011) 621 0000
Fax: (011) 621 0059
email: sales.za@wika.com

Figure D. 2. Calibration certificate for pressure transducer after pump

**WIKA Instruments (Pty) Ltd.
South Africa**

**SANAS Accredited Laboratory
Number 246
for
Pressure Metrology**

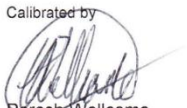



Certificate Number 01-00001751

CALIBRATION CERTIFICATE

Calibration of a	Pressure transmitter	This calibration certificate documents the traceability to national standards and international standards, which realise the units of measurement according to the International System of Units (SI).
Manufacturer	SENSOTEC	
Type	FPG	The South African National Accreditation System (SANAS) is a member of the International Laboratory Accreditation Cooperation (ILAC) Mutual Recognition Arrangement (MRA). This arrangement allows for the mutual recognition of technical test and calibration data by member accreditation bodies worldwide. For more information on the arrangement please consult www.ilac.org
Serial number	1063497	
Customer	University of Pretoria Engineering 3 - Lynnwood Road Hatfield Campus Hatfield 0083	
Order No.	560172	The measurement results recorded in this certificate were correct at the time of calibration and the results are only valid for the instrument calibrated. The subsequent accuracy of the instrument will depend on factors such as care, handling, frequency of use, operating temperature and use under conditions other than specified by the manufacturer and or conditions of calibration. It is recommended that recalibration be undertaken, by the user, at an interval that will ensure that the instrument remains within the desired limits.
Number of pages of the calibration certificate	5	Legal liability shall be limited to the cost of recalibration and or certification, but the applicant indemnifies WIKA INSTRUMENTS against any consequential or other loss.
Date of calibration	23/02/2018	
Recalibration Date As Per Customer	February 2019	

This calibration certificate may not be reproduced other than in full except with the permission of the issuing laboratory. Calibration certificates without Technical Signatory's signature and seal are not valid.

Date of issue	Calibrated by	Technical Signatory	Seal
23/02/2018	 Peresh Wellcome Metrologist and Lab Manager	 Peresh Wellcome	

WIKAL Instruments (Pty) Ltd.
Chilvers Street, Denver, 2094
Johannesburg, South Africa
PO Box 75225, Gardenview, 2047

Tel: (011) 621 0000
Fax: (011) 621 0059
email: sales.za@wika.com

Figure D. 3. Calibration certificate for pressure transducer ahead of preheater

**WIKA Instruments (Pty) Ltd.
South Africa**

**SANAS Accredited Laboratory
Number 246
for
Pressure Metrology**



Certificate Number 01-00001752

CALIBRATION CERTIFICATE

<p>Calibration of a Manufacturer Type Serial number Customer Order No. Number of pages of the calibration certificate Date of calibration Recalibration Date As Per Customer</p>	<p>Pressure transmitter SENSOTEC FPG 1062912 University of Pretoria Engineering 3 - Lynnwood Road Hatfield Campus Hatfield 0083 560172 5 23/02/2018 February 2019</p>	<p>This calibration certificate documents the traceability to national standards and international standards, which realise the units of measurement according to the International System of Units (SI).</p> <p>The South African National Accreditation System (SANAS) is a member of the International Laboratory Accreditation Cooperation (ILAC) Mutual Recognition Arrangement (MRA). This arrangement allows for the mutual recognition of technical test and calibration data by member accreditation bodies worldwide. For more information on the arrangement please consult www.ilac.org</p> <p>The measurement results recorded in this certificate were correct at the time of calibration and the results are only valid for the instrument calibrated. The subsequent accuracy of the instrument will depend on factors such as care, handling, frequency of use, operating temperature and use under conditions other than specified by the manufacturer and or conditions of calibration. It is recommended that recalibration be undertaken, by the user, at an interval that will ensure that the instrument remains within the desired limits.</p> <p>Legal liability shall be limited to the cost of recalibration and or certification, but the applicant indemnifies WIKA INSTRUMENTS against any consequential or other loss.</p>
--	---	---

This calibration certificate may not be reproduced other than in full except with the permission of the issuing laboratory. Calibration certificates without Technical Signatory's signature and seal are not valid.

<p>Date of issue 23/02/2018</p>	<p>Calibrated by  Peresh Wellcome Metrologist and Lab Manager</p>	<p>Technical Signatory  Peresh Wellcome</p>	<p>Seal </p>
--	--	---	---

WIKA Instruments (Pty) Ltd.
Chilvers Street, Denver, 2094
Johannesburg, South Africa
PO Box 75225, Gardenview, 2047

Tel: (011) 621 0000
Fax: (011) 621 0059
email: sales.za@wika.com

Figure D. 4. Calibration certificate for pressure transducer after condenser

**WIKA Instruments (Pty) Ltd.
South Africa**

**SANAS Accredited Laboratory
Number 246
for
Pressure Metrology**



Certificate Number 01-0001753

CALIBRATION CERTIFICATE

Calibration of a	Pressure transmitter
Manufacturer	SENSOTEC
Type	FPG
Serial number	1064716
Customer	University of Pretoria Engineering 3 - Lynnwood Road Hatfield Campus Hatfield 0083
Order No.	560172
Number of pages of the calibration certificate	5
Date of calibration	23/02/2018
Recalibration Date As Per Customer	February 2019

This calibration certificate documents the traceability to national standards and international standards, which realise the units of measurement according to the International System of Units (SI).

The South African National Accreditation System (SANAS) is a member of the International Laboratory Accreditation Cooperation (ILAC) Mutual Recognition Arrangement (MRA). This arrangement allows for the mutual recognition of technical test and calibration data by member accreditation bodies worldwide. For more information on the arrangement please consult www.ilac.org

The measurement results recorded in this certificate were correct at the time of calibration and the results are only valid for the instrument calibrated. The subsequent accuracy of the instrument will depend on factors such as care, handling, frequency of use, operating temperature and use under conditions other than specified by the manufacturer and or conditions of calibration. It is recommended that recalibration be undertaken, by the user, at an interval that will ensure that the instrument remains within the desired limits.

Legal liability shall be limited to the cost of recalibration and or certification, but the applicant indemnifies WIKA INSTRUMENTS against any consequential or other loss.

This calibration certificate may not be reproduced other than in full except with the permission of the issuing laboratory. Calibration certificates without Technical Signatory's signature and seal are not valid.

Date of issue	Calibrated by	Technical Signatory	
23/02/2018	 Peresh Wellcome Metrologist and Lab Manager	 Peresh Wellcome	

WIKAI Instruments (Pty) Ltd.
Chivers Street, Denver, 2094
Johannesburg, South Africa
PO Box 75225, Gardenview, 2047

Tel: (011) 621 0000
Fax: (011) 621 0059
email: sales.za@wika.com

Figure D. 5. Calibration certificate for pressure transducer ahead of calming section

**WIKA Instruments (Pty) Ltd.
South Africa**

**SANAS Accredited Laboratory
Number 246
for
Pressure Metrology**



Certificate Number 01-00001754

CALIBRATION CERTIFICATE

<p>Calibration of a Manufacturer Type Serial number Customer Order No. Number of pages of the calibration certificate Date of calibration Recalibration Date As Per Customer</p>	<p>Pressure transmitter SENSOTEC FPG 1064919 University of Pretoria Engineering 3 - Lynnwood Road Hatfield Campus Hatfield 0083 560172 5 23/02/2018 February 2019</p>	<p>This calibration certificate documents the traceability to national standards and international standards, which realise the units of measurement according to the International System of Units (SI).</p> <p>The South African National Accreditation System (SANAS) is a member of the International Laboratory Accreditation Cooperation (ILAC) Mutual Recognition Arrangement (MRA). This arrangement allows for the mutual recognition of technical test and calibration data by member accreditation bodies worldwide. For more information on the arrangement please consult www.ilac.org</p> <p>The measurement results recorded in this certificate were correct at the time of calibration and the results are only valid for the instrument calibrated. The subsequent accuracy of the instrument will depend on factors such as care, handling, frequency of use, operating temperature and use under conditions other than specified by the manufacturer and or coditions of calibration. It is recommended that recalibration be undertaken, by the user, at an interval that will ensure that the instrument remains within the desired limits.</p> <p>Legal liability shall be limited to the cost of recalibration and or certification, but the applicant indemnifies WIKA INSTRUMENTS against any consequential or other loss.</p>
--	---	--

This calibration certificate may not be reproduced other than in full except with the permission of the issuing laboratory. Calibration certificates without Technical Signatory's signature and seal are not valid.

<p>Date of issue 23/02/2018</p>	<p>Calibrated by  Peresh Wellcome Metrologist and Lab Manager</p>	<p>Technical Signatory  Peresh Wellcome</p>	<p>Seal </p>
--	--	---	---

WIKAI Instruments (Pty) Ltd.
Chivers Street, Denver, 2094
Johannesburg, South Africa
PO Box 75225, Gardenview, 2047

Tel : (011) 621 0000
Fax: (011) 621 0059
email: sales.za@wika.com

Figure D. 6. Calibration certificate for pressure transducer ahead of heated length

**WIKA Instruments (Pty) Ltd.
South Africa**

**SANAS Accredited Laboratory
Number 246
for
Pressure Metrology**



Certificate Number 01-00001755

CALIBRATION CERTIFICATE

<p>Calibration of a Pressure transmitter</p> <p>Manufacturer SENSOTEC</p> <p>Type FPG</p> <p>Serial number 1064720</p> <p>Customer University of Pretoria Engineering 3 - Lynnwood Road Hatfield Campus Hatfield 0083</p> <p>Order No. 560172</p> <p>Number of pages of the calibration certificate 5</p> <p>Date of calibration 23/02/2018</p> <p>Recalibration Date As Per Customer February 2019</p>	<p>This calibration certificate documents the traceability to national standards and international standards, which realise the units of measurement according to the International System of Units (SI).</p> <p>The South African National Accreditation System (SANAS) is a member of the International Laboratory Accreditation Cooperation (ILAC) Mutual Recognition Arrangement (MRA). This arrangement allows for the mutual recognition of technical test and calibration data by member accreditation bodies worldwide. For more information on the arrangement please consult www.ilac.org</p> <p>The measurement results recorded in this certificate were correct at the time of calibration and the results are only valid for the instrument calibrated. The subsequent accuracy of the instrument will depend on factors such as care, handling, frequency of use, operating temperature and use under conditions other than specified by the manufacturer and or conditions of calibration. It is recommended that recalibration be undertaken, by the user, at an interval that will ensure that the instrument remains within the desired limits.</p> <p>Legal liability shall be limited to the cost of recalibration and or certification, but the applicant indemnifies WIKA INSTRUMENTS against any consequential or other loss.</p>
--	---

This calibration certificate may not be reproduced other than in full except with the permission of the issuing laboratory. Calibration certificates without Technical Signatory's signature and seal are not valid.

<p>Date of issue</p> <p>23/02/2018</p>	<p>Calibrated by</p>  <p>Peresh Wellcome Metrologist and Lab Manager</p>	<p>Technical Signatory</p>  <p>Peresh Wellcome</p>	<p>Seal</p> 
--	---	--	---

WIKAI Instruments (Pty) Ltd.
Chivers Street, Denver, 2094
Johannesburg, South Africa
PO Box 75225, Gardenview, 2047

Tel.: (011) 621 0000
Fax: (011) 621 0059
email: sales.za@wika.com

Figure D. 7. Calibration certificate for pressure transducer after heated section

**WIKA Instruments (Pty) Ltd.
South Africa**

**SANAS Accredited Laboratory
Number 246
for
Pressure Metrology**



Certificate Number 01-00001756

CALIBRATION CERTIFICATE

<p>Calibration of a Manufacturer Type Serial number Customer Order No. Number of pages of the calibration certificate Date of calibration Recalibration Date As Per Customer</p>	<p>Pressure transmitter SENSOTEC FPG 1064722 University of Pretoria Engineering 3 - Lynnwood Road Hatfield Campus Hatfield 0083 560172 5 23/02/2018 February 2019</p>	<p>This calibration certificate documents the traceability to national standards and international standards, which realise the units of measurement according to the International System of Units (SI).</p> <p>The South African National Accreditation System (SANAS) is a member of the International Laboratory Accreditation Cooperation (ILAC) Mutual Recognition Arrangement (MRA). This arrangement allows for the mutual recognition of technical test and calibration data by member accreditation bodies worldwide. For more information on the arrangement please consult www.ilac.org</p> <p>The measurement results recorded in this certificate were correct at the time of calibration and the results are only valid for the instrument calibrated. The subsequent accuracy of the instrument will depend on factors such as care, handling, frequency of use, operating temperature and use under conditions other than specified by the manufacturer and or conditions of calibration. It is recommended that recalibration be undertaken, by the user, at an interval that will ensure that the instrument remains within the desired limits.</p> <p>Legal liability shall be limited to the cost of recalibration and or certification, but the applicant indemnifies WIKAL INSTRUMENTS against any consequential or other loss.</p>
--	---	--

This calibration certificate may not be reproduced other than in full except with the permission of the issuing laboratory. Calibration certificates without Technical Signatory's signature and seal are not valid.

<p>Date of issue 23/02/2018</p>	<p>Calibrated by  Peresh Wellcome Metrologist and Lab Manager</p>	<p>Technical Signatory  Peresh Wellcome</p>	
--	--	---	---

WIKAL Instruments (Pty) Ltd.
Chivers Street, Denver, 2094
Johannesburg, South Africa
PO Box 75225, Gardenview, 2047

Tel.: (011) 621 0000
Fax: (011) 621 0059
email: sales.za@wika.com

Figure D. 8. Calibration certificate for pressure transducer after test section

